

http://researchcommons.waikato.ac.nz/

Research Commons at the University of Waikato

Copyright Statement:

The digital copy of this thesis is protected by the Copyright Act 1994 (New Zealand).

The thesis may be consulted by you, provided you comply with the provisions of the Act and the following conditions of use:

- Any use you make of these documents or images must be for research or private study purposes only, and you may not make them available to any other person.
- Authors control the copyright of their thesis. You will recognise the author's right to be identified as the author of the thesis, and due acknowledgement will be made to the author where appropriate.
- You will obtain the author's permission before publishing any material from the thesis.

AN INTEGRATED STRATIGRAPHY OF TAURANGA HARBOUR

A thesis

submitted in partial fulfilment

of the requirements for the degree

of

Master of Science (Research)

at

The University of Waikato

by

DAVID MACPHERSON



THE UNIVERSITY OF
WAIKATO
Te Whare Wānanga o Waikato

2016

Abstract

Tauranga Basin is a Quaternary basin filled with successions of terrestrial and coastal sediments. The largest feature of Tauranga Basin is Tauranga Harbour, a 570km^2 estuary. This is home to the Port of Tauranga, New Zealands largest export port. Studies conducted following an initial study by Davis and Healy (1993) have found complex distributions of the sediments within the dredged shipping channel. This research used 86 vibracores and limited seismic data to identify four main facies within the shallow subsurface of the dredged channel and establish their distribution.

Four facies were identified within the shallow subsurface: the Volcanic Sand facies, a silt to fine sand volcaniclastic succession; the Silt facies, a silt to very fine sand lacustrine deposit; the Coastal Sands facies, a medium to coarse coastal sand deposit; and the Pumiceous Sand Facies, a medium to coarse sand succession with abundant pumice.

Within the dredged shipping channel, the Volcanic Sands and Silt facies outcrop at the surface, and appear as ridges in the subsurface. Draped over these ridges is the Coastal Sands facies, which in some cores is overlain by Pumiceous Sands. The Volcanic Sands facies represents a succession of tephra deposits, with some reworking between depositional events. In the Maunganui Roads region of the harbour this is overlain by the lacustrine Silt facies, formed from the reworking of the Volcanic Sands. The region was then inundated by the Holocene marine transgression, leading to the deposition of the Coastal Sands facies, sourced from offshore. This Coastal Sands facies is then overlain in areas by Pumiceous Sands, small mobile sand waves that exist within the shipping channel. These are formed following the erosion of ignimbrite cliffs around the harbour, with some input from the outside the harbour. This represents a change in source for sedimentation in the harbour.

An updated model of the paleogeographic development of the harbour is presented, using data from this and other studies. This model shows the presence of a braided river flowing through Stella Passage, before the development of a lake and the subsequent Holocene marine transgression leading to the evolution of the sand spit and Matakana barrier island.

Acknowledgements

First and foremost I would like to thank my chief supervisor, Dr Bethany Fox. Our weekly meetings kept me on the right track and were incredibly helpful in guiding me through this. Your mountains of feedback were much appreciated. Thanks also to my secondary supervisor, Dr Willem de Lange. I am grateful to have been able to tap into your wealth of knowledge about Tauranga Harbour. Your assistance and feedback was much appreciated.

Secondly, I would like to thank Rowan Johnston and the Port of Tauranga who allowed me to use use the vibracores and the facilities at the port for this research. Without your support this research would not have been possible. Thanks also to Grant Sedgewick for opening the facilities on a daily basis for me, and providing assistance with the generator.

Thank you also to Mike Goble, David Jones and the rest of the team at Pak 'n Save Te Awamutu for accommodating my study requirements alongside work. This was a great experience and hugely appreciated.

Thank you also to all of the staff in the Earth Science programme, in particular Renat Radosinsky for your persistence in teaching me how to make thin sections, and Annette Rodgers for your XRF assistance and for fixing the Laser Sizer on several occasions after a stray shell or three had fallen in. Thank you also to Janine Ryburn and Kirsty Vincent for providing helpful assistance and tuition. Thanks must also go to Lynne Baxter for allowing me to use the greenhouses. Thanks you to Dr Shaun Barker and Dr Vicki Moon for your assistance and feedback, and to Dr Adrian Pittari for your help with thin sections and for organising the Geoscience Conference trip.

Thanks must also go to my parents, family and friends, for providing me with unwavering support and encouragement throughout. Last, but most certainly not least, thank you to my fellow Master's students for providing support and ideas throughout this, it has been an incredible experience, made so much more enjoyable with great people.

Contents

1 Introduction **1**

1.1 Objectives 1

1.2 Thesis Structure 4

2 Literature Review **5**

2.1 Facies Analysis 5

2.2 Grain Size 6

2.2.1 Mathematical Methods 7

2.2.2 Two-Component Diagrams 9

2.3 Magnetic Susceptibility 9

2.4 Geochemistry 10

2.5 Tauranga Basin 12

2.5.1 Stratigraphy 13

2.5.1.1 Basement 13

2.5.1.2 Matua Subgroup 13

2.5.1.3 Pahoia Tephras 17

2.5.1.4 Te Puna Ignimbrite 17

2.5.1.5 Te Ranga Ignimbrite 18

2.5.1.6 Hamilton Ash and Taupo Volcanic Zone Tephras . 18

2.5.1.7 Holocene Sediments 18

2.5.2 Structure 19

2.5.3 Tauranga Harbour 20

2.5.3.1 Dredging 20

2.5.3.2 Sub Surface 22

2.5.4 Paleogeography 24

2.5.4.1 Dates 28

2.5.4.2 Sedimentation Rates 28

2.6 Conclusion 29

3 Methods **31**

3.1 Introduction 31

3.2 Core Description 31

3.3 Grain Size Analysis . . . 32
3.4 Optical Petrography . . . 33
3.5 Magnetic Susceptibility . . . 33
3.6 Portable X-Ray Fluoresence . . . 34
3.7 Scanning Electron Microscope . . . 34
3.8 3-Dimensional Model . . . 35

4 Core Description And Facies Analysis 37
4.1 Introduction . . . 37
4.2 Stella Passage . . . 37
4.2.1 Texture . . . 41
4.2.2 Composition . . . 42
4.2.2.1 Geochemistry . . . 46
4.3 Maunganui Roads South . . . 46
4.3.1 Texture . . . 52
4.3.2 Composition . . . 52
4.3.2.1 Geochemistry . . . 54
4.3.2.2 Magnetic Susceptibility . . . 57
4.4 Maunganui Roads . . . 57
4.4.1 Texture . . . 64
4.4.2 Composition . . . 67
4.4.2.1 Geochemistry . . . 70
4.4.2.2 Scanning Electron Microscope . . . 70
4.4.2.3 Magnetic Susceptibility . . . 71
4.5 Cutter Channel . . . 76
4.5.1 Texture . . . 78
4.5.2 Composition . . . 85
4.5.2.1 Geochemistry . . . 85
4.6 Entrance Channel . . . 87
4.6.1 Texture . . . 89
4.6.2 Composition . . . 94
4.6.2.1 Geochemistry . . . 95
4.7 Facies Analysis . . . 99
4.7.1 Volcanic Sand (VS) . . . 99
4.7.2 Silt (S) . . . 102
4.7.3 Coastal Sand (CS) . . . 105
4.7.4 Pumiceous Sand (PS) . . . 108
4.8 Conclusion . . . 109

5 Distribution **111**
5.1 Introduction 111
5.2 Stella Passage and Maunganui Roads 111
5.3 Cutter Channel 116
5.4 Entrance Channel 119

6 Discussion **125**

7 Conclusion **133**

List of Figures

1.1 Map of the North Island and Tauranga Basin. 2
1.2 Map of the study area showing the locations of the groups of vibracores. See Figure 1.1a for broader geographical location. 3

2.1 Hjulstrom diagram from Press and Siever (1986) showing the current velocity required to move quartz grains on a plane bed at 1 m water depth. This diagram is not valid for other minerals due to variations in density. 8
2.2 Two-component diagram from Friedman (1979) showing skewness vs sorting, with a line plotted to show the distinction between beach and river sands. 9
2.3 Geological map of the Tauranga Region. From Briggs et al. (2005) . 14
2.4 Generalised Stratigraphy of the Tauranga region, from Christophers (2015) using data from Briggs et al. (1996) and Leonard et al. (2010). 15
2.5 Cross section of Stella Passage, developed by Moon et al. (2013) . . 16
2.6 Seismic from offshore Bay of Plenty showing a heavily faulted block overlain by a relatively undeformed sedimentary sequence. From Davey et al. (1995) 19
2.7 Map of Tauranga Harbour showing a broad outline of the dredged shipping channel and the areas within it. See Figure 1.1b 21
2.8 Cross section through Stella Passage from Davis and Healy (1993). It uses data from a range of sources prior to captial dredging. 23
2.9 Map of Matakana Island, showing the locations of two potential Holocene tidal inlets. After Shepherd et al. (1997) and de Lange et al. (2015). 26
2.10 Changes in the bathymetry of Tauranga Harbour Entrance between 1852 and 2006. From de Lange et al. (2015) using data from Brannigan (2009). 27
2.11 Sedimentation rates calculated from the assumed Pleistocene - Holocene boundary in Christophers (2015) 29

3.1 One vibracore (VC29) obtained by the Port of Tauranga Ltd with a portion removed in order to log the sediments. 32

3.2 Plastic pot used in pXRF analysis. 35

4.1 Map showing locations of the areas in which vibracores have been taken. 38

4.2 Map showing locations of vibracores taken from Stella Passage and Manganui Roads South. See Figure 1.1b 39

4.3 Stratigraphic log of VC1, taken from Stella Passage. The colours represent hues from the Munsell spectrum from when the vibracore was first observed. 40

4.5 Grain size distribution chart of a sub-sample of VC1 taken from 253 cm depth. 41

4.4 Silt bed found in VC1. These beds are only found in VC1 and VC79, indicating that they occur in discontinuous lenses. 41

4.6 Clumps of sediment present in VC78. There are some areas of 2.5YR 7/10 discolouration present in this unit (interpreted to be iron staining). This discolouration continues through to the base of the core. 42

4.7 Grain size statistics plotted against depth for sub-samples taken from Stella Passage. 43

4.8 Skewness plotted against sorting for sub-samples taken from Stella Passage. There is a trend of samples becoming more less finely skewed as they are more poorly sorted. 44

4.9 Stella Passage thin sections of compositional plots 45

4.10 Map showing locations of vibracores taken from Manganui Roads South. See Figure 1.1b for geographic context. 47

4.11 Stratigraphic log of VC3, taken from Manganui Roads South. . . . 48

4.12 Stratigraphic log of VC74, taken from Manganui Roads South. . . 49

4.13 Stratigraphic log of VC77, taken from Manganui Roads South. . . 50

4.14 A selection of XRF data for sediments from Stella Passage. These sediments have a high Zr/Fe ratio, indicating high volcanic input. They also have low Sr and low Ca/Al levels, indicating little or no biogenic input. High levels of potassium are present, indicating a terrestrial environment. Orange = Volcaniclastic sediment. Light blue = silt. Dark blue = medium to coarse sand. Grey = pumiceous sand. 51

4.15 Grain size statistics plotted against depth for sub-samples obtained from Maunganui Road's South vibracores. 53

4.16 Skewness plotted against sorting for sub-samples taken from Manganui Roads South. Three groups are present: A, a well sorted unit containing medium to coarse sands with bioclasts; B, a poorly sorted group containing pumiceous coarse sands from the tops of cores; and C, a poorly to very poorly sorted group containing volcaniclastic sediments and silt. 54
4.17 Pie charts and thin section images of Manganui Roads South thin sections. 55
4.18 Elemantal proportion by depth data for select sites from Manganui Roads South. 56
4.19 Magnetic susceptibility of the silt units measured in VC3. 58
4.21 Map showing locations of vibracores taken from Maunganui Roads. See Figure 1.1b for geographic context. 61
4.22 Stratigraphic log of VC12, taken from Manganui Roads. 62
4.23 Stratigraphic log of VC7, taken from Manganui Roads. 63
4.24 Shell bed in VC63, at 190 cm depth. 64
4.25 Grain size statistics plotted against depth for sub-samples obtained from Manganui Roads vibracores. 65
4.26 Grain size populations from VC12, representative of the variation in grain size in the units in this area. The three samples from 10cm, 150 cm and 180 cm are medium to coarse sands. The sample from 250 cm is a silt. 66
4.27 Cumulative grain size plot for sub-samples analysed from VC12. . 66
4.28 Mean grain size plotted against sorting for sub-samples from Maunganui Roads. 67
4.29 Pie charts and thin section images of sediments from Manganui Roads. 68
4.30 Elemantal proportion by depth data for select sites from Manganui Roads. The silt samples are light blue, coastal sands samples are dark blue and pumiceous sands samples are grey. Light blue = silt. Dark blue = medium to coarse sand. Grey = pumiceous sand. . . . 69
4.31 Framboidal pyrite found in VC12. Only one framboid was found in this sub-sample. However, geochemical analysis suggests more are present at other depths in this core (Section 4.4.2.1). 71
4.33 Selection of images of diatoms found under SEM. The images in the top line are from VC7 and the images in the bottom line are from VC12. All diatoms are damged. 73
4.34 Magnetic susceptibility of the silt units measured in the Manganui Roads group. 75
4.35 Map showing locations of vibracores taken from Cutter Channel. See Figure 1.1b for geographic context. 76

4.36 Oxidising units seen in VC57 at 30 - 70 cm depth. 77
4.37 Rip up clasts present in VC29 at 40 cm depth. 78
4.38 Stratigraphic log of VC18, taken from Cutter Channel. 79
4.39 Stratigraphic log of VC29, taken from Cutter Channel. 80
4.40 Grain size statistics plotted against depth for sub-samples obtained from Cutter Channel vibracores. 81
4.41 Comparison of the cumulative grain size curves for two samples from VC29, showing the difference in grain size. 82
4.42 Skewness versus sorting for sub-samples taken from Cutter Channel. 82
4.43 Pie charts and thin section images of sediments from Cutter Channel. A) shows pumiceous sediment, with abundant volcanic glass. B) shows a medium to coarse sand sample. C) is volcaniclastic sediment from VC29, predominantly composed of lithics. D) is predominantly composed of plagioclase, lithics and bioclasts. 83
4.44 Elemantal proportion by depth data for select sites from Cutter Channel. 84
4.46 Map showing locations of vibracores taken from the Entrance Channel. See Figure 1.1b for geographic context. 88
4.47 Clumps of yellow sand in VC25 at 190 cm depth. 89
4.48 Stratigraphic log of VC52, taken from the Entrance Channel. . . . 90
4.49 Stratigraphic log of VC87, taken from Cutter Channel. 91
4.50 Stratigraphic log of VC92, taken from Cutter Channel. 92
4.51 Grain size statistics plotted against depth for sub-samples obtained from the Entrance Channel vibracores. 93
4.52 Skewness vs Sorting bivariate plot for grain size samples from the Entrance Channel. 94
4.53 Pie charts and thin section images of sediments from the Entrance Channel. 96
4.54 Elemantal proportion by depth data for select sites from the Entrance Channel. Orange = Volcaniclastic sediment. Dark blue = medium to coarse sand. Grey = pumiceous sand. 97
4.56 A selection of grain size data for VS samples. The data shows the range of grain size distributions present within this facies. 100
4.57 a) Average composition of all VS units. b) Thin section image of a Volcanic Sand sample. 100
4.58 A selection of geochemical data for each sample collected. The facies are coloured as follows: VS = brown, S = light blue, CS = blue, CS-Y = yellow and PS = grey. 101
4.59 Skewness plotted against sorting for sub-samples taken from Stella Passage and VC74, from Manganui Roads South. 102

4.60 A selection of grain size data for S samples. 103
4.61 a) Average composition of all Silt units. b) Thin section image of a S sample. 104
4.62 A selection of grain size data for CS samples. The data shows the range of grain size distributions present within this facies. 106
4.63 a) Average composition of all CS units. b) Thin section image of a CS sample. 106
4.64 A selection of grain size data for PS samples. The data shows the range of grain size distributions present within this facies. 108
4.65 a) Average composition of all Pumiceous Sand units. b) Thin section image of a PS sample. 109

5.1 Cross section of Stella Passage and Maunganui Roads. The black lines protruding down into the sediment show the locations of boreholes within 100 m of the cross section. Note that the model show a Silt succession extending through Stella Passage. This is not seen in vibracore data, however it does appear in core descriptions by Moon et al. (2013) 112
5.2 Seismic data from one line through Stella Passage. A shows the location of the line and nearby vibracores. B shows the unedited processed seismic line (from (de Lange et al., 2014)). C shows the interpretted seismic line with identified facies from core logs overlaid. 114
5.3 Seismic data from one line through Maunganui Roads. A shows the location of the line and nearby vibracores. B shows the unedited processed seismic line (from (de Lange et al., 2014)). C shows the interpretted seismic line with identified facies from core logs overlaid. 115
5.4 Map showing the location of the cross section through Cutter Channel. The black lines protruding down into the sediment show the locations of boreholes within 100 m of the cross section. 116
5.5 Cross section across Cutter Channel, showing the ridge of VS sediment present in this area. 117
5.6 Seismic data from one line through Cutter Channel. A shows the location of the line and nearby vibracores. B shows the unedited processed seismic line (from (de Lange et al., 2014)). C shows the interpreted seismic line with identified facies from core logs overlaid. 118
5.7 Map showing the locations of Cross Section (a) and (b). 119
5.8 Seismic data from one line through the Entrance Channel. A shows the location of the line and nearby vibracores. B shows the unedited processed seismic line (from (de Lange et al., 2014)). C shows the interpreted seismic line with identified facies from nearby core logs overlaid. 120

5.9 Cross section (a) of the Entrance Channel. The black lines protruding down into the sediment show the locations of boreholes within 100 m of the cross section. 121
5.10 Cross section (b) of the Entrance Channel. The black lines protruding down into the sediment show the locations of boreholes within 100 m of the cross section. 122

6.1 Generalised stratigraphic column of Maunganui Roads, showing the generalised layout of the facies. 127
6.2 Evolution of Tauranga Harbour as proposed by Davis and Healy (1993). 128
6.3 Chronology of Tauranga Harbour proposed by this study. It shows the presence of a braided river channel (a) transporting coarse sediment through the region. Then between >10,000 - 8,000 yr B.P. a lake develops in the area of what is now Stella Passage, with an alluvial system proposed to be nearby (b). Then following the Holocene marine transgression, sand spits begin to form, and the coastal sands facies is deposited. At 6,000 yr B.P. two inlets exist in Matakana island. Around 5,000 yr B.P. one of these closes up (d). Coastal sands continue to develop, leading to the creation of the Mount Maunganui tombolo. 131

List of Tables

2.1 Radiocarbon dates collected by Davis and Healy (1993) 28
2.2 Radiocarbon dates collected by Christophers (2015) 28

4.1 List of vibracores obtained from Stella Passage. 37
4.2 List of vibracores obtained from Maunganui Roads South. 47
4.3 List of vibracores taken from the Maunganui Roads area. 60
4.4 Table showing the potential sedimentation between the 2 events indicated in magnetic susceptibility data 74
4.5 List of all vibracores obtained from Cutter Channel, and their depth. 76
4.6 List of vibracores obtained from the Entrance Channel. 87
4.7 List of facies identified and the areas in which they are found in the vibracores used for this project. 99
4.8 Facies summary table. 110

Chapter 1

Introduction

Tauranga Basin is a Quaternary basin located in the Bay of Plenty, North Island, New Zealand (Figure 1.1a). It is occupied by a large estuary, Tauranga Harbour, and is home to New Zealand's largest export port, the Port of Tauranga (PoT). Tauranga City (population 114,789 (Statistics New Zealand, 2013)) also occupies this basin. The harbour has been dredged twice in the past to accommodate export growth (Thompson, 2010), and is presently being dredged again over the summer of 2015–16.

Capital dredging in 1991–92 encountered silty sediments within Stella Passage that caused milky-white turbid plumes (de Lange et al., 2014). These plumes were highly visible, causing public concern (de Lange et al., 2014). As a result different dredging techniques need to be used when dredging silty sediment. An intial study was conducted by Davis and Healy (1993) and several technical reports have been produced subsequently attempting to constrain the extent of this silty sediment within the harbour (Healy and Roberts, 1997; Michels and Healy, 1998; Healy et al., 2009; Opus International Consultants Ltd, 2011; Moon et al., 2013; de Lange et al., 2014; Upiap, 2015). These have found contrasting results to the initial research done by Davis and Healy (1993). This thesis will extend our understanding of the distribution of these silty sediments, particularly outside of the harbour.

The field area for this project is an area within the dredged shipping channel within the southern part of Tauranga Harbour, shown in Figure 1.2. The material data set for this project is a set of vibracores between 1 and 3 m long obtained by PoT as part of preliminary dredging investigations. These vibracores were obtainedfrom five areas within the shipping channel. These locations are shown in Figure 1.2.

1.1 Objectives

The main aim of this thesis to produce a detailed description of the subsurface sediments within the harbour, and to use this to describe and model the subsurface stratigraphy of the harbour. In order to complete this aim, I will complete the fol-

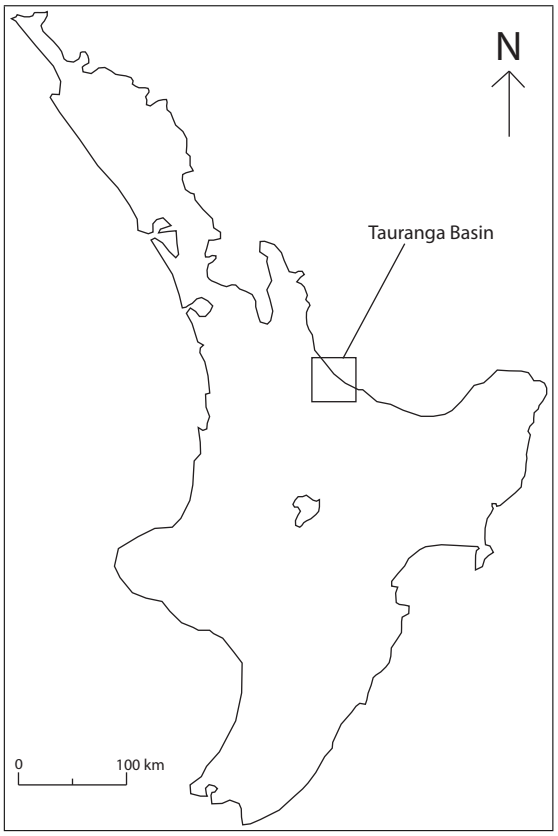

(a) Map of the North Island. Tauranga Basin is marked and enlarged below.

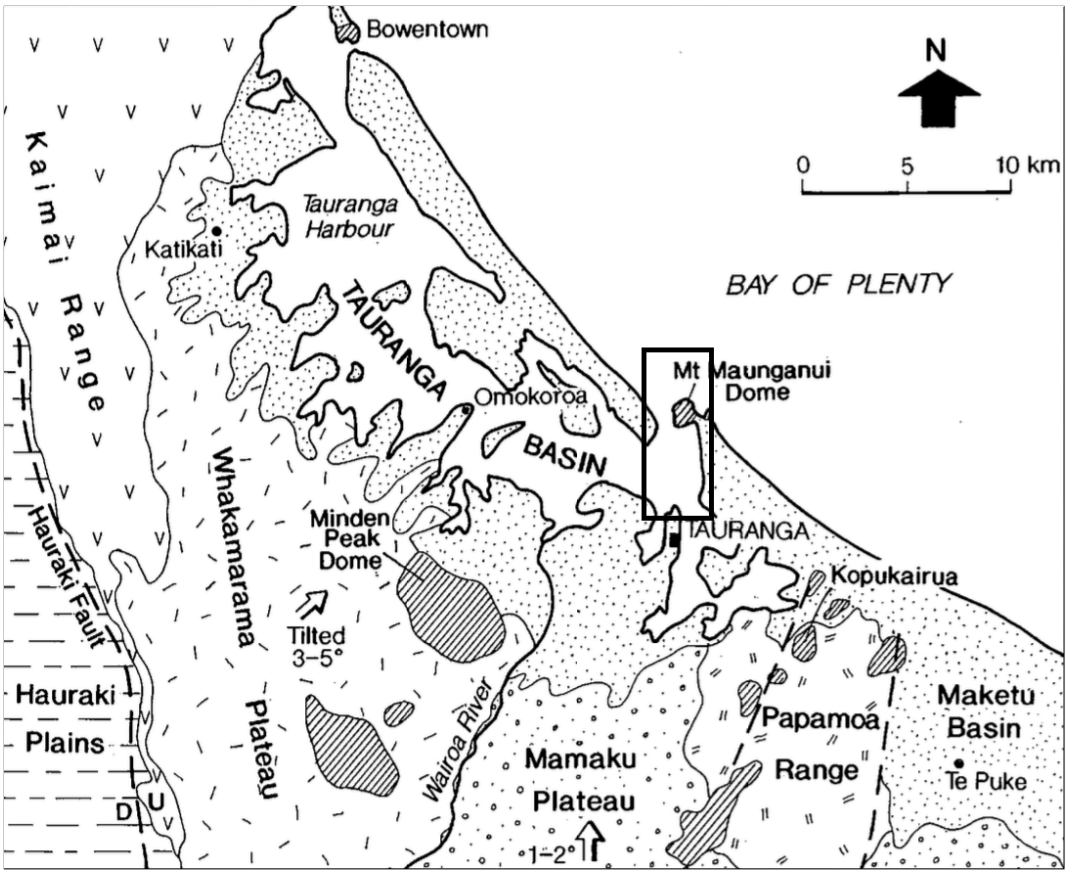

(b) Broad geological map of Tauranga Basin from Briggs et al. (1996). The field area is marked.

Figure 1.1: Map of the North Island and Tauranga Basin.

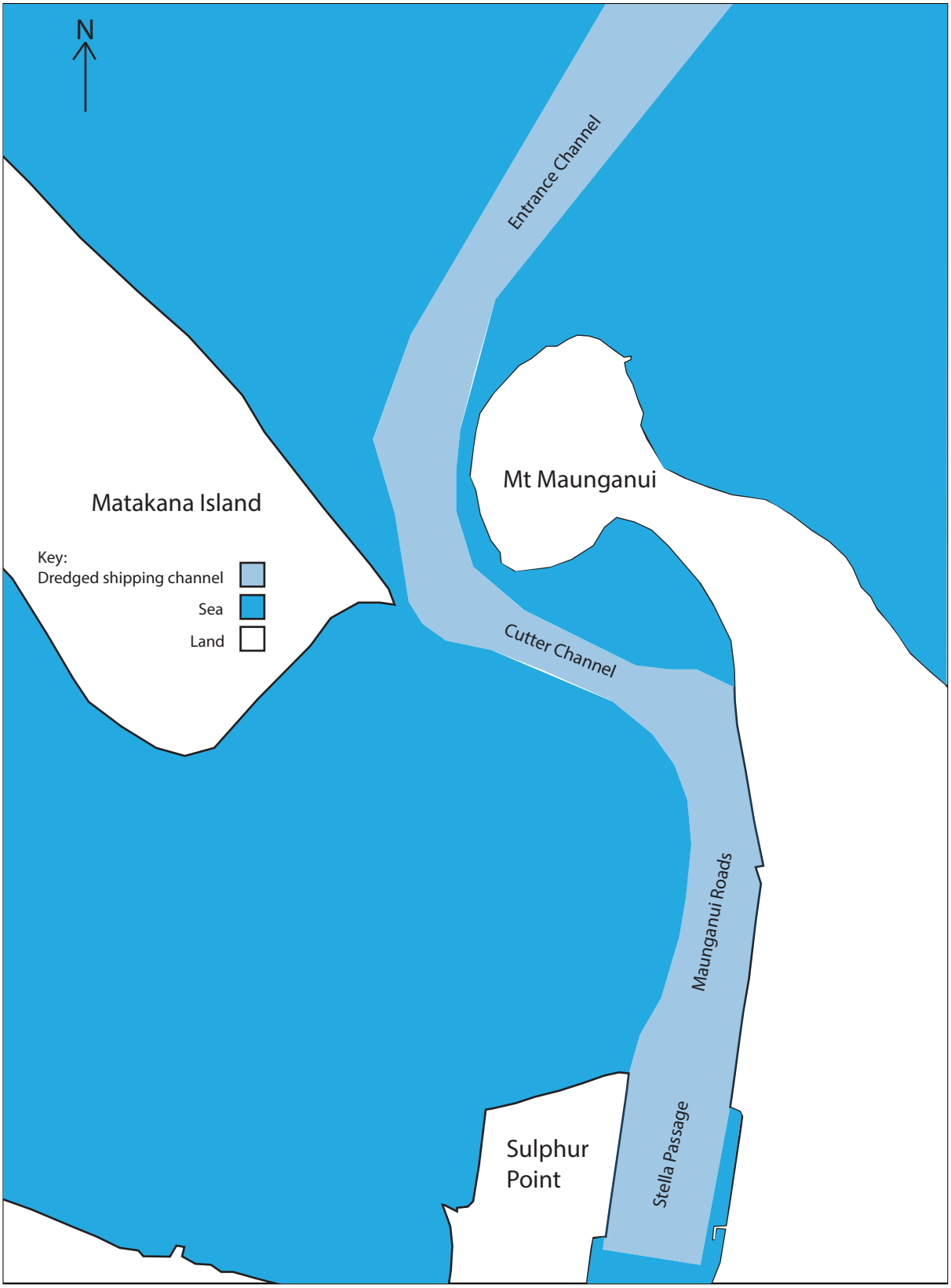

Figure 1.2: Map of the study area showing the locations of the groups of vibracores. See Figure 1.1a for broader geographical location.

lowing objectives:

1. Describe the 86 vibracores obtained by the Port Of Tauranga Limited. Describe grain size, shape, structures, and composition. Conduct grain size, magnetic susceptibility, optical mineralogy and geochemical analysis.

2. Using the data collected, conduct a facies analysis on the identified lithologies within the cores.

3. Develop a 3-D stratigraphic model for the subsurface of Tauranga Harbour using the data collected in this project, along with limited seismic and core data from other research.

1.2 Thesis Structure

Chapter Two: Literature Review
This chapter reviews the background literature on Tauranga Habour and its geology, as well as the surrounding regional geology.

Chapter Three: Methods
This chapter summarizes the methods that were used for this study.

Chapter Four: Core Description and Facies Analysis
This chapter describes the vibracores that were analysed, and presents results of analytical work undertaken on sub-samples. It presents a facies model with interpretations of processes and depositional environment.

Chapter Five: Facies Distribution
This chapter presents a three-dimensional model of the subsurface sediments within the harbour, and describes the distribution of the facies identified in Chapter Four.

Chapter Six: Discussion
This chapter discusses the results of this work, and how they compare with previous work done on the subsurface of Tauranga Harbour.

Chapter Seven: Conclusion
This chapter summarizes the findings of this research and presents some recommendations for areas of further research.

Chapter 2

Literature Review

The following chapter outlines the background of the methods used in this project, and gives some examples of where and how these methods have been used. It then outlines the previous work on the geology of the Tauranga Basin, before looking more closely at the previous research on the geology of and processes occuring in Tauranga Harbour.

2.1 Facies Analysis

Facies analysis is a process used to interpret the genesis of a sedimentary succession (Dalrymple, 2010). It uses the sum of the features of a succession (for example structures, textures, fossils) to give an environmental interpretation of how the succession was deposited (Allaby, 2013; Dalrymple, 2010). This is based on the idea that each of the features of a succession is the result of a process that acted upon it (Dalrymple, 2010).

Facies analysis, as described by Dalrymple (2010) is broken up into the following steps:

1. Make observations in outcrop or core. This includes describing colour, grain size, sorting, composition, structures and fossils present. Not all features in a facies analysis are treated the same and primary attributes, such as grain size, sorting, structures and fossils are given greater value in an interpretation than diagenetic characteristics such as rock colour and cement.

2. Break succession into facies. Often this can only happen after the deposit has been described in detail so that the full range of deposit characteristics are known. This is one of the last things to be done before the interpretation phase begins.

3. Deduce processes responsible for each facies. Involves using all the of the characteristics described in the time spent making observations to make interpretations about a deposit. Facies can be defined using observations of

outcrops and cores, or data from seismic, boreholes, or statistics. The scale of facies depends on the size and scope of the the project, as facies can range in size from individual beds to formations.

4. Combine facies into facies associations and/or facies successions. Individual facies may not suggest any particular environment. However, analysing all of the facies in context may provide more information than the facies individually would. There are two methods of achieving this: facies associations and facies successions. Facies associations are a 1group of facies genetically related to one another and which have some environmental significance' (Collinson, 1969). A facies succession, on the other hand, is the concept that properties of a facies will change progressively in a specific direction (Dalrymple, 2010). This could include the grain size of a section (eg. coarsening upward) or the amount of bioturbation present. Once each facies association and/or succession had been worked out, the depositional environment can be suggested.

5. Combine associations or successions into systems tracts, tectonic facies, etc. Undertake more advanced analysis, such as sequence stratigraphy, paleoclimate reconstruction, environmental change, etc.

Facies analysis was used in the original study of Tauranga Harbour by Davis and Healy (1993). They used it to identify 3 main lithofacies, and then expanded on those lithofacies to reconstruct paleoenvironments. It has also been used in other stratigraphic studies on Holocene estuaries around New Zealand, such as Abrahim et al. (2008), Heap and Nichol (1997), and Wilson et al. (2007).

2.2 Grain Size

The grain size of a particle affects its entrainment, transport, and deposition, making grain size data one of the most useful properties in classifying sedimentary environments (Blott and Pye, 2001; Boggs, 2011). In general, coarser grain size implies higher energy conditions (Figure 2.1). However, the varying density of different minerals can affect this. The grain size of unconsolidated sediment can be measured in several ways, including sieving, laser diffraction and thin-section measurement. These results are categorised using scales such as the Udden-Wentworth scale (Wentworth, 1922), and can be used to provide clues on the depositional conditions, processes and depositional environments occurring at the time of deposition (Boggs, 2009). Syvitski (2007) summarized the uses of grain size data as follows:

1. To interpret coastal stratigraphy and sea-level fluctuations

2. To trace glacial sediment transport and the cycling of glacial sediments from land to sea

3. By marine geochemists to understand the fluxes, cycles , budgets, sources and sinks of chemical elements in nature.

4. To understand the mass physical (geotechnical) properties of sea floor sediment, i.e. the degree to which these sediments are likely to undergo slumping, sliding, or other deformation.

In this study, grain size has been used to identify hydrodynamic conditions and give clues about the depositional environment. Graphical plots have been used as a way of further investigating this.

2.2.1 Mathematical Methods

There are two methods of obtaining mathematical grain size statistics: graphical methods and the method of moments (Boggs, 2011). Graphical methods are faster to compute; however, they cannot find the true statistic for a sample as they do not count every grain in a sample. Instead, graphical methods work by picking selected percentiles from a cumulative curve and averaging those values in ϕ (Boggs, 2011). The method of moments computes statistics with no reference to graphical plots by multiplying a weight (weight frequency of the sample) by a distance (the midpoint of each size grade). Thus, the method of moments can calculate grain size more accurately than the graphical method and does not require conversion of grain size data into ϕ (Boggs, 2011). Various statistics can be obtained by both of these methods, including:

1. **Average grain size.** The average grain size can be calculated in three different ways: the mode, the mean and the median. Depending on the shape of the distribution, the average grain size value returned by each of these methods may not be the same. For this research, the mean grain size was used extensively, and the mode was observed graphically. The logarithmic method of moments equation to find the mean ($\bar{x}_\phi$) was used:

$$\bar{x}_\phi = \frac{\Sigma f m_\phi}{100} \tag{2.1}$$

Where f = weight of, m = midpoint of, n = total number of in sample. The size of a grain can give clues to sediment provenance, transport and deposition.

2. **Sorting.** The sorting (σ_ϕ) of a sample is a measure of the range of grain sizes present and the magnitude of the spread or scatter of these sizes around the

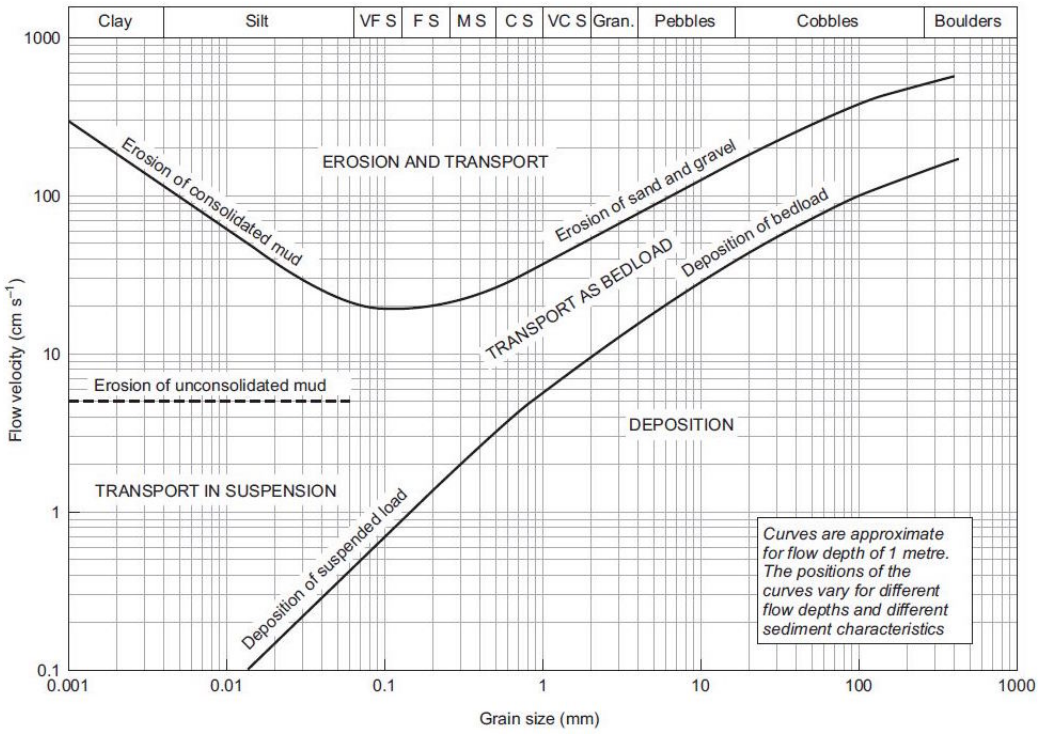

Figure 2.1: Hjulstrom diagram from Press and Siever (1986) showing the current velocity required to move quartz grains on a plane bed at 1 m water depth. This diagram is not valid for other minerals due to variations in density.

mean size. It can be obtained by referencing the sample against a visual estimation chart, or by calculating the standard deviation of a sample.

$$\sigma_\phi = \sqrt{\frac{\Sigma f(m_\phi - \bar{x}_\phi)^2}{100}} \tag{2.2}$$

3. **Skewness and Kurtosis.** The majority of grain size distributions studied in nature do not show a normal, or bell-shaped, distribution. Instead they show an element of asymmetry, or skewness (Boggs, 2011). The skewness value (Sk_ϕ) of a distribution reflects the sorting in a 'tail' of a sample (Boggs, 2011).

$$Sk_\phi = \frac{\Sigma f(m_\phi - \bar{x}_\phi)^3}{100\sigma_\phi^3} \tag{2.3}$$

Kurtosis (K_ϕ) is a measure of the degree of peakedness in a distribution. The geological significance of kurtosis is unknown (Boggs, 2011), however it is used in some two-component diagrams (Syvitski, 2007).

$$K_\phi = \frac{\Sigma f(m_\phi - \bar{x}_\phi)^4}{100\sigma_\phi^4} \tag{2.4}$$

Verbal terms for each of the grain size statistics calculated exist (eg. poorly sorted, symmetrical, fine sand) and are used in this study.

2.2.2 Two-Component Diagrams

Two-component diagrams work by plotting one statistical parameter against another. First popularised by Friedman (1967, 1979)(Figure 2.2), they are one method of graphical presentation of grain size data. Two-component diagrams were used by Friedman (1967, 1979) to attempt to distinguish between depositional environments by plotting grain size statistics on a bivariate plot. In Friedman (1967) skewness was plotted against sorting, and a separation between beach and river sands was identified (Figure 2.2).

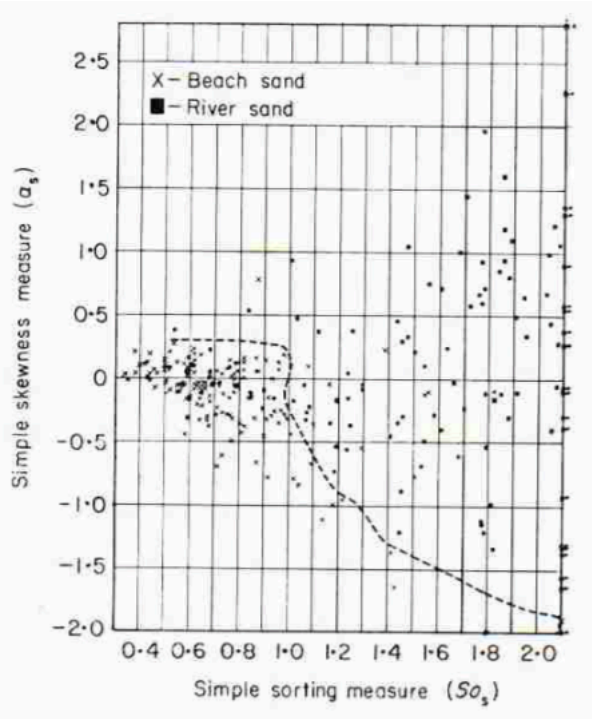

Figure 2.2: Two-component diagram from Friedman (1979) showing skewness vs sorting, with a line plotted to show the distinction between beach and river sands.

The effectiveness of two component diagrams has been questioned (eg. Seminar (1981)) as they can fail to effectively predict the depositional environment. However, they can be an effective way of graphically separating grain size data. For example, Tanner (2007) used kurtosis plotted against skewness to separate river, beach and eolian environments. Gale and Hoare (1991) conclude that attempting to use grain size data as the sole component of paleoenvironment reconstruction is inadequate, and it needs to be combined with other evidence. As such, in this study it is used as a method of identifying clusters and trends in grain size data, before being used alongside other data to identify the depositional environment.

2.3 Magnetic Susceptibility

All substances on earth exhibit some form of magnetic behavior. Magnetic susceptibility measures the “magnetisability” of a material, in this case sediments. Rocks

such as basalt, with relatively high proportions of magnetite, have much higher magnetic susceptibility values than rocks such as limestone which do not usually contain magnetite (Dearing, 1999). Magnetic susceptibility is useful as it is fast, non destructive, can be used on all materials and may complement many other types of environmental analysis (Dearing, 1999). Dearing (1999) summarized the applications of magnetic susceptibility measurements as:

- Identify the Fe-bearing minerals that are present in a sample
- Calculate their concentration or total volume with high resolution
- Classify different types of materials
- Identify the processes of their formation or transport
- Create "environmental fingerprints" for matching materials

Magnetic susceptibility can also be used for core-correlation (Thompson et al., 1975; Dearing et al., 1981), which is its main use in this study. Biogenic materials are diamagnetic (weak, negative magnetic susceptibility) while terrigenous materials usually contain a proportion of ferrimagnetic (strong, positive magnetic susceptibility) material, allowing magnetic susceptibility to be used as a proxy for terrigenous vs biogenic input into a deposit (Blanchet et al., 2007). Magnetic susceptibility can also be used to identify diagenetic alteration (Section 2.4). Blanchet et al. (2007) used magnetic susceptibility to identify terrigenous sediment input in southern Baja California. Yamazaki (2012) used magnetic susceptibility to show variations in ocean productivity between glacials, due to the effect dilution from diagenetic carbonate.

2.4 Geochemistry

Geochemistry uses the principles of chemistry to explain geological processes (Albarède, 2003). Geochemical data can be used as indicators of various processes. Examples are listed below:

- **Iron (Fe)** variations can be used to show variations in terrigenous sediment delivery, continental humidity/aridity and precipitation or river run off changes (Croudace and Rothwell, 2015). Variations in Fe are often related to the terrigenous fraction of the sediment, as Fe is less prominent in clastic sediments (Croudace and Rothwell, 2015). High Fe along with high Sulphur has been interpreted to be a marker of reducing conditions (Sluijs et al., 2008, 2009). This is due to high levels of sulphur available from the biomass of marine plants and high levels of iron available for pyritisation (Croudace and Rothwell, 2015). Decreasing Fe towards the tops of cores has been attributed to increasing water content causing dilution (Mohtadi et al., 2007).

- **Barium (Ba)** has a strong relationship to productivity (Croudace and Rothwell, 2015). Relatively high concentrations of Ba particles occur in near-surface waters of high-productivity (Dehairs et al., 1992; Cardinal et al., 2005). However, Ba diagenesis can reduce Ba concentrations in anoxic sediments, causing lower concentrations (van Os et al., 1991; Brunsack and Gieskes, 1983).

- High **Sulphur (S)** can indicate reducing conditions (Sluijs et al., 2011). S is closely linked to organic matter.

- **Sulphur/Chlorine (S/Cl)** was used by Thomson et al. (2006) to detect enhanced sulphur associated with pyrite or organic carbon, in excess of the constant S/Cl sea-salt ratio.

- **Silica/Aluminum (Si/Al)** has been used as a proxy for biogenic production due to increased biogenic silica. Dickson et al. (2010) found that higher Si/Al suggested a higher nutrient availability due to increased accumulation rates of organic carbon.

- **Arsenic (As)** is an indicator of pyrite authigenesis (Thomson et al., 2006). It substitutes sulphur in pyrite (Peterson and Carpenter, 1986; Huerta-Diaz and Morse, 1992). It is occurs at close to the limit of detection in detrital sediments, making it an excellent pyrite proxy.

- **Strontium (Sr)** is a marker of biogenic carbonate. It is fixed by calcifying organisms at the same time as Ca (Croudace and Rothwell, 2015).

- **Potassium (K)** is an important terrigenous indicator, representing terrestrial siliciclastics (Croudace and Rothwell, 2015).

- **Calcium/Aluminum (Ca/Al)** represents the biogenic/detrital ratio (Croudace and Rothwell, 2015). Ca is related to biogenic carbonate production, while Al is mostly contained in terrigenous silicates and oxides (Blanchet et al., 2009).

- The **Calcium/Strontium (Ca/Sr)** ratio can be used to identify detrital carbonate when Sr is low but Ca is high (Hodell et al., 2008). This is due to biogenic Ca precipitated by coccoliths and foraminifera to be higher in Sr than inorganic Ca (Hodell et al., 2008).

- **Zirconium/Iron (Zr/Fe)** can be an indicator of volcanic input (Konfirst et al., 2011). It occurs in igneous rocks as a product of crystallisation (Croudace and Rothwell, 2015).

- **Iron/Magnetic susceptibility** is a proxy for magnetite diagenesis and Fe reduction (Funk et al., 2003; Hepp et al., 2009). Fe reduction can result in magnetic susceptibility signal loss (Croudace and Rothwell, 2015).

Using these and other geochemical proxies alongside of additional diagnostic methods can give further evidence for source, depositional conditions and diagenesis. In this study, a portable X-ray florescence (pXRF) scanner is used to measure the elemental abundances present in samples. pXRF is fast and non-destructive, making it ideal to use on large numbers of samples.

2.5 Tauranga Basin

Tauranga Basin is a 570km^2 fluvial and estuarine basin of Pleistocene age ((Harmsworth, 1983)) (Figure 2.3). On the west it is bound by the Kaimai Range, an uplifted block of Miocene-Pliocene basaltic to rhyolitic volcanic rocks (Houghton and Cuthbertson, 1989). At the south-eastern end of the basin, it is bordered by the Papamoa Range, separating the Tauranga Basin from the Maketu Basin (Briggs et al., 1996). The Papamoa Range is a series of Pliocene andesitic volcanics, dacitic and rhyolitic domes, and dacitic ignimbrites (Briggs et al., 1996). It separates the Tauranga and Maketu Basins. In the south, the basin is bordered by the Mamaku Plateau, an ignimbrite plateau whose surface dips approximately 1-2°towards Tauranga Basin. The Mamaku Ignimbrite is sourced from the Rotorua Caldera (Nathan, 1976; Wilson et al., 1984). The gentle dip on the Mamaku Plateau is caused by the gradual thinning of the fans and lobes of the deposit towards the Tauranga Basin (Briggs et al., 1996) (Figure 2.3).

Terraces also occur in the Tauranga Basin, typically occurring as NE or NNE trending peninsulas that extend into Tauranga Harbour (Harmsworth, 1983) (Figure 2.3). These flat surfaces are underlain by a variety of deposits representing various depositional processes. These include successions of fluvial, lacustrine, lignite, and estuarine deposits that are intercalated with ignimbrites and airfall tephras overlain by a two to five metre thick succession of younger airfall tephras (Harmsworth, 1983). Tauranga City, Omokoroa and Greerton are built on of these terraces. Harmsworth (1983) attributes these terraces to four major origins:

1. Volcanic constructional surfaces, such as the lobes of pyroclastic flow deposits.

2. Volcanic or fluvial dregedation surfaces that are subsequently covered by airfall tephra.

3. Fluvial terraces formed by aggradation or lateral erosion.

4. Marine aggradation due to higher than present sea level.

A number of volcanic domes also occur within the Tauranga Basin (Figure 2.3). Mount Manganui is a steep sided, flat topped rhyolite dome, and forms a one end

of a tombolo connected to the Papamoa region (Briggs et al., 1996) (Figure 2.3). Mount Drury and the islands of Moturiki and Motuotau are the erosional remnants of rhyolite lavas associated with Mount Maunganui. Other volcanic domes present include Minden Peak, Manawata and Kaikaikaroro, all of which have been flowed around by the younger Waitetariki Ignimbrite (Briggs et al., 1996). These are all part of the Tauranga Volcanic Centre (Briggs et al., 2005).

Volcanic activity in the North Island over the last 7 Myr has shifted from the Coromandel Volcanic Zone (CVZ) down through to the current Taupo Volcanic Zone (Briggs et al., 2005). The Tauranga Volcanic Centre was active from 2.7–1.9 Ma, and comprises the Minden Rhyolite domes and flows of the Tauranga area (Briggs et al., 2005) (Figure 2.3). It is adjacent to the Kaimai Volcanic Centre (2.9–2.1 Ma), which includes the Kaimai and Kakahu domes in the southern Kaimai Range (Kear, 1994). The migration to the Taupo Volcanic Zone has occurred with the continual development of the plate boundary (Kear, 1994). The Taupo Volcanic Zone has been active since 1.8 Ma (Houghton et al., 1995).

2.5.1 Stratigraphy

2.5.1.1 Basement

The Waitetariki Ignimbrite forms the basement rock of the western Tauranga Basin (Figure 2.4). The depth to the formation top ranges from 50 m to 150 m, and the formation is up to 220 m thick (Briggs et al., 1996). It was deposited at 2.18 ± 0.15 Ma (Briggs et al., 2005). The origin of the Waitetariki Ignimbrite is unknown. However, its depositional characteristics suggest a source within the Kaimai Volcanic Centre (Briggs et al., 2005). It is a welded ignimbrite that has been tilted by the uplift of the Kaimai Ranges (Houghton and Cuthbertson, 1989).

2.5.1.2 Matua Subgroup

The Pleistocene Matua Subgroup includes the terrestrial and estuarine sediments deposited following the deposition of the Waitetariki Ignimbrite but excludes the more recent fluvial deposits (Briggs et al., 1996) (Figures 2.3 and 2.4). The Matua Subgroup deposits are the main infilling of the Tauranga Basin, and have been found up to 150 m deep in drill-holes (Harmsworth, 1983). The Matua Subgroup is a very broad group, and includes fluvial pumiceous and rhyolitic silts, sands and gravels, lacustrine and estuarine muds, lignites and peats, air fall tephras and ignimbrites (Harmsworth, 1983). There have been no attempts to construct fence diagrams of the Matua Subgroup across the basin due to the large lateral and vertical variations of the individual beds (Briggs et al., 2005).

Sediments within the Matua Subgroup are thought to originate from the reworking of consolidated and unconsolidated volcanics within the region (Harmsworth,

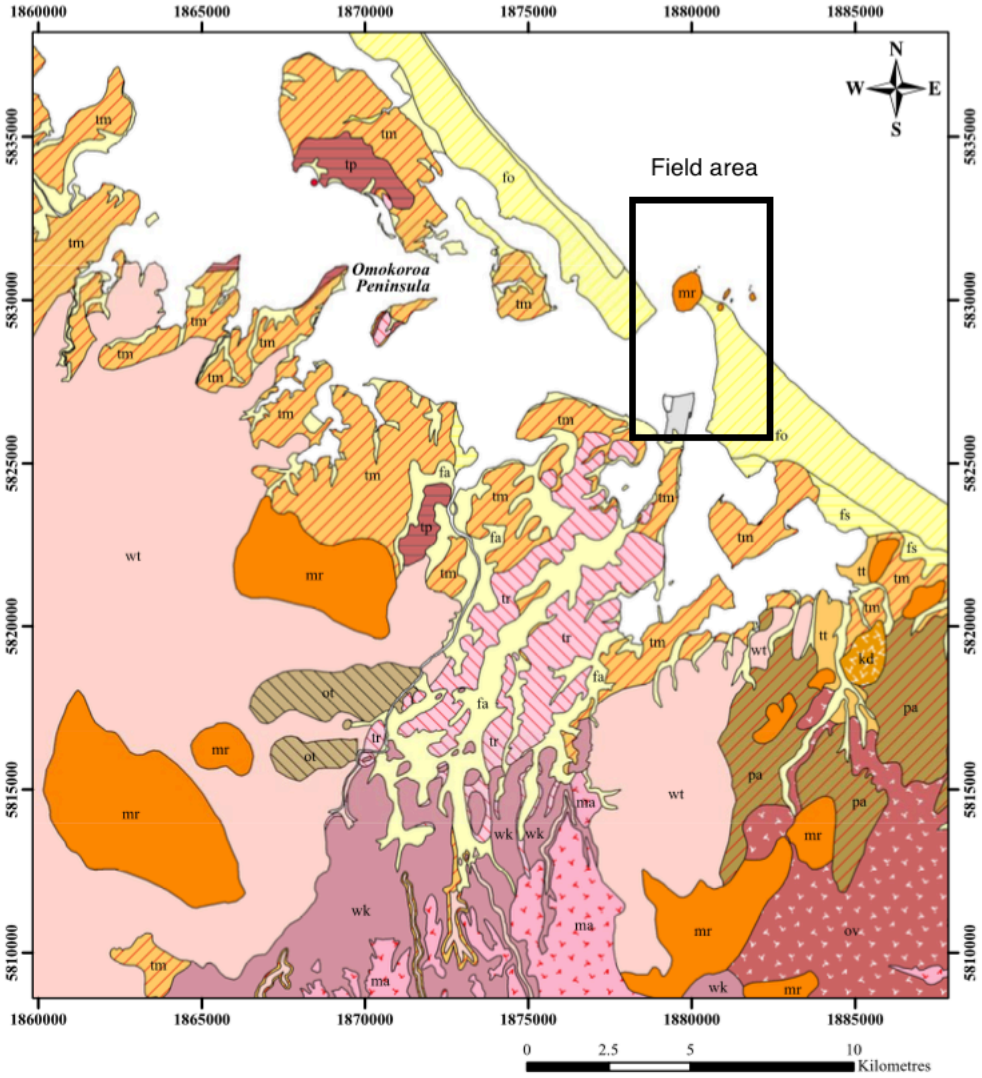

Geological Legend

Reclaimed land	Te Ranga Ignimbrite
Sand, silt and gravel of modern streams	Te Puna Ignimbrite
Fixed foredunes	Ongatiti Ignimbrite
Moving dune sand	Papamoa Ignimbrite
Peat	Waitieariki Ignimbrite
Fluvial terrace deposits post-dating Hamilton Ash	Kopukairua Dacite
Fluvial terrace deposits post-dating Waiteariki Ig.	Matakana Basalt
Mamaku Ignimbrite	Minden Rhyolite
Waimakariri Ignimbrite	Otawa Volcanics

Figure 2.3: Geological map of the Tauranga Region. From Briggs et al. (2005)

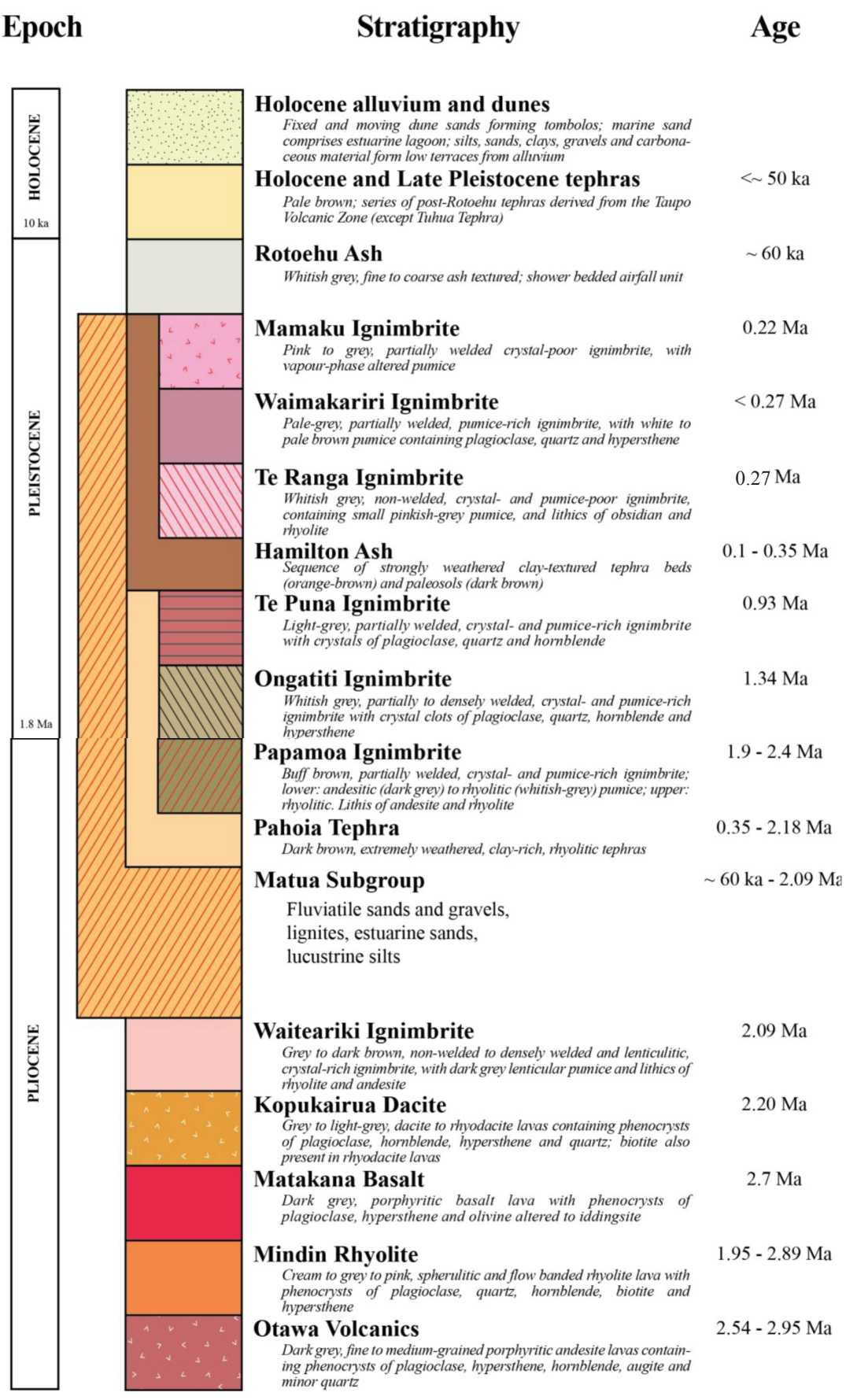

Figure 2.4: Generalised Stratigraphy of the Tauranga region, from Christophers (2015) using data from Briggs et al. (1996) and Leonard et al. (2010).

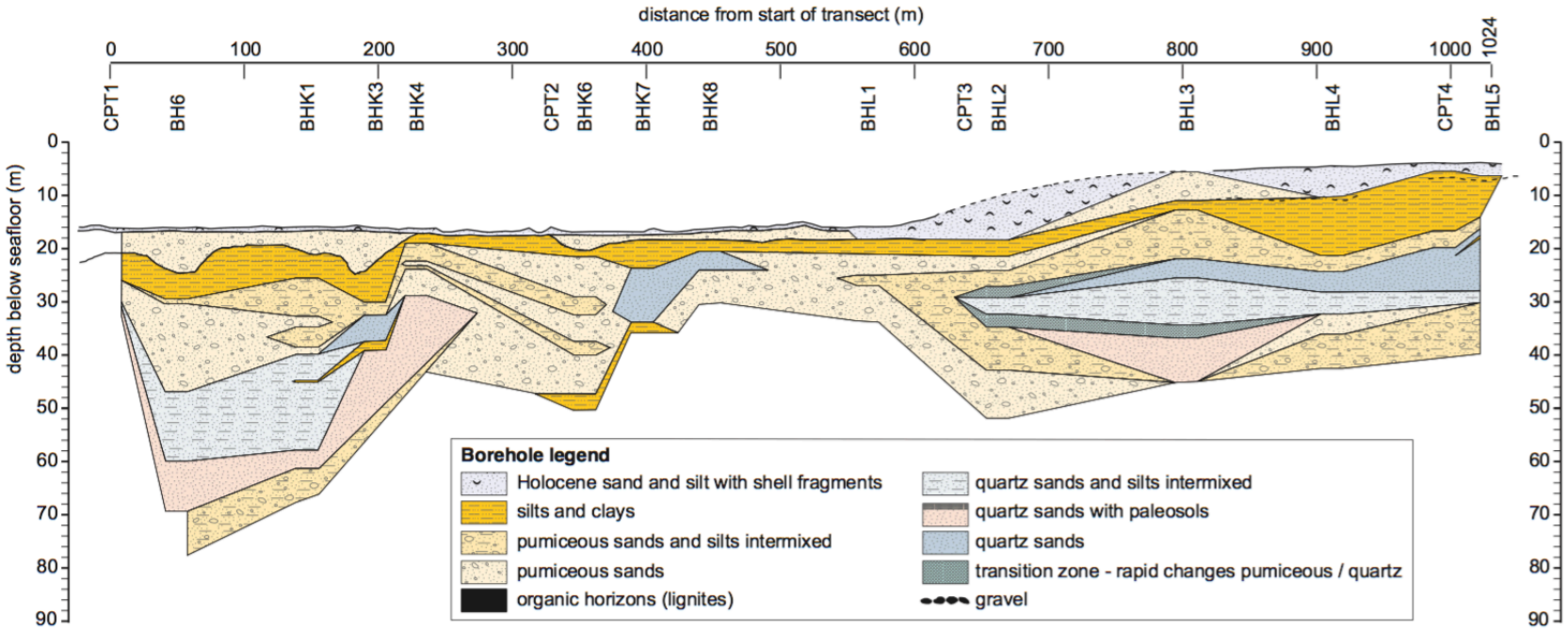

Figure 2.5: Cross section of Stella Passage, developed by Moon et al. (2013). It is a mosaic of deposits, with very few laterally continuous units.

1983), such as the Pahoia Tephra, Te Puna Ignimbrite, Te Ranga Ignimbrite, and the other volcanic deposits shown in Figure 2.4. A range of sedimentary structures occur within the Matua Subgroup, including cross-bedding, planar stratified and massive units, and post-depositional slump and water escape structures (Harmsworth, 1983), indicating large variations in depositional conditions.

The Matua Subgroup was identified in a study of Stella Passage by Moon et al. (2013) below the inferred Pleistocene-Holocene boundary (Figure 2.5). This boundary is inferred by Moon et al. (2013) and de Lange et al. (2014) as an unconformity between marine sands and terrestrial silts. The Matua Subgroup deposits identified in this study included pumiceous sediments, paleosols and swamp deposits, indicating terrestrial deposition for the majority of the succession, and are described by Moon et al. (2013) as a complex unit. Moon et al. (2013) suggested deposition in an alluvial-fan environment with rapidly migrating river channels depositing coarse channel sediments, finer overbank deposits, and small swamps and lakes with peat formation. They estimated that the main river channel is estimated as up to 300 m across, indicating a braided river with multiple shallow channels (Moon et al., 2013) (Figure 2.5).

2.5.1.3 Pahoia Tephras

The Pahoia Tephras include all tephras older than the Hamilton Ash Formation within the Tauranga Basin (Briggs et al., 1996). The Pahoia Tephras are intercalated with fluvial and other sediments in the Matua Subgroup, as well as with distal ignimbrites and paleosols (Harmsworth, 1983). The Pahoia Tephras may be related to the Kauroa Ash Formation that underlies the Hamilton Ash in much of the Waikato Region (Briggs et al., 1996). The Pahoia Tephras have a date range of 2.18–0.35 Ma (Briggs et al., 1996) (Figure 2.4).

2.5.1.4 Te Puna Ignimbrite

The Te Puna Ignimbrite is a non-welded to partially welded buff brown ignimbrite containing white to fibrous grey pumice (Whitbread-Edwards, 1994) (Figure 2.3, 2.4). It was first identified by Harmsworth (1983) then described in more detail by Whitbread-Edwards (1994). It is confined to outcrops around Tauranga Harbour, so initially it was classified as a small volume ignimbrite (Whitbread-Edwards, 1994). However, Briggs et al. (2005) dated it to 0.98 Ma, indicating it is more likely a distal equivalent of widespread ignimbrites from the Taupo Volcanic Zone. At an outcrop in Omokoroa the Te Puna ignimbrite overlies lignites and fluvial pumiceous sands, suggesting it flowed into an estuarine or swampy lake margin environment (Briggs et al., 2005).

2.5.1.5 Te Ranga Ignimbrite

The Te Ranga Ignimbrite is a light grey, non-welded, crystal-poor, sandy textured ignimbrite (Hollis, 1995) (Figure 2.3, 2.4) . It is characterised by a coarse glass-shard texture with shards colourless or tinted light brown (Hollis, 1995). It is unconsolidated and non-welded. However its texture and the presence of carbonised logs indicate a hot emplacement and pyroclastic flow origin (Hollis, 1995). At the Chadwick Road section of Te Ranga ignimbrite, described by Hollis (1995), the Te Ranga ignimbrite is intercalated with underlying lake sediments and overlying volcanogenic fluvial sands, indicating it may have been emplaced subaqueously, at least in part, into a lake (Briggs et al., 1996).

2.5.1.6 Hamilton Ash and Taupo Volcanic Zone Tephras

The Hamilton Ash is a succession of strongly weathered, clay-textured tephra beds and paleosols that occurs across the Waikato, South Auckland, and Tauranga regions (Briggs et al., 1996) (Figure 2.4). There are up to eight units included in the Hamilton Ash, one of which has been dated to 0.35 ± 0.04 Ma (Briggs et al., 1996). The Hamilton Ash overlies the Matua Subgroup within the Tauranga Basin, and is exposed at Omokoroa where it is up to 2.5 m thick (Briggs et al., 1996).

The Rotoehu Ash overlies the Hamilton Ash and is found in deposits up to 2.4 m thick across the across the Tauranga Basin (Vucetich and Pullar, 1969) (Figure 2.4). It is an airfall unit deposited following large phreatic eruptions which occurred when the Rotoiti Ignimbrite reached the sea (Froggatt and Lowe, 1990). The Rotoehu ash has been dated as >c.50 ka (Froggatt and Lowe, 1990).

Ten further tephras overlie the Rotoehu Ash, nine of which originated from the Taupo Volcanic Zone (Briggs et al., 1996). These tephras are the dominant parent materials for the soils in the region (Briggs et al., 1996). These tephras have decimetre scale bedding (Briggs et al., 1996) and have been dated in full by Froggatt and Lowe (1990).

2.5.1.7 Holocene Sediments

The Holocene sediments of the Tauranga Basin are comprised of shallow marine sands intercalated with tephras from the Taupo Volcanic Zone, as well as silts, sands, clays and gravels from alluvium (Briggs et al., 1996), deposited during and after the Holocene marine transgression (Davis and Healy, 1993) (Figures 2.3, 2.4 and 2.5). The sediments contain many shell horizons, and are present across the basin, including the sediments that make up the tombolo between Tauranga and Mount Maunganui (Davis and Healy, 1993) (Figure 2.3).

2.5.2 Structure

The Waiteariki Ignimbrite forms the basement for the Tauranga Basin, and is assumed to overlie Pliocene-Miocene andesitic volcanics and Mesozoic greywacke (Briggs et al., 1996) (Figure 2.3). The Waiteraiki Ignimbrite dips 3–5°NE into the Tauranga Basin (Briggs et al., 1996). Faults have not been observed in the Tauranga Basin. Two faults have been mapped in the Papamoa Ranges based on the alignment of rhyolite domes (Healy et al., 1964). The Kaikaikaroro, Manawata and Minden Peak rhyolite domes also show a 030°alignment that may be structurally controlled (Whitbread-Edwards, 1994).

Briggs et al. (1996) suggest that it is likely that deeper-seated faulting occurs that is obscured by subsequent deposition of sedimentary and pyroclastic rocks. Significant deep-seated faulting has been identified in off-shore seismic by Davey et al. (1995) (Figure 2.6), underneath an undeformed sedimentary sequence.

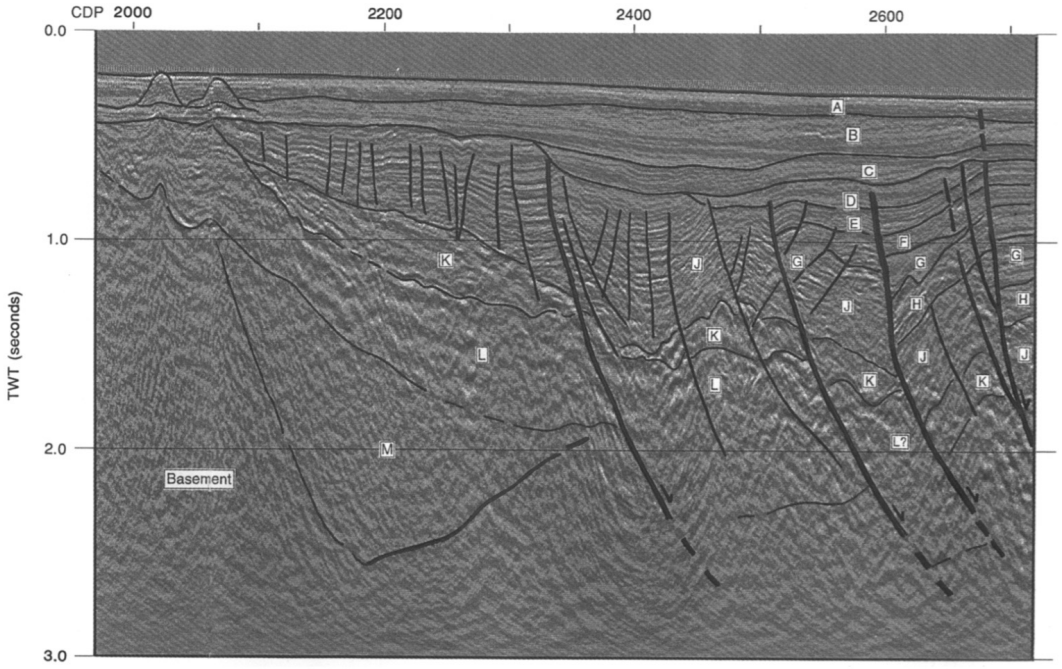

Figure 2.6: Seismic from offshore Bay of Plenty showing a heavily faulted block overlain by a relatively undeformed sedimentary sequence. From Davey et al. (1995)

Briggs et al. (1996) suggest that there could be a series of predominantly NNE-striking normal faults that occur in the basement that control the localisation of volcanic vents and potentially the alignment of the terraced peninsulas in Tauranga Harbour and the dominant NNE direction of major rivers. Some terraces have a 1 – 2°dip to the NE or N which Briggs et al. (1996) suggest could be cause by late stage rejuvenation of NNE-striking faults and associated minor tilting. Christophers (2015) attributed a sharp discontinuity in the Pahoia Tephras along the Omokoroa Peninsula to vertical displacement. A series of stepped blocks west of the Peninsula

was suggested, but not proven.

Caldera structures within the Tauranga Basin have been proposed by Briggs et al. (1996). This is based on studies that show rhyolite domes and flows within or on the rim of calderas (Briggs and Fulton, 1990), and a negative gravity anomaly between Aongatete and Matakana Island (Woodward and Ferry, 1973). If caldera structures do exist it would likely be Pliocene in age and buried beneath younger deposits Briggs et al. (1996, 2005). Christophers (2015) suggests a ridge of inferred-Pleistocene sediments that runs through the middle of Tauranga Harbour could be the boundary of two calderas, separating the two basins within the Harbour.

Christophers (2015) identified evidence of tilting around Omokoroa to the south south-west, the opposite direction to that identified on Matakana Island by Shepherd et al. (1997, 2000). Christophers (2015) suggests that this could be evidence of doming stretching from Omokoroa to Matakana Island, with some deformation occurring since 7,626 $\pm$ 30 BP.

2.5.3 Tauranga Harbour

Tauranga Harbour is bounded from the sea by a tombolo at either end of the harbour, Bowentown in the NW and Mt Manganui (Mauao) in the SE (Figure 1.1b). Between these lie two harbour entrances at either end of a barrier island, Matakana Island, the largest barrier island in New Zealand (Shepherd et al., 2000). Due to shallow intertidal flats within the harbour, there is limited exchange of water in the middle of the harbour, creating two basins: the Katikati Basin and the Tauranga Basin (Spiers et al., 2009).

The earliest research into the subsurface sediments of Tauranga Harbour was carried out by Davis and Healy (1993) using a set of pre-existing boreholes, borehole descriptions, limited seismic and surface samples. Subsequently, investigations were undertaken by Healy et al. (2009), who used data from a number of boreholes in the southern area of the harbour, both within and adjacent to the shipping channel. A study by Moon et al. (2013) used boreholes, CPT and some seismic data to make interpretations about the depositional environment within Stella Passage. De Lange et al. (2014) used some of the same dataset (vibracores and seismic) as is used in this thesis to determine the distribution of silty sediments within the shipping channel. Technical reports on the sediments have also been prepared by Healy and Roberts (1997) and Opus International Consultants Ltd (2011). Thesis of the harbour and surrounding area have also been produced by Christophers (2015), Harmsworth (1983), Hollis (1995) and Whitbread-Edwards (1994).

2.5.3.1 Dredging

Dredging has occurred in the Tauranga Harbour to allow for expansion of the Port, the Port of Tauranga. The Port has existed since the 1950s, and initially took advan-

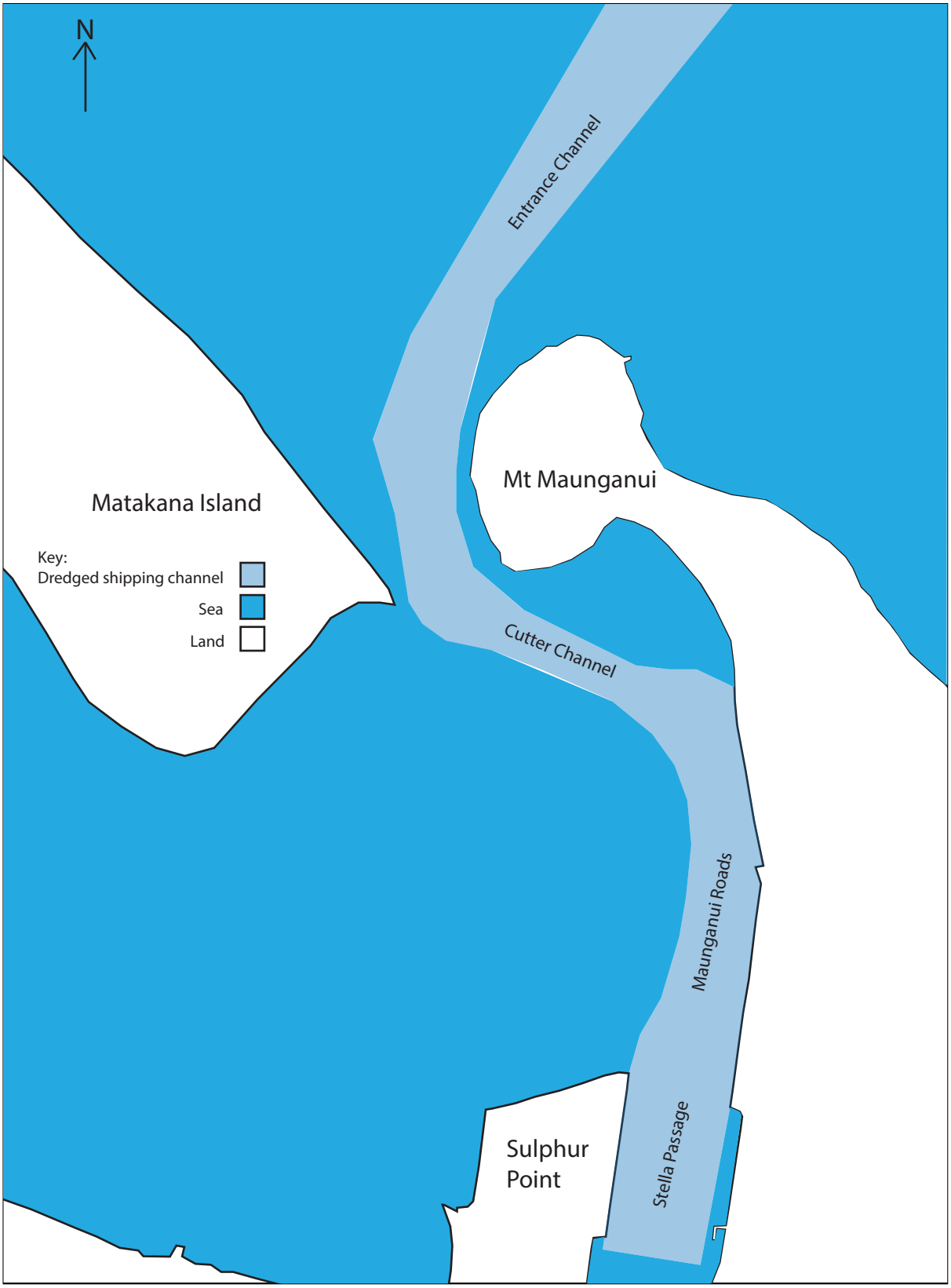

Figure 2.7: Map of Tauranga Harbour showing a broad outline of the dredged shipping channel and the areas within it. See Figure 1.1b

tage of the natural channel systems that occur in the South Eastern portion of the harbour (Thompson, 2010). The natural depth was 7.5 - 8 m below mean sea level. To accommodate larger ships, two captial dredging phases have occurred (Thompson, 2010), with a third occurring in 2015-16 (Port of Tauranga Ltd, 2013). The first phase occurred during 1968 - 78 and removed 4.7 million cubic metres of sediment to create a channel 10.7 m deep at high water (Thompson, 2010). Some of this work was done by trailer-suction dredging, removing 'clean, loose sand' and was deposited offshore of Mount Maunganui (Thompson, 2010). The remainder of the dredging was done using a bucket conveyor dredger in order to dredge through a boulder field overlying predominantly cemented silt and sand (Thompson, 2010).

The second case of capital dredging occurred in 1991-92 and removed 4.5 million cubic metres of sediment to widen and deepen the channel to 12.9 m inside the harbour and 14.1 m outside the harbour (Thompson, 2010). Tanea Shelf was again widened and this time rocks and boulders were recovered and relocated to re-establish the marine community that had existed at the original boulder reef (Graeam, 1995).

Maintenance dredging occurs within the harbour every two years to remove the 200,000 - 300,000 cubic metres of sediments that accumulates using a trailer suction dredge (Thompson, 2010). The 2015-16 dredging phase will deepen the channel further, to 16.0 m inside the harbour and 17.4 m outside the harbour (Thompson, 2010).

2.5.3.2 Sub Surface

Port of Tauranga has heavily dredged Stella Passage, the main shipping channel in Tauranga Harbour (Figure 2.7). Stella Passage has been the main site of research into the subsurface stratigraphy of Tauranga Harbour, due to the potential of the stratigraphy to influence future dredging.

In their study of the Holocene sediments, Davis and Healy (1993) constructed a model with 3 primary, distinct, lithofacies to representing different paleoenvironments. The first, a pumiceous facies, was suggested to represent a terrestrial setting (reworked alluvial fan and fluvial deposits), likely a result of the Late Quaternary volcanic activity in the area following the last glaciation (Davis and Healy, 1993). A wood fragment found in this unit was dated to be 9420 $\pm$ 100 years BP, indicating this was deposited during the Holocene when sea level was 25 m lower than it is at present Davis and Healy (1993). The second, a shelly mud facies, was suggested to represent a normal marine embayment or estuarine setting, and is composed of thick muds with irregularly distributed shell material (Davis and Healy, 1993). Davis and Healy (1993) suggest this unit represents a protected embayment subjected to occasional storms with an insignificant fresh water input. The geometry of the facies is constrained, indicating deposition in narrow valleys or paleochannels (Davis and

Healy, 1993). The third, a shelly sand facies, is sorted, contains abundant shell fragments and shell beds (Davis and Healy, 1993). This is interpreted to have accumulated in a shallow marine shore face dominated by waves, at a time when sea level reached its present level, around 6500 years ago (Davis and Healy, 1993). They used the borehole and seismic data to create a cross section through the harbour, shown in Figure 2.8. This cross section was created prior to dredging, and used data from 71 boreholes of varying ages.

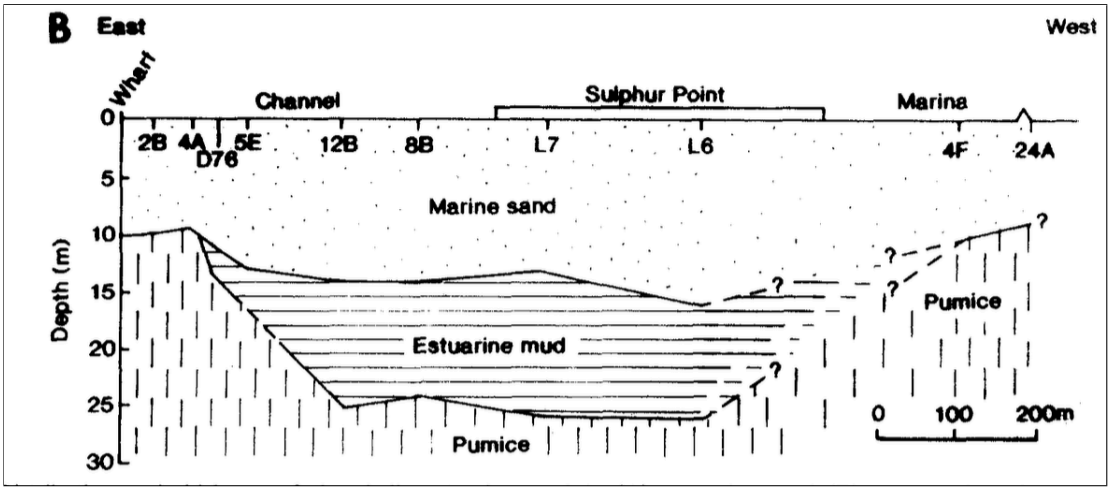

Figure 2.8: Cross section through Stella Passage from Davis and Healy (1993). It uses data from a range of sources prior to captial dredging.

Moon et al. (2013) found an unconformity separating grey sands from silts containing bioclastic material (Figure 2.5). They propose that this represents a boundary between the Holocene and Pleistocene successions. Below the unconformity, they found a thick succession of various pumiceous sediments interspersed with paleosols and swamp deposits, which they infer to represent the Matua Subgroup. Moon et al. (2013) describe it as a ”complex unit”, containing primary and reworked pyroclastic materials. Healy et al. (2009) found that the sediments within Stella Passage contained a high proportion of silt-sized grains. Diver observations in March 2014 found exposures of “papa” rock (soft grey mudstone), thought to be the Pleistocene volcaniclastic sediments (de Lange et al., 2014). Moon et al. (2013) developed a 2D transect and a 3D model, shown in Figures 2.5 and using cores from the western side of Stella Passage. The model illustrates the distribution of the lithofacies in Stella Passage and shows a ridge and valley morphology, with the ridges trending east. The unconsolidated sandy and silty materials in Stella Passage are thought to correlate with the Pahoia Tephra sequence (Moon et al., 2013). These silty sediments contain a large quantity of clay, are light coloured and were thought to be likely to cause discolouration of the water column during dredging (Moon et al., 2013). Moon et al. (2013) found they occur in lenses, making it difficult to constrain their location, and suggest it could contain halloysite as a key clay mineral (hallyosite was found in upper Matua Subgroup sediments by Harmsworth (1983)).

Moon et al. (2013) suggested that the shallow Pleistocene sediments found in Stella Passage probably extended into the Manganui Roads area (Figure 2.7), and seismic data analysed in de Lange et al. (2014) found a strong subsurface reflector in this area. Vibracores collected within the Manganui Roads section of the channel for de Lange et al. (2014) show the presence of some silty sediment that forms a SW-NE trending ridge across the channel.

Cutter Channel, an area dredged through the flood tidal delta (Section 2.5.3.1), was assumed to be predominantly Holocene sand (Thompson, 2010; de Lange et al., 2014). Previous dredging however uncovered some isolated boulders in parts of the channel (Healy et al., 2009), and further investigation using sidescan sonar and diver observations found some outcrops of hard resistant silty material (de Lange et al., 2014). Seismic data analysed by de Lange et al. (2014) found that there is a ridge of older sediment that runs parallel to the channel. This ridge is flanked by Holocene sand deposits. The ridge outcrops at several locations in the southern portion of the channel, however the central and northern portions of the channel appear to be over a valley, filled by Holocene sands (de Lange et al., 2014). The seismic data also identified the presence of strong isolated reflectors at depth, interpreted to be isolated boulders or buried trees. Sediment cores from the northwestern parts of the channel identified the presence of a shell accumulation, and one core was observed to be "black and smelly" and was described by de Lange et al. (2014) as similar to the geothermal discharge found at Pilot Bay.

Outside of the harbour, seismic data interpreted by de Lange et al. (2014) found that the Mount Maunganui rhyolite dome does not extend into the entrance channel in the shallow subsurface.

2.5.4 Paleogeography

The Pleistocene sediments were deposited in a terrestrial environment, with overlapping volcanic and sedimentary successions (Moon et al., 2013; Harmsworth, 1983). The sediments are determined to be Pleistocene due to their position in the stratigraphy beneath an unconformity with shallow marine sands. Moon et al. (2013) suggest that a predominantly alluvial fan system with rapidly migrating river channels was the most likely depositional environment. Moon et al. (2013) suggest that the paleosols they identify in boreholes to represent periods of terrestrial weathering and erosion in periods between depositional events. Lacustrine, overbank and swamp deposits are also identified (Moon et al., 2013) (Figure 2.5). These sediments are suggested to represent the Matua Subgroup.

The Holocene evolution of the harbour has been influenced heavily by the Holocene marine transgression. Peats overlain by estuarine sands on the Omokoroa Peninsular were dated at 7636 $\pm$ 30 y BP (Christophers, 2015). Radiocarbon dates from Gibb (1986) suggest modern sea levels were achieved in New Zealand around ~7200 BP.

Clement et al. (2010) estimated a date of ~7550 BP for the Manawatu coastal plain. Sea level was 0.3 – 0.5 m higher than present at this time, and there is evidence around Tauranga Harbour of small sea cliffs at this level (de Lange et al., 2015). This represents the earliest Holocene shoreline (de Lange et al., 2015). The oldest Holocene sediments dated within the harbour are 9420 $\pm$ 100 BP (Davis and Healy, 1993). Around 65 % of the barrier dunes that enclose the harbour were formed during the sea level rise to the Holocene high stand (Shepherd et al., 1997).

The mid-Holocene High Stand occurred at 4500 - 3500 BP in the Pacific Ocean Yokoyama et al. (ress) and 4000 BP for New Zealand (Dougherty and Dickson, 2012). At this time sea level was ~2 m higher than present (Dougherty and Dickson, 2012). Until this time Shepherd et al. (1997) suggest that Matakana Island contained two tidal inlets, one at Blue Gum Bay and one at Hunters Creek (Figure 2.9). Rapid accretion of Holocene barrier dunes resulted in the closing of these two tidal inlets, and the migration of the tidal inlet south towards Mount Maunganui (de Lange et al., 2015). The ebb-tidal deltas of these two inlets provided the source for sediment of the present day ebb-tidal delta (de Lange et al., 2015). The oldest Holocene sands within the ebb-tidal delta are dated at 3370 $\pm$ 100 y BP (Davis and Healy, 1993). There is no evidence of the modern day Tauranga Basin tidal inlet existing during the early Holocene. However, de Lange et al. (2015) suggest it existed during the mid-Holocene. Several tsunami have occurred in the region over the past 3000 years (Bell et al., 2004). One event is dated at 582 $\pm$ 66 BP (Bell et al., 2004) and caused large scale erosion of both spits at Matakana Island (Shepherd et al., 1997). Seismic data identifying shell beds indicates that the tidal inlet post tsunami was established further towards the west, before migrating eastwards with ongoing accretion (de Lange et al., 2015) (Figure 2.9). It is currently confined by the Mount Maunganui rhyolite dome (de Lange et al., 2015).

The tidal inlet has deepened and narrowed between when it was first mapped in 1852 and today (Brannigan, 2009) (Figure 2.10). Between 1852 and 1879 the channel deepened by ~6 m. However, the width was largely unchanged (de Lange et al., 2015). Between 1879 and 1954 the tidal inlet narrowed by 300 m and there was a large increase in the size of the flood tidal delta (de Lange et al., 2015). The creation of the entrance dredge channel appears to have moved the zone of accretion to the Matakana Island shoreline (de Lange et al., 2015). The stability of the ebb tidal delta has not been affected by the dredging associated with Port of Tauranga, due to the ebb tidal delta likely resting upon more resistant Pleistocene sediments (de Lange et al., 2015). Resistant Pleistocene sediments may also occur on the western side of the tidal inlet (marked reef in Figure 2.10, 1852). Shepherd et al. (1997) suggested that Matakana Island was underlain by Pleistocene sands. However, SCUBA observations in the 1980s identified rhyolite cobbles embedded in Pleistocene sediment (de Lange et al., 2015).

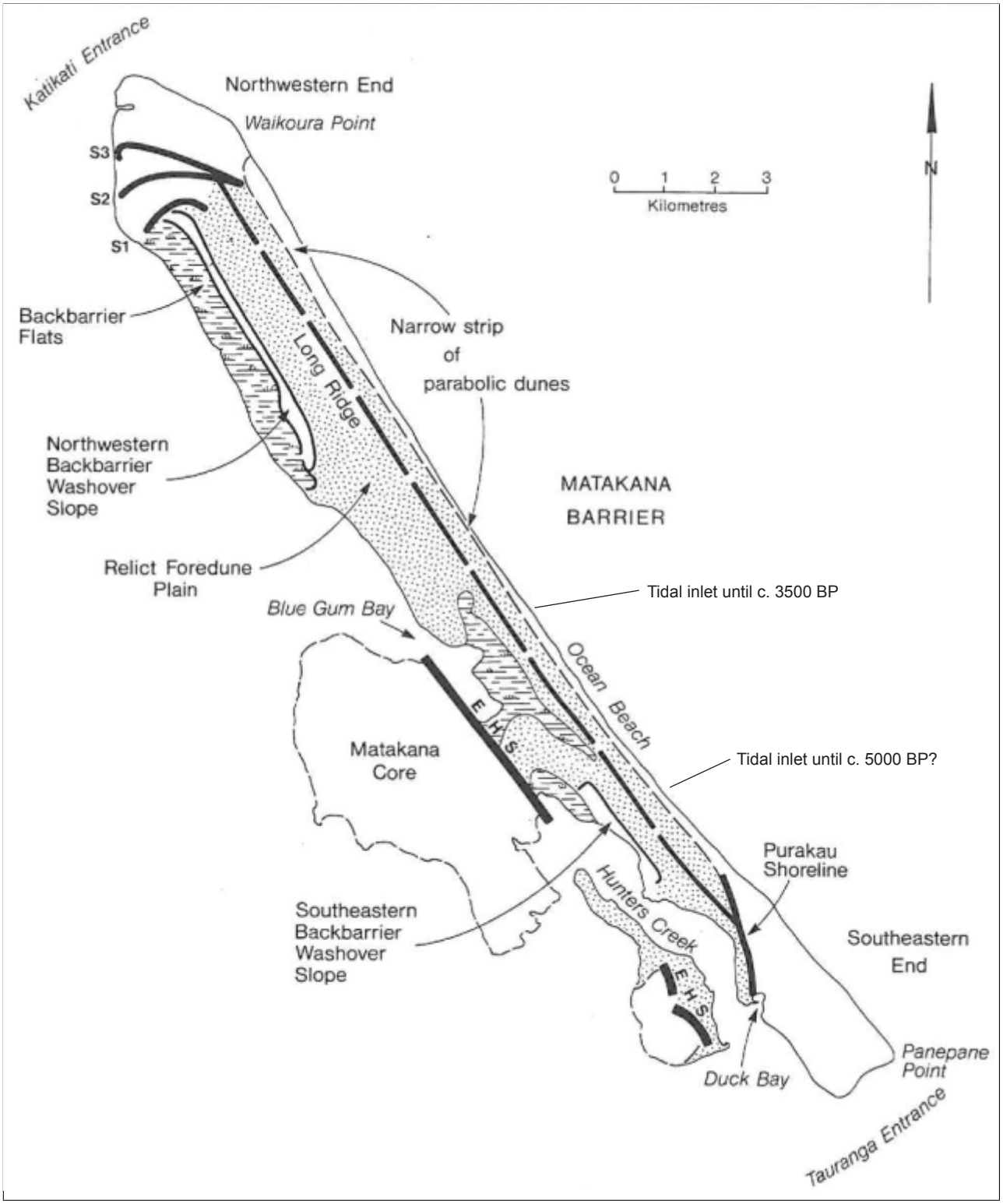

Figure 2.9: Map of Matakana Island, showing the locations of two potential Holocene tidal inlets. After Shepherd et al. (1997) and de Lange et al. (2015).

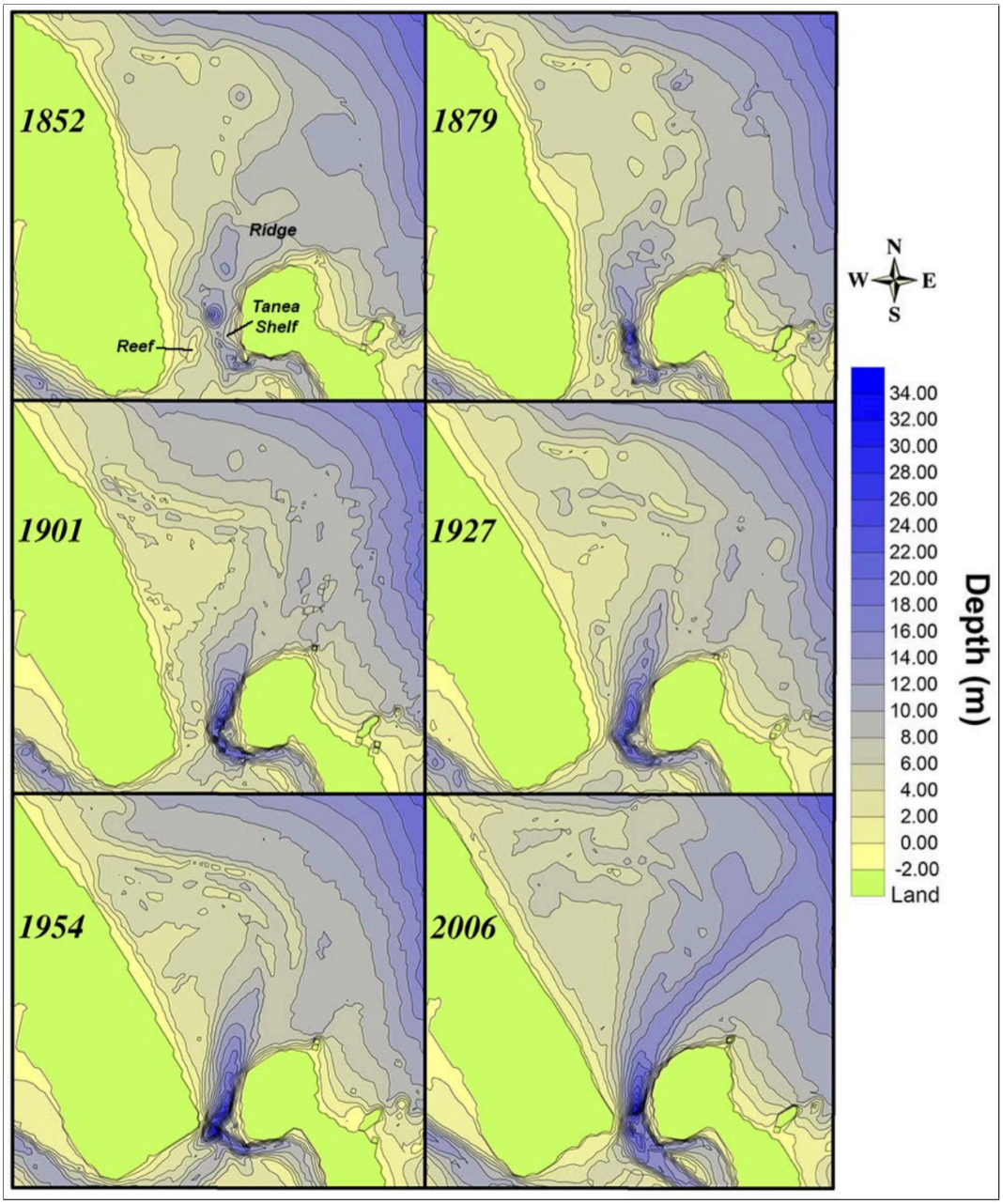

Figure 2.10: Changes in the bathymetry of Tauranga Harbour Entrance between 1852 and 2006. From de Lange et al. (2015) using data from Brannigan (2009).

2.5.4.1 Dates

Moon et al. (2013), de Lange et al. (2014) and Christophers (2015) all infer the unconformity between the coastal sands and the terrestrial sediments below to represent the Pleistocene – Holocene boundary, due to the Holocene marine transgression. Cooper and Agterberg (2004) determined the New Zealand Pleistocene as 2.58 – 0.0117 Ma, and the Holocene as 0.117 Ma to present.

Davis and Healy (1993) used radiocarbon dating on 12 samples listed in Table 2.1. They show a large variation in the dates for their marine sand facies. Some radiocarbon dates were also obtained by Christophers (2015) and are listed in Table 2.2.

Table 2.1: Radiocarbon dates collected by Davis and Healy (1993)

Core	Depth below sea level (m)	Facies	Material	Date (yr BP)
L-4	8.30	Marine sand	Wood	>40,000
B-81	10.50	Marine sand	Shell	6670 $\pm$ 110
E-15	11.35	Marine sand	Shell	6110 $\pm$ 80
E-13	11.45	Marine sand	Shell	2330 $\pm$ 70
D-80	11.60	Marine sand	Shell	740 $\pm$ 110
D-79	13.30	Marine sand	Shell	960 $\pm$ 100
K-14	13.40	Marine sand	Shell	6180 $\pm$ 100
E-10	13.50	Marine sand	Shell	3370 $\pm$ 100
D-82	13.60	Marine sand	Shell	6790 $\pm$ 100
E-12	13.85	Marine sand	Shell	2610 $\pm$ 90
L-5	14.25	Estuarine mud	Wood	8100 $\pm$ 80
L-7	31.20	Pumiceous	Wood	9420 $\pm$ 100

Table 2.2: Radiocarbon dates collected by Christophers (2015)

Core	Unit	Material Used	Date (yr BP)
4.1	Medium to coarse sand	Pipi	106.6 $\pm$ 0.2
1.1	Silt	Cockle	1,652 $\pm$ 20
4.1	Sandy peat	Soil, organics	7,676 $\pm$ 30
2.1	Organic medium sand	Soil, organics	20,131 $\pm$ 66

2.5.4.2 Sedimentation Rates

In Christophers (2015), sedimentation rates were calculated for the northern side of the Omokoroa domain based on radiocarbon dates and the inferred Holocene Pleistocene boundary identified in several vibracores (Figure 2.11. Between 7676 $\pm$ 30 BP and 1970 AD the sedimentation rate was calculated at 0.0045 mm/yr. Since 1970 sedimentation rates have increased to 0.455 mm/yr. On the southern side of the Omokoroa domain since 1652 $\pm$ 20 BP the sedimentation rate has been 0.0524 mm/yr. These rates are much slower than those calculated for southern Tauranga

Harbour by Hancock et al. (2009) who calculated sedimentation rates to be between 0.75 and 1.57 mm/yr.

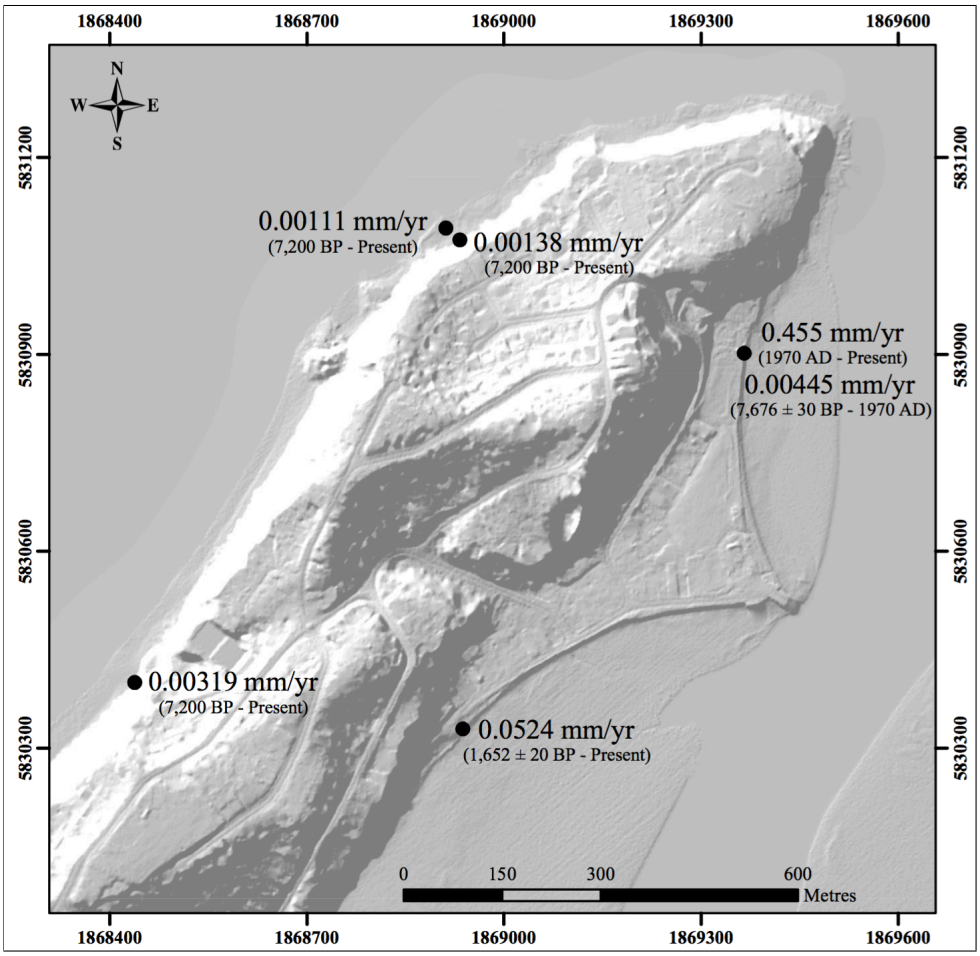

Figure 2.11: Sedimentation rates calculated from the assumed Pleistocene - Holocene boundary in Christophers (2015)

2.6 Conclusion

Tauranga Harbour is part of the Tauranga Basin and has successions of volcanic, fluvial, lacustrine, estuarine and shallow marine sediments. Research has been done in the past on sediments in Tauranga Harbour by several authors, however there is some discrepancy between the results. Much of this research has focussed on the position and the extent of the silty sediments within the dredge channel. Some work has been done in the past of the paleogeography of the harbour, however new information is now available.

Chapter 3

Methods

3.1 Introduction

This study used a number of different methods to achieve the overall objective of developing a three-dimensional model of the subsurface stratigraphy of Tauranga Harbour. The different methods used are as follows:

1. Core description of 86 vibracores obtained by the Port Of Tauranga Limited.
2. Grain size analysis on two hundred subsamples taken from the vibracores.
3. Optical petrography on 67 thin sections to identify minerals.
4. Magnetic susceptibility measurements of silty units in selected vibracores.
5. Portable X-Ray Fluoresence on 223 subsamples to determine the elemental composition of the sediments.
6. The scanning electron microscope (SEM) was used on two samples to establish the presence of diatoms, and to investigate the composition of a diagenetic coating.
7. A three-dismensional model of the subsurface of the harbour was developed using Leapfrog3D (ARANZ Geo Ltd, 2015).

3.2 Core Description

Eighty-six cores obtained by the Port of Tauranga Ltd (PoT) were described for this project. The cores were obtained using a vibracorer, and were limited in penetration depth either by the resistance of the strata or the maximum 3 metre penetration depth of the vibracorer. The sediments were captured in aluminium barrels, of which a portion was removed in order to log the sediments held within.

The cores were initially described over the summer of 2014–15 using standard qualitative sedimentological methods. This included identifying units and recording their approximate composition. It also included identifying any structures or other distinguishing features that occurred within the cores, and recording them. Textural properties such as grainsize, particle shape were recorded. Colour, weathering, bioclast type, condition and abundance were also recorded. The composition of each unit was estimated. Subsamples were taken from each unit logged.



Figure 3.1: One vibracore (VC29) obtained by the Port of Tauranga Ltd with a portion removed in order to log the sediments.

3.3 Grain Size Analysis

Grain size analysis was undertaken using the samples from each unit identified in the vibracores. These samples were analysed using a Malvern Particle Laser Sizer at the University of Waikato. Subsamples were not dried initially as they had low water content. Approximately 5 g of sample was passed through a 2 mm sieve and analysed by the laser sizer. The > 2 mm fraction was made up largely of bioclasts and not measured. Over 200 samples were processed in order to give an accurate representation of grain size distributions throughout the harbour.

There was very little (if any) organic material in the sediments and I determined that this would not affect the results significantly. Some samples had large amounts of articulated and disarticulated shells, but these were sieved out of the sample using the 2 mm sieve prior to analysis. Therefore, no digestion techniques were used prior to grain size analysis.

The samples were run through the Malvern Particle Laser Sizer. The laser sizer

works by measuring the amount of light diffracted as grains pass through the laser. The amount of light diffracted gives the particle size (Boggs, 2009). The results can be skewed by organic matter, which can 'clump' into larger grains, and by shells, which are much larger on one angle than they are on another.

The software used produced a data file that gave the volume percentage of grains between each measured grain size. Grain size distribution graphs were then generated, and sample statistics were calculated using the GRADISTAT grain size tool (Blott and Pye, 2001). Gradistat uses both the graphical method and the method of moments to compute grain size statistics. In this study, the logarithmic method of moments results were used.

3.4 Optical Petrography

Optical petrography was performed on at least one sample from each of the fifty initial units. This was achieved by impregnating the loose sediment subsamples with resin, before mounting the resulting block on a slide and slicing off a thin portion of the sediment block. This slide was then ground down until the sediment was 30 μm thick atop of the slide. A cover slip was lain over the top to preserve the sediment.

These thin sections were then examined using an Olympus microscope. The approximate percentages of each mineral observed were estimated, and the data were used to group similar thin sections. Other features, such as grain size and shape, birefringence, and diagenetic features were noted. Photographs were taken of each thin section.

3.5 Magnetic Susceptibility

Magnetic susceptibility measurements were performed on silty units with few distinguishing features to assist with core correlation. This was done by taking a sub sample of each silty unit at 10 cm intervals using a plastic utensil. The plastic utensil was used to avoid any contamination of the samples magnetism. The sample was placed into a 10 cc plastic sample pot. These samples were then dried for at least 24 hours at 40°C before being weighed.

The magnetic susceptibility of the samples was then measured using a Bartington MS2 Magnetic Susceptibility System in the University of Waikato Biological Sciences Glasshouse Compound to reduce contamination by ambient electrical fields. The greenhouses were chosen as they have very few electric devices running and are kept at a fairly consistent temperature. Both low and high frequency magnetic susceptibility measurements were taken using the MS2B sensor, and measurements down to 0.1 decimal places were recorded.

A measurement was also taken for air to correct for thermal drift and identify

any electromagnetic contamination. This was done by zeroing the empty sensor, recording the sample (R_1) and then recording the subsequent reading of the empty sensor (air) (R_2). This air measurement was then used to provide a corrected value (R_k).

$$R_k = R_1 - R_2/2 \tag{3.1}$$

The MS2B sensor used was calibrated for a sample mass of 10 g. As none of the samples used were exactly 10 g, sample measurements had to be corrected using the following equation:

$$\chi = a * b/c \tag{3.2}$$

Where a is the measured value, b is the calibration mass and c is the sample mass. The corrected measurements (χ) were then plotted by depth. The results were correlated across the cores measured.

3.6 Portable X-Ray Fluoresence

Portable x-ray fluorescence (pXRF) analysis was undertaken on several sub-samples of each unit identified during the core description phase. The samples were placed into small pots and covered using a polypropylene slip (Figure 3.2). The pXRF analysis used a 40 KV Olympus Delta X held in a bracket to a x-ray chamber. Each sample was analysed for 60 seconds to measure the composition of the samples. 202 sub-samples were measured. XRF works by emitting high energy X-rays upon an object, exciting the electrons and causing them to fill vacant orbital poisitions. This process releases energy that is measured by the XRF device (Allaby, 2013).

The equipment was set up in geochemistry mode, which measures the proportions of the following elements: Al, Si, P, S, Cl, K, Ca, Ti, V, Cr, Mn, Fe, Co, Ni, Cu, Zn, As, Se, Rd, Sr, Y, Nb, Mo, Ag, Cd, Sn, Sb, Ba, La, Ce, Pr, Nd, Ta, W, Hg, Pb, Bi, Th, and U. The data were then put into ioGAS, a computer package, in order to analyse the geochemical variations in the field area.

3.7 Scanning Electron Microscope

The scanning electron microscope (SEM) was used on three samples to establish the presence of diatoms and to identify weathering features on individual grains. This involved taking a small sample of sediment and coating it in platinum for use within the SEM. The sample was then analysed in a vacuum within the SEM, and images were taken. The EDX component of the SEM was used to identify the composition of individual grains, using an X-ray to measure the proportions of the elements present. EDX is the X-ray component of the SEM, and works by measuring the characteristic response from an element to an X-ray. This allows the proportions of

elements for any given mineral to be measured.

3.8 3-Dimensional Model

A digital 3-dimensional model of Tauranga Harbour was created using the geological modelling software Leapfrog3D. All core descriptions were imported into Leapfrog3D along with bathymetric data from the shipping channel to constrain the model. Grain size statistics were also imported into the model in order to visualise variations within the channel. Contact surfaces were modelled using the vibracore data, and these were used to model subsurface successions. These successions were then refined using additional seismic and borehole data. This produced a 3-dimensional model that could be sliced through at any point and angle to analyse the facies distribution.



Figure 3.2: A small pot covered in a polypropelene slip ready for use with the pXRF device. Approximately 3 cm in diameter.

Chapter 4

Core Description And Facies Analysis

4.1 Introduction

This chapter describes the sediments logged from the 86 vibracores that were obtained from Stella Passage. Sediment texture and composition is described, and the results of magnetic susceptibility and geochemical analysis are presented for each of the of the groups of vibracores analysed. The vibracores were obtained by the Port of Tauranga Limited in five areas (Figure 4.1; Stella Passage, Maunganui Roads South (the southern potrtion of Maunganui Roads on Figure 4.1), Manganui Roads, Cutter Channel and the Entrance Channel. At the end of this chapter, a facies analysis is conducted. The resulting lithofacies are presented.

4.2 Stella Passage

Stella Passage is located in southern Tauranga Harbour, and is the southern-most portion of the dredged channel used by the Port of Tauranga Ltd (see Figure 4.1). Four vibracores were obtained from this area (Table 4.1, locations shown in Figure 4.2), in water depths of 12.9–14 m from the centre of the channel. The vibracores have a spacing of 140–250 m apart.

Table 4.1: List of vibracores obtained from Stella Passage.

Vibracore	Length (m)	Depth below sea level (m)
VC1	2.75	13.35
VC78	2.52	13.99
VC79	2.4	13.11
VC80	2.12	12.95

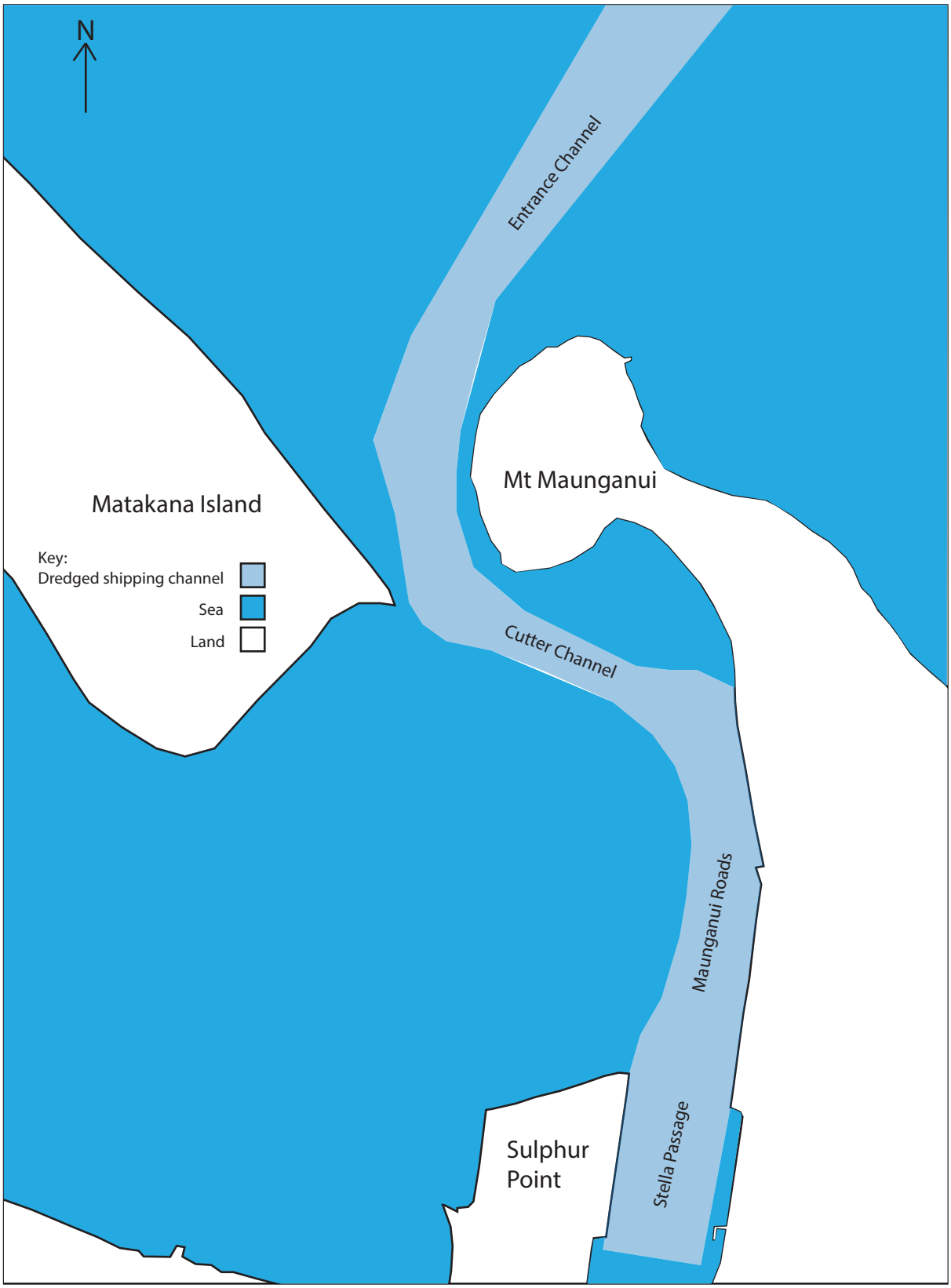

Figure 4.1: Map showing locations of the areas in which vibracores have been taken.



Figure 4.2: Map showing locations of vibracores taken from Stella Passage and Manganui Roads South. See Figure 1.1b

There is large variation between the sediments in the four vibracores obtained from Stella Passage, both in texture and composition. A stratigraphic column of VC1 is presented in Figure 4.3, and compositional pie charts with thin section images are shown in Figure 4.9. In the following stratigraphic logs, the colours in the graphical log represent approximations of the sediment colour when it was described. The sediment ranges from fine to medium sand, and is composed of volcanic glass, lithics, plagioclase, and hornblende. Thin (2 mm) silt beds (Munsell scale 2.5YR 7/10, orange) are found in VC1 and VC79. Only such one bed is found in VC1. However, several are found in VC79, indicating that these beds occur in discontinuous lenses (Figure 4.4).

Similarly, a ‘pod’ of silt was found in VC80 that is unique to that core. There is colour variation through all units in these cores. However, they all fall in the Y to YR Munsell colour spectrum. In VC78 there is a unit (82–156 cm) that has formed into ‘clumps’, and within some of these clumps there are areas of 2.5YR 7/10 discolouration (Figure 4.6). I interpret this discolouration to be patches of iron staining (the amber or red coating of grains (Sullivan and Koppu, 1998)) and it occurs sporadically and through to the base of the core. At the base of VC1 (Figure 4.3), there is a bed of articulated and disarticulated bioclasts. This unit has a bimodal poorly sorted medium sand matrix (Figure 4.5). In this area, this bed is unique to this core. I interpret it as a tsunami deposit, based on the presence of worn bivalves (Donato et al., 2008). Tsunami deposits commonly have bimodal distributions (eg

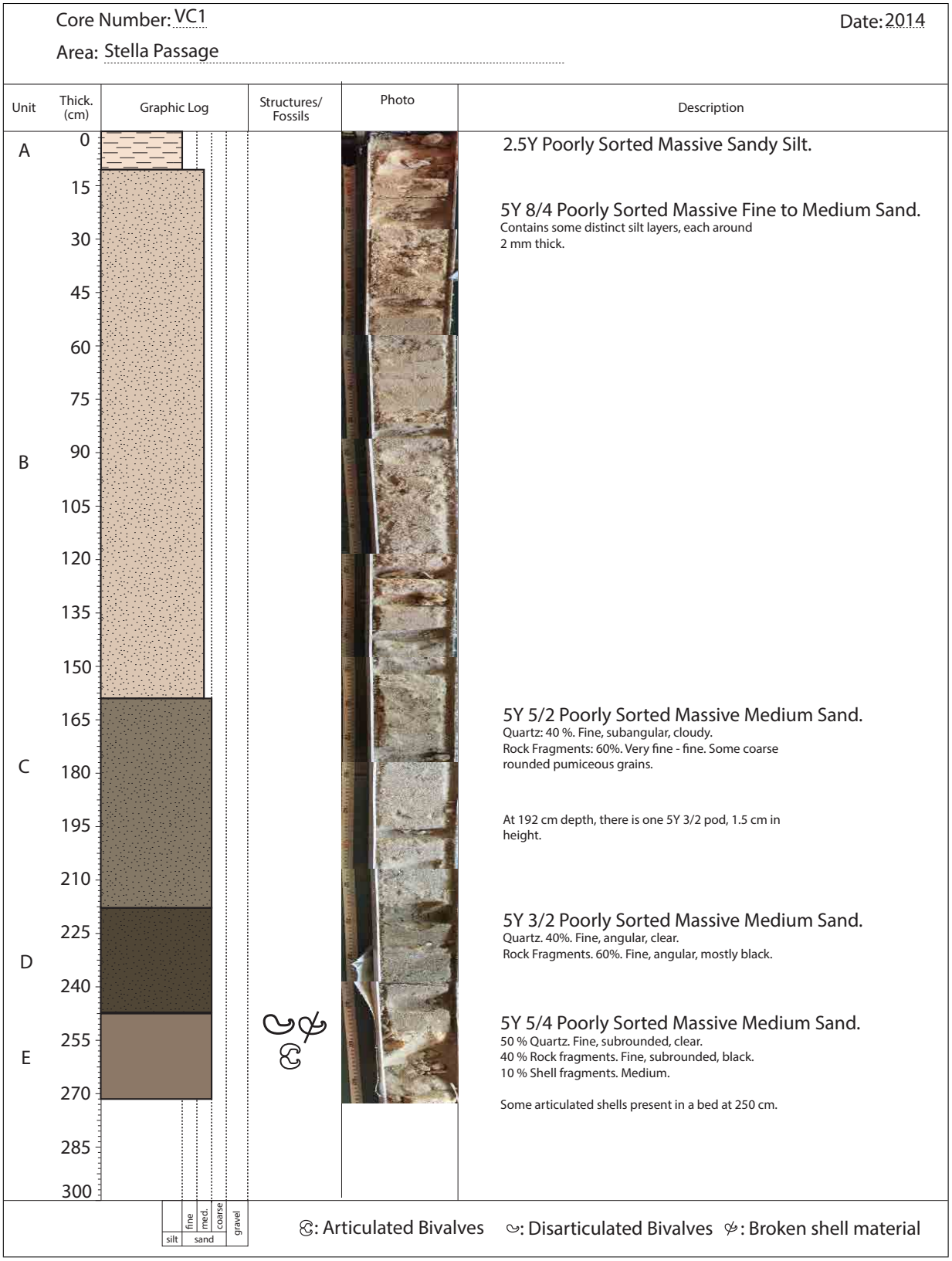

Figure 4.3: Stratigraphic log of VC1, taken from Stella Passage. The colours represent hues from the Munsell spectrum from when the vibracore was first observed.

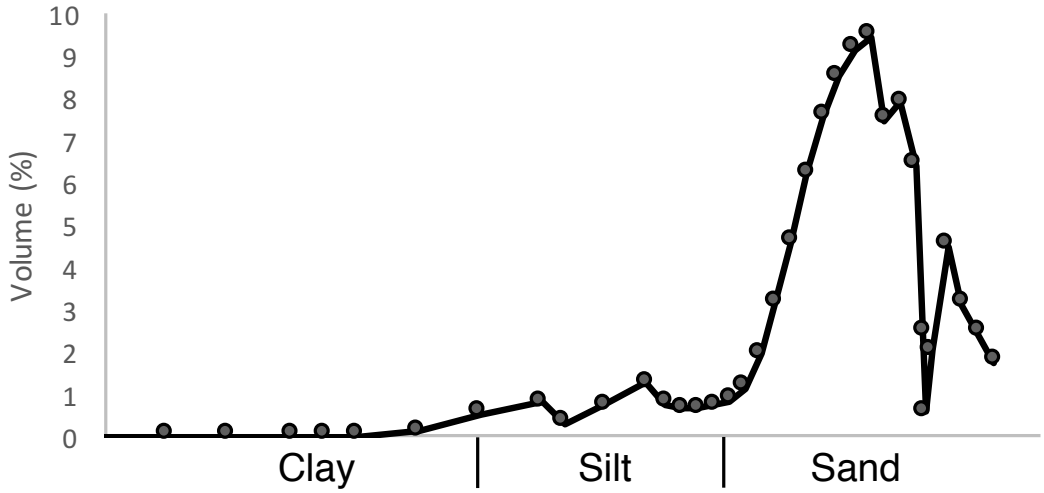

Figure 4.5: Grain size distribution chart of a sub-sample of VC1 taken from 253 cm depth.

(Babu et al., 2006; Paris et al., 2007; Nentwig et al., 2015)). A rip up clast is found at 192 cm depth in unit B (Figure 4.3), which could be another tsunami signature (Srisutam and Wagner, 2009). Other features commonly found in tsunami deposits, such as an erosional basal contact (no basal contact is present in this vibracore), basal load structures, and cross bedding (Engel and Brückner, 2011) are not present in this deposit.



Figure 4.4: Silt bed found in VC1. These beds are only found in VC1 and VC79, indicating that they occur in discontinuous lenses.

4.2.1 Texture

Mean grain size is plotted against depth in Figure 4.7a and shows substantial variation, not only within Stella Passage but within each core. VC79, for example, coarsens with depth overall. However there are orange 'silt' beds within the core where the grain size fines substantially (e.g. 68 cm depth). A similar bed occurs in VC1 (Figure 4.4). However, it is much thinner and the grain size was not measured. It is the same colour and has similar cohesive characteristics to those occurring in VC79, so I assume it to be of similar origin. VC1 also coarsens with depth. How-

ever, VC78 fines with depth throughout much of the core. Grain size in VC80 was observed to be uniform throughout the core, so only two measurements were taken, and these show little variation. A bed of articulated and disarticulated bioclasts is present at 250 cm depth in VC1, and although these larger bioclasts were not included in the grain size measurements, there is very little variation between the grain size statistics of the sediment measured at 205 cm and 253 cm. It could be that this is a deposit from a successive tsunami. Of the 18 samples measured, 11 were polymodal, 5 were trimodal and 2 were bimodal.

As shown in Figure 4.7b, the sediments are poorly to very poorly sorted, indicating very little (if any) reworking. While there is variation with depth within the cores, there are few trends. VC1 and VC79 become more poorly sorted with depth in the top 100 cm of the core, before becoming more well-sorted towards the bottom of the core. VC78 and VC80 are largely uniform throughout.



Figure 4.6: Clumps of sediment present in VC78. There are some areas of 2.5YR 7/10 discolouration present in this unit (interpreted to be iron staining). This discolouration continues through to the base of the core.

Skewness is plotted against depth in Figure 4.7c and shows large variations with depth in VC78 and VC79. Overall, VC78 and VC79 become slightly more coarsely skewed with depth. Overall, all but one sub-sample measured is strongly fine skewed. VC1 and VC80 show a largely uniform skewness with depth.

Figure 4.8 shows a skewness versus sorting plot. While there are no major clusters, the two sub-samples from VC80 do occur in a very similar position to two sub-samples from VC79. VC1 also appears to have a similar variation in sorting to VC79, but is much more uniform in skewness. There is a trend of samples becoming less finely skewed as they are more poorly sorted.

4.2.2 Composition

The sediments in the Stella Passage area are dominated by volcanic glass and lithics. There is significant variation down core, particularly in the highly variable VC79. Unit A in VC1 (0–10 cm) is a mixture of volcanic glass, lithics, hornblende, plagioclase, and bioclasts, whereas the silt bed measured at 68 cm depth is very lithic rich

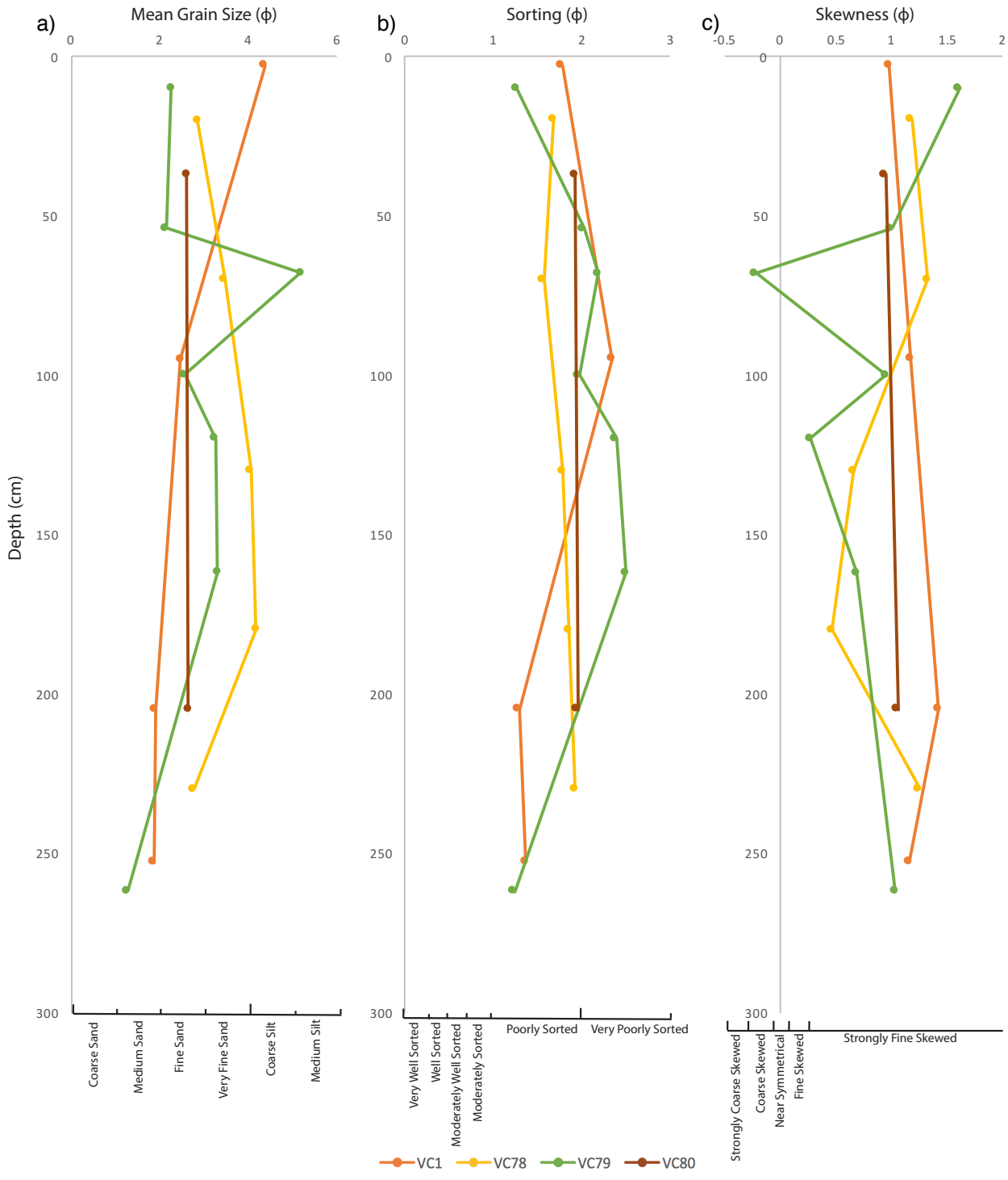

Figure 4.7: Grain size statistics plotted against depth for sub-samples taken from Stella Passage. This shows the variation in grain size, sorting and skewness within each core.

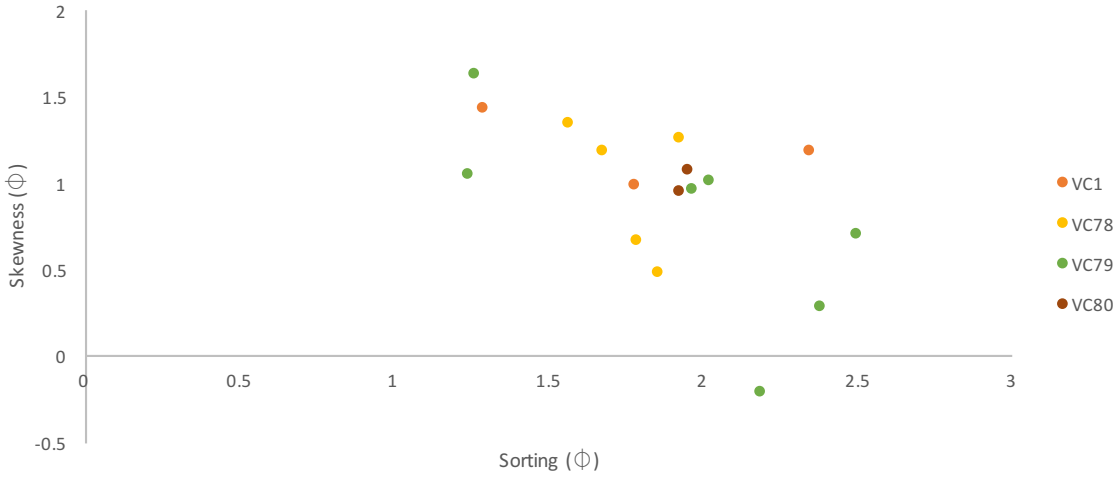

Figure 4.8: Skewness plotted against sorting for sub-samples taken from Stella Passage. There is a trend of samples becoming more less finely skewed as they are more poorly sorted.

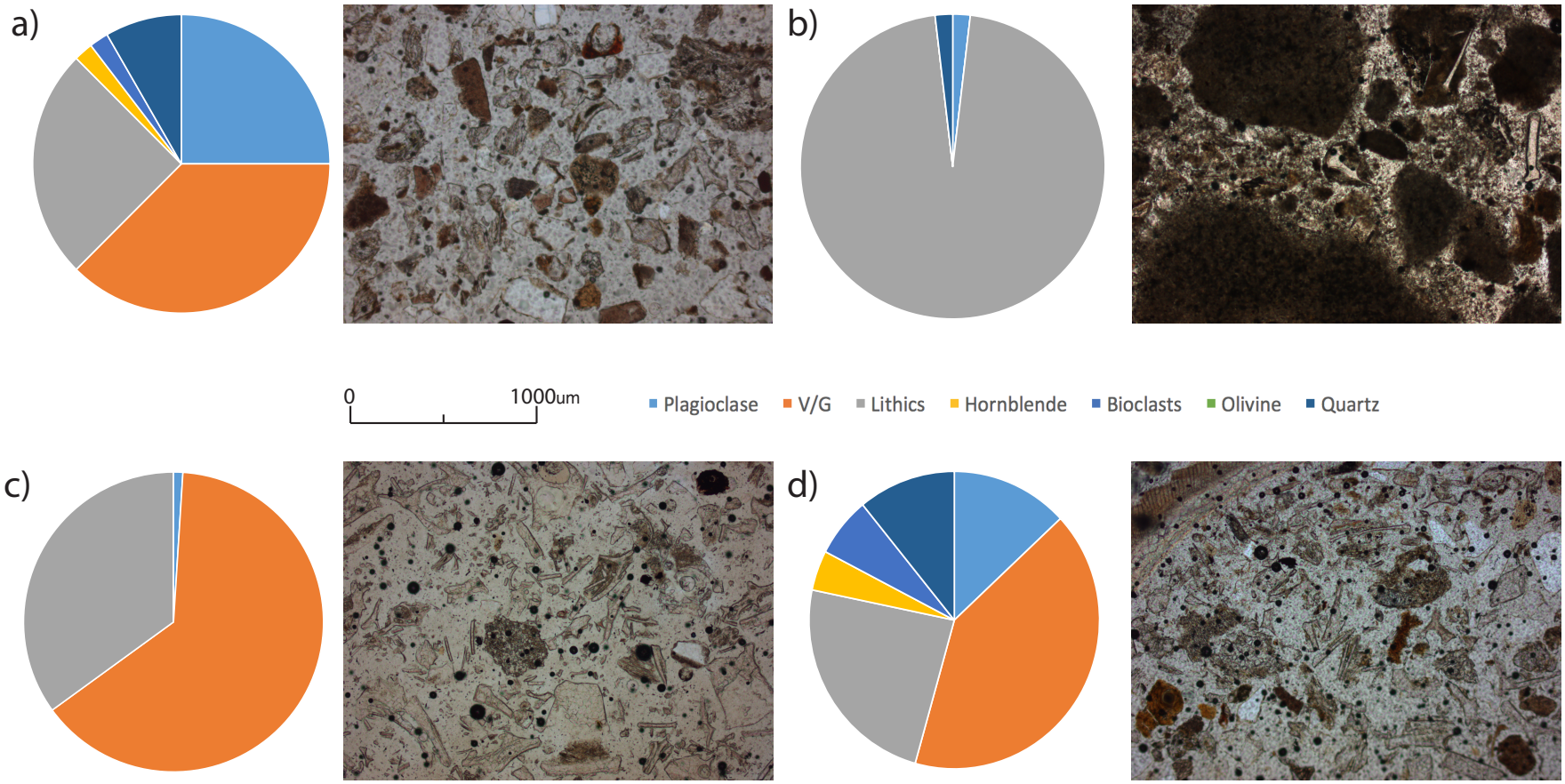

Figure 4.9: Thin sections and compositional plots from Stella Passage. A) VC79 10 cm and contains an abundance of volcanic glass and lithics. Plagioclase, hornblende and some thin bioclasts are also present. B) VC79 68 cm is almost entirely lithics. Some quartz and plagioclase are also present. C) VC79 54 cm has an abundance of volcanic glass. Some lithics and plagioclase are also present. Note the sharp edges and corners of volcanic glass shards. D) VC1 253 cm contains very thin shards of volcanic glass. Larger bioclast fragments are also present.

(Figure 4.9b). I interpret this bed to indicate a period between depositional events, where erosion removes volcanic glass, due to its chemical instability (Staudigel and Hart, 1983). Honblende and bioclasts are found in Unit A in VC1. Unit B contains only volcanic glass, lithics and plagioclase. Volcanic glass is very prominent in these deeper sediments, with more than 30 % found in each sample (Figure 4.9). The volcanic glass that is present is grey in colour and very angular (such as that presented in Figure 4.9c), indicating that it is a series of deposits with very little reworking potentially from a rhyolitic eruption.

Similar compositional variations exist in sediments in the other vibracores of this group. The unit at the base of VC1 contains similar minerals to the unit at the top of VC79, with the addition of quartz. VC78 contains abundant volcanic glass in all units except the lowermost one, which has no volcanic glass but a very high lithic content. In VC80 the proportion of volcanic glass is much higher at the base of the core than it is at the top of the core.

4.2.2.1 Geochemistry

Geochemical data is plotted against aluminum (commonly used to normalize geochemical data (Croudace and Rothwell, 2015)), and presented in Figure 4.14. The Stella Passage sediments have very high levels of Zr/Fe. This is indicative of volcanic sediments due to the high levels of zirconium, commonly found in igeous rocks (Konfirst et al., 2011). They also have low levels of strontium, indicative of low to no biogenic activity (Croudace and Rothwell, 2015). High levels of potassium are present, indicative of a terrestrial environment (Croudace and Rothwell, 2015). Very low Ca/Al levels are present, indicating a terrestrial environment as it is very low in biogenic material (Ca) but high in detrital material (Al) (Croudace and Rothwell, 2015).

4.3 Maunganui Roads South

Six vibracores were obtained from Maunganui Roads South (Table 4.2, Figure 4.10). Four of the cores were taken on the flanks of the dredged shipping channel, while two were taken from the centre (Figure 4.10). The vibracores are taken from water depths of 12.9–13.4 m, and are 70–160 m apart.

There is large textural and compositional variation within the sediments from the Manganui Roads South group. Stratigraphic logs of VC3, VC74 and VC77 are presented in Figures 4.11, 4.12 and 4.13 respectively. These three logs show the distinct units that occur in this area. Three main sediment populations are present in the Manganui Roads South group: silt, fine sand and medium – coarse sand. Volcanic glass, lithics, hornblende, plagioclase, and quartz are present in all sediments from this group. However, there are variations in the abundance of each. A silt unit (B,

Table 4.2: List of vibracores obtained from Maunganui Roads South.

Vibracore	Length (m)	Depth Below Sea Level (m)
VC3	1.98	13.25
VC5	2.38	13.18
VC74	1.83	13.32
VC75	1.42	12.72
VC76	1.77	13.34
VC77	1.87	13.59

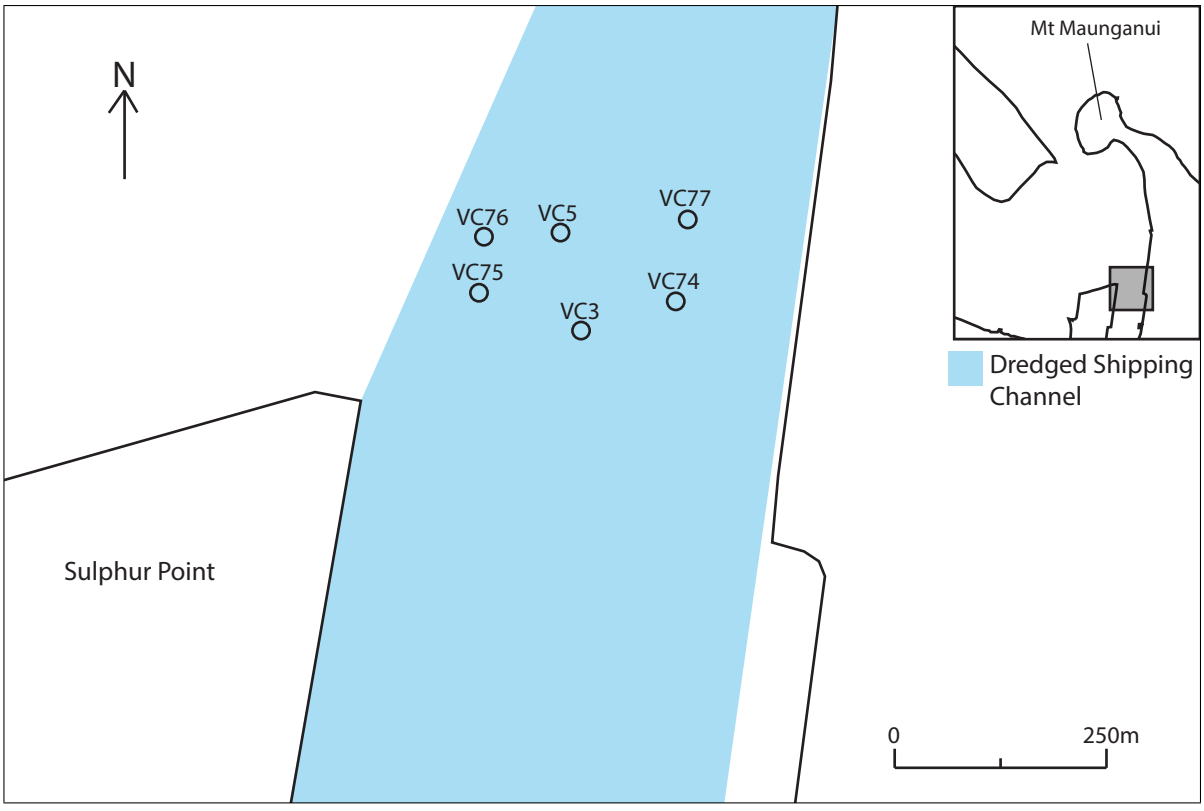

Figure 4.10: Map showing locations of vibracores taken from Manganui Roads South. See Figure 1.1b for geographic context.

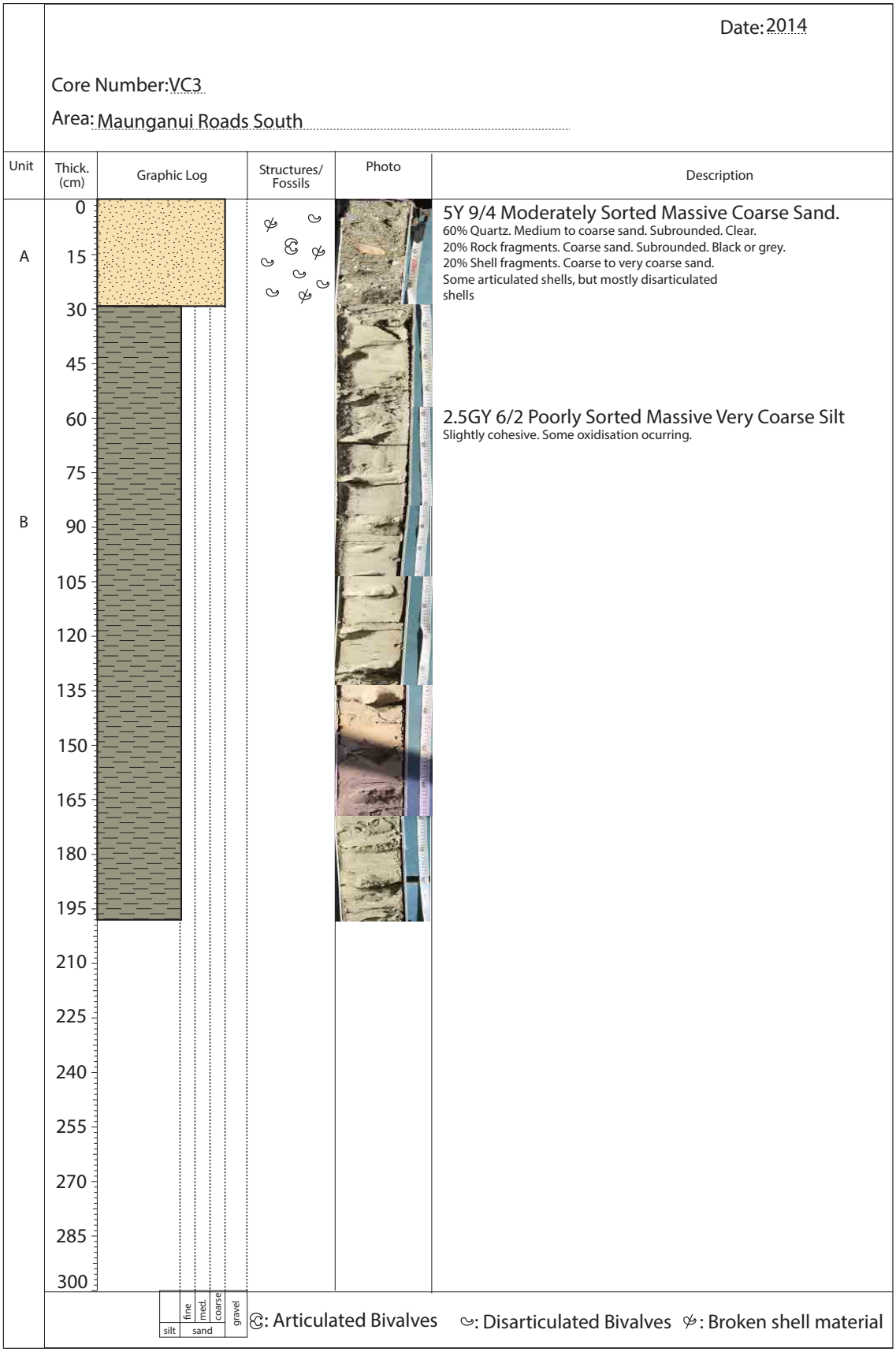

Figure 4.11: Stratigraphic log of VC3, taken from Manganui Roads South.

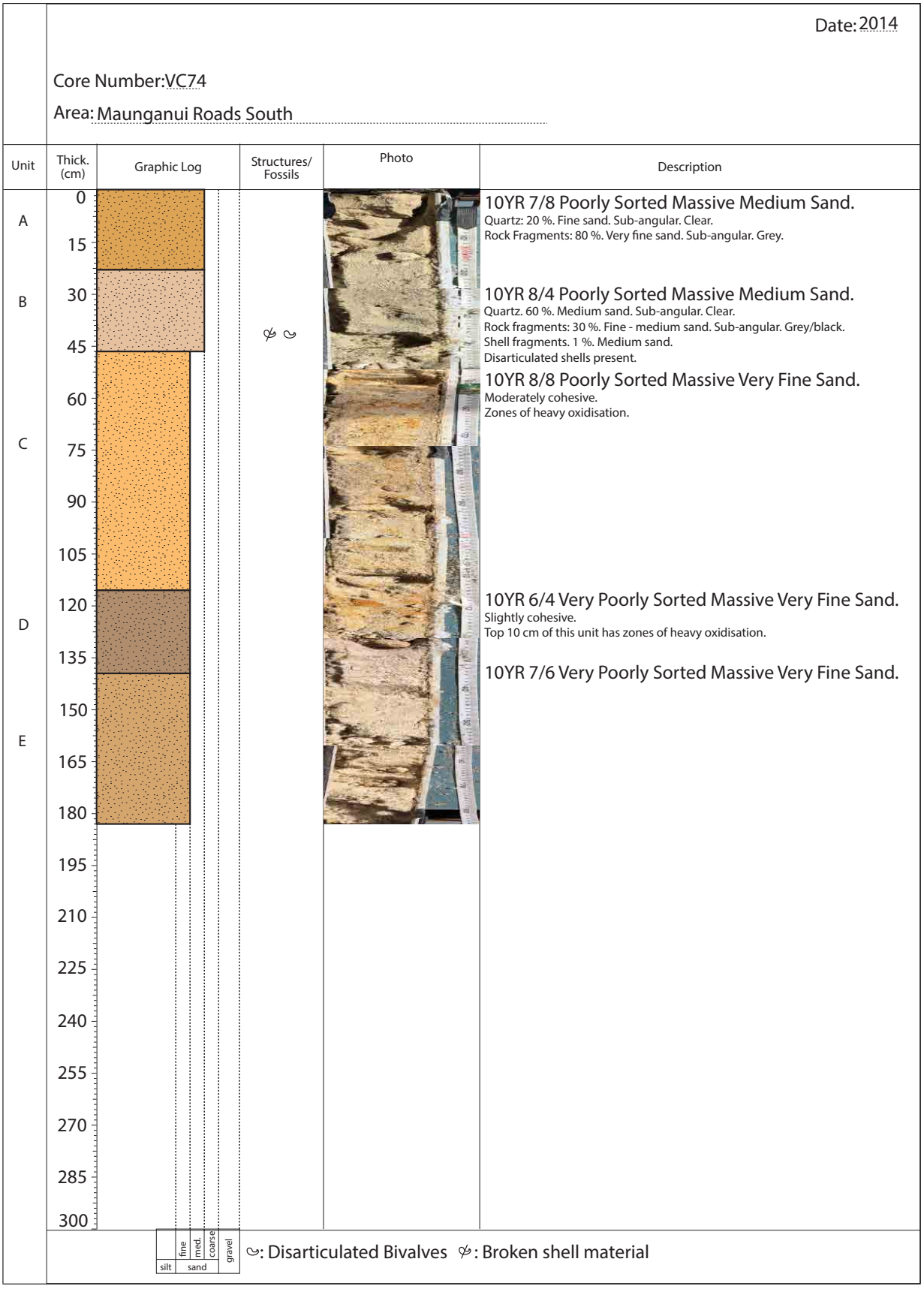

Figure 4.12: Stratigraphic log of VC74, taken from Manganui Roads South.

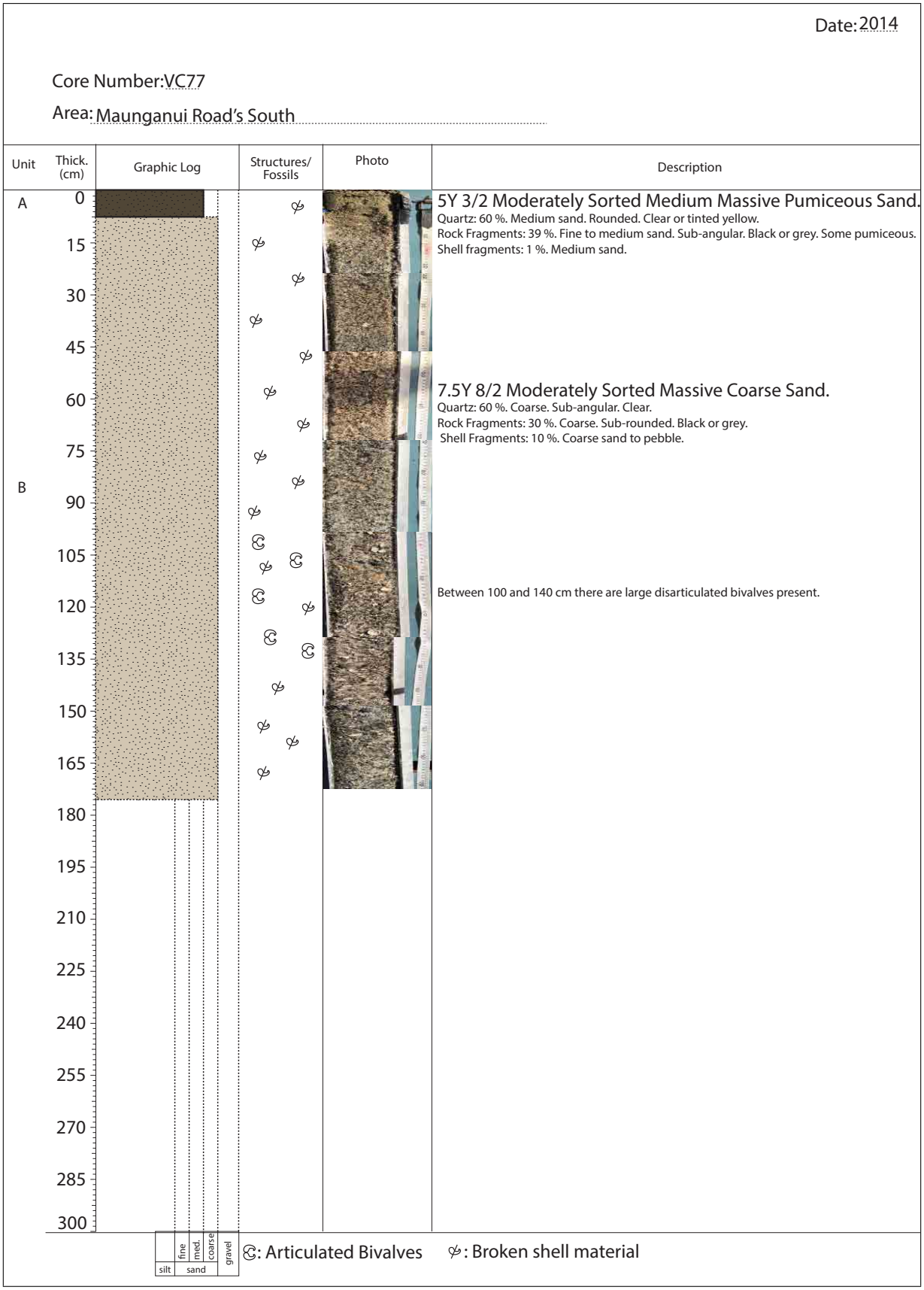

Figure 4.13: Stratigraphic log of VC77, taken from Manganui Roads South.

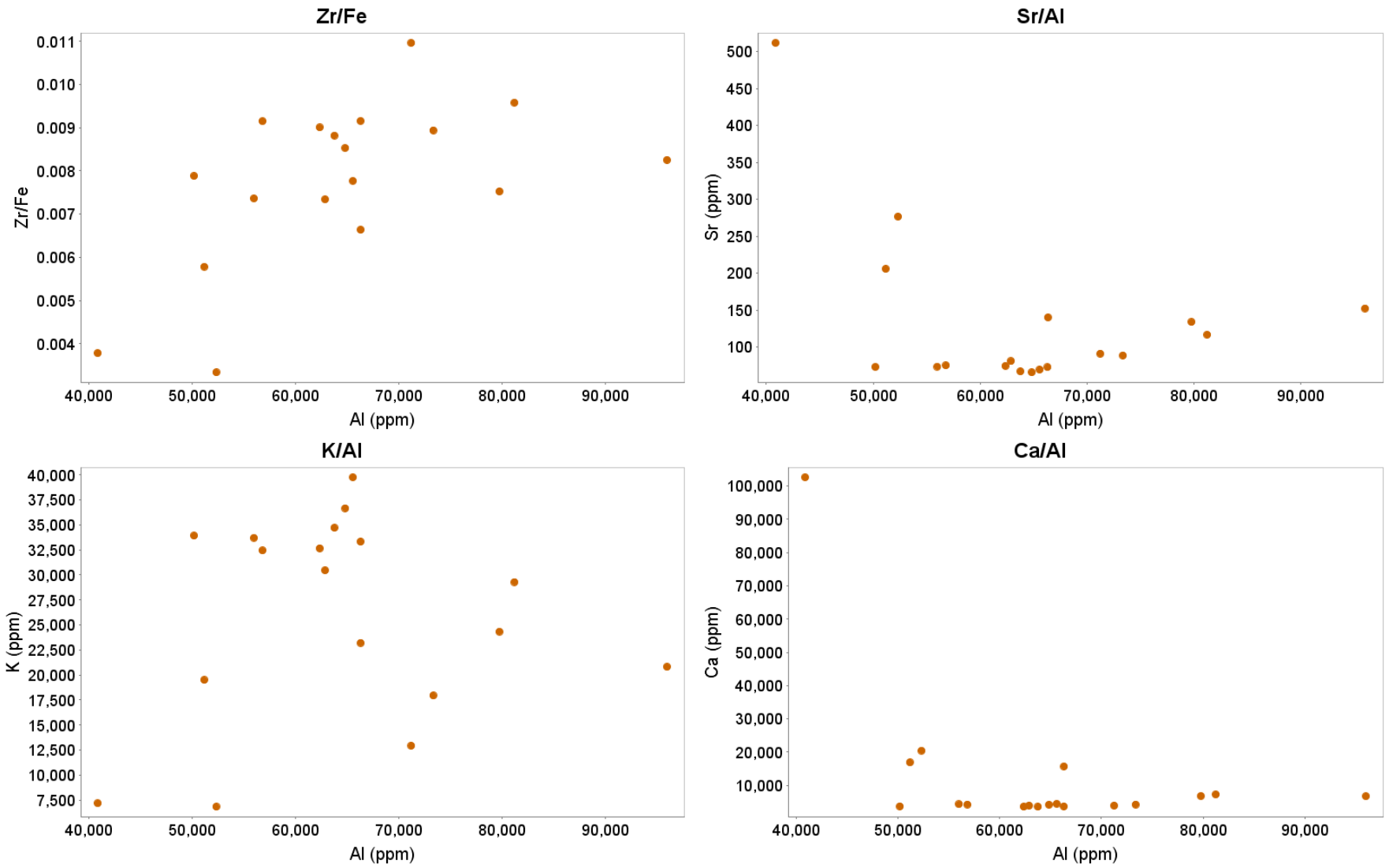

Figure 4.14: A selection of XRF data for sediments from Stella Passage. These sediments have a high Zr/Fe ratio, indicating high volcanic input. They also have low Sr and low Ca/Al levels, indicating little or no biogenic input. High levels of potassium are present, indicating a terrestrial environment. Orange = Volcaniclastic sediment. Light blue = silt. Dark blue = medium to coarse sand. Grey = pumiceous sand.

29–198 cm) is present below 29 cm depth in VC3 (Figure 4.11), but does not occur in any of the other cores. VC74 (Figure 4.12) contains multiple volcaniclastic fine sand units, some of which have distinct bronze patches, which I interpret to be iron staining. The sediments in this core are similar in texture, distribution, colour and composition to those seen in Stella Passage. The other vibracores contain medium to coarse sands predominantly composed of plagioclase, quartz, rock fragments and bioclasts (Figure 4.17). VC77 has a pumiceous sand unit at 0–7 cm (Figure 4.13), which is similar to Unit A in VC3 but contains an abundance of pumice.

4.3.1 Texture

Grain size statistics are presented in Figure 4.15 and show two distinct patterns of variation. In Figure 4.15a, Three cores (VC5, VC75, and VC77) have similar mean grain sizes, coarsening with depth. However, there are also two cores (VC3 and VC74) have a mean grain size that fines with depth. VC3 shows a large change in grain size between its top unit (A) (0 – 29 cm) and the rest of the core (B). This suggests a change in hydrodynamic conditions. VC3 and VC74 do have two distinctly different mean grain sizes however, as well as showing significant variation in the sorting and skewness statistics (Figure 4.15b, c). This difference in mean grain size is also seen in the composition, discussed in Section 4.3.2

There are two distinct trends in sorting statistics with depth. VC5, VC75, and VC77 all become moderately well sorted by 40 to 50 cm. This is not the case with VC75 and VC74, where sorting decreases with depth. All sites become more coarsely skewed with depth. However all samples are still finely skewed.

A bivariate plot of skewness plotted against sorting is presented in Figure 4.16 and shows there are three clusters present, all of which are defined by the composition of the sediment (discussed further in Section 4.3.2). A, the more well sorted sediment cluster, represents coarser grained sediment like that identified at the top of VC3 in Figure 4.11. Group B is made up of sediment from the tops of cores VC74, VC75, VC76 and VC77 (the latter three are pumiceous). The rest of the samples have a sorting greater than 1.5 and a skewness less than 1.2, and include two of the volcaniclastic fine sand sub-samples from VC74 and the three silt sub-samples from VC3.

4.3.2 Composition

The composition of the sediments in the Manganui Roads South area is variable. The coarse sand unit (A) (0–29 cm) in VC3 is composed of quartz, bioclasts, lithics and augite (Figure 4.17a). The presence of augite indicates that some of this sediment has originated from a mafic parent rock. In contrast, the silt unit (B) is composed of a very high proportion of lithics, as well as plagioclase and some bioclasts (Fig-

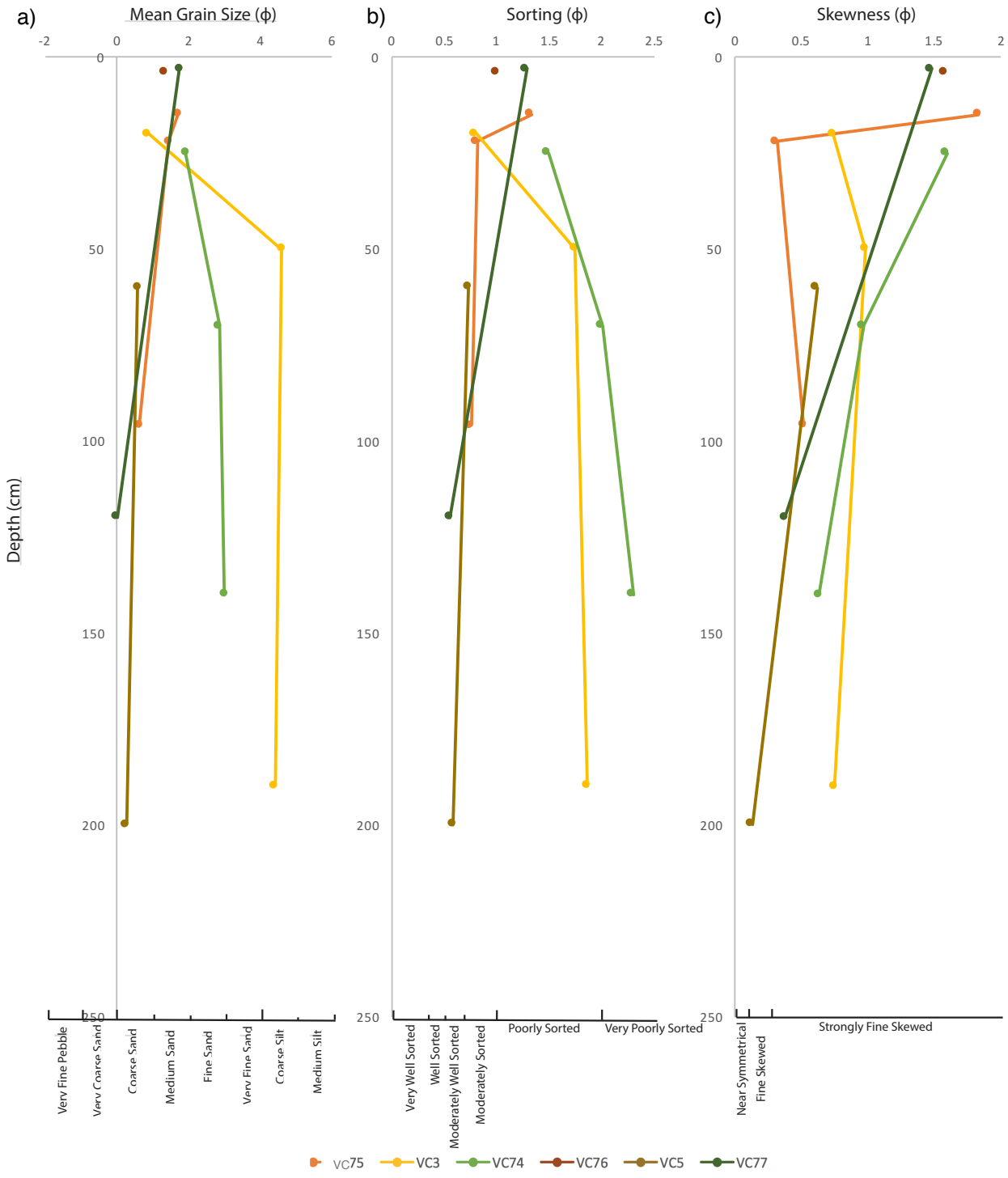

Figure 4.15: Grain size statistics plotted against depth for sub-samples obtained from Maunganui Road's South vibracores.

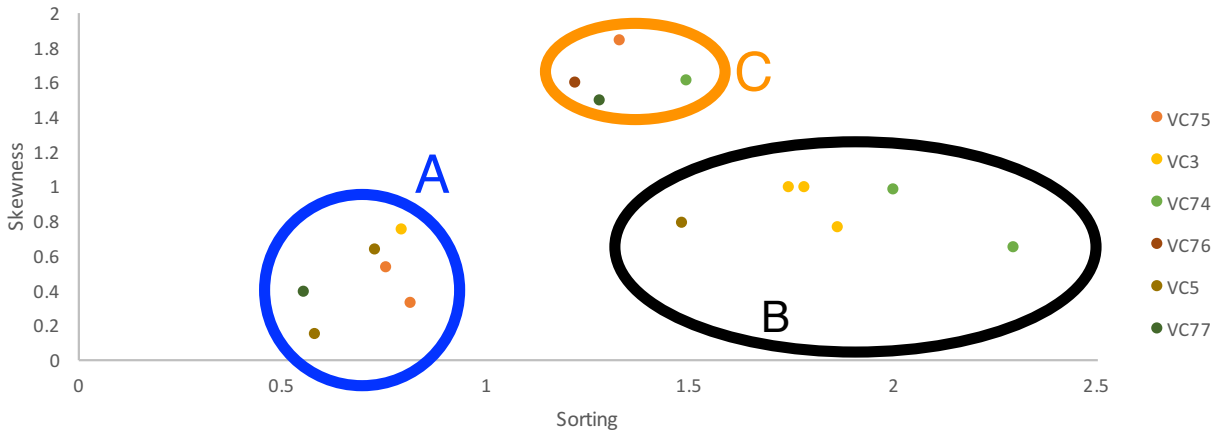

Figure 4.16: Skewness plotted against sorting for sub-samples taken from Manganui Roads South. Three groups are present: A, a well sorted unit containing medium to coarse sands with bioclasts; B, a poorly sorted group containing pumiceous coarse sands from the tops of cores; and C, a poorly to very poorly sorted group containing volcaniclastic sediments and silt.

ure 4.17b). VC74 is composed throughout of very fine sand with a fairly consistent mineralogy (a representative thin section is shown in Figure 4.17c). All three sub-samples contain volcanic glass, lithics, and plagioclase. In this vibracore, volcanic glass is the most abundant element. Quartz is also present, as well as hornblende in two of the samples. The other vibracores (VC75, VC76, VC77) contain pumiceous and medium to coarse sands with abundant lithics at the tops of the cores (Figure 4.17d), underlain by medium to coarse sands with varying proportions of plagioclase, lithics and bioclasts (Figure 4.17e). Hornblende is also present as a minor component in several samples (Figure 4.17c, d and e).

4.3.2.1 Geochemistry

Geochemical data is plotted against aluminiuim and presented in Figure 4.18. Overall, the silt and volcaniclastic sediments in Maunganui Roads South have slightly higher Zr/Fe than most of the medium to coarse sand sediments. The pumiceous sediments also have elevated Zr/Fe. The medium to coarse sand and pumiceous sediments also have higher Ca/Sr and Si/Al than the silt and volcaniclastic sediments, indicating increased biogenic production in the medium to coarse and pumiceous sediments (Hodell et al., 2008; Dickson et al., 2010).

The volcaniclastic and silt sediments are enriched in aluminium and iron, which I interpret to indicate greater terrigenous input (Croudace and Rothwell, 2015). Arsenic, a marker of pyrite authigenesis (Thomson et al., 2006), is present in all sediments but elevated in one of the silt samples. Sulphur, a useful marker of reducing conditions (Croudace and Rothwell, 2015), is present in the silt, medium to coarse sand and pumiceous sediments but not the volcaniclastic sediment.

I interpret the lower sulphur and arsenic levels indicate that the medium to coarse

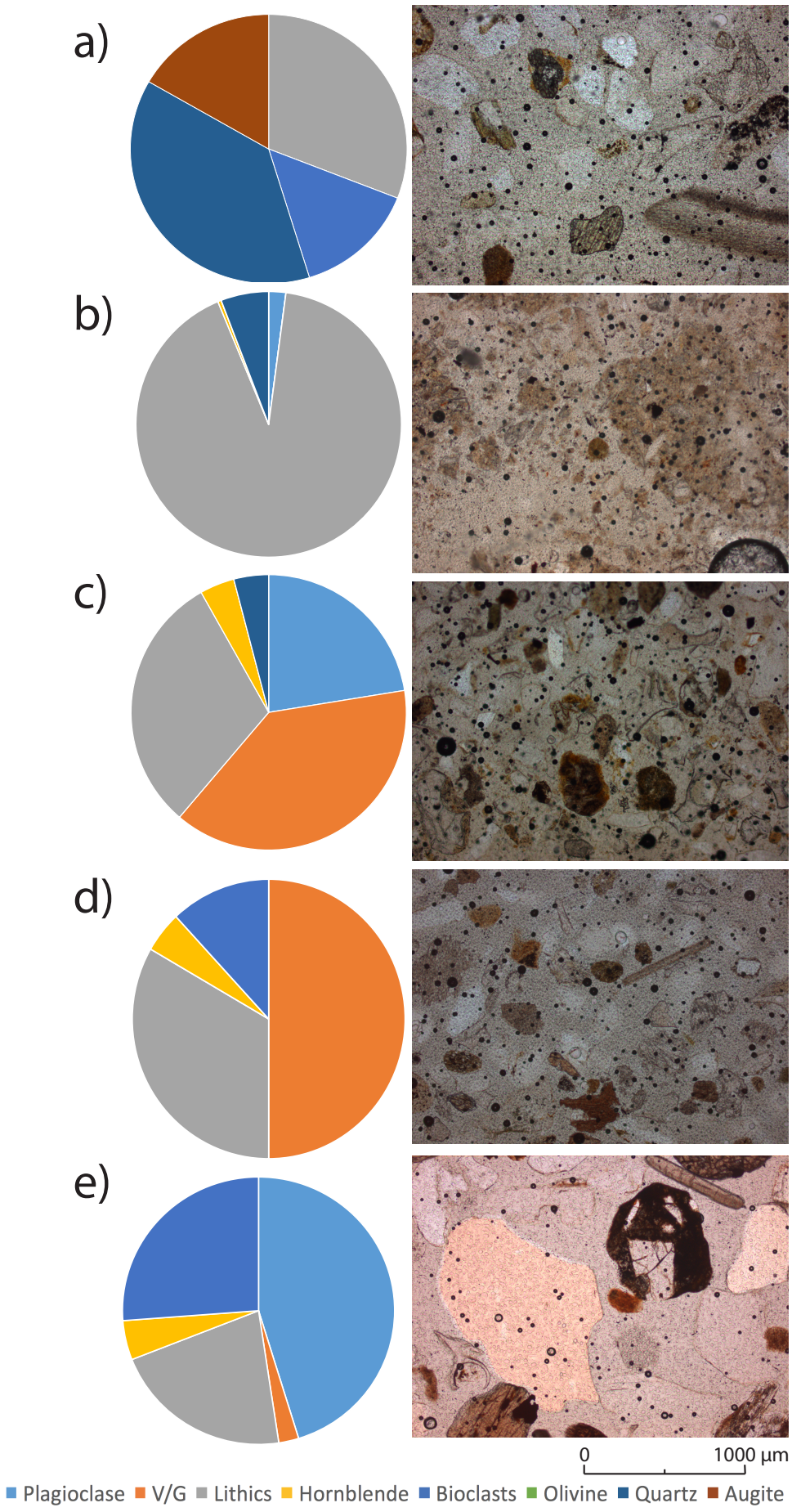

Figure 4.17: Pie charts and thin section images of Manganui Roads South thin sections. A) Coarse sand unit A from VC3. Contains plagioclase and bioclasts, as well augite and lithics. B) Silt unit B from VC3 is abundant in lithics. C) Volcaniclastic sediment from VC74. Contains abundant volcanic glass and lithics. D) Pumiceous sand from VC77, rich in volcanic glass and lithics. E) Coarse sediments from VC75, containing plagioclase, bioclasts, lithics, and hornblende.

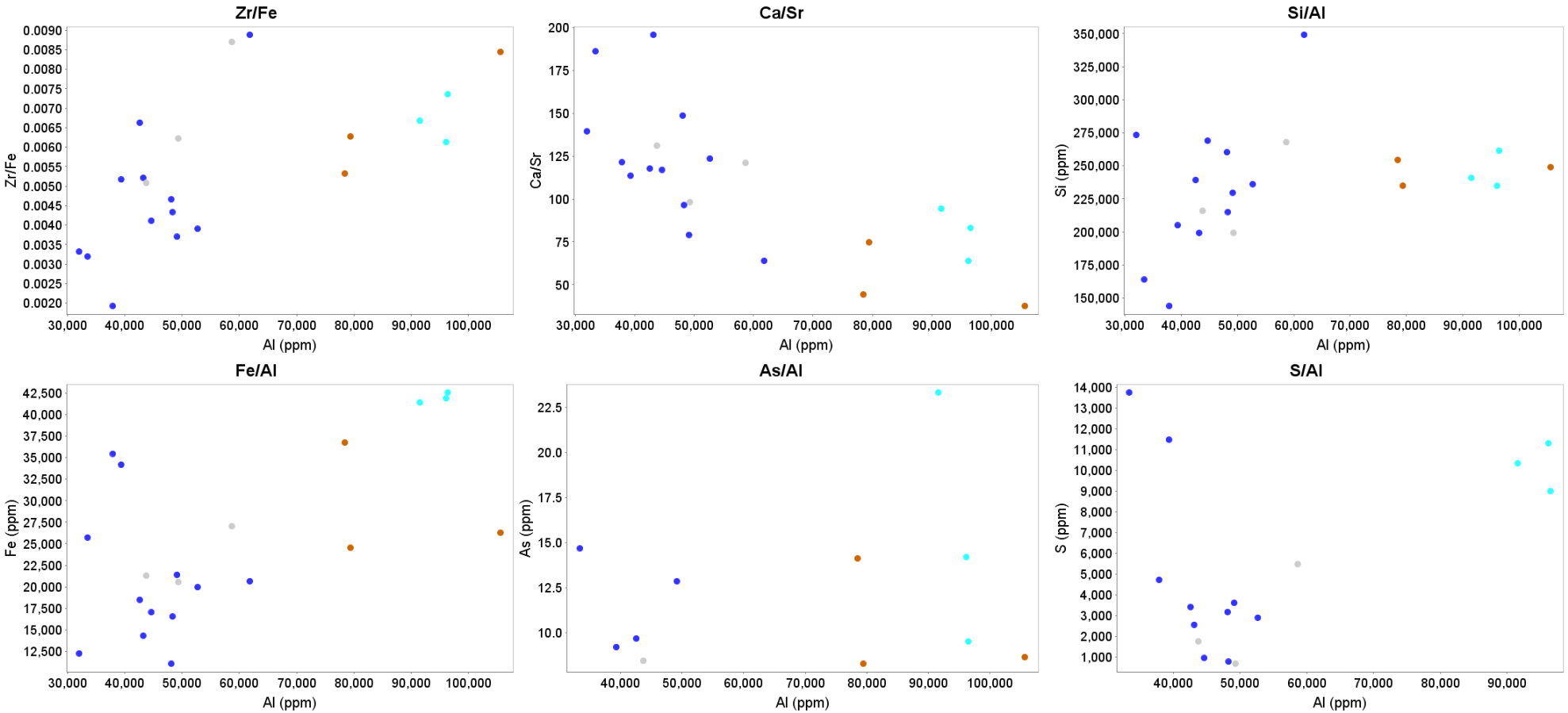

Figure 4.18: Elemantal proportion by depth data for select sites from Manganui Roads South.

sand and pumiceous sediments were deposited in a partially suboxic environment, likely due to enhanced productivty. I interpret the elevated As and S present in the silt to be indicative of deposition in an anoxic environment.

Much of the variation in the elemental data in Figures 4.20a and 4.20b is caused by changes in facies. In VC75, the sample at 15 cm depth is pumiceous sand (Figure 4.20b). It has lower Ba, Sr and Ca (biogenic indicators (Croudace and Rothwell, 2015)) than the medium to coarse sand sediments below it. It also has higher Fe, and K than the medium to coarse sand sediments below (indicators of terrestrial input (Croudace and Rothwell, 2015)). The silt unit in VC3 (Figure 4.20a) has lower Ba but higher Sr and S than the coarse sand unit above it. Fe is also enriched in the silt unit, but it is lower in Si and K than the coarse sands unit above it. Ca is consistently low in this core.

Oxidising was observed in the silt unit in VC3 (Figure 4.11), and this is also seen in the high Fe and high S which has been used as a marker for reducing conditions (eg. Sluijs et al. (2011); Croudace and Rothwell (2015)). Reducing conditions would explain the low levels of Barium, which is affected by anoxic conditions. This is consistent with that found in other studies (eg. (van Os et al., 1991; Brunsack and Gieskes, 1983)).

4.3.2.2 Magnetic Susceptibility

The magnetic susceptibility of the silt unit (B) in VC3 was measured and the results are displayed in Figure 4.19. The results show low magnetic susceptibility throughout. Peaks in this data are closely followed by troughs, and this is fairly consistent throughout this vibracore. There is some variation between the low and high frequency measurements, however these variations are very small and do not deviate from the general trends of the data. Air variation measurements averaged -0.17 SI x 10^{-5} for low frequency measurements and 0.11 SI x 10^{-5} The measurements peak at 170 cm depth. however even these are only at a maximum of 18 SI x 10^{-5}. Overall, there is a trend of the magnetic susceptibility values increasing with depth.

The Fe and Fe/Magnetic Susceptibility data for the silt unit presented in figure 4.20a shows high levels of Fe. This, combined with the low levels of magnetic susceptibility in VC3 (Figure 4.19), can indicate magnetite diagenesis (Croudace and Rothwell, 2015). Although there are only three Fe samples available for this, the presence of other indicators of diagenesis such as pyrite (arsenic) support this interpretation.

4.4 Maunganui Roads

Twenty-two vibracores were taken from the Maunganui Roads area (Table 4.3, Figure 4.21). The cores were obtained from the full width of the channel, in water

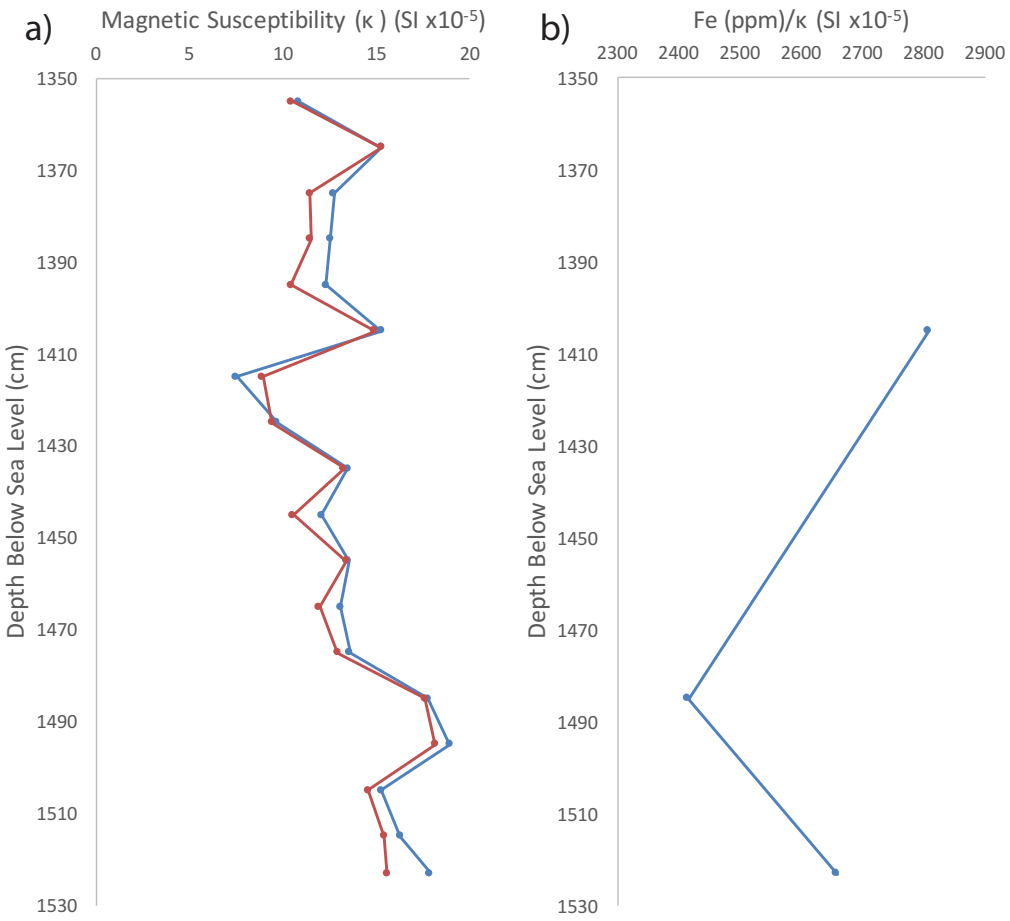

Figure 4.19: a) Magnetic susceptibility of the silt units measured in VC3. The blue line is low frequency measurements and the red line is high frequency measurements. b) Ratio of magnetic susceptibility by Fe for the silt units measured in VC3. Only 3 Fe measurements were taken for the silt unit in VC3.

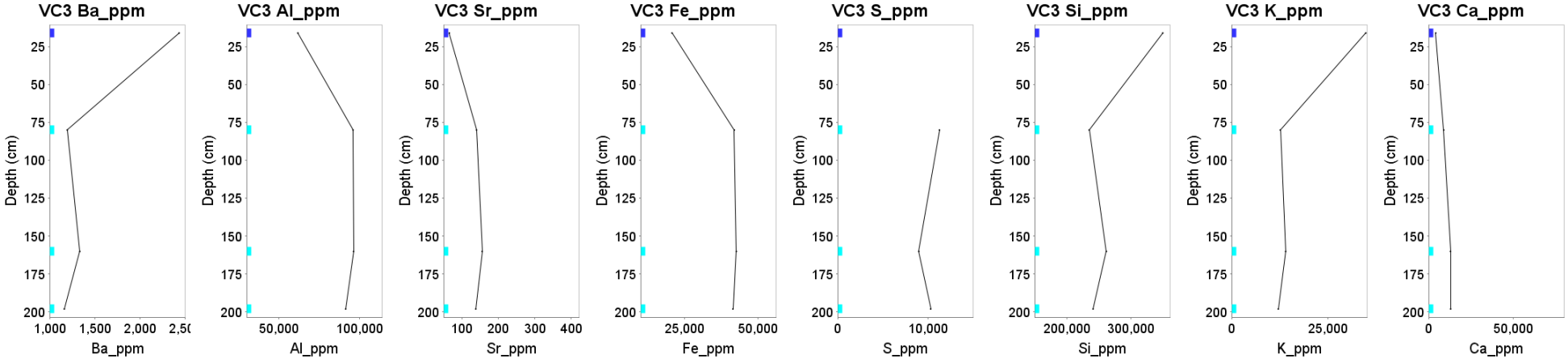

(a) Elemental data plotted against depth for VC3.

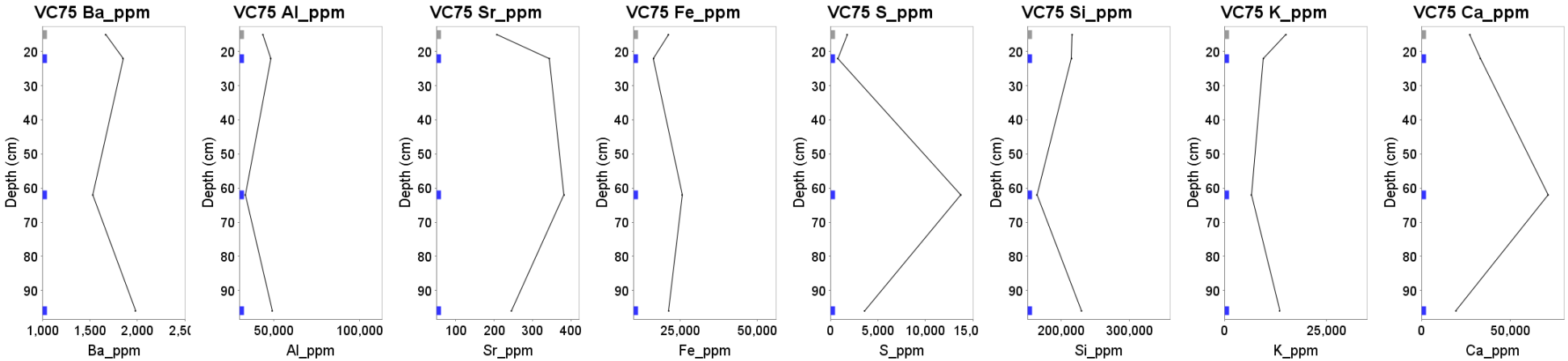

(b) Elemental data plotted against depth for VC75.

depths of 12–14.1 m, and with a lateral spacing of 20–100 m.

Table 4.3: List of vibracores taken from the Maunganui Roads area.

Vibracore	Length (m)	Depth Below Sea Level (m)
VC6	1.96	14.07
VC7	1.76	13.71
VC8	2.42	14.34
VC9	2.66	14.26
VC12	3	13.47
VC61	2.26	13.40
VC62	1.98	14.33
VC63	2	13.84
VC64	1.98	12.94
VC65	2.17	10.01
VC66	1.2	12.02
VC67	1.29	13.53
VC68	1.69	13.57
VC69	1.8	13.73
VC70	0.77	12.74
VC71	2.27	12.93
VC72	1.97	13.71
VC73	1.79	13.73

There are large variations in the grain size and composition within the sediments obtained from Manganui Roads. A stratigraphic log of VC12 is presented in Figure 4.22 and shows the variation that is present in the sediments in this area. Two main sediment populations occur in the Manganui Roads area: a medium to coarse sand and a silt (Figure 4.26).

Of note is the erosional boundary in this core between the medium to coarse sand units and the silt unit (Figure 4.22). This boundary also occurs in VC6, VC64, VC67, VC68, VC69 and VC71. VC7, presented in a stratigraphic log in Figure 4.23, is the only vibracore in this area that is entirely a cohesive very fine sand to silt. All other vibracores have unconsolidated medium to coarse sand-sized sediments overlying the silt succession. This boundary commonly has prod and skip marks (Reineck and Singh, 1980), suggesting saltating flow (Boggs, 2009).

VC7, shown in Figure 4.23, contains two types of cohesive consolodated sediment. The top unit (0–21 cm) is a very fine sand whereas the unit below (21–176 cm) is coarse silt. A gradational boundary separates the two units. I interpret this to suggest a change in hydrodynamic conditions. In VC12, a small silt/clay pod occurs in Unit B, similar in texture to the unit 20 cm below. I interpret this as a rip up clast, suggesting that Unit B represents a hydrodynamic regime characterised by at least intermittent high energy conditions. The contact between the coarser sand units and the siltier units does not occur at the same depth in each core, indicating that while the contact may be continuous throughout the area, it is irregular. I interpret this as

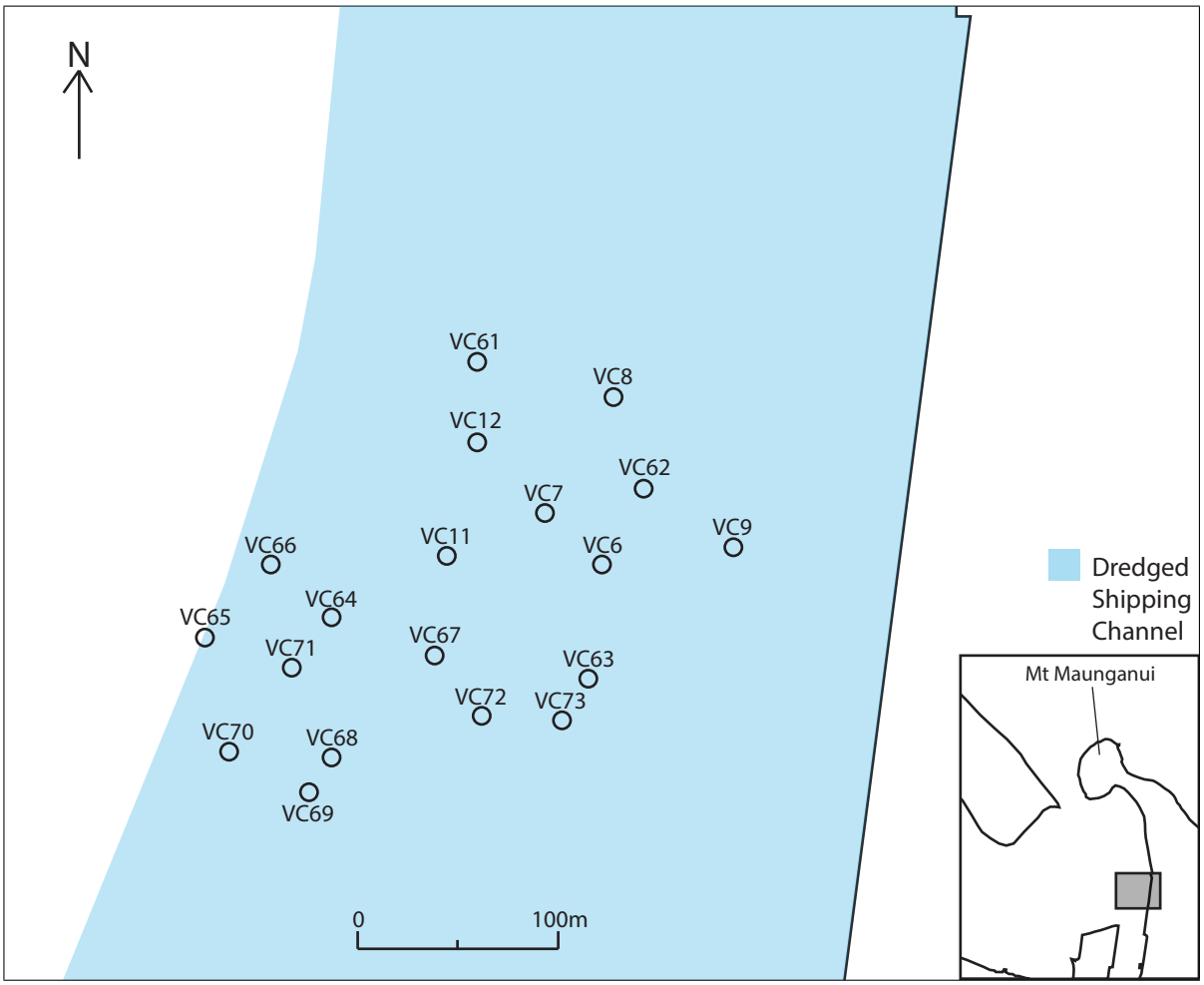

Figure 4.21: Map showing locations of vibracores taken from Maunganui Roads. See Figure 1.1b for geographic context.

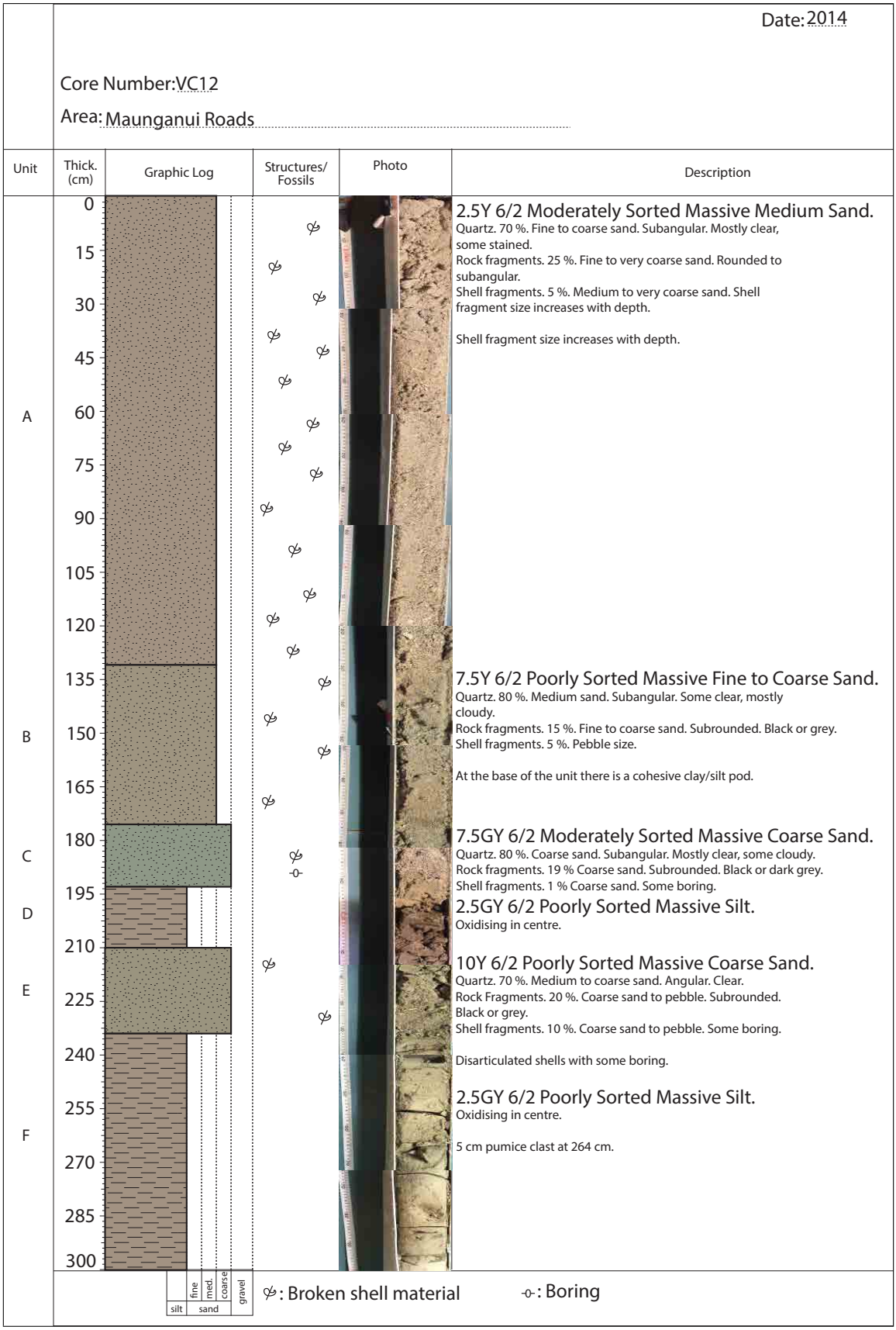

Figure 4.22: Stratigraphic log of VC12, taken from Manganui Roads.

Date: 2014

Core Number: VC7

Area: Maunganui Road's

Unit	Thick. (cm)	Graphic Log	Structures/ Fossils	Photo	Description
A	0–180				2.5GY 6/2 Poorly Sorted Massive Very Fine Sand. Cohesive.
					2.5GY 6/2 Poorly Sorted Massive Very Coarse Silt. Cohesive.
B	90				Pumice clast at 88 cm depth, 4.5 cm long.



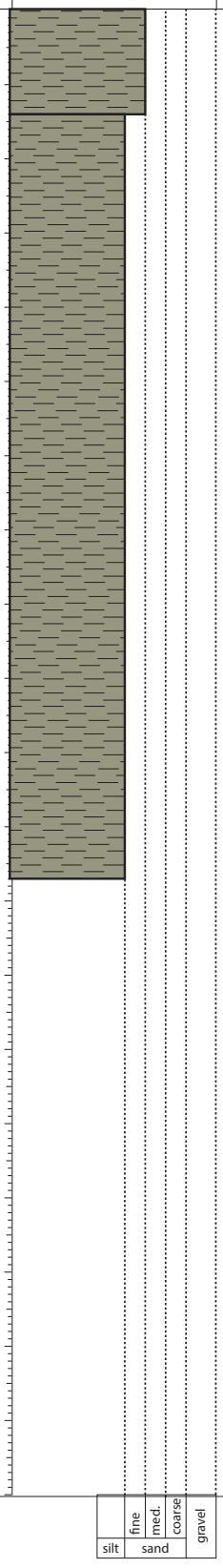

Figure 4.23: Stratigraphic log of VC7, taken from Manganui Roads.

suggesting some high velocity channels may have developed, where sediment was scoured away. Medium to coarse sand units are found at a number of the contact sites above silt units. The silt unit at the base of VC12 contains a 5 cm long well rounded pumice clast, which is anomalous in the context of the grain size of the rest of the sediment in that unit. A similar clast is also found in VC7. I interpret this to indicate terrigenous input of volcanogenic sediment from a distal source.

The medium to coarse sand units that overlie the finer, siltier sediments are composed of plagioclase, quartz, bioclasts (articulated and disarticulated), and lithics. The siltier sediments are made up of lithics and plagioclase, with trace amounts of hornblende and bioclasts also present. Pumiceous sands are also present in this area, occurring at the tops of some cores. These sediments are coarse sand, and are predominantly composed of lithics and volcanic glass, with minor components of plagioclase and bioclasts.

When observed, some of the siltier sediments were oxidising, as were some of the medium to coarse sand units, indicating that this area has undergone periods of anoxic conditions. Distinct accumulations of bioclasts occur in some vibracores, such as VC63 (Figure 4.24). Articulated and disarticulated bivalves are present in most cores, although the abundance of each varies (5–20 %). VC66 contains an accumulation of flake-like organic matter in a thin bed at 40 cm depth, and vegetation fragments were also found in VC70 (sporadically between 47 and 70 cm depth). Some of the quartz grains in sediments in this area are stained yellow. However they are predominantly clear and colourless.

4.4.1 Texture

For most cores in the Maunganui Roads area the mean grain size fines with depth. There are two distinct ranges of mean grain size shown in Figure 4.25a; units with grain size coarser than 2 ϕ, and units with grain size finer than 3 ϕ. This reflects the distinct units that are present in this area. The varying depth of the contact between the contrasting grain size units can also be seen in Figure 4.25a. For instance, in VC12, the silty sediment is only present below 190 cm depth, whereas in VC7 the silty sediment is present throughout the entire core. In most cores the silty sediment is a continuous unit. However, in VC12 (Figure 4.22) it is interrupted by a 20 cm coarse sand unit (210–230 cm). This could suggest a change in depositional environment, or it could indicate a sudden input of coarser grained sediment into the area.



Figure 4.24: Shell bed in VC63, at 190 cm depth.

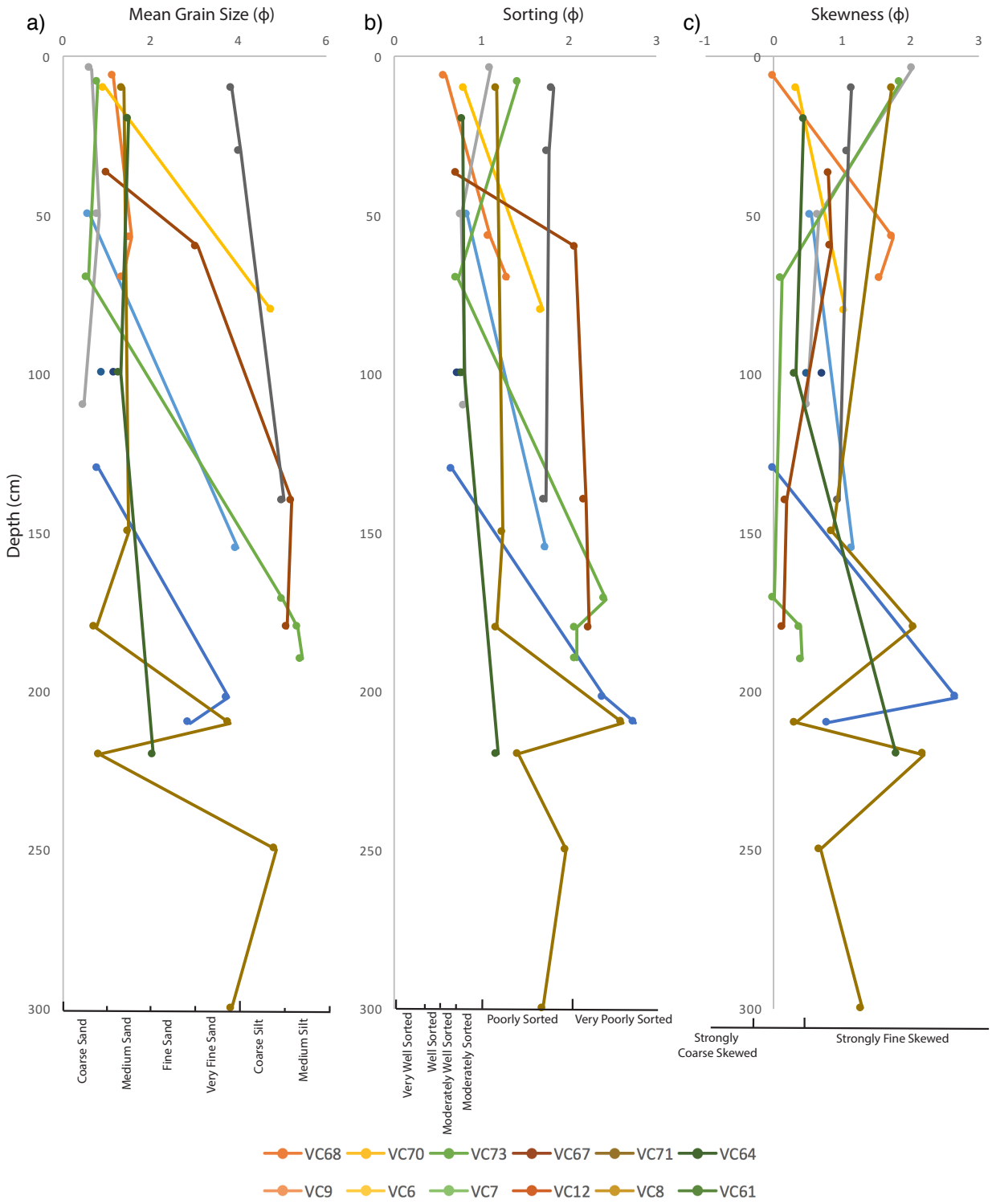

Figure 4.25: Grain size statistics plotted against depth for sub-samples obtained from Manganui Roads vibracores.

All of the siltier units in this area are very poorly sorted (see Figure 4.25b). The coarser sand units are moderately sorted. The majority of the sub-samples measured are strongly fine skewed. However, some are near symmetrical. In VC12, the finer sediments are more finely skewed and more poorly sorted.

The variation between the units present in this area is shown in 4.27, where the cumulative grain size distribution curves show the sand units clustering together, whereas the silt unit is an outlier with a much higher proportion of finer grains.

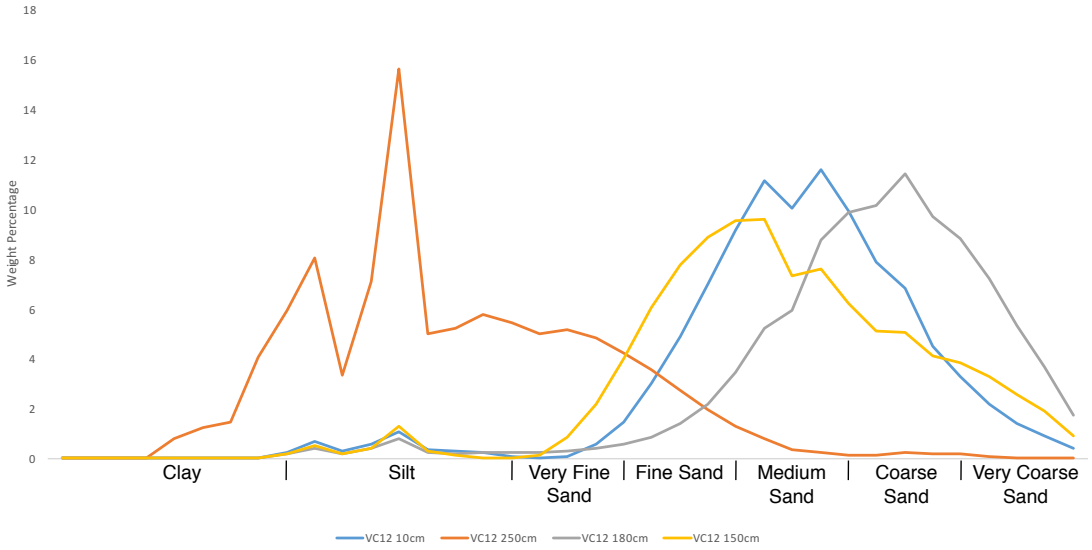

Figure 4.26: Grain size populations from VC12, representative of the variation in grain size in the units in this area. The three samples from 10cm, 150 cm and 180 cm are medium to coarse sands. The sample from 250 cm is a silt.

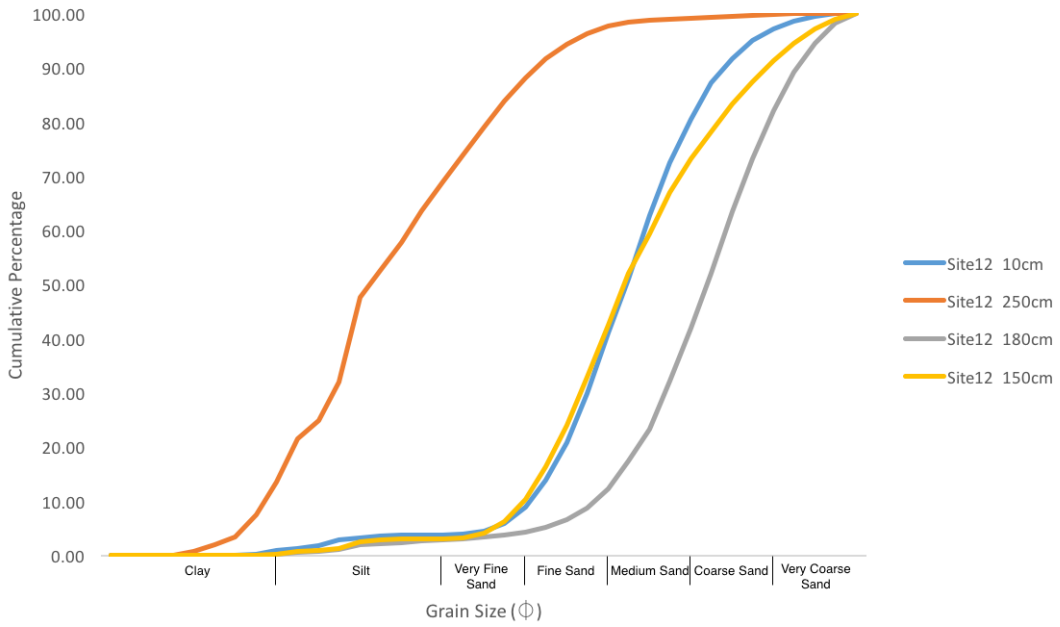

Figure 4.27: Cumulative grain size plot for sub-samples analysed from VC12.

Mean grain size is plotted against sorting in Figure 4.28. It shows two distinct

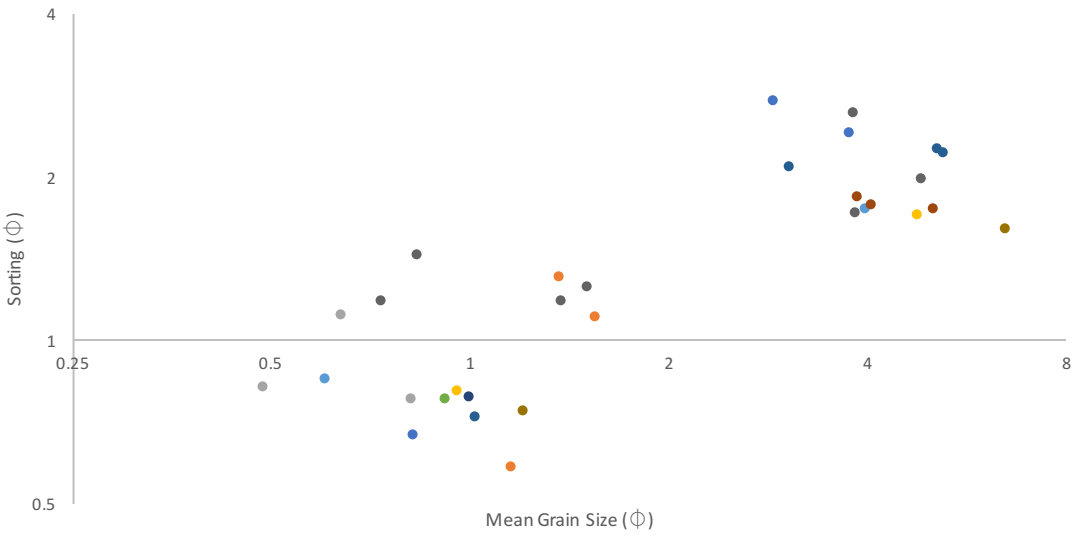

Figure 4.28: Mean grain size plotted against sorting for sub-samples from Maunganui Roads. Two groups are present; Group A, with medium to coarse sand and pumiceous sand units and Group B, with silt units.

groups; Group A which contains medium to coarse sand and pumiceous sand units and Group B, which contains silt units. This graph separates two distinct hydrodynamic regimes that have existed in this area; one with high velocity and a lot of movement leading to coarse grained moderately sorted units and one with low velocity and little movement leading to silty poorly sorted units.

4.4.2 Composition

The composition of the sediments in the Maunaguni Roads set of vibracores is variable depending on the type of sediment being cored. At the tops of some cores there is a pumiceous sand, which is composed predominantly of volcanic glass, but also contains lithics, bioclasts and in some cases hornblende (Figure 4.29a).

This sediment often overlies medium to coarse sand units that are predominantly composed of plagioclase, lithics, quartz, bioclasts and trace amounts of hornblende (Figure 4.29b). VC70 includes some sediments that were identified as oxidising (32–38 cm, and 41–44 cm). These sediments are composed predominantly of lithics, with trace amounts of hornblende.

The silty sediment at the base of some cores (or in the case of VC7, the whole core) is composed of lithics, plagioclase and bioclasts (Figure 4.29d). There are variations in the proportions of lithics and plagioclase present in this sediment. In contrast to the sediments in Stella Passage and part of Manganui Roads South, the sediments in this area have much less volcanic glass present.

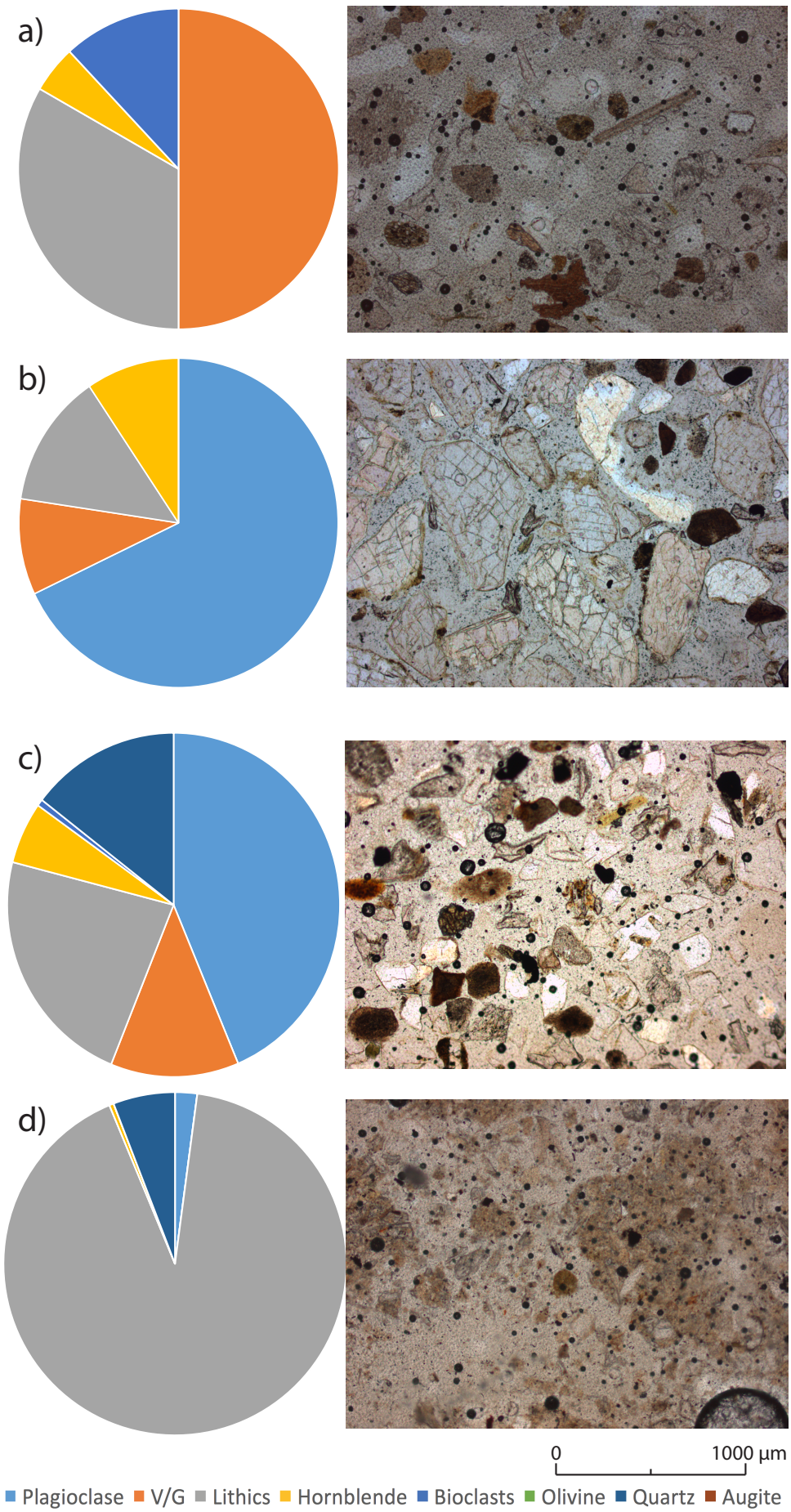

Figure 4.29: Pie charts and thin section images of sediments from Manganui Roads. A) shows pumiceous sand, with abundant lithics and volcanic glass. B) shows medium to coarse sand, with plagioclase and lithuics. C) shows a medium sand sample containing bioclasts. D) shows a silt sample, with abundant lithics.

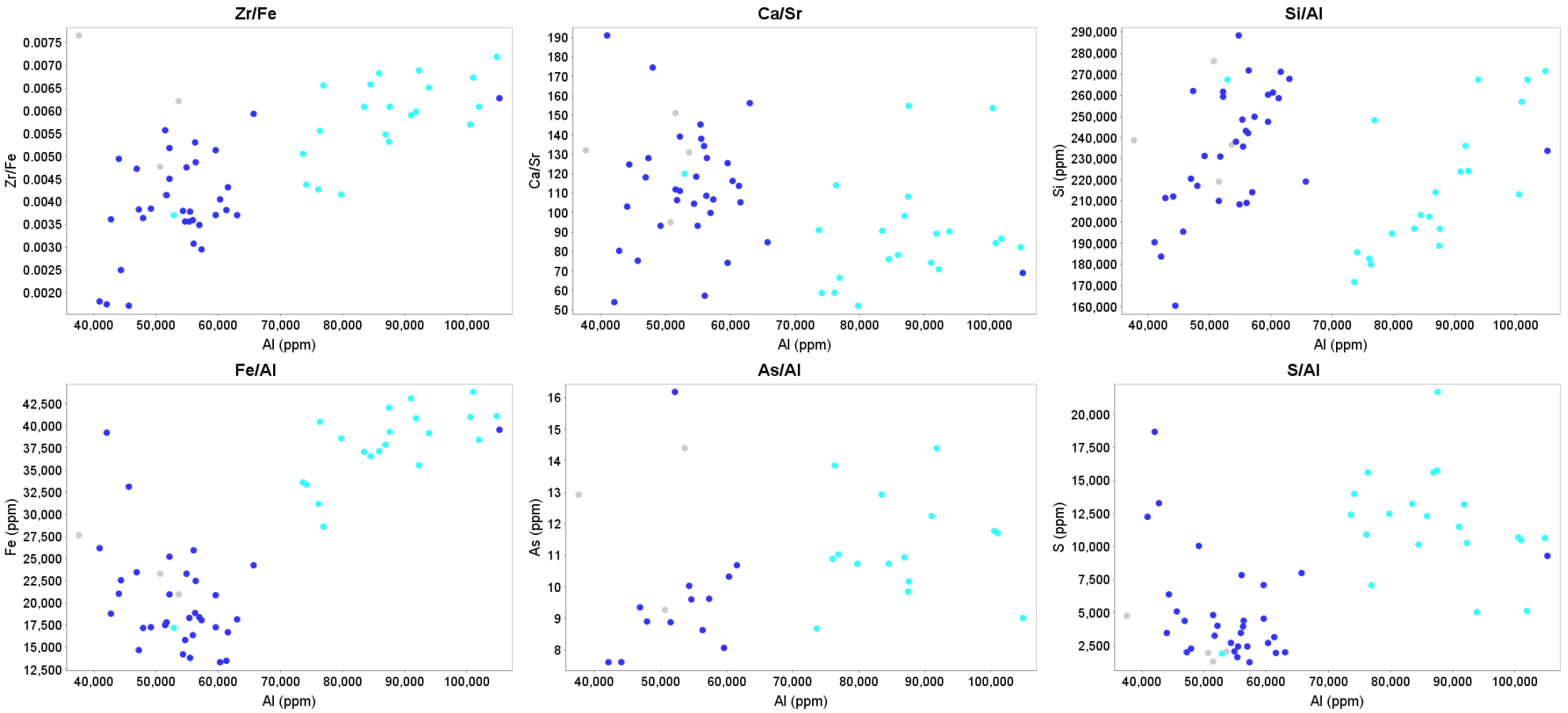

Figure 4.30: Elemantal proportion by depth data for select sites from Manganui Roads. The silt samples are light blue, coastal sands samples are dark blue and pumiceous sands samples are grey. Light blue = silt. Dark blue = medium to coarse sand. Grey = pumiceous sand.

4.4.2.1 Geochemistry

There are major geochemical differences between the silt and the medium to coarse sand sediments in Maunganui Roads (Figure 4.30). Aluminium in the silty sediments is greater than 70,000 ppm, and lower than 70,000 ppm in the medium to coarse sands. Iron is also elevated in the silt, suggesting higher proportions of detrital material (Croudace and Rothwell, 2015). Arsenic is present in all types of sediment, but it is not as prevalent in the coarser grained sediments. Silt samples have higher levels of S/Cl than the medium to coarse sand sediments. Framboidal pyrite was found under SEM (Figure 4.31), suggesting an anoxic environment (Wilkin and Barnes, 1997). I interpret the presence of arsenic and elevated S/Cl levels to suggest that further pyrite is present in the silt units (Thomson et al., 2006). The medium to coarse sand units have a higher Si/Al ratio than the silt. I interpret this to be indicative of increased biogenic production (Dickson et al., 2010). The pumiceous sands have higher potassium, indicating greater detrital input (Croudace and Rothwell, 2015).

Several elements are plotted against depth for vibracores VC12 (Figure 4.32a) and VC64 (Figure 4.32b). The higher levels of arsenic and S/Cl (indicative of pyrite) are clear in the silt units (light blue). Si/Al, Fe, and K show strong variation caused by changes in facies. The pumiceous sand samples are enriched in potassium, and in VC64 exhibit a higher Zr/Fe ratio (a marker of volcanism).

4.4.2.2 Scanning Electron Microscope

Moon et al. (2013) suggested diatoms may be present in some of the silty sediments close to the surface, indicating a lacustrine environment. The scanning electron microscope was used on one sub-sample from VC12 (280 cm depth) and one from VC7 (50 cm depth). Diatoms were present in both sub-samples, but not in great abundances. All diatoms that were identified were broken or partially dissolved (Figure 4.33) indicating that they were transported to the core location, rather than in-situ. They could also have also been dissolved in a saline environment (Ryves et al., 2001). One instance of framboidal pyrite was found in the sub-sample from VC12 (Figure 4.31). Elemental analysis of the framboid showed it was made up of 50 % iron and 20 % sulphur. Framboidal pyrite is the dominant form of pyrite in modern anoxic environments (Wilkin et al., 1996; Wilkin and Barnes, 1997). It is also found in hydrothermal deposits (eg. (Oswald and England, 1977)) and can be found preserved in ancient sedimentary rocks (eg. (Honjo et al., 1965)). I interpret this instance of framboidal pyrite to be due to reducing conditions, and indicative of early diagenesis.



Figure 4.31: Framboidal pyrite found in VC12. Only one framboid was found in this sub-sample. However, geochemical analysis suggests more are present at other depths in this core (Section 4.4.2.1).

4.4.2.3 Magnetic Susceptibility

The magnetic susceptibilities of the silt units present in VC12, VC8, VC7, and VC67 were measured and are presented in Figure 4.34. They show peaks at both the top and base of the silt units within the Maunganui Roads cores. VC67 has a peak at 1383 cm and again at 1463 cm. The low frequency measurements are consistently higher than the high frequency measurements at all but one point. The occurrence of two distinct peaks in the data is true for most cores within this set, potentially indicating an input of more magnetic sediment into the basin on two occasions. Each core measured in this set has a peak at the top and the base of the silt unit, and interpretive lines have been drawn on Figure 4.34 to show these potential correlations. This has been used to estimate sedimentation, shown in Table 4.4. The results show high levels of sedimentation at VC8 and VC7, and lower rates at VC12 and VC67. These numbers are subject to relatively large error, as samples were only taken every 10 cm. The data used for VC12 do also include a coarse sand unit, introducing a further source of error. VC8 does not have a peak at the base of the unit, which I suggest indicates that the peak is deeper in the sediment that below the penetration depth. These peaks do occur at different levels of magnetic susceptibility (VC67 ranges between 8 and 20 whereas VC12 ranges between 250 and 15), which I interpret to mean there are different types of magnetically susceptible sediment present, potentially indicating

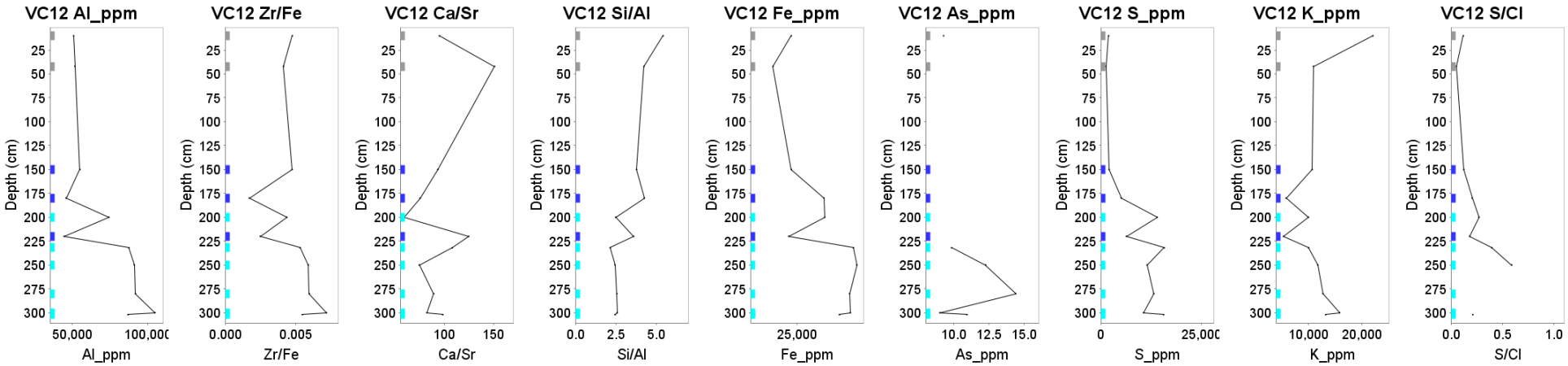

(a) Elemental data plotted against depth for VC1. The silt samples are light blue, coastal sands samples are dark blue and pumiceous sands samples are grey.

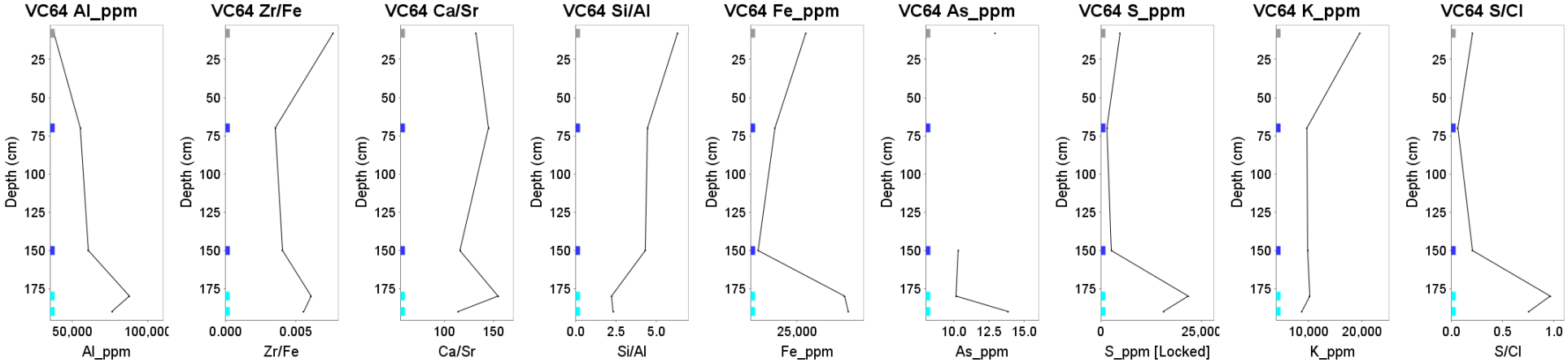

(b) Elemental data plotted against depth for VC64. The silt samples are light blue, coastal sands samples are dark blue and pumiceous sands samples are grey.

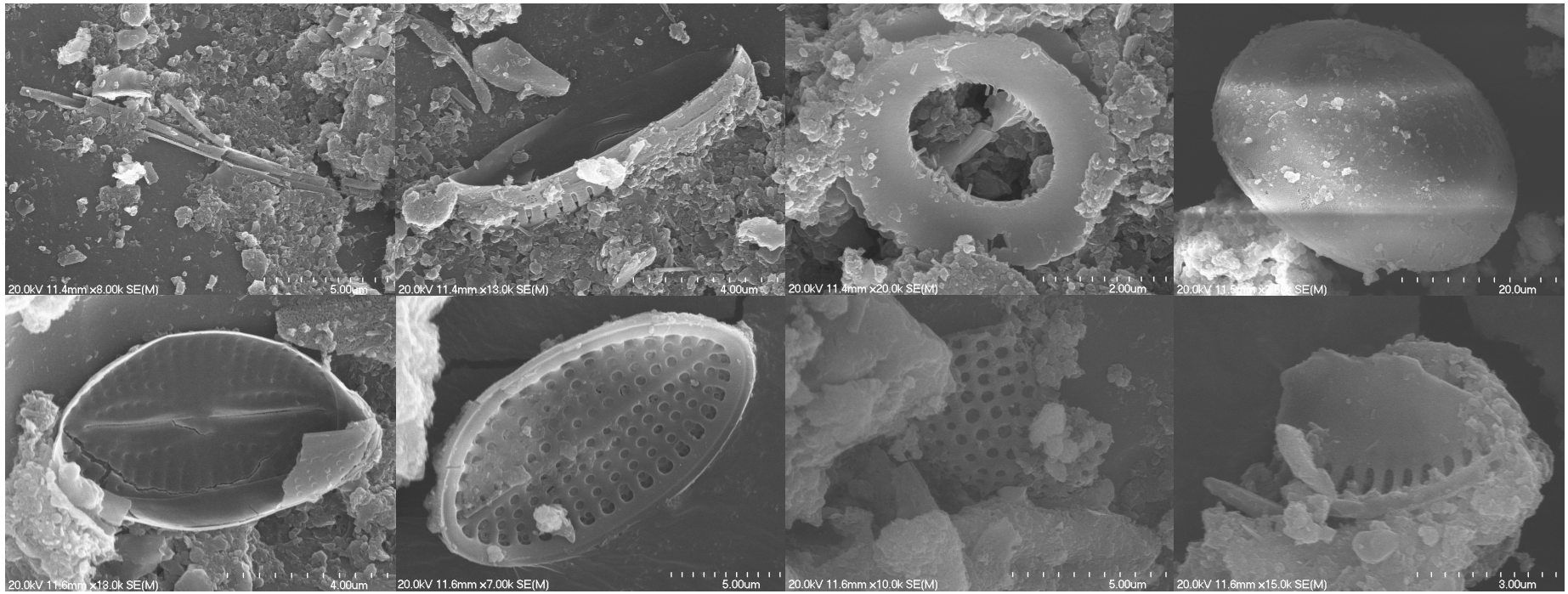

Figure 4.33: Selection of images of diatoms found under SEM. The images in the top line are from VC7 and the images in the bottom line are from VC12. All diatoms are damged.

that VC67 was further away from the source than other cores in this group. Using the strength of the magnetic susceptibility measurements, the source was likely close to VC12.

This data could potentially correlate with that from VC3 in Maunganui Roads South (Figure 4.19). The data for VC3 is highly variable, but very weak. This could be due to diagenesis, or suggesting that VC3 is further from the sediment source. A number of 'peaks' are present on the plot. However, the range of data is only 9 SI$\times 10^{-5}$.

Table 4.4: Table showing the potential sedimentation between the 2 events indicated in magnetic susceptibility data

Vibracore	Potential sedimentation (cm)
VC8	>130
VC12	110
VC7	168
VC67	80

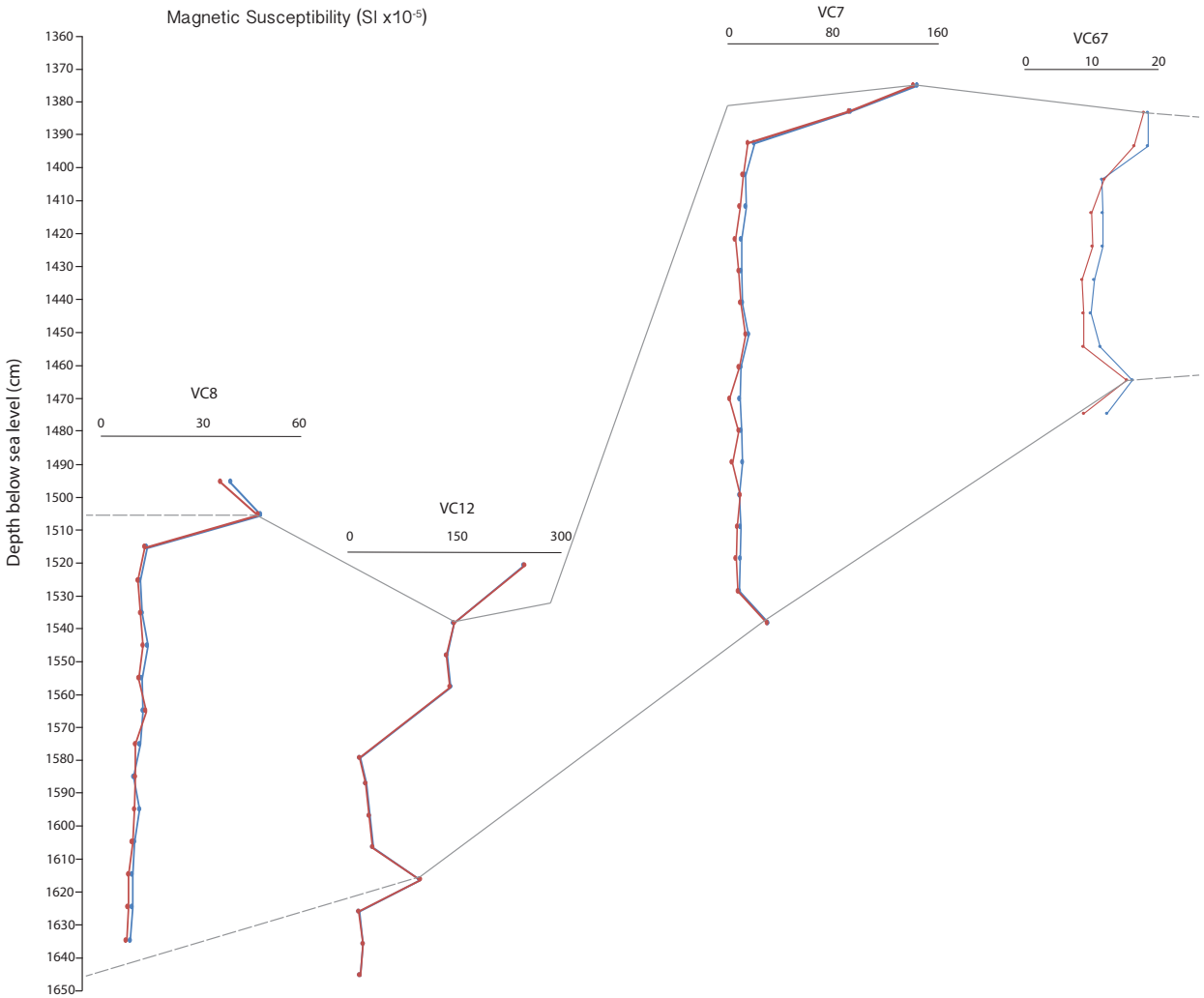

Figure 4.34: Magnetic susceptibility of the silt units measured in the Manganui Roads group. Lines have been added to indicate potential successions. Note that between 210 cm to 230 cm there is a coarse sand unit in VC12. The measurement taken at 170 cm is of a silt pod. Low frequency measurements are in blue and high frequency measurements are in red.

4.5 Cutter Channel

Sixteen vibracores were taken from within Cutter Channel (Table 4.5, Figure 4.35). The majority of the cores were obtained from one area of the channel, spaced 20–50 m apart. There is also one group of three vibracores taken in an area 500 m north west of the main group, and these are spaced between 3 and 15 m apart. Much of the

Table 4.5: List of all vibracores obtained from Cutter Channel, and their depth.

Vibracore	Length (m)	Depth Below Sea Level (m)
VC16	2.9	14.05
VC17	2.71	14.10
VC18	2.9	14.38
VC26	0.32	15.02
VC27	2.53	15.13
VC28	2.5	14.66
VC29	2.63	14.74
VC30	2.43	14.99
VC32	2.75	14.78
VC33	2.46	14.66
VC57	1.26	14.42
VC58	2.11	14.08
VC59	1.05	14.07
VC60	1.09	13.48

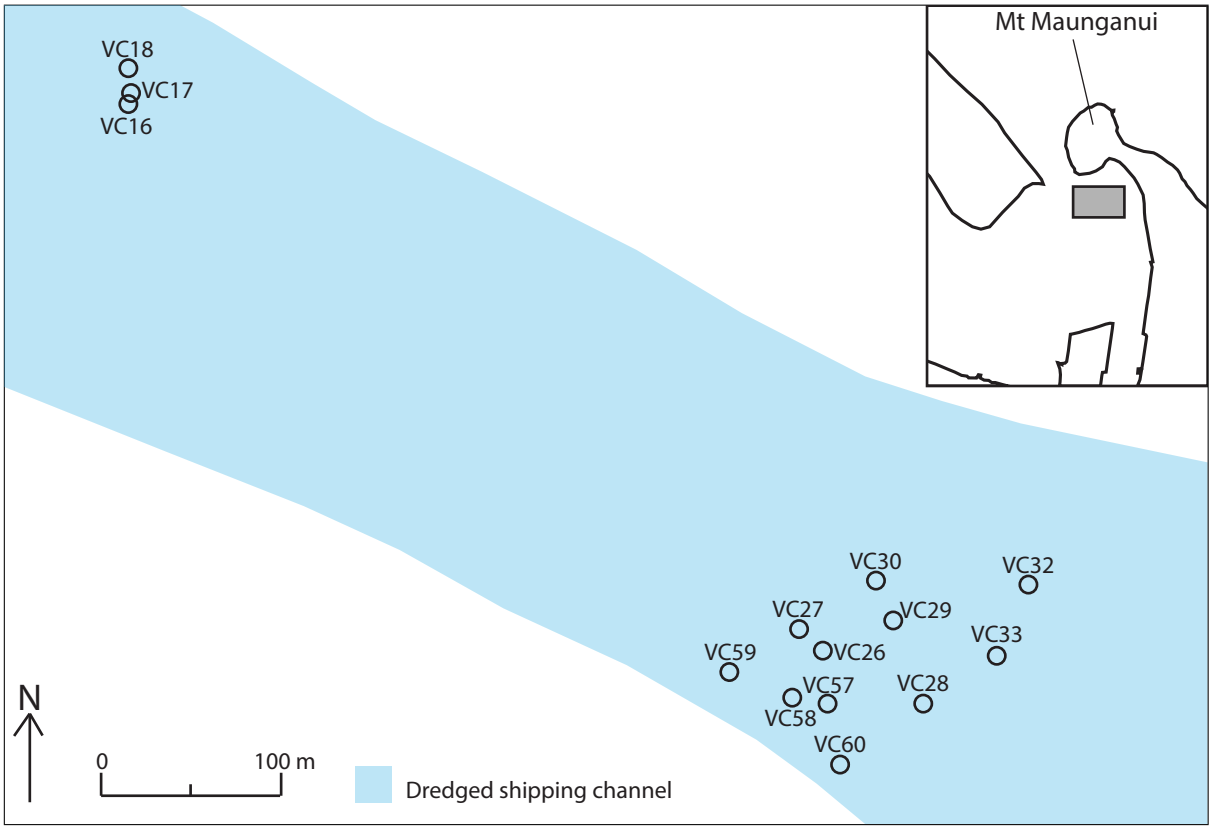

Figure 4.35: Map showing locations of vibracores taken from Cutter Channel. See Figure 1.1b for geographic context.

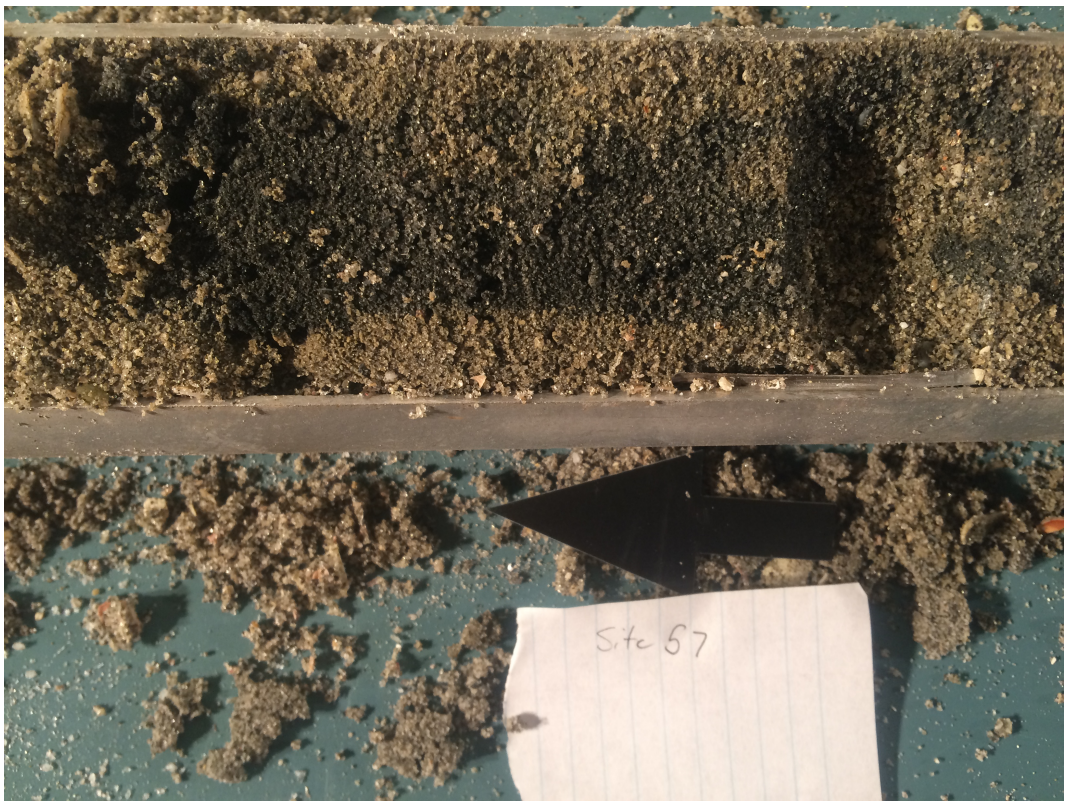

Figure 4.36: Oxidising units seen in VC57 at 30 - 70 cm depth.

sediment within the Cutter Channel vibracores consists of medium to coarse sands with variations in the amounts and types of bioclasts present (Figures 4.38, 4.39). There are dense accumulations of bioclasts present in some cores, such as VC29 (Figure 4.39). There are also variations in the condition of the bioclasts found in the vibracores: some have been bored, others have not. Many are disarticulated, but some are articulated. Fragments of bioclasts are found throughout most of the sediments in this area. This indicates that there were varying hydrodynamic conditions within the harbour at the time of deposition. The presence of articulated bioclasts and boring indicates that organisms lived in this area (Boggs, 2009). The fragments of bioclasts are indicative of a more distal source, with the transport processes breaking up the bioclasts (Al-Dabbas and McManus, 1987).

In some cores, areas of the sediment were anoxic when retrieved, such as that pictured in Figure 4.36, again indicating the variations in hydrodynamic conditions and productivity within the harbour. This shows that these areas of sediment were deposited in an anoxic environment, suggesting either low energy or high productivity (Demaison and Moore, 1980). In some vibracores, there is a thin (10–30 cm) unit of pumiceous sand sediment at the top of the core, with a gradational boundary with the underlying medium to coarse sand units.

VC29 is unique in this area as it is the only vibracore to contain volcaniclastic sediment. This unit occurs at the base of the core (200–263 cm) and is cohesive, unlike any of the other sediments that occur in this area. It is very similar to some

of the sediments from Stella Passage. A fine sand pod occurs in VC26 and VC29 (Figure 4.37). I interpret this to be a rip up clast sourced from the fine sand unit in VC29 as it is texturally very similar (Figure 4.39).

Sediments in this area are commonly composed of plagioclase, quartz, lithics, hornblende, bioclast and minor amounts of volcanic glass (Figure 4.43). Some small fragments of vegetation are present at various depths in the cores.



Figure 4.37: Rip up clasts present in VC29 at 40 cm depth.

4.5.1 Texture

Grain size data from sub-samples of the Cutter Channel cores show a fairly consistent grain size, with little variation with depth (Figure 4.40)a. Some variation is seen in VC29, with two very fine sand samples measured. The sharp peak in the curve of VC29 at 40 cm is caused by the presence of a small number of finer grained pods, likely rip-up clasts from the unit below (Figure 4.37, 4.39). VC29 is the only vibracore with mean grain size data finer than 3 ϕ in the Cutter Channel area. The mean grain size of all other samples varies between medium sand and coarse sand. The cumulative grain size curve shown in Figure 4.41 shows the distinct difference in facies between the unit at 140 cm depth and the unit at 212 cm depth in VC29. In Cutter Channel, this distinct difference is only seen in the unit at the base of VC29 and in the rip up clasts measured in VC26 (32 cm depth) and VC29 (40 cm depth).

Figure 4.42 shows two groups. Group A includes those with sorting less than 1.5 ϕ and Group B includes those with sorting greater than 1.5 ϕ. In Group A, sorting and skewness are positively correlated. The Group B includes only three data points, each with skewness between 0.5 and 1.0 ϕ. Each of the samples in this group are from volcaniclastic fine sand units from VC26 (including the fine sand pod) (Figure 4.39). Similarly poorly sorted silt to fine sand units appear in cluster in Maunganui Roads South (Figure 4.16).

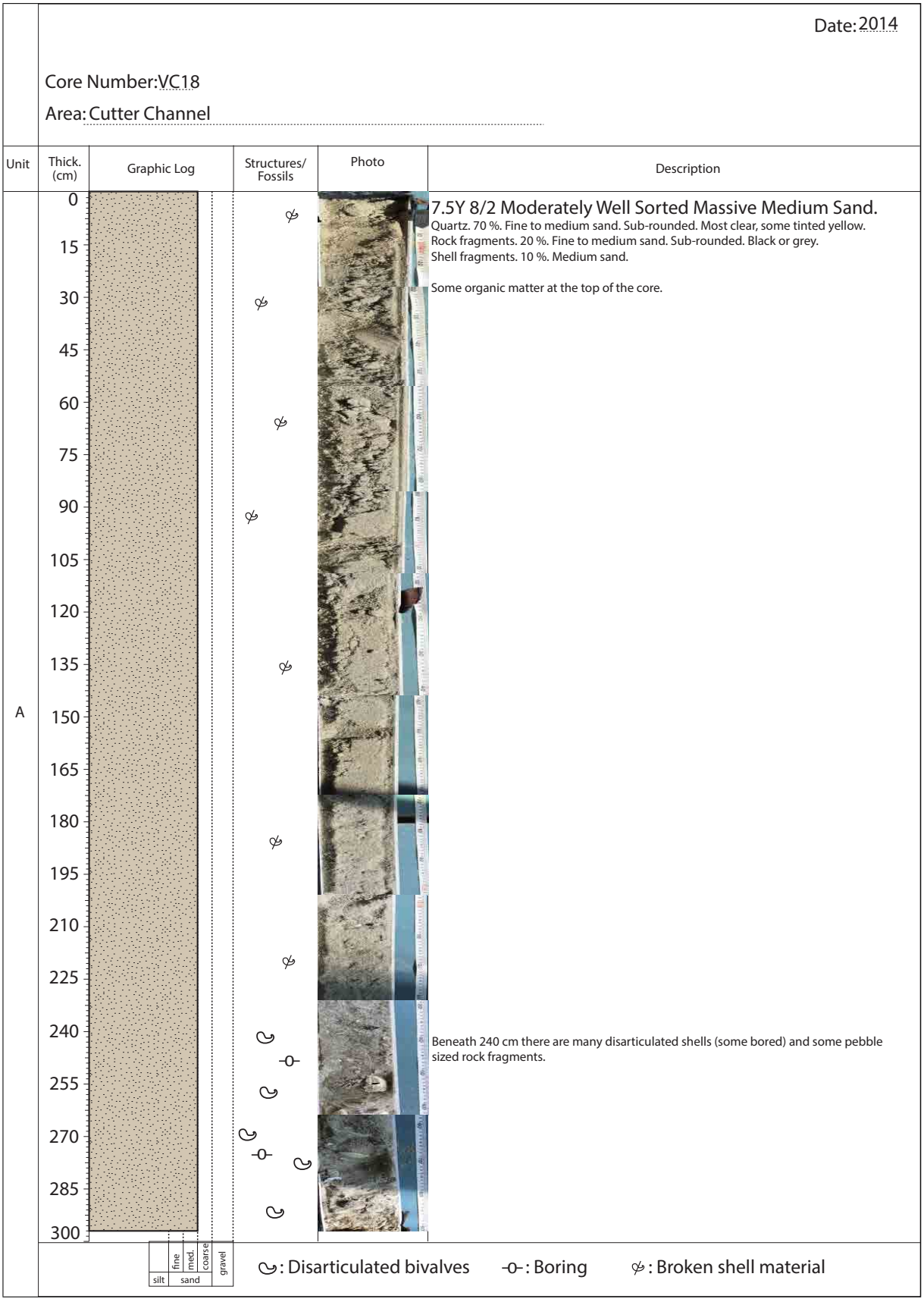

Figure 4.38: Stratigraphic log of VC18, taken from Cutter Channel.

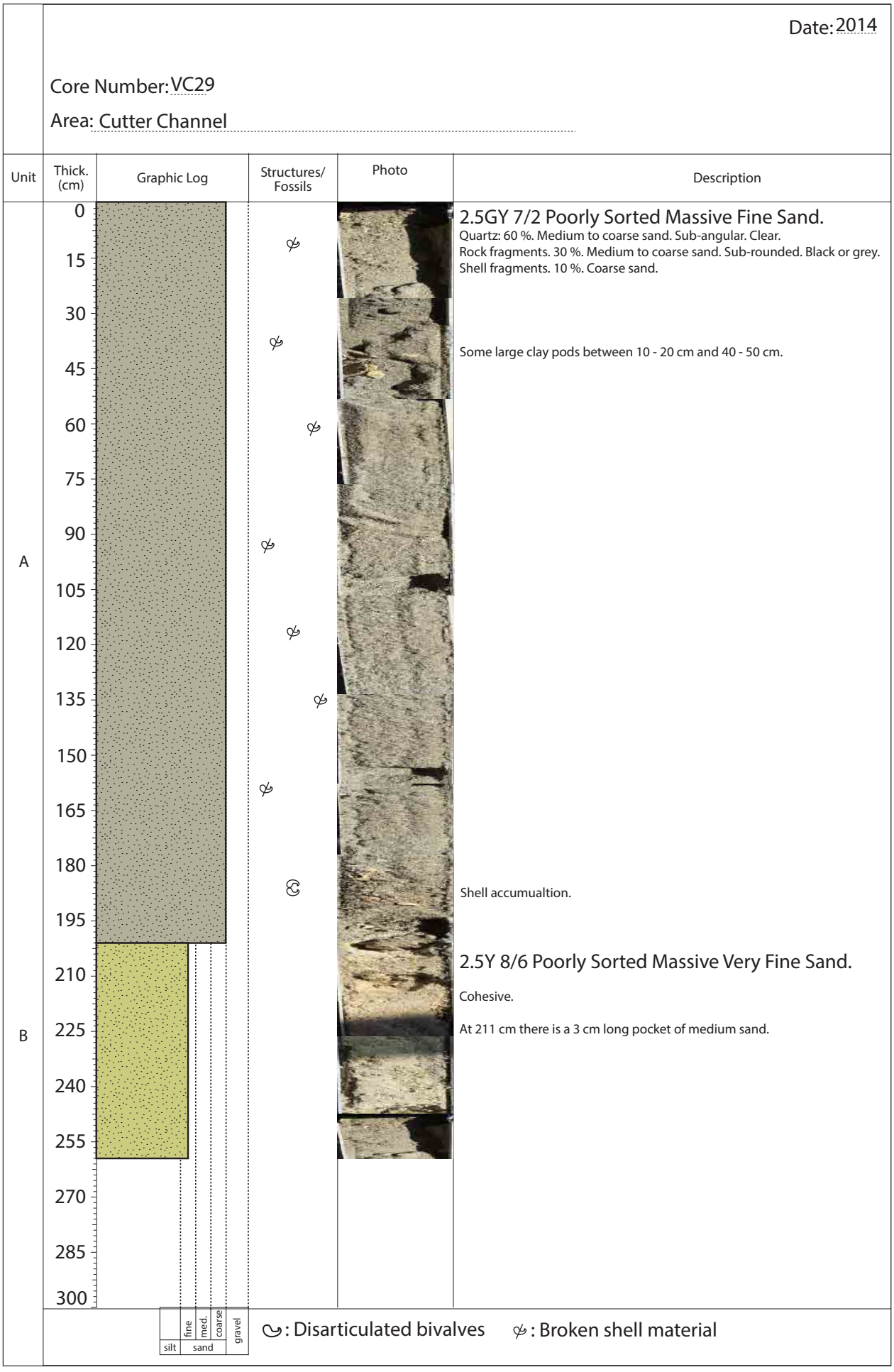

Figure 4.39: Stratigraphic log of VC29, taken from Cutter Channel.

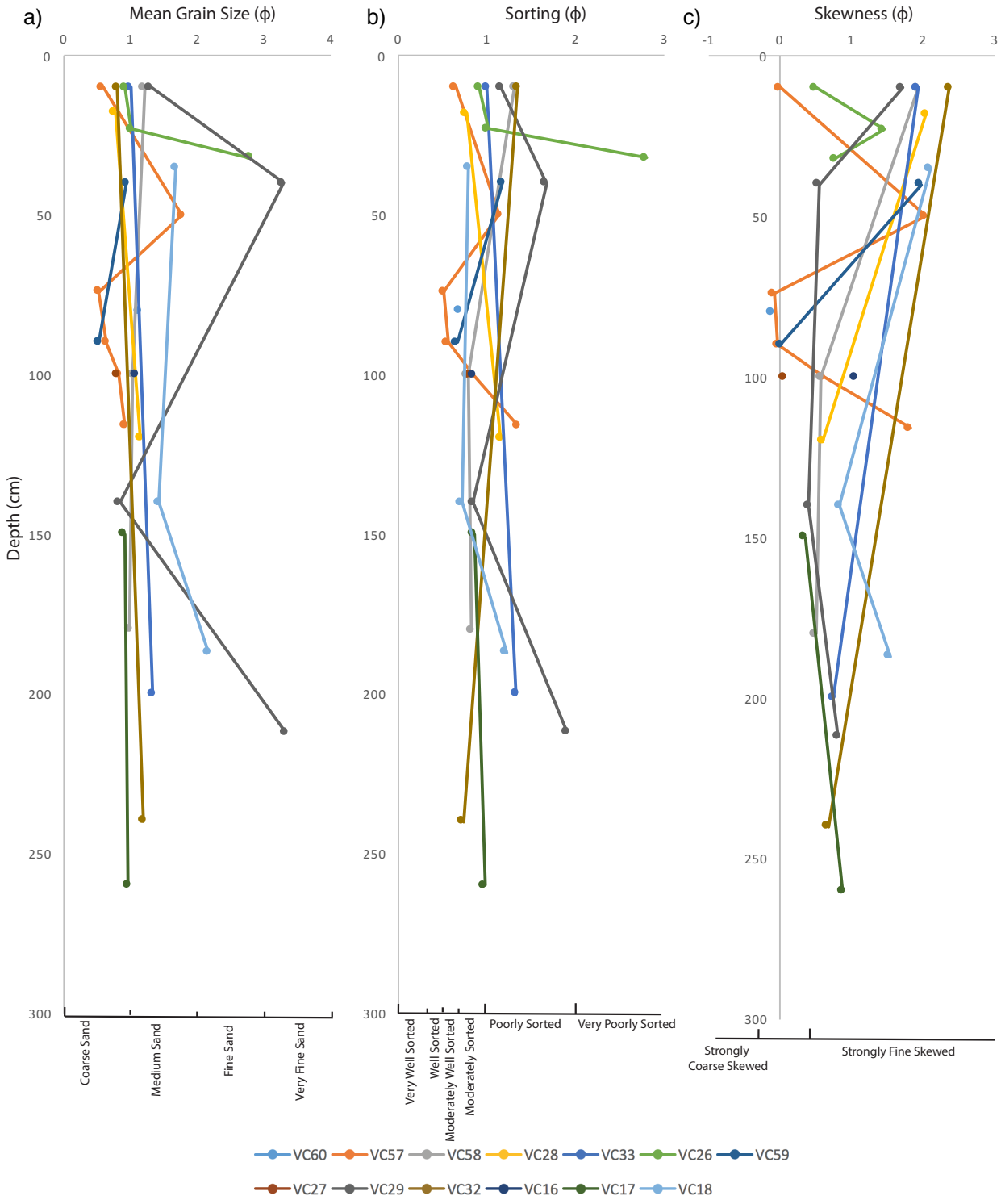

Figure 4.40: Grain size statistics plotted against depth for sub-samples obtained from Cutter Channel vibracores.

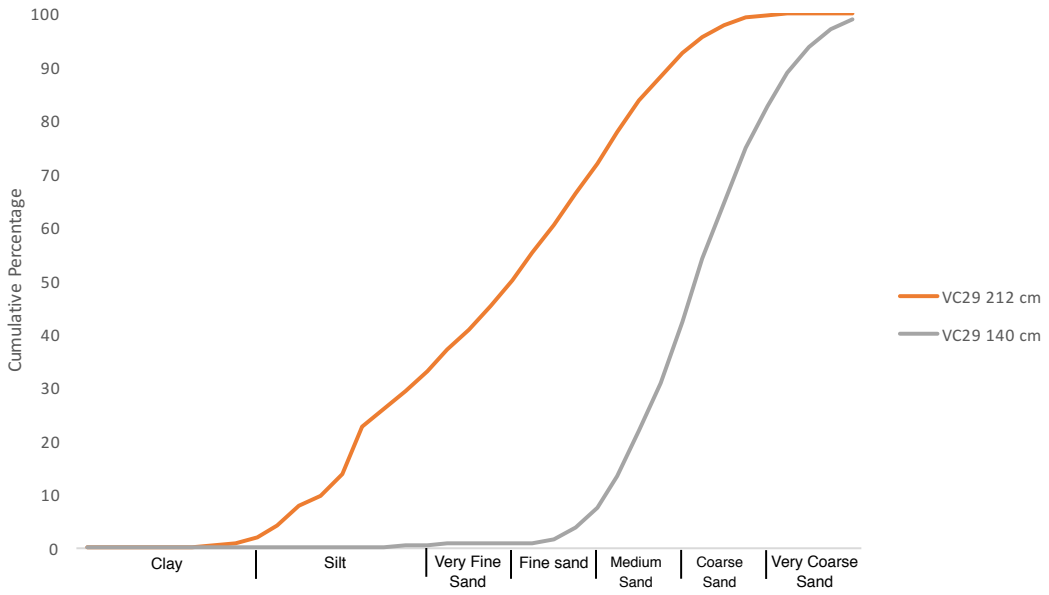

Figure 4.41: Comparison of the cumulative grain size curves for two samples from VC29, showing the difference in grain size.

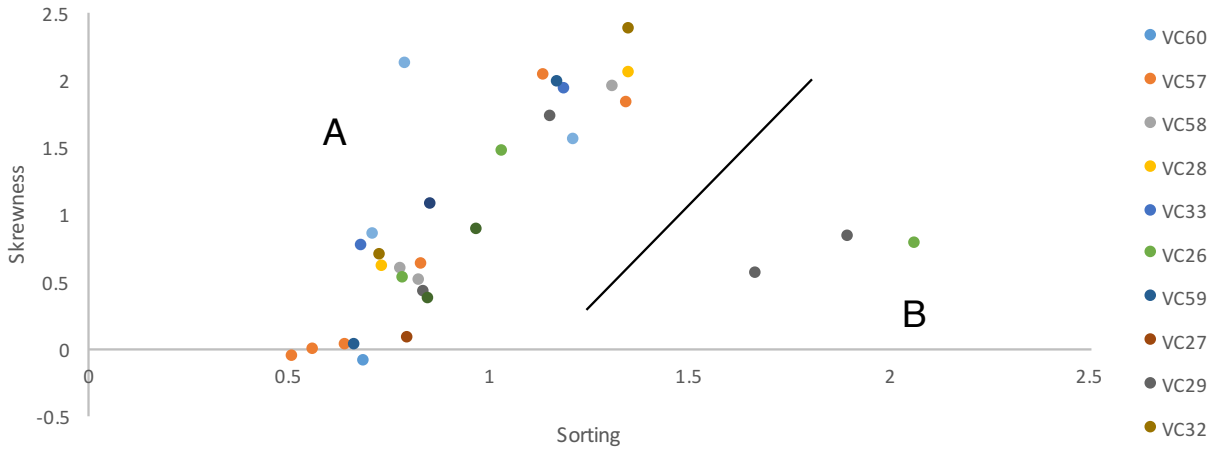

Figure 4.42: Skewness versus sorting for sub-samples taken from Cutter Channel. There is a trend of samples becoming more finely skewed as they become more poorly sorted. Two groups are present; those with sorting less than 1.5 ϕ and those with sorting greater than 1.5 ϕ.

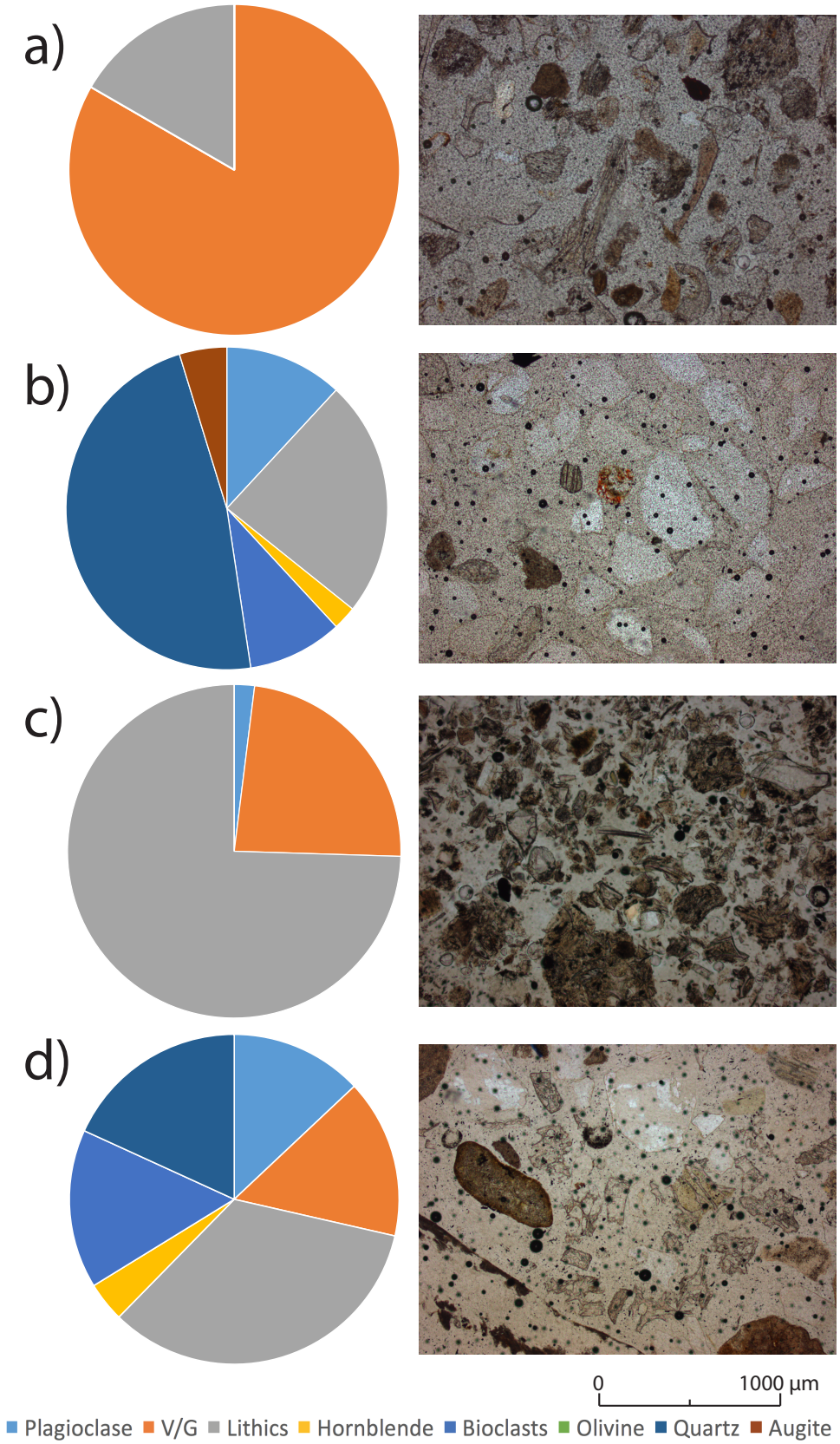

Figure 4.43: Pie charts and thin section images of sediments from Cutter Channel. A) shows pumiceous sediment, with abundant volcanic glass. B) shows a medium to coarse sand sample. C) is volcaniclastic sediment from VC29, predominantly composed of lithics. D) is predominantly composed of plagioclase, lithics and bioclasts.

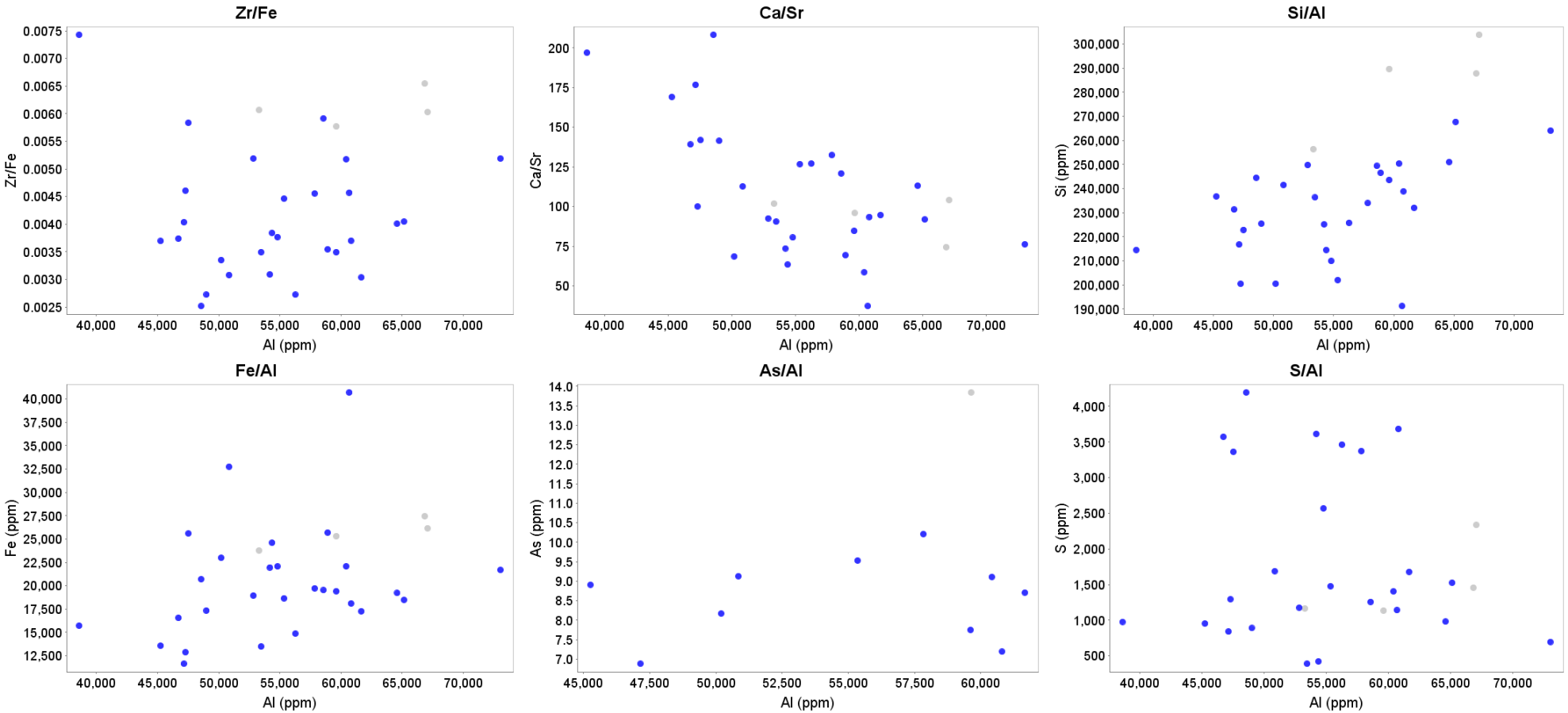

Figure 4.44: Elemantal proportion by depth data for select sites from Cutter Channel. The graphs show a limited presence of Arsenic, low sulphur, and low S/Cl. The pumiceous sand samples have higher iron, potassium, and Zr/Fe. Dark blue = medium to coarse sand. Grey = pumiceous sand.

4.5.2 Composition

The sediments of the Cutter Channel set of vibracores are compositionally fairly consistent (Figure 4.43). They contain plagioclase, quartz, lithics and hornblende. Some also contain volcanic glass. Coarse pumiceous sediment is also present at the tops of cores here, and contains high proportions of volcanic glass (Figure 4.43a). Almost all other sediment is medium to coarse sand, comprising plagioclase, quartz (the two most abundant minerals in this sediment), lithics, bioclasts and trace amounts of hornblende (Figure 4.43b and d). The one exception to this is the fine sand unit towards the bottom of VC29. This is primarily made up of lithics although volcanic glass and some plagioclase are also present (Figure 4.43c).

4.5.2.1 Geochemistry

Cutter Channel geochemical results are presented in Figure 4.44. They show a limited presence of arsenic, and lower S/Cl (indicators of pyrite (Thomson et al., 2006)) than some of the Maunganui Roads samples (Figure 4.30). Sulfur, an indicator of reducing conditions (Croudace and Rothwell, 2015), is lower in these samples than it was in the silt samples in Maunganui Roads. There is a cluster of samples above 2,500 ppm, potentially indicating reducing conditions. Pumiceous sand samples have higher Zr/Fe levels (indicator of volcanic provinence), higher Fe and K (terrigenous indicators) than the medium to coarse sand units. The pumiceous sand also has elevated levels of Si/Al, an indicator of biogenic production.

VC57 has high levels of Iron and Sulfur in the samples from above 70 cm. In Sluijs et al. (2011) this was interpreted as a marker of reducing (anoxic) conditions. Sulphur also increases above 70 cm in VC57. Barium levels reduce closer to the surface. I interpret all of these factors to indicate reducing conditions in VC57, and this is also seen in Figure 4.36.

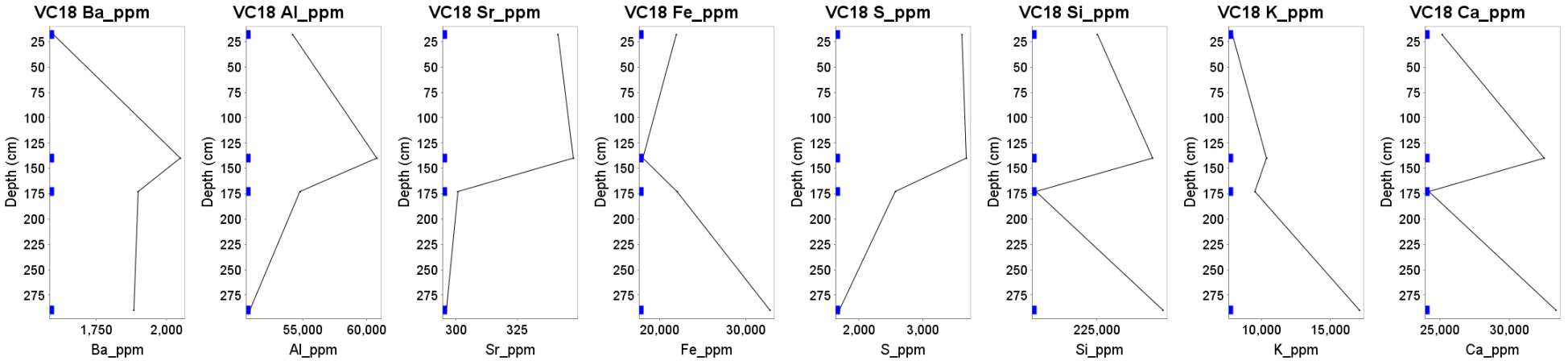

(a) Elemental data plotted against depth for VC18.

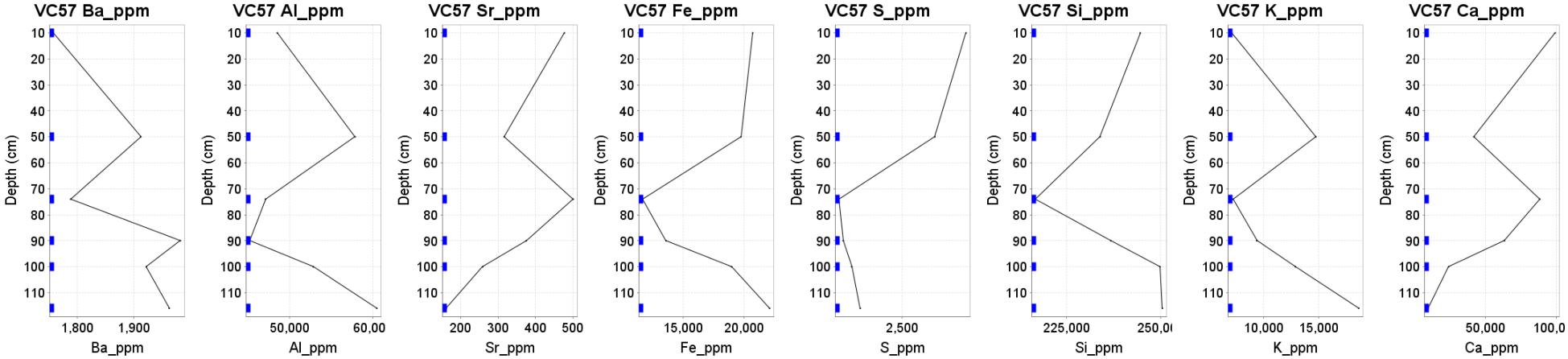

(b) Elemental data plotted against depth for VC57.

4.6 Entrance Channel

Thirty-five vibracores were taken by the Port of Tauranga from the Entrance Channel (Table 4.6, Figure 4.46). The vibracores are largely evenly spaced in the centre of the channel, 70–120 m apart and 12.97–14.38 m water depth.

Table 4.6: List of vibracores obtained from the Entrance Channel.

Vibracore	Length (m)	Depth Below Sea Level (m)
VC19	2.64	14.27
VC20	2.59	14.30
VC21	0.46	14.22
VC22	3.08	13.92
VC25	2.19	13.83
VC34	1.79	13.95
VC35	1.66	14.06
VC36	0.67	14.27
VC37	1.79	14.38
VC42	2.19	14.25
VC43	1.35	14.30
VC44	0.92	14.21
VC45	2.88	13.16
VC46	2.9	13.33
VC47	2.8	13.22
VC48	2.4	12.97
VC49	2.79	14.3
VC50	0.8	14.22
VC51	0.74	14.34
VC52	1.61	14.28
VC53	0.6	14.24
VC55	1.3	13.54
VC56	0.9	13.88
VC81	2.27	14.38
VC82	2.3	14.29
VC83	1.78	14.16
VC84	2.14	14.27
VC85	2.17	14.29
VC86	2.09	13.46
VC87	2.12	13.26
VC88	1.75	13.67
VC89	2.26	13.73
VC90	1.67	14.36
VC91	2.2	14.35
VC92	1.68	13.77

There are substantial variations in the types of sediment present in the vibracores from the Entrance Channel. The majority of the sediment is a medium to coarse grey sand (Figure 4.50), with varying proportions of bioclasts.

Some of this sand is yellow in colour, but otherwise compositionally similar to

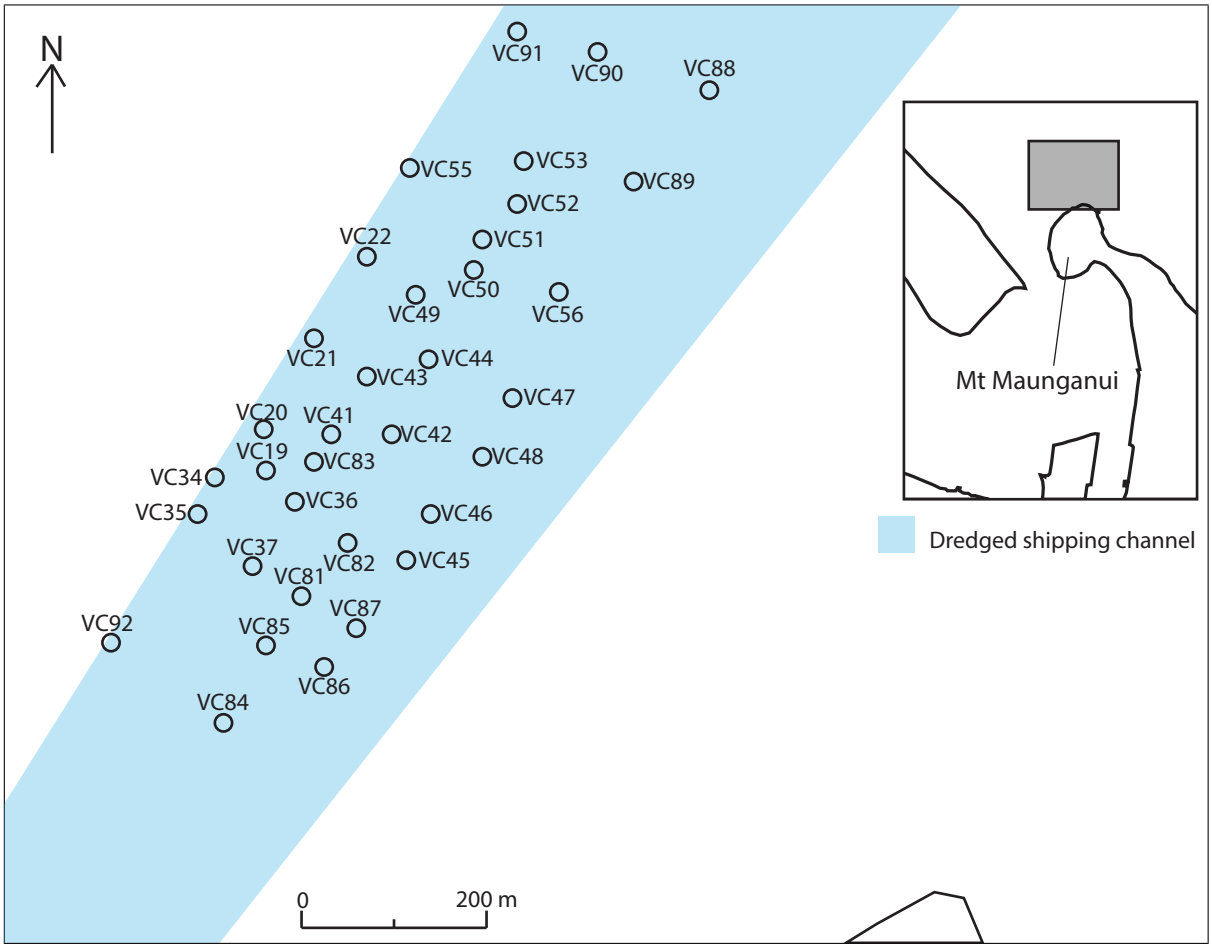

Figure 4.46: Map showing locations of vibracores taken from the Entrance Channel. See Figure 1.1b for geographic context.

the grey medium to coarse sand units (Figure 4.47). Healy et al. (2009) observed this feature and suggested it was caused by geothermal fluid seepage. EDX analysis was undertaken on some of these grains and showed that the coating on one of the grains had a Fe weight percentage of 6.32 %, and a Al weight percentage of 8.80 %. Oxides of both these elements can cause the 'iron stain' (Thompson and Bowman, 1984; Thompson, 1992; Sullivan and Koppu, 1998). In some vibracores, this sediment has been cemented into clumps. In thin section, there are distinct yellow borders around the grains (Figure 4.53d). I agree with the interpretation of Healy et al. (2009).

In some vibracores, such as VC87 (Figure 4.49) the medium sand unit was initially anoxic, indicating reducing conditions. Another sediment type present in these vibracores is a pumiceous sand similar to that found in Cutter Channel that occurs at the tops of the cores. In some areas the vibracorer also penetrated into a silt to fine sand material similar to some of the sediments found in Stella Passage.



Figure 4.47: Clumps of yellow sand in VC25 at 190 cm depth.

The composition of the sediment in this area varies depending on the units. Plagioclase, quartz, lithics, and volcanic glass are found in nearly all units. Trace amounts of hornblende are found in some units. The proportions of each component differs between units. Bioclasts are also present in several units. However the condition and abundance of these varies considerably between cores. VC37 contains a unit (115–179 cm) with an abundance of bioclasts, some of which are articulated, others of which have been bored.

4.6.1 Texture

Grain size statistics are shown in Figure 4.51. The vast majority of sub-samples are between medium and coarse sand (2–0 ϕ). However a few are much finer. VC46, for example, has fine sand for much of the core, with a silt layer at 230 cm depth followed by a medium sand unit at the base of the core. The volcaniclastic sediments that are present at the base of some cores all have a similar grain sizes to sediments in Stella Passage (coarse silt to medium sand).

The sorting statistics follow a similar pattern for nearly all sub-samples as mean grain size (Figure 4.51b). Coarser sand units are moderately sorted, whereas the finer sand units are poorly to extremely poorly sorted. There appears to be a trend

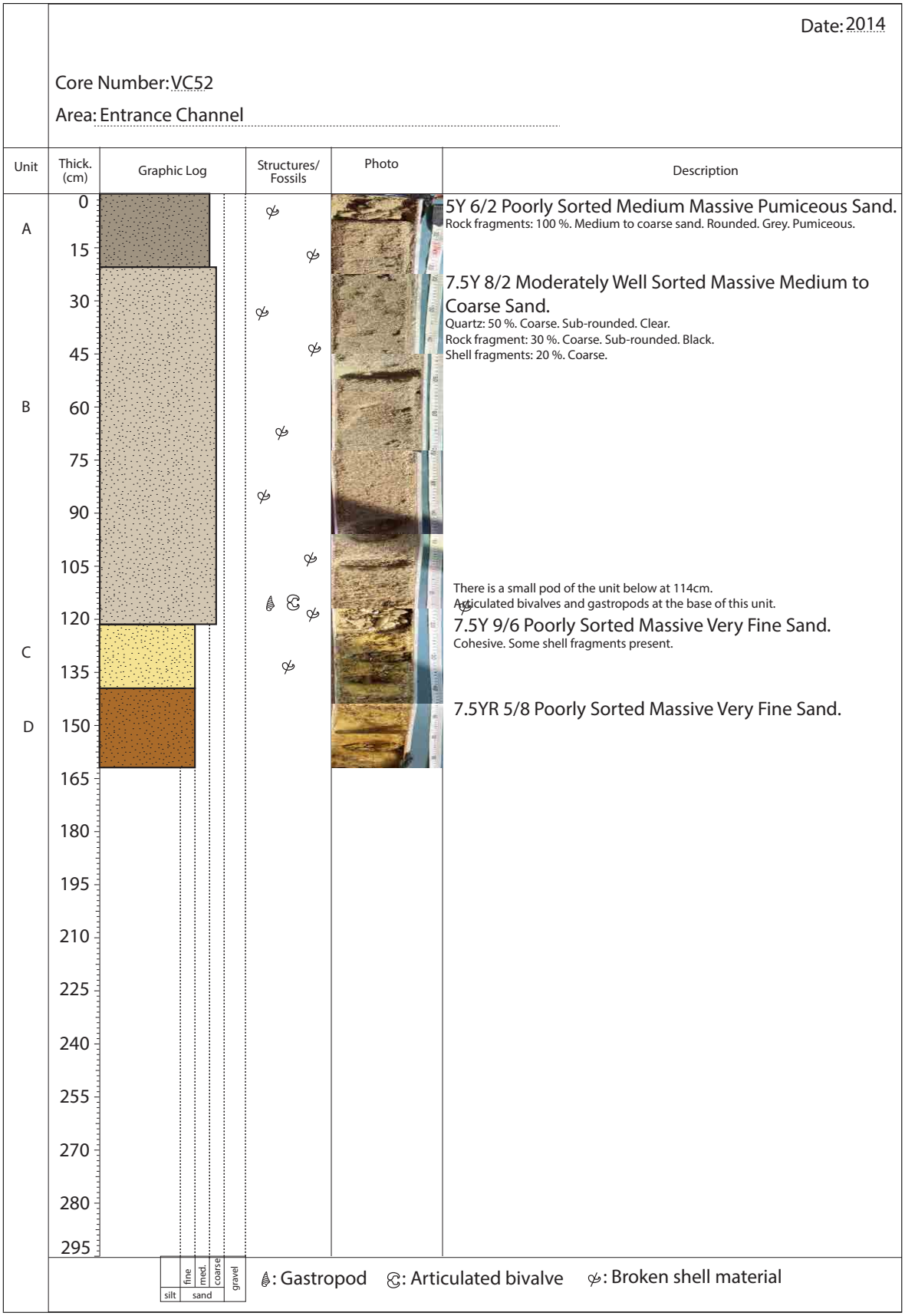

Figure 4.48: Stratigraphic log of VC52, taken from the Entrance Channel.

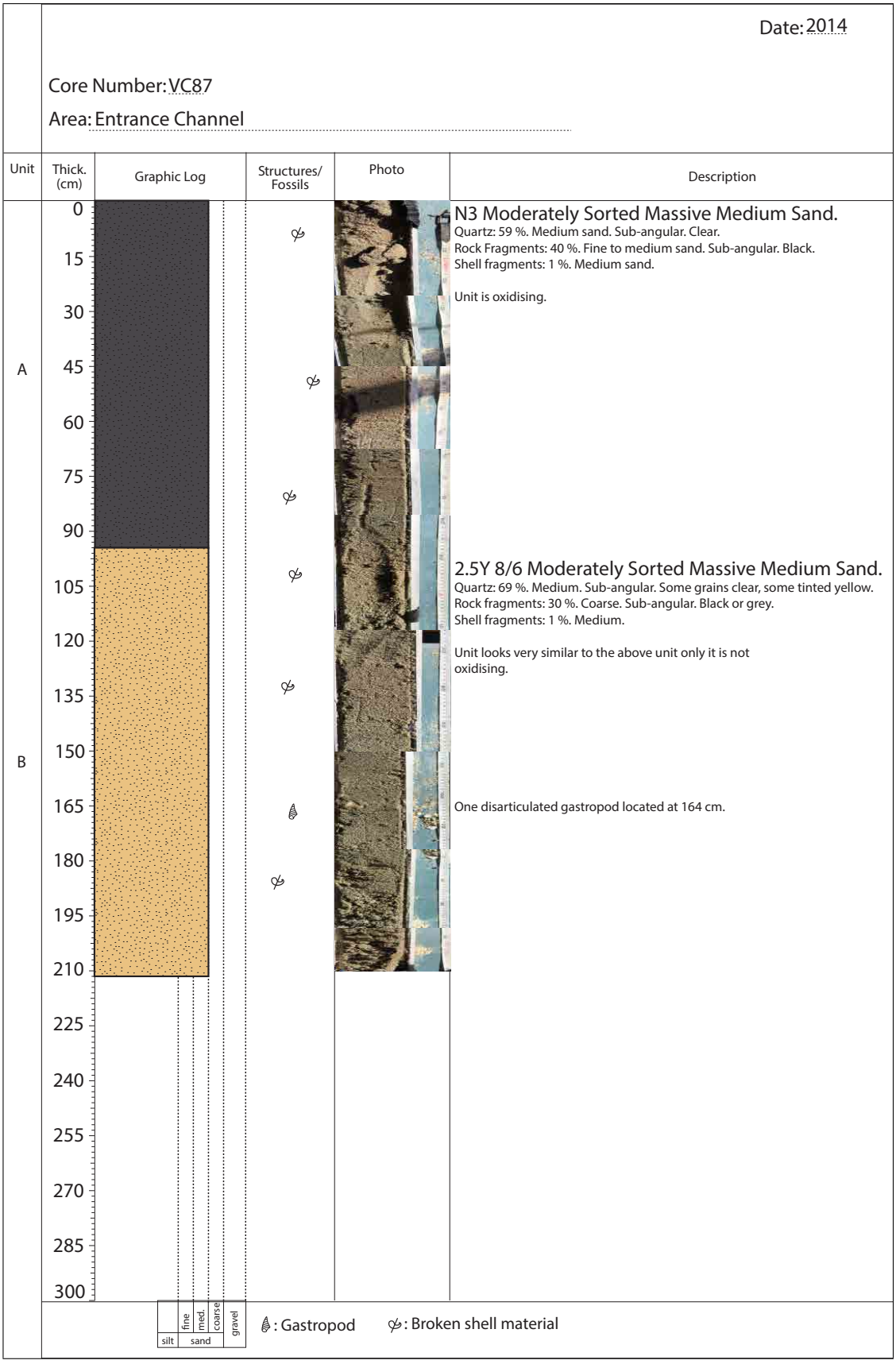

Figure 4.49: Stratigraphic log of VC87, taken from Cutter Channel.

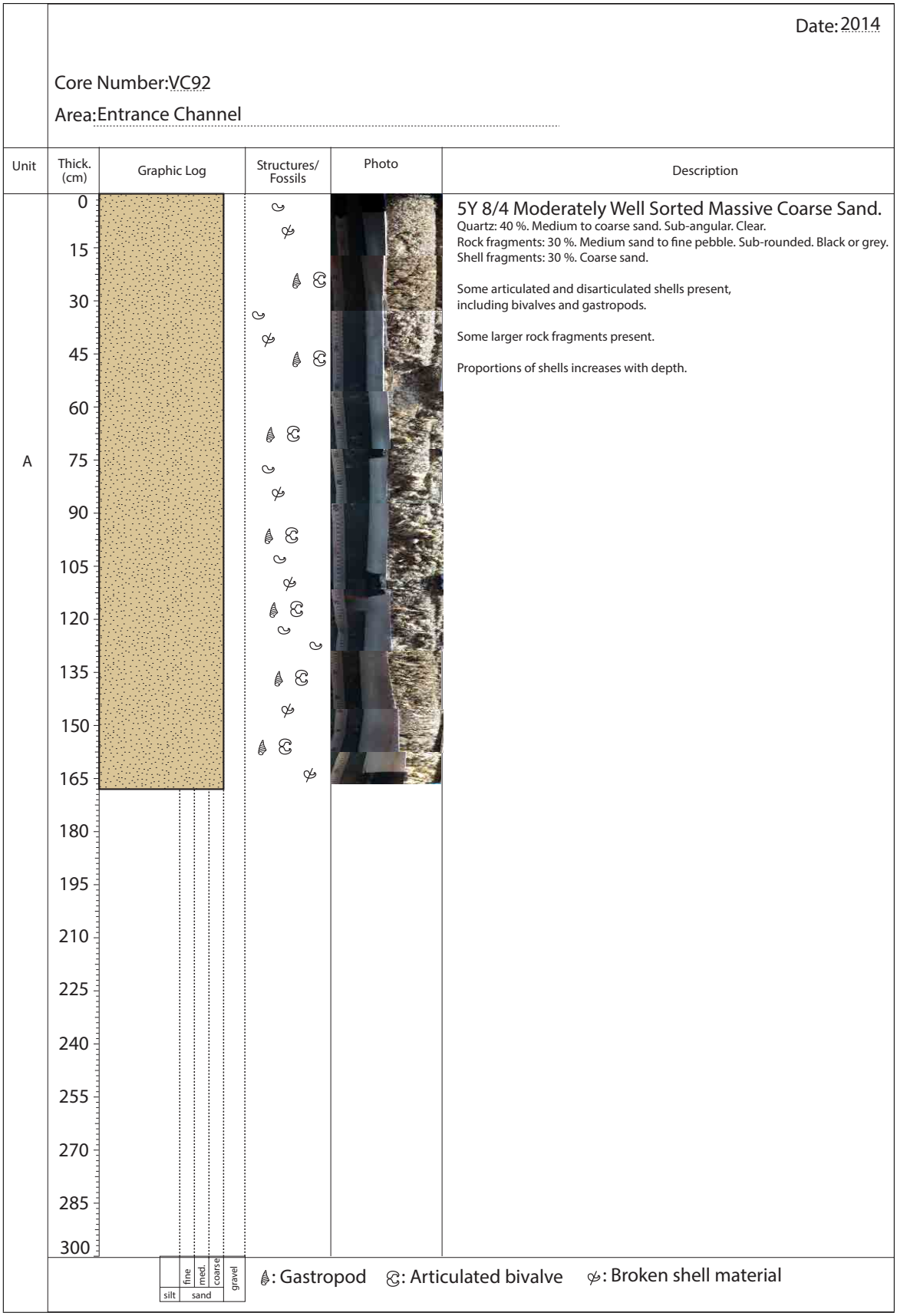

Figure 4.50: Stratigraphic log of VC92, taken from Cutter Channel.

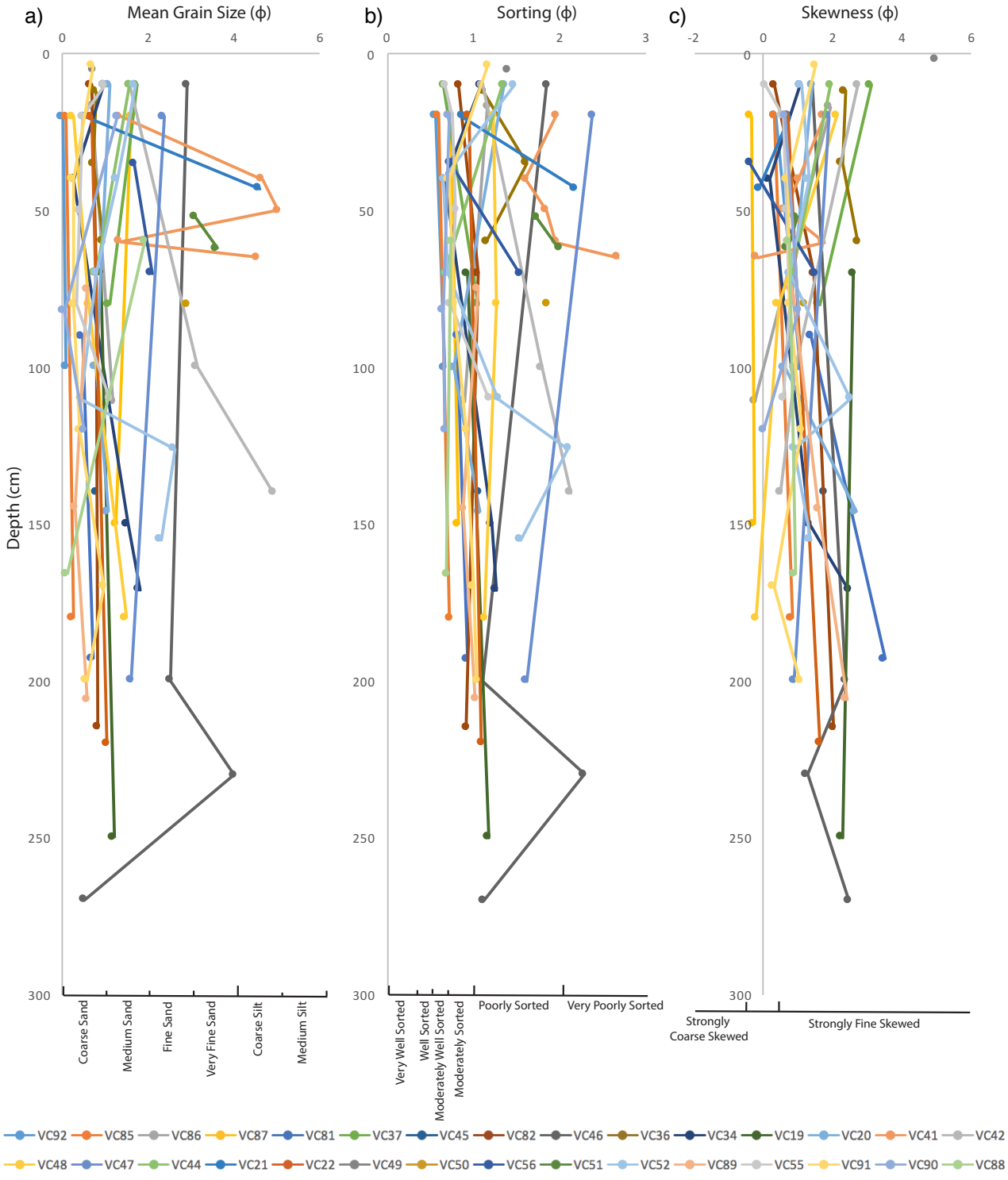

Figure 4.51: Grain size statistics plotted against depth for sub-samples obtained from the Entrance Channel vibracores.

of poorer sorting with depth amongst the vibracores with mostly coarse sand. The skewness statistics have no clear trends and can vary hugely. However, the vast majority of the sub-samples measured were fine to strongly finely skewed.

In the skewness vs sorting plot, shown in figure 4.52, two groups emerge; Group A, those with sorting less than 1.5 ϕ and Group B, those with sorting greater than 1.5 ϕ. Group A are medium to coarse sand sub-samples whereas Group B are volcaniclastic silt to fine sand sub-samples.

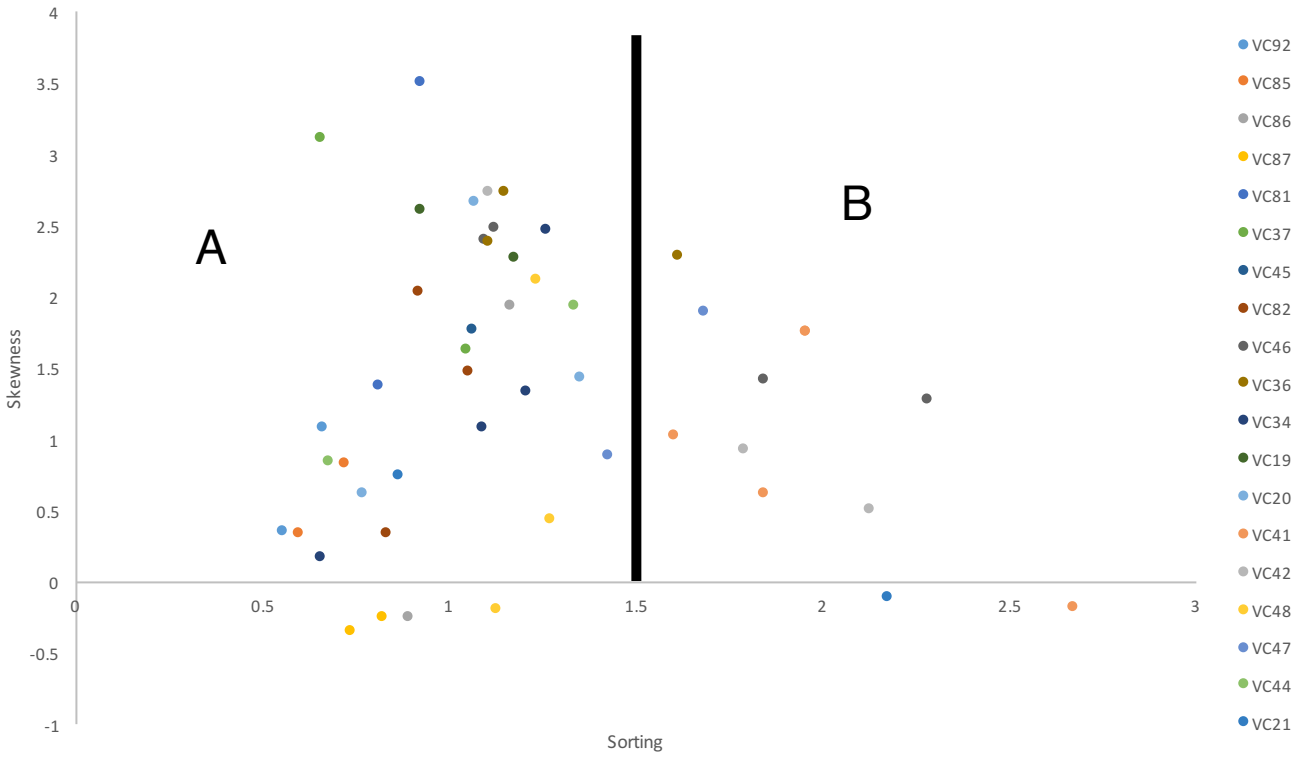

Figure 4.52: Skewness vs Sorting bivariate plot for grain size samples from the Entrance Channel. Two groups are present, those with sorting less than 1.5 ϕ and those with sorting greater than 1.5ϕ.

4.6.2 Composition

The composition of the sediments within the Entrance Channel set of vibracores is highly variable. An example of this is the sediments within VC52, which contain medium and coarse sand units between 0 and 121 cm (units A and B, Figure 4.48). These units are composed of plagioclase, quartz, lithics, bioclasts and some traces of hornblende. At the base of the core, however, are silt and very fine sand sediments (units C and D), which contain abundant lithics and volcanic glass, as well as less abundant quartz and plagioclase (Figure 4.53b).

Figure 4.53d shows the appearance of the yellow iron-stained grains in thin section, with the characteristic yellow border around the grains. One sample of this sediment was found to contain some pyroxene, indicating some basaltic input. Horn-

blende was found to be slightly more prominent in these sediments than in the compositionally similar sediments described in Cutter Channel and Maunganui Roads.

4.6.2.1 Geochemistry

The results of geochemical analysis are presented in Figure 4.54. They show that the volcaniclastic sediment and the pumiceous sand units contain a higher Zr/Fe ratio than the medium to coarse sand samples, indicative of volcanic input (Konfirst et al., 2011). There are a handful of medium to coarse sand samples that also have very high Zr/Fe ratios. Sulphur, an indicator of reducing conditions, is present in some of the medium to coarse and pumiceous sands. Iron is high in the volcaniclastic sediment, as well as the limonite-stained medium to coarse sand sediment. The pumiceous sands also have elevated iron. The Ca/Sr ratio, indicative of biogenic activity, is elevated in the medium to coarse and pumiceous sands. The limionite-stained medium to coarse sands and the volcaniclastic sediments have lower Ca/Sr ratios. Arsenic, an indicator of pyrite, is detected in some samples.

Much of the variation in VC42 (Figure 4.55a) is due to the change in facies beneath 89 cm, where it goes from medium to coarse sand to volcaniclastic sediments. Aluminum, iron, potassium (linked to terrigenous input (Croudace and Rothwell, 2015)) are lower in the medium to coarse sand unit. Calcium and strontium, linked to biogenic activity (Hodell et al., 2008), are higher in the medium to coarse sand unit. The change in facies is not represented in barium, which is consistent above 140 cm.

VC52 (Figure 4.55b) shares similar variation to VC42 due to the change in facies. The pumiceous sand unit is high in potassium, iron, and low in calcium and strontium, indicating greater terrestrial input. The medium to coarse sand unit (A and B) have higher strontium, and calcium, but lower potassium and iron, suggesting lower terrestrial input. Unit B has a lower amount of strontium and calcium. However, this is likely due to the absence of articulated bivalves and gastropods which were not included in the XRF analysis. The volcaniclastic sediment at the base of the core is high in barium and iron. Sulphur is not measured in either of the volcaniclastic units in VC42 or VC52.

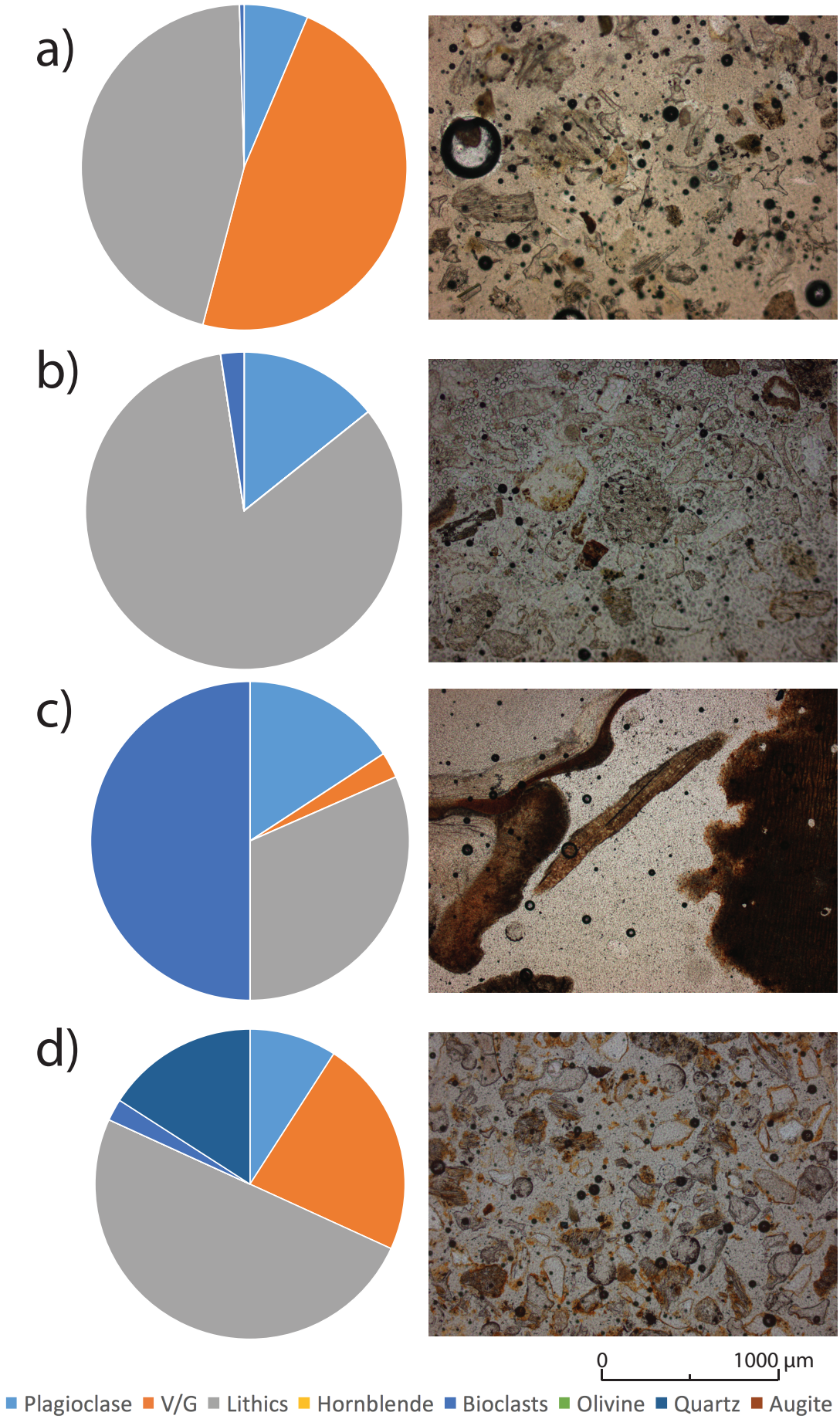

Figure 4.53: Pie charts and thin section images of sediments from the Entrance Channel. A) shows a pumiceous sand, with abundant volcanic glass and lithics. B) contains high proportions of volcanic glass and lithics. C) shows the large disctinctive bioclast fragments that are present in the medium to coarse sand. D) shows the distinctive yellow limonite boarders that are present on some minerals.

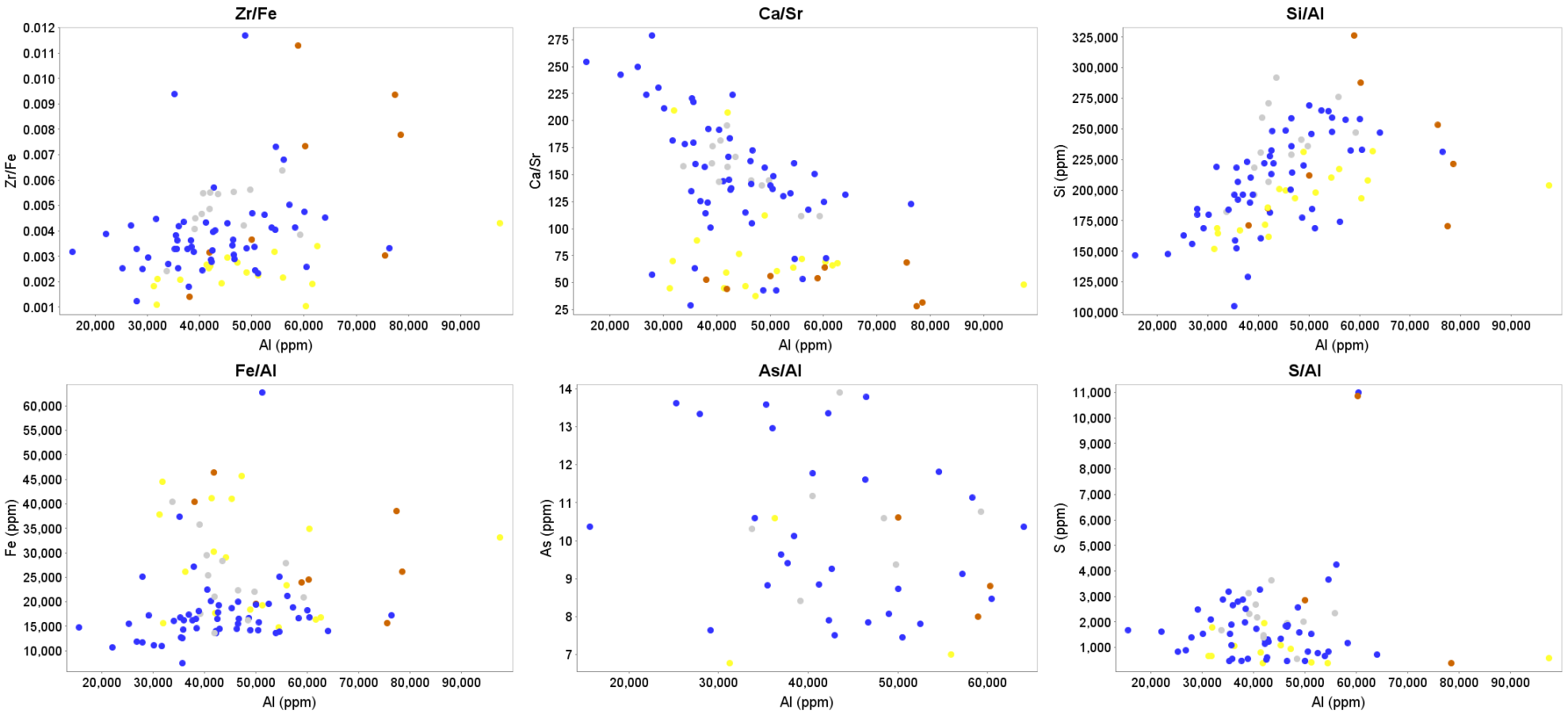

Figure 4.54: Elemantal proportion by depth data for select sites from the Entrance Channel. Orange = Volcaniclastic sediment. Dark blue = medium to coarse sand. Grey = pumiceous sand.

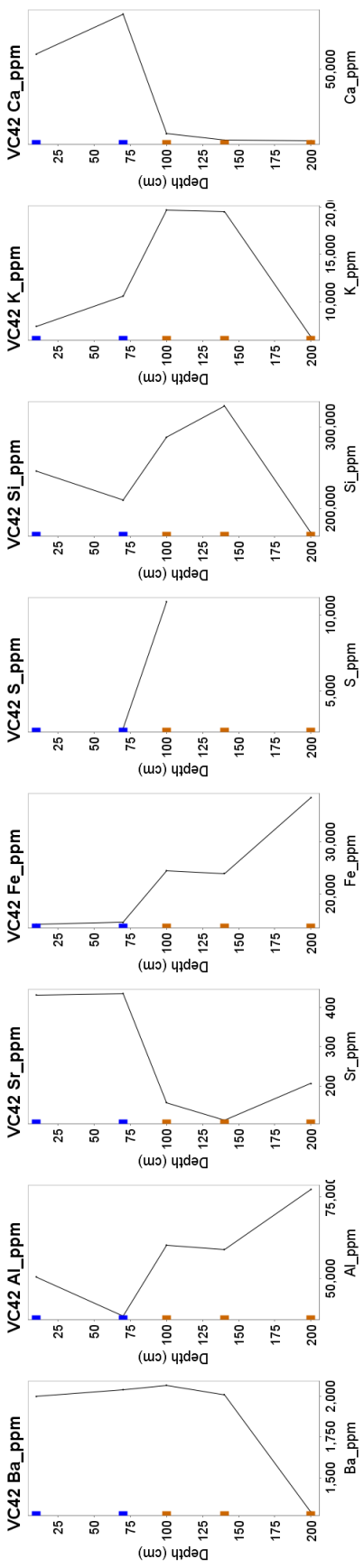

(a) Elemental data plotted against depth for VC42.

(b) Elemental data plotted against depth for VC52.

4.7 Facies Analysis

I used the foregoing descriptive and quantitative data to classify the Tauranga Harbour sediments into four facies. The distributions of these facies are discussed in Chapter 5, summarized in Table 4.7. The facies described in detail over the rest of this chapter.

Table 4.7: List of facies identified and the areas in which they are found in the vibracores used for this project.

Facies	Areas found
VS	Stella Passage, Maunganui Roads South, Cutter Channel, Entrance Channel
S	Maunganui Roads South, Maunganui Roads
CS	Maunganui Roads South, Maunganui Roads, Cutter Channel, Entrance Channel
PS	Maunganui Roads South, Maunganui Roads, Cutter Channel, Entrance Channel

4.7.1 Volcanic Sand (VS)

The volcanic sand facies is found in all Stella Passage vibracores, one Manganui Roads South vibracore, and a handful of vibracores in the Entrance Channel group. The sediment grain size is silt to fine sand (Figure 4.56), and commonly shows colours from the Y to YR Munsell colour hues. The sediment is more compacted than some of the unconsolidated sands that overlie it, and cohesive intervals are present. In some instances there are patches of iron staining (Figure 4.6). These are sporadic and only appear in some units. The sediment is poorly sorted and very strongly finely skewed (Figure 4.56. It is often polymodal. Structures are only visible in areas where a thin layer has been oxidised, which only occurs in two vibracores (VC1 and VC79). The majority of this sediment is compacted. However, in some instances it is friable or unconsolidated.

The grain size of this facies, as shown in Figure 4.56, is variable between coarse silt and very fine sand. This facies is predominantly composed of volcanic glass and lithics. Quartz and plagioclase are also present, as well as hornblende (Figure 4.57). Bivalves are also found in some units; however, these are uncommon. The volcanic glass grains are predominantly grey in colour and sharply angular, indicating a rhyolitic source with very little reworking (Figure 4.57b).

Geochemically, the volcanic sand facies has an elevated Zr/Fe ratio (Figure 4.58). Zr/Fe ratios have been used to discriminate sediment supply from volcanic sources, as Zirconium is a resistant material from igneous rocks (Konfirst et al., 2011; Croudace and Rothwell, 2015). It is high in potassium, a terrigenous indicator (Croudace and Rothwell, 2015). It has low levels of sulphur and a low Ca/Sr ratio, both biogenic indicators (Croudace and Rothwell, 2015), which would be expected in a terrestrial environment.

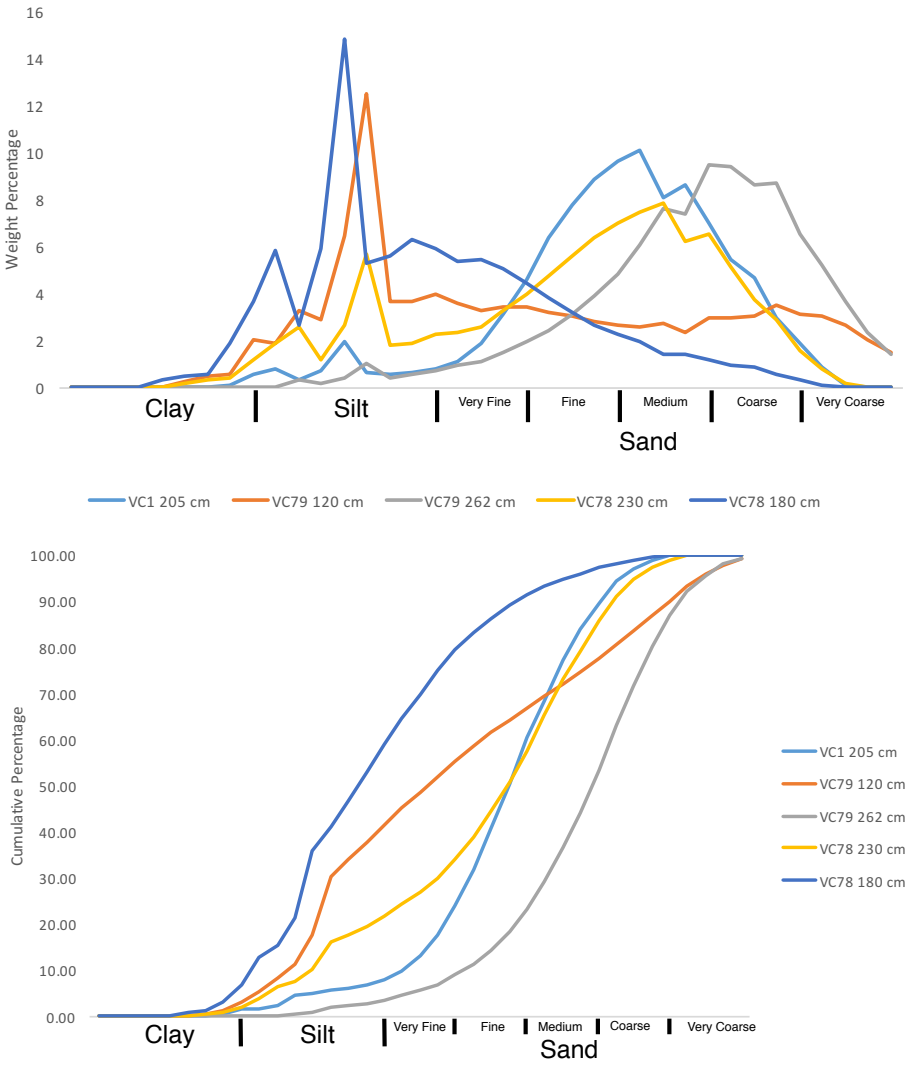

Figure 4.56: A selection of grain size data for VS samples. The data shows the range of grain size distributions present within this facies.

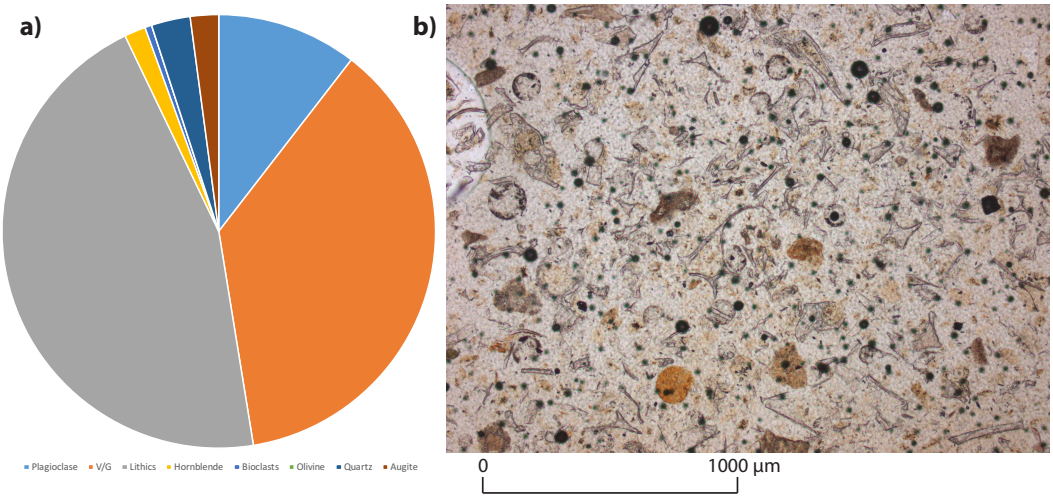

Figure 4.57: a) Average composition of all VS units. b) Thin section image of a Volcanic Sand sample.

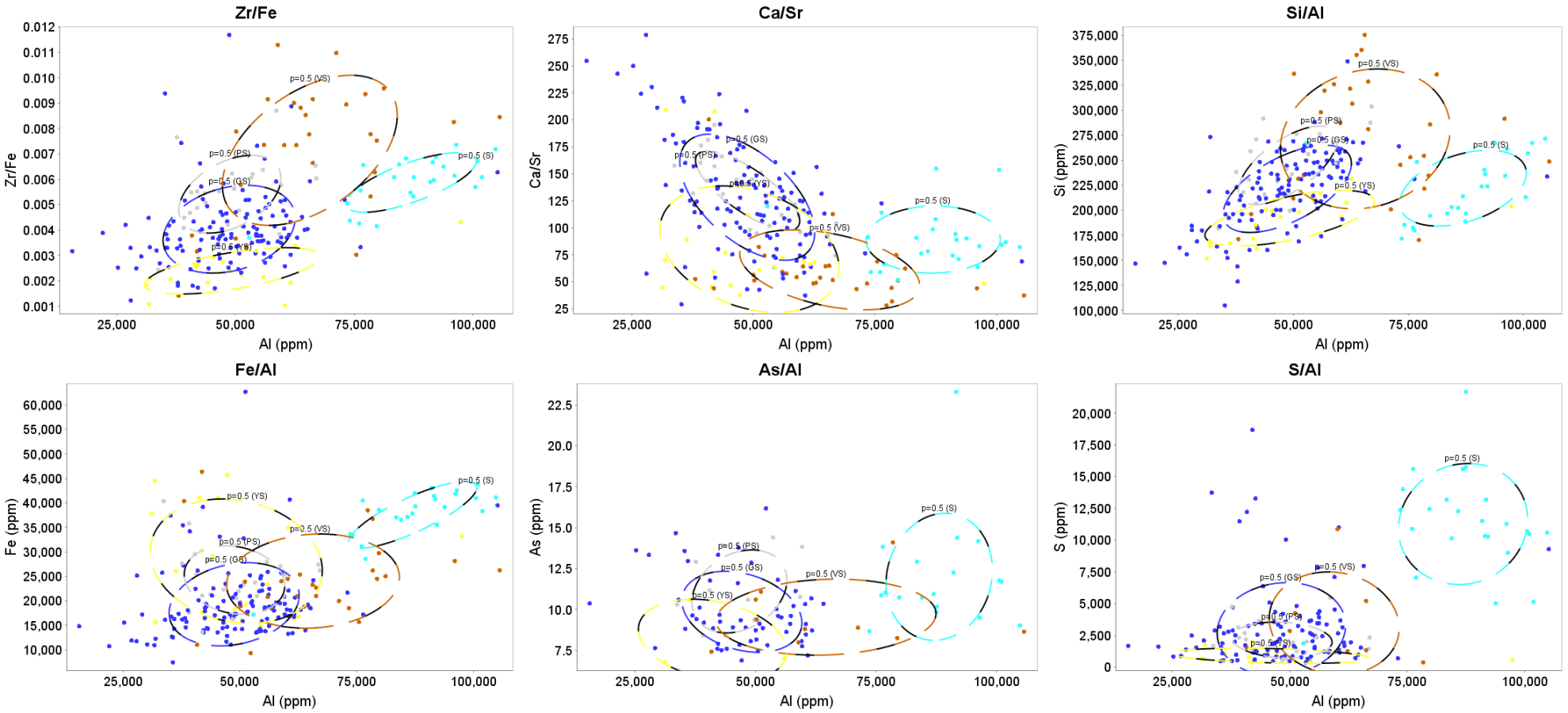

Figure 4.58: A selection of geochemical data for each sample collected. The facies are coloured as follows: VS = brown, S = light blue, CS = blue, CS-Y = yellow and PS = grey.

I interpret this facies to be a terrestrial deposit of volcanic origin. It is likely a reworked tephra, based upon the high Zr/Fe ratio, general sediment character (poorly sorted, fine grained, polymodal) and abundance of volcanic glass and lithics. It is sourced regionally to locally, based on the condition of the volcanic glass and the presence of plagioclase. Plagioclase is is less resistant to weathering than quartz so its presence indicates a regional to local source. I interpret the thin oxidising beds as paleosols (Figure 4.4), which indicates that the VS facies not one single tephra, but rather a succession of tephras, with periods of weathering in between. In Figure 4.59 there is a potential correlation in the data from VC74 with that of VC79. It has the same trend of being more sorted and less coarsely skewed as VC79. A t-test was run to determine the significance of the correlation between the two. The relationship between sorting was very strong (0.978) however the relationship between skewness was weaker (0.440).

Based on the geochemical data, texture and presence of paleosols, I interpret the VS facies to have been deposited in a terrestrial environment, but one which was nearby the sea. At one point in time it may have been inundated by tsunami or a storm event (Figure 4.5).

Where the facies is found with another facies in these vibracores, it is always the lowermost facies and is overlain by Coastal Sands. Contacts, however, are only seen in the Entrance Channel. This facies represents a series of tephras that were deposited in a terrestrial environment.

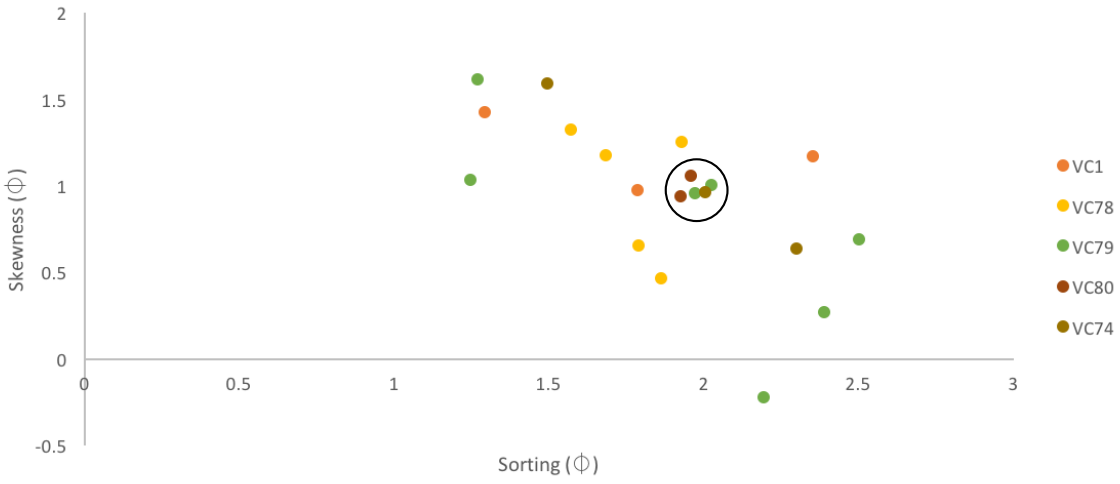

Figure 4.59: Skewness plotted against sorting for sub-samples taken from Stella Passage and VC74, from Manganui Roads South.

4.7.2 Silt (S)

The Silt facies is found in some vibracores from Manganui Roads and Manganui Roads South. The sediment texture is predominantly silt, but also in some cases very fine sand (Figure 4.60). The sediment is poorly sorted, strongly fine skewed

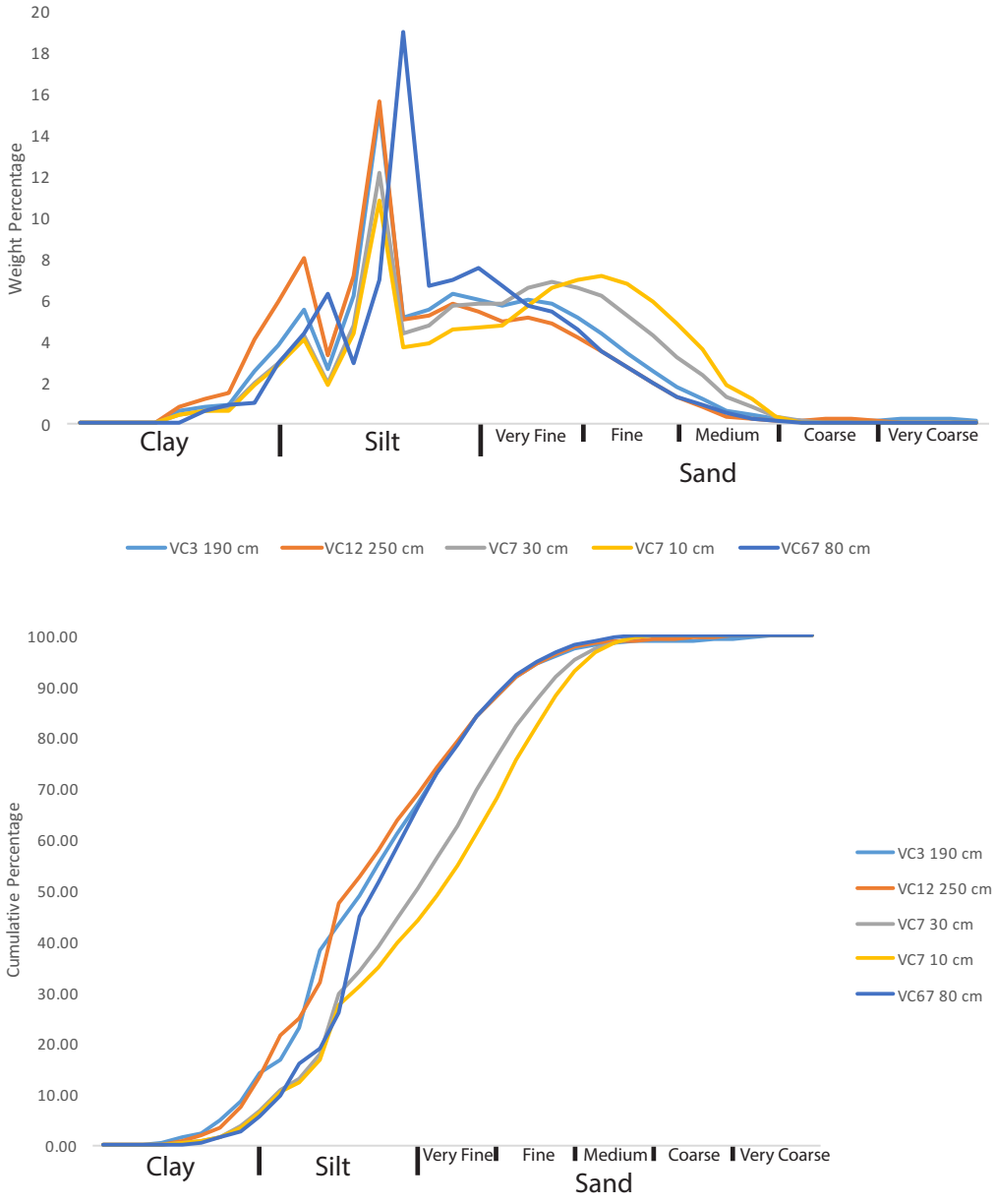

Figure 4.60: A selection of grain size data for S samples. The data shows the range of grain size distributions present within this facies. Note the similar peaks in the silt region.

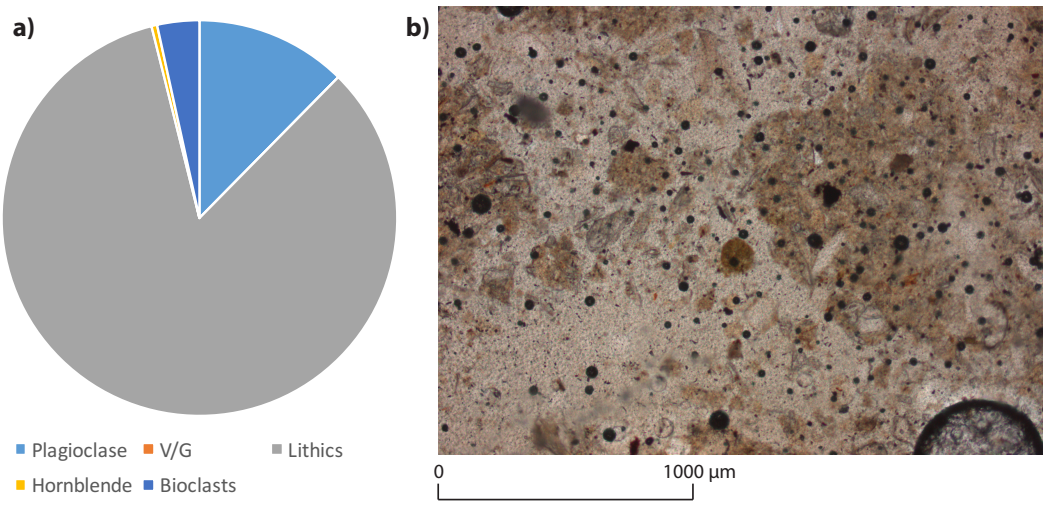

Figure 4.61: a) Average composition of all Silt units. b) Thin section image of a S sample.

and often polymodal. There is a trend of upward coarsening in many of the cores with this facies. No structures were observed in any of the cores. This could be a sign of bioturbation. Like the Volcanic Sand facies, this sediment is very compacted, and in many cases it is cohesive. When observed, many instances of this facies were also in the process of oxidising, giving it colours in the GY Munsell colour spectrum.

This facies is composed predominantly of lithics (Figure 4.61). Plagioclase is also present, as well as some bioclast fragments that are only visible under the microscope. Geochemically this facies is rich in aluminum, sulphur and iron, but low in strontium, barium and calcium. I interpret the elevated iron and aluminum to indicate high terrigenous input. The elevated Zr/Fe ratio indicates some volcanic input.

Diatoms were observed under SEM (Figure 4.33). However, these were not found in any great abundance. Some appeared to be partially dissolved, and many appeared to be broken. This could indicate a saline environment, as diatoms are prone to biogenic silica dissolution (Ryves et al., 2001). This presence of broken diatoms could indicate that they were transported there.

There are several indicators of reducing conditions within this facies. First is the colour of the sediment, which was oxidising when observed. Second is the presence of framboidal pyrite when observed under the SEM (Figure 4.31). The presence of arsenic and the high S/Cl ratio are further indicators of pyrite presence (Figure 4.30, 4.32a). The third are the several geochemical indicators that are discussed in sections 4.3.2.1 and 4.4.2.1. These include elevated sulphur and reduced barium. I use all these markers to interpret this facies as being deposited in a anoxic environment.

This facies underlies the grey sand facies described below in several cores. Where this contact occurs, it is an erosional surface. This boundary commonly has prod and skip marks, indicating saltating flow. The only instance of this unit being interrupted by unconsolidated coarse sand occurs in VC12 (Figure 4.22), between 210 and 230

cm.

Very little variation occurs visually with this sediment, although some areas of it are very fine sand. These coarser grained units are found to have a higher abundance of plagioclase present and a lower abundance of lithics. The abundance of bioclasts is the same. There was no difference in the abundance of diatoms between the two different grain-sized units.

I interpret this facies to be deposited in a lacustrine environment. The fine grain size is indicative of a low energy velocity. The oxidising sediment indicates reducing conditions, which suggests this could be a thermally stratified lake. The lower layer of the lake, the hypolimnion, is cold, dense and anoxic, while the upper layer of the lake (the epilimnion) receives oxygen from contact with the air (Nichols, 2009). This anoxia at the base of the lake is shown in the reduced character of the sediments when observed in core, and the various geochemical proxies used. The lack of invertebrates is probably due to a short lake lifespan, based also on the inferred thinness of the deposit (discussed in Chapter 5). Lake depth is difficult to ascertain, however it likely was not very deep based on the structure of the deposit (Chapter 5), but it would have been deep enough to have stratification. I interpret the discontinuity of the silt unit in VC12 between 210 and 230 cm to be a sudden influx of sediment from a fluvial source, suggesting that the fluvial input into the lake came from somewhere close to VC12. VC12 also has the highest levels of magnetic susceptibility, indicating close proximity to the source.

This facies could also be interpreted as an overbank deposit. Overbank deposits however commonly have a interbedded silts and sands, paleosols and vegetation present, which is not the case here. The only case of interbedded sands and silts in the entire group of silt sediments is found in VC12 (Figure 4.22). Because of this, I interpret the Silt facies as a lacustrine deposit.

This facies was likely sourced from the VS facies (Section 4.7.1). The silt facies has a similar grain size spike as the VS facies around 4 or 5 ϕ. This indicates that the fine grained sediment from the VS has been transported to this deposit.

4.7.3 Coastal Sand (CS)

The Coastal Sand facies is found in many vibracores in Maunganui Roads South, Manganui Roads, Cutter Channel, and Entrance Channel sets. The sediment texture is a fine to very coarse sand (Figure 4.62). In most cases, the sediment is moderately sorted, and fine to strongly fine-skewed. The colour of this sediment can vary considerably depending on the composition, however it is commonly observed to be in the Y to GY hues in the Munsell colour spectrum. Some intervals of this sediment were oxidising when first observed, giving it a colour in the N Munsell spectrum. There were no obvious structures in this sediment.

This facies is composed of plagioclase, quartz, bioclasts, lithics and trace amounts

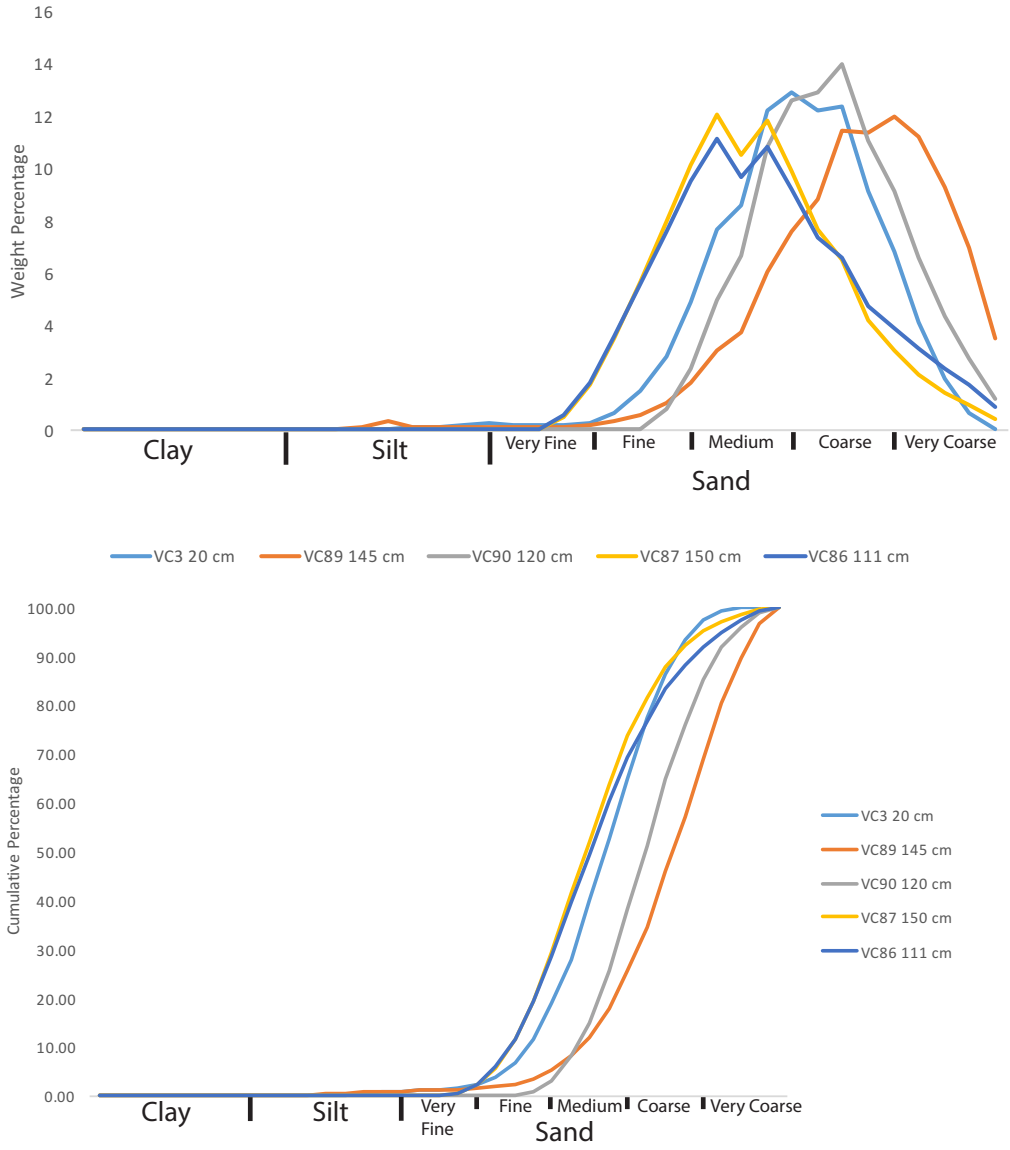

Figure 4.62: A selection of grain size data for CS samples. The data shows the range of grain size distributions present within this facies.

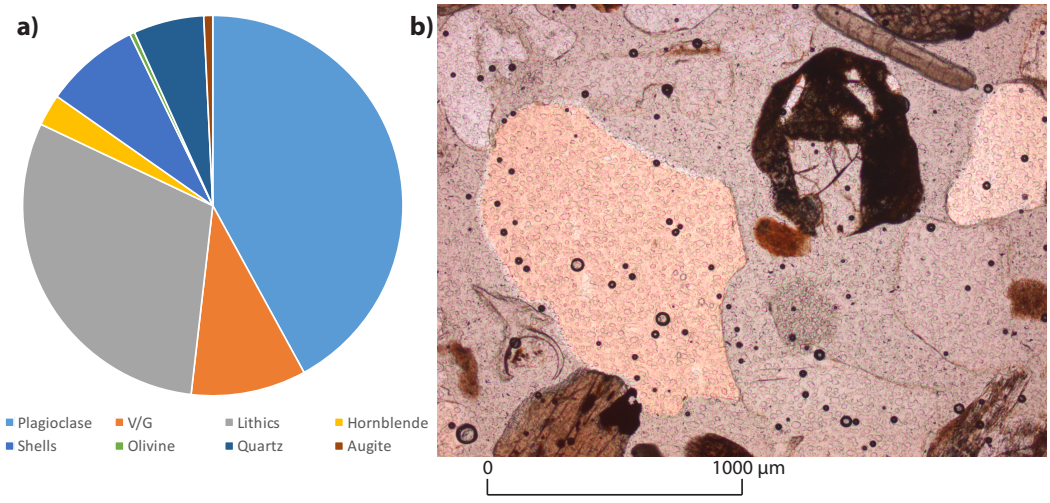

Figure 4.63: a) Average composition of all CS units. b) Thin section image of a CS sample.

of hornblende (Figure 4.63). Some units also contain some volcanic glass, likely from pumice as this is seen in some samples. The bioclasts that are present in this sediment occur in a variety of conditions, indicating marine sedimentation. The bioclasts that are present are seen in a range of conditions, including articulated, disarticulated, fragmented and bored. The differing shell condition shows the variations in hydrodynamics that have occurred during the deposition of this sediment. It also indicates that some of the bioclasts have been deposited in-situ.

Geochemically the Coastal Sands facies is different from the VS and S facies (Figure 4.58). It has a lower Zr/Fe ratio, which can be a signature of volcanism (Konfirst et al., 2011). It has a high Ca/Sr ratio, an indicator of detrital carbonate (Croudace and Rothwell, 2015). It has a lower Fe abundance, which has been used as a terrigenous signature (Croudace and Rothwell, 2015). It has a higher Si/Al ratio, which can be a proxy for biogenic production (Dickson et al., 2010; Croudace and Rothwell, 2015), than the other facies. I interpret these geochemical characteristics to suggest a highly productive marine environment. Some oxidising sediment was identified (e.g. Figure 4.36) and this is reflected in the geochemical data. In the sulphur chart in Figure 4.58), several samples have sulphur values higher than 10,000 ppm, indicating reducing conditions (Sluijs et al., 2008; Croudace and Rothwell, 2015). The oxidisation was likely caused by high productivity, based on the surrounding sediments. This high productivity would reduce the amount of oxygen available in the water column. Oxidising sediments are found in individual cores rather than large areas.

There are major variations in the Coastal Sand facies. The most immediate visual difference is the yellow sand units (CS-Y). These are compositionally very similar (Figure 4.58) but the grains are coated in limonite (iron-staining), giving it the yellow appearance. This is likely from a discharge of geothermal fluid in the subsurface, which causes the yellow coating. These yellow sand units commonly have higher iron contents than other Coastal Sand samples. However, aside from this geochemically they are very similar (Figure 4.58). Variations also occur within this yellow sand sediment. In some cases, the sediment is a dark red colour, and has been partially cemented forming clumps.

This facies was deposited in a coastal environment, based on the abundance of bioclasts. It has been reworked, with the majority of bioclasts exhibiting at least partial breakages. Some boring of bioclasts has also occurred. Geochemically it has low terrigenous indicators and higher biogenic production indicators, again pointing towards a marine environment.

Contacts for this facies are observed at both the top and bottom of the units. The top boundary is a gradational one, indicating a gradual change in sedimentation conditions. The bottom boundary is an erosion surface, representing an unconformity.

4.7.4 Pumiceous Sand (PS)

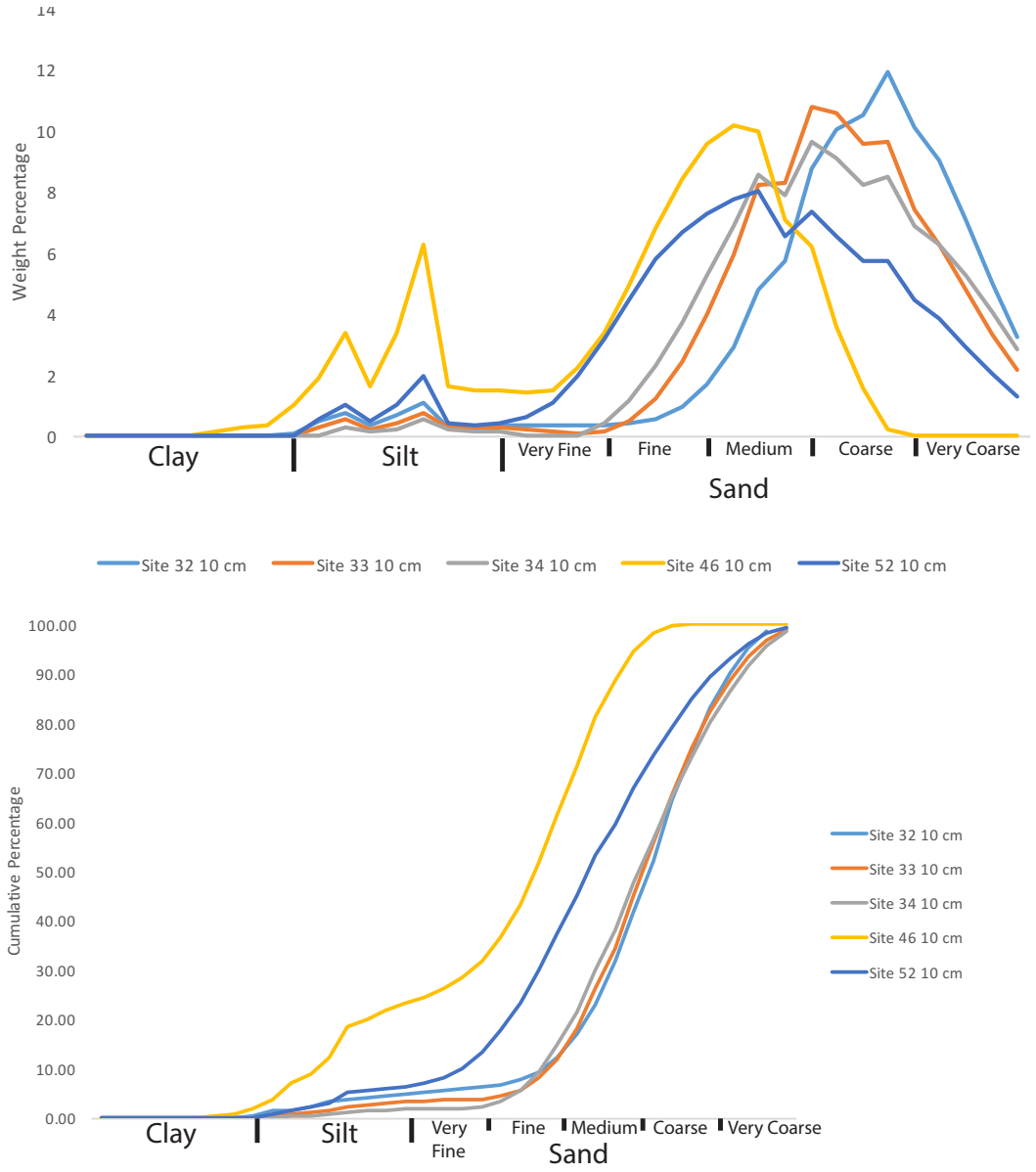

Figure 4.64: A selection of grain size data for PS samples. The data shows the range of grain size distributions present within this facies.

The Pumiceous Sand facies is found at the tops of many vibracores in the Manganui Roads, Cutter Channel and Entrance Channel sets. The sediment texture is medium to coarse sand, although there are some fine sand units (Figure 4.64). The sediments are poorly to moderately sorted, and often finely skewed. They commonly appear in the Y to YR hues of the Munsell colour spectrum.

This PS facies is composed predominantly of lithics and volcanic glass (Figure 4.65). Plagioclase is also present, as are bioclasts and hornblende. Bioclasts that were present were often in the form of fragments. Geochemically (Figure 4.58), this facies is similar to the CS facies. However, it does have higher a higher Zr/Fe ratio (a volcanic signature (Konfirst et al., 2011)), higher potassium (a terrigenous indicator (Croudace and Rothwell, 2015)), and high barium (an indicator of produc-

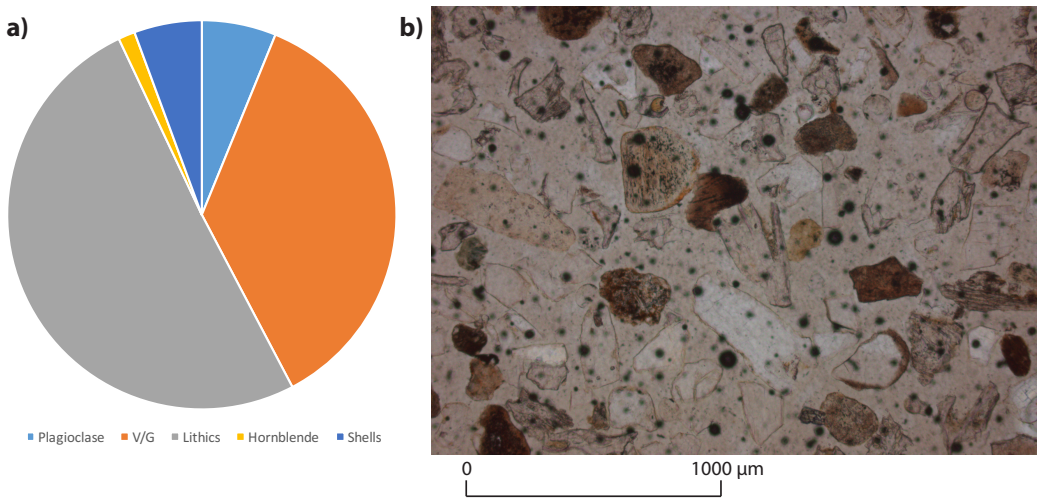

Figure 4.65: a) Average composition of all Pumiceous Sand units. b) Thin section image of a PS sample.

tivity (Croudace and Rothwell, 2015)).

This facies only appears at the tops of some cores. It always contacts a Coastal Sand unit below at a gradational boundary. Christophers (2015) found ignimbrites around the harbour eroding into the sea. I propose that this facies represents modern deposition, with the eroded sediment then reworked and transported around the harbour, mixing with CS sediment being transported into the harbour. De Lange (1988) found that pumiceous sand sediment occurs in crests on the sea floor while shelly sediment occurs in troughs. If this is the case, the PS sediments in this study represent these sediment crests. De Lange et al. (2015) found several 'sand waves' in multibeam echosounder surveys and suggested that these appeared to be migrating northwards. I suggest that this pumiceous sand facies represents these mobile sand waves.

4.8 Conclusion

86 vibracores that were obtained by the Port of Tauranga were logged and described within this chapter. Further core logs are within the Appendices. Grain size, magnetic susceptibility, XRF and optical mineralogy data was used alongside the core descriptions to define four facies. These four facies have been summarised in Table 4.8.

Table 4.8: Facies summary table.

Facies Name	Code	Description	Environment
Volcanic Sands	VS	Poorly sorted, silt to fine sand. Composed of volcanic glass, lithics, plagioclase, quartz and hornblende. High Zr/Fe, and K.	Terrestrial
Silt	S	Poorly sorted silt to very fine sand. Composed of lithics, plagioclase and trace amounts of bioclasts. Contains diatoms. High Al, Fe, S.	Lacustrine
Coastal Sand	CS	Moderately sorted medium to coarse sand. Composed of plagioclase, lithics, quartz, bioclasts, and hornblende. High Ca/Sr, low Fe, Zr/Fe.	Shallow marine
Pumiceous Sand	PS	Poorly sorted medium to coarse sand. Composed of volcanic glass, lithics, plagioclase, quartz and hornblende. High Ba, elevated K and Zr/Fe.	Shallow marine

Chapter 5

Distribution

5.1 Introduction

This chapter describes the distribution of the facies identified within the harbour. These data were modelled using the software package Leapfrog3D (as described in Section 3.8), and some results are shown below. The Leapfrog model was built using core data from my observations and analysis. Borehole data (BHL1, 2 and 3) from Moon et al. (2013) was also used to further constrain facies within Stella Passage. Seismic data was also made available from de Lange et al. (2014) from throughout the shipping channel and across the Matakana Banks. The Knudsen Pinger SBP seismic reflection system was configured for maximum depth, resulting in a loss of resolution. Because of this, the data is of variable quality, so only select lines have been chosen. As a result, the results in the Leapfrog model from outside of the channel and in between vibracore groups are to an extent uncertain.

The overall model shows the upper boundary of the Volcanic Sands facies dipping away from Stella Passage and rising in two ridges, one in Cutter Channel and one in the Entrance Channel. The Coastal Sands facies is then draped across this erosional surface. The CS-Y facies is limited in extent to the Entrance Channel, occurring close to the VS contacts. The Pumiceous Sand facies occurs at the tops of some cores in Maunganui Roads South, Maunganui Roads, Cutter Channel and Stella Passage. Due to the nature of the PS sediment (sand waves propagating through the dredge channel) it is modelled as part of the CS facies. This is due to the limitations of the model, unable to model sand waves. All vibracore data collected for this project are available in the appendices.

5.2 Stella Passage and Maunganui Roads

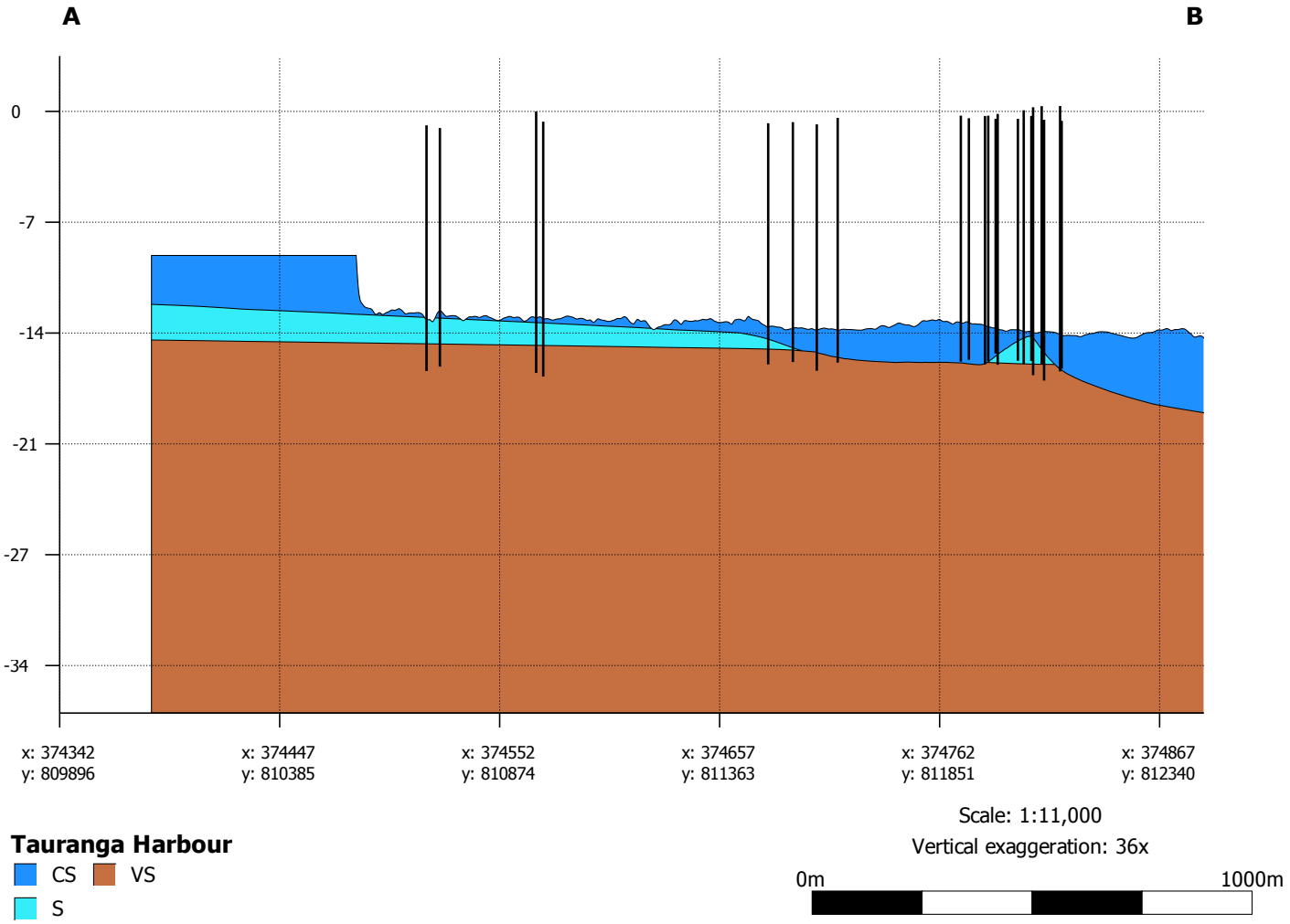

Figure 5.1: Cross section of Stella Passage and Maunganui Roads. The black lines protruding down into the sediment show the locations of boreholes within 100 m of the cross section. Note that the model show a Silt succession extending through Stella Passage. This is not seen in vibracore data, however it does appear in core descriptions by Moon et al. (2013)

All four vibracores described within the dredged Stella Passage channel consist of VS (Section 4.2). This differs from descriptions of boreholes from Moon et al. (2013) and Upiap (2015) which have successions of silt above the volcanic sands. The vibracore data obtained was modelled and shows a succession of Silt extending from Stella Passage to Maunganui Roads (Figure 5.1). The succession of Silt thins northwards past Maunganui Roads, where it reaches the surface of the dredge channel. The model indicates that this Silt succession ends just past the Maungaui Roads set of vibracores, but there is no vibracore data in between Maunganui Roads and Cutter Channel, so it is possible that this Silt succession extends up to Cutter Channel. In the vibracore dataset, no instances of this silt unit are found beyond Maunganui Roads to the North or Maunganui Roads South to the South. However, it is found in the 3 boreholes to the South in Stella Passage from Moon et al. (2013), and it has been modelled as extending down through Stella Passage. The top contact of the Silt facies is the Coastal Sand facies. No bottom contact of the Silt facies is present in the vibracore dataset. However, in the boreholes used by Moon et al. (2013) the bottom contact of the Silt unit is with a 'Pumiceous sands and silt' succession identified by Moon et al. (2013). As is shown in Figure 5.1, the vibracores do not penetrate very deep into the VS facies. So, although the model shows that the VS forms the base of the harbours stratigraphy, deeper boreholes from Moon et al. (2013) and Upiap (2015) show that there are several further successions underlying the VS. A deeper transect of Stella Passage, developed by Moon et al. (2013) is presented in Figure 2.5.

The one line of Stella Passage seismic data is of variable quality (Figure 5.2b, c). One strong reflector is present in the area showing large, rapid changes in depth. This reflector is not continuous across the whole area. When the core logs are overlaid, it is apparent that the area in Figure 5.2C without a strong reflector is VS sediment. VC78 runs through a reflector, indicating that the sediment below the reflector is VS. Based on this data set however, it is uncertain just how thick the VS succession is. In data from Moon et al. (2013) the VS succession (termed 'pumiceous sands' and 'pumiceous and silts intermixed') is up to 40 m thick. However, in areas it is interrupted by quartz sands and paleosol units.

De Lange et al., 2014 observed that the data was of poor quality but showed an eastward extension of the ridges and valleys identified by Moon et al. (2013). The valleys identified in this data are very narrow and deep. In Moon et al. (2013) the valleys are interpreted to be the main threads of a river system during alluvial fan development.

One strong reflector is identified in the Maunganui Roads seismic data (Figure 5.3B and C). This reflector is not penetrated by any cores however I assume it to be a VS succession, based on penetration of a similarly strong reflector in Stella Passage and its depth (18 m below sea level). A silt succession is penetrated by

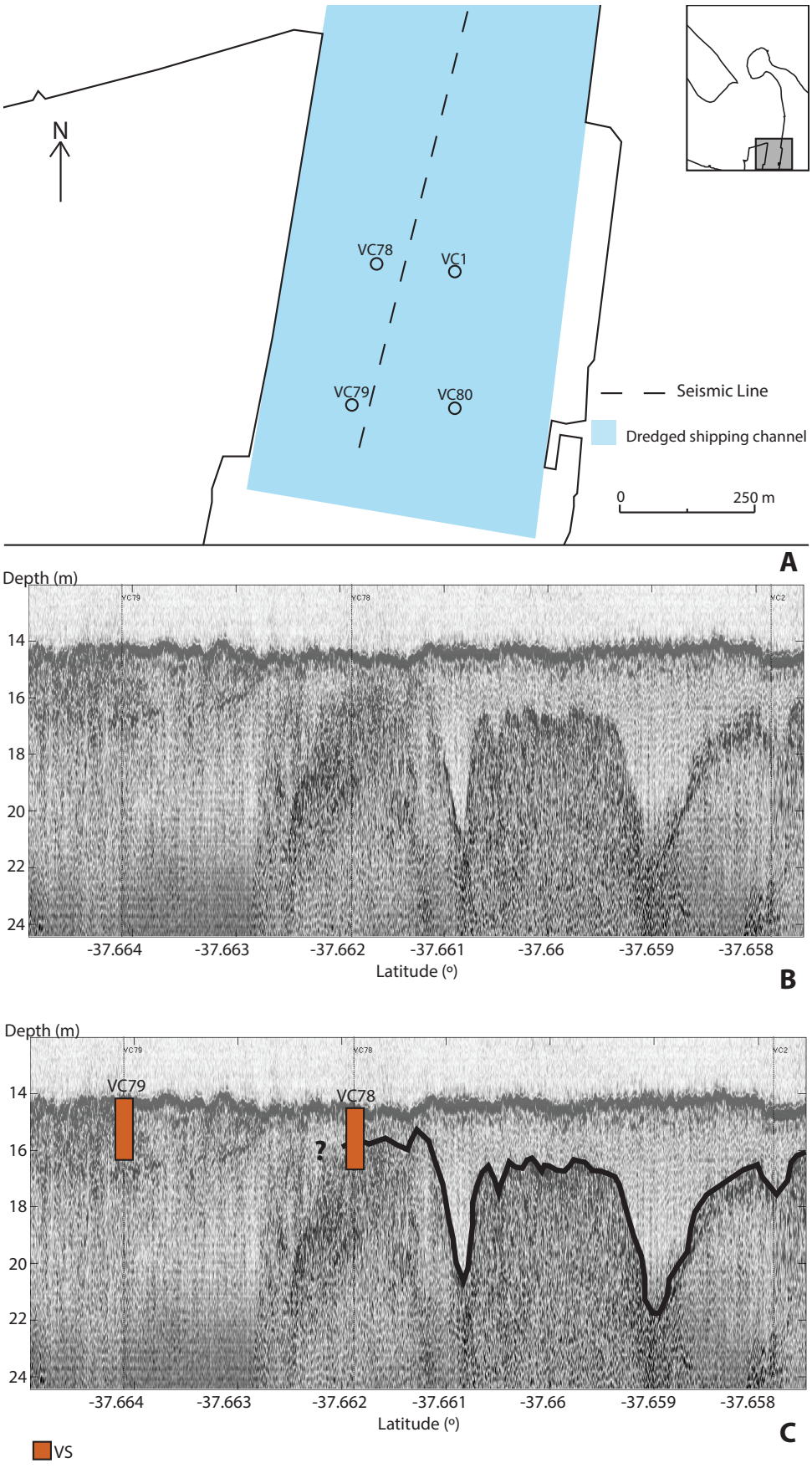

Figure 5.2: Seismic data from one line through Stella Passage. A shows the location of the line and nearby vibracores. B shows the unedited processed seismic line (from (de Lange et al., 2014)). C shows the interpretted seismic line with identified facies from core logs overlaid.

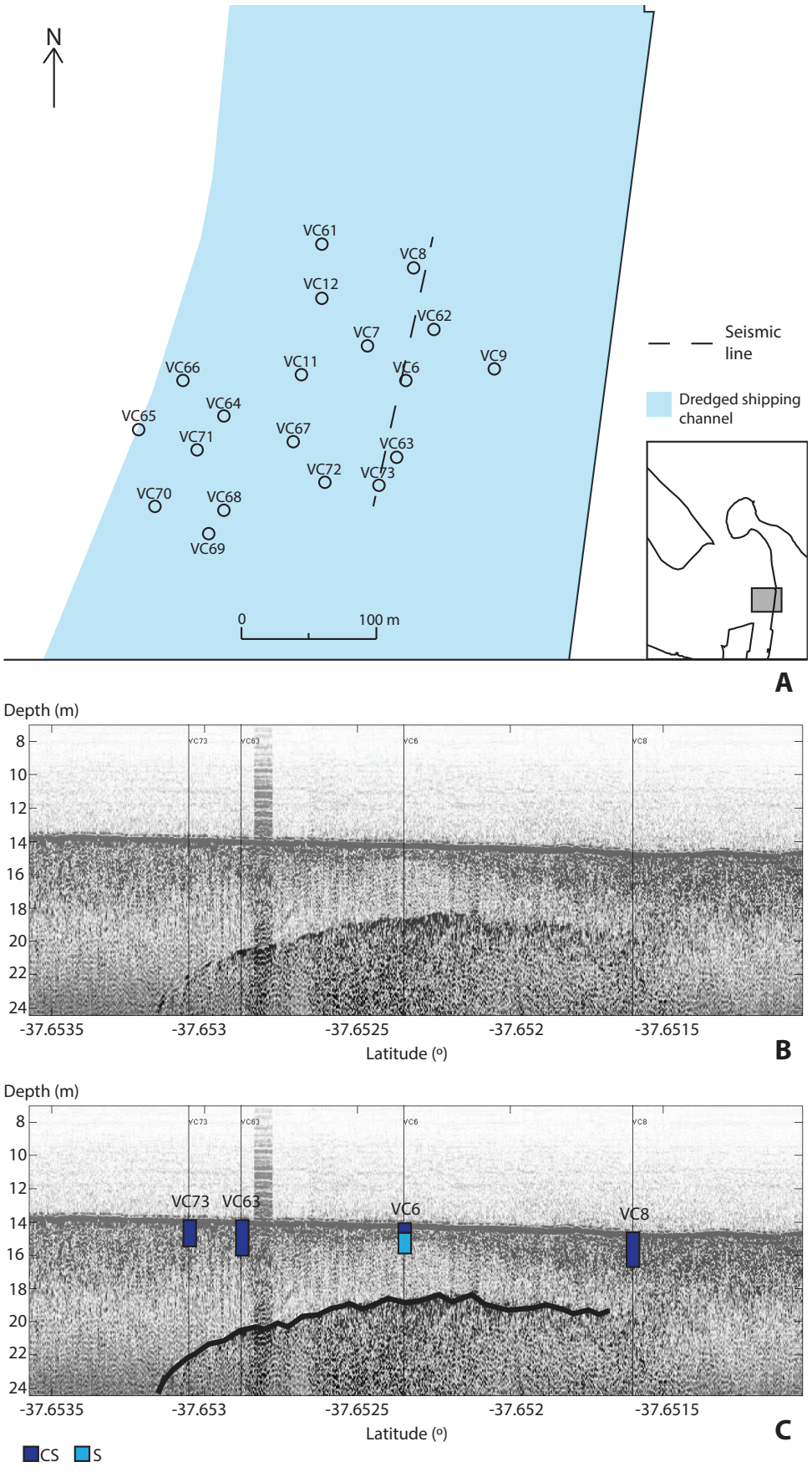

Figure 5.3: Seismic data from one line through Maunganui Roads. A shows the location of the line and nearby vibracores. B shows the unedited processed seismic line (from (de Lange et al., 2014)). C shows the interpretted seismic line with identified facies from core logs overlaid.

several vibracores in this area, however it doesn't clearly show up on the seismic data. It could be identified as the lighter area of sediments in between the seafloor and the strong reflector however the data is not clear enough to confidently make that assertion.

5.3 Cutter Channel

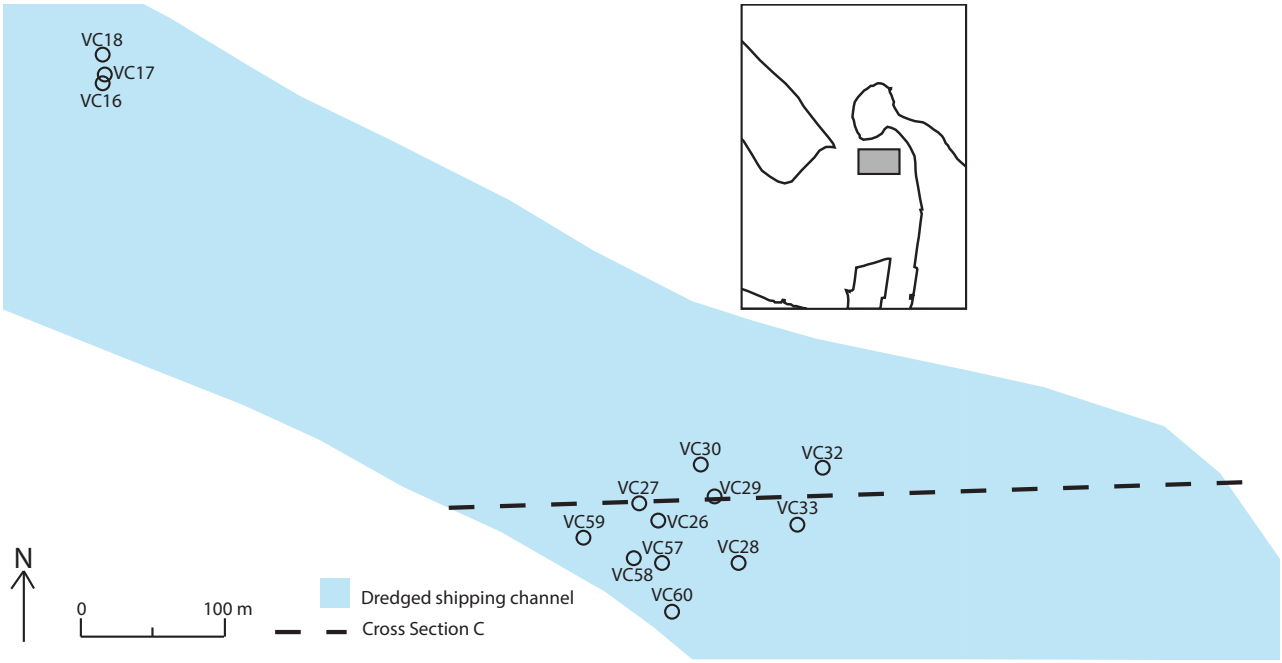

Figure 5.4: Map showing the location of the cross section through Cutter Channel. The black lines protruding down into the sediment show the locations of boreholes within 100 m of the cross section.

A cross section across Cutter Channel is presented in Figure 5.5. It shows the presence of a ridge of VS with a long wavelength beneath the CS facies. This differs from the short wavelength ridges found in the Entrance Channel (Figure 5.9, 5.10). However, this ridge is constrained by just one core, VC26. The Coastal Sand succession is draped across the VS facies with an erosional contact. The modelled surface of the CS succession shows the bedforms that are present in this part of the channel. The thickness of the CS succession in this area is limited by the dredging. At the tops of VC32, VC33, and VC58 in this area there are intervals of CS-P that is 10 – 28 cm thick.

A seismic line for Cutter Channel is presented in Figure 5.6. It shows a reflector underlying the flanks of the dredged shipping channel. In this area, one vibracore penetrates a VS succession, the rest is CS. This is not clear in the seismic data (see Figure 5.6), perhaps due to the poor resolution. De Lange et al. (2014) investigated additional seismic data to identify buried logs or boulders, which had affected dredging in the previous capital dredging operation. In additional seismic data interpreted

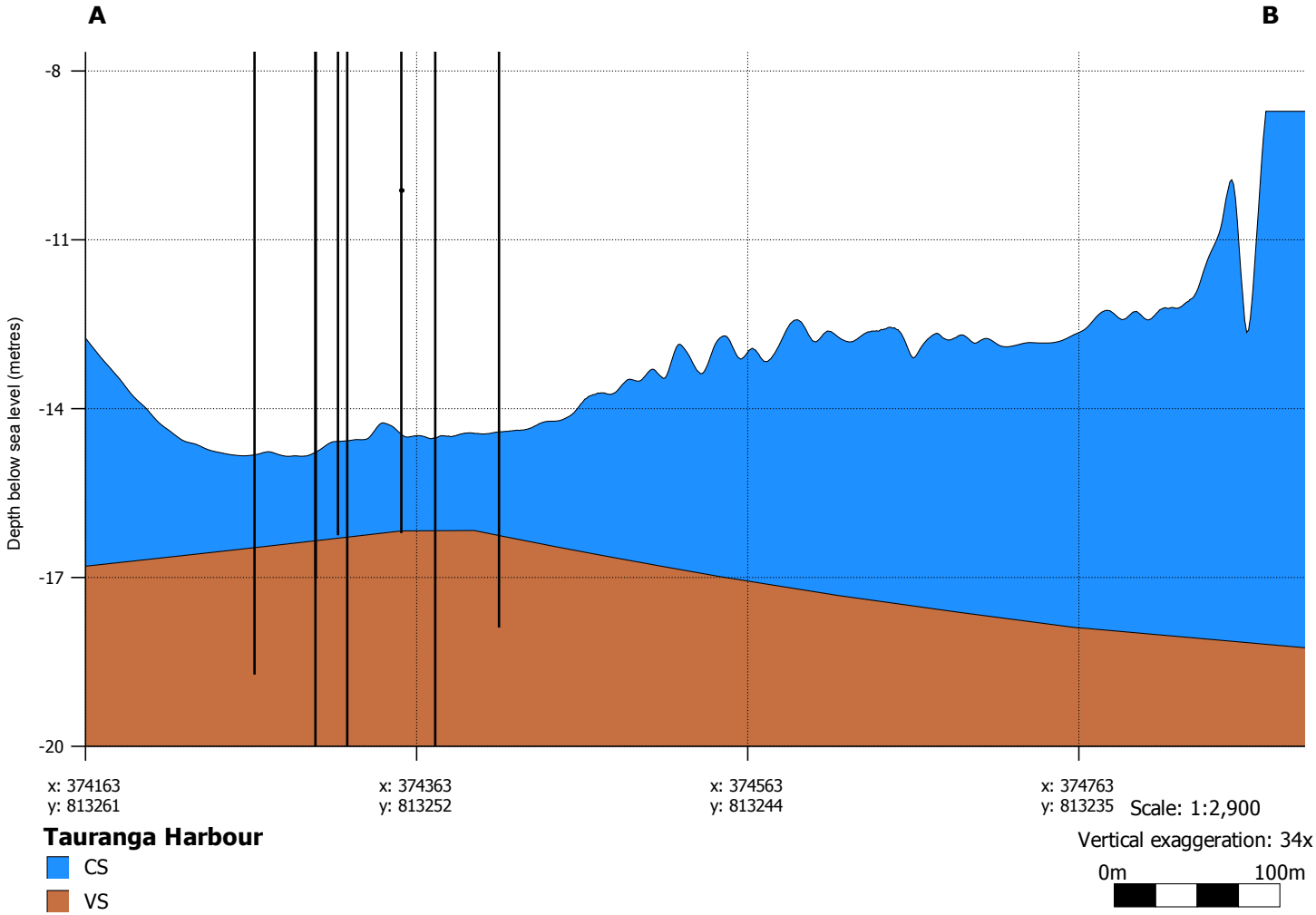

Figure 5.5: Cross section across Cutter Channel, showing the ridge of VS sediment present in this area.

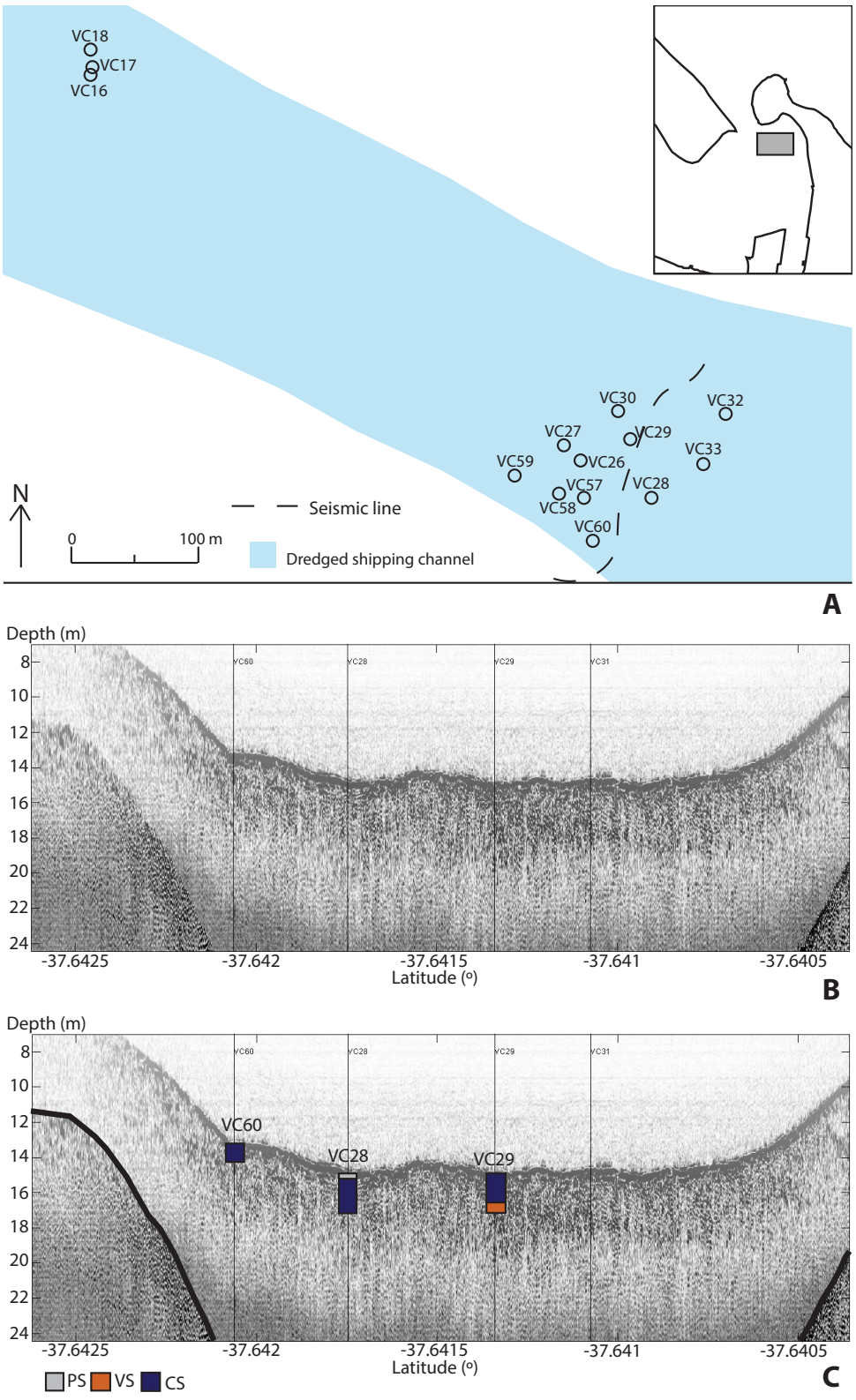

Figure 5.6: Seismic data from one line through Cutter Channel. A shows the location of the line and nearby vibracores. B shows the unedited processed seismic line (from (de Lange et al., 2014)). C shows the interpreted seismic line with identified facies from core logs overlaid.

by de Lange et al. (2014), a ridge of 'older sediment' runs parallel to the channel, outcropping in several locations.

5.4 Entrance Channel

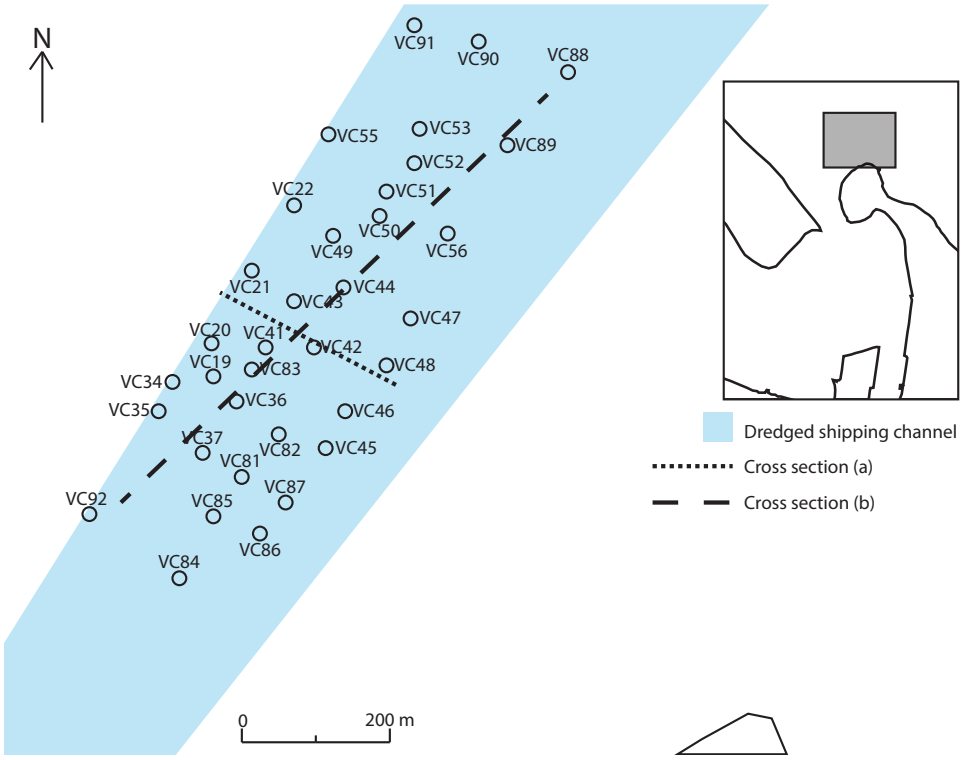

Figure 5.7: Map showing the locations of Cross Section (a) and (b).

Figures 5.9 and 5.10 present cross sections of the 3-D model through the Entrance Channel. They show two ridges running beneath the centre of the Entrance Channel, trending in what appears to be a northern direction. In Figure 5.9 it shows one large ridge of VS centred beneath the dredge channel, with the top of the ridge less than half a metre from the sediment surface at its peak. The shape of this ridge outside of the dredge channel is uncertain, due to the lack of vibracore data. The thickness of the VS interval is also uncertain. Data from Moon et al. (2013) within Stella Passage suggests that this succession may be 5–30 m thick. Figure 5.10 shows the presence of a second ridge adjacent to the one identified in Figure 5.9. This ridge has a longer wavelength than the ridge closer to the shore.

Across the tops of these ridges the Coastal Sand develops into a distinct yellow colour (CS-Y, 4.7.3), which I infer to suggest the presence of geothermal seepage from these ridges. This CS-Y facies only occurs around these ridges, although there are individual grains in other areas such as Cutter Channel that are tinted yellow.

The Entrance Channel seismic data (presented in figure 5.8b and c) is of poor quality and difficult to interpret. Core logs have been overlain across Figure 5.8c. These core logs show that it is very difficult to extrapolate the different successions identified in the cores into the seismic. A series of seismic lines were interpreted by de Lange et al. (2014) as indicating a series of ridges and valleys underlying the dredge channel and Matakana Banks. Parts of these ridges and valleys are visible in the 3D model presented in Figures 5.9 and 5.10. However, if the interpretation by

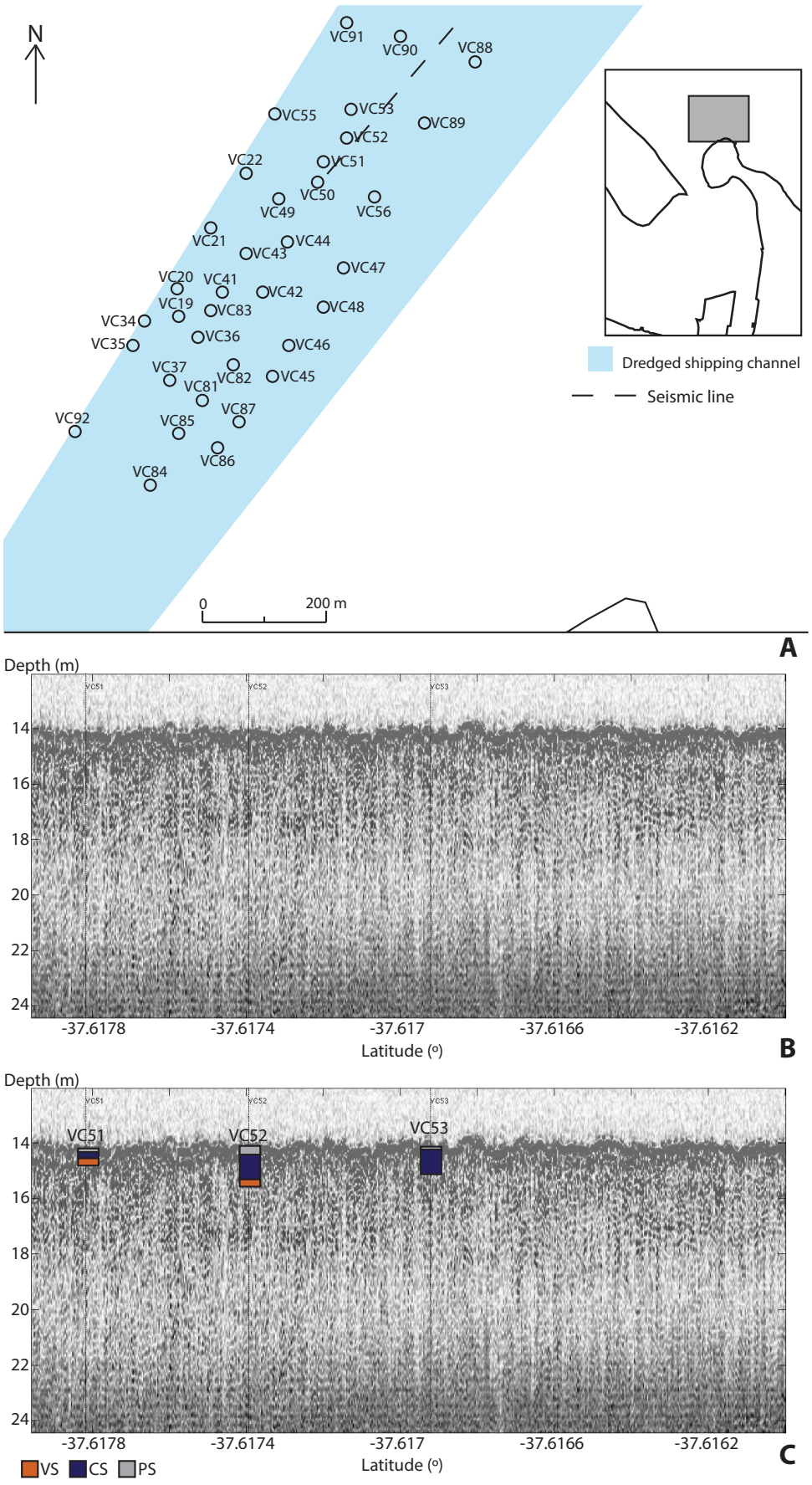

Figure 5.8: Seismic data from one line through the Entrance Channel. A shows the location of the line and nearby vibracores. B shows the unedited processed seismic line (from (de Lange et al., 2014)). C shows the interpreted seismic line with identified facies from nearby core logs overlaid.

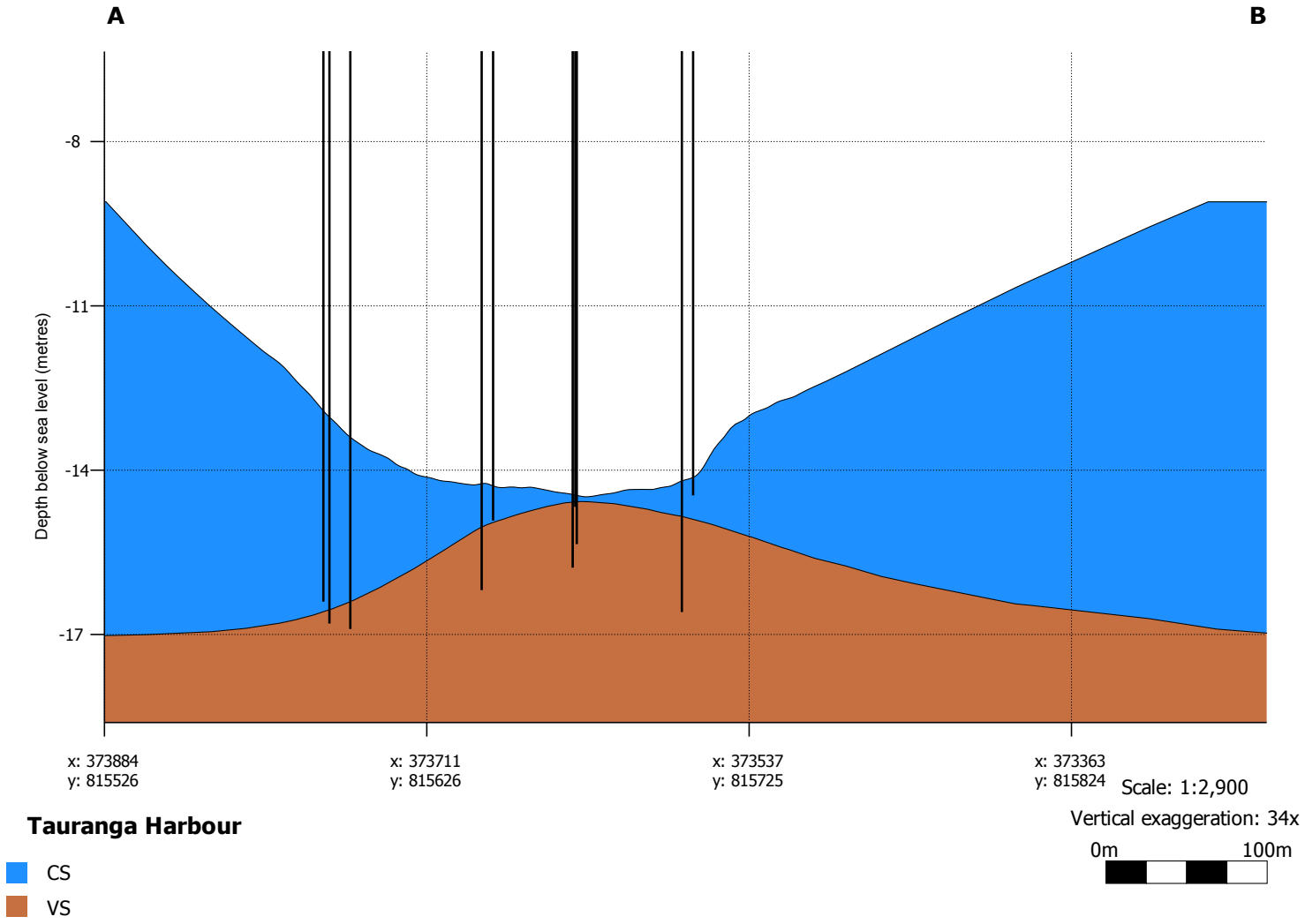

Figure 5.9: Cross section (a) of the Entrance Channel. The black lines protruding down into the sediment show the locations of boreholes within 100 m of the cross section.

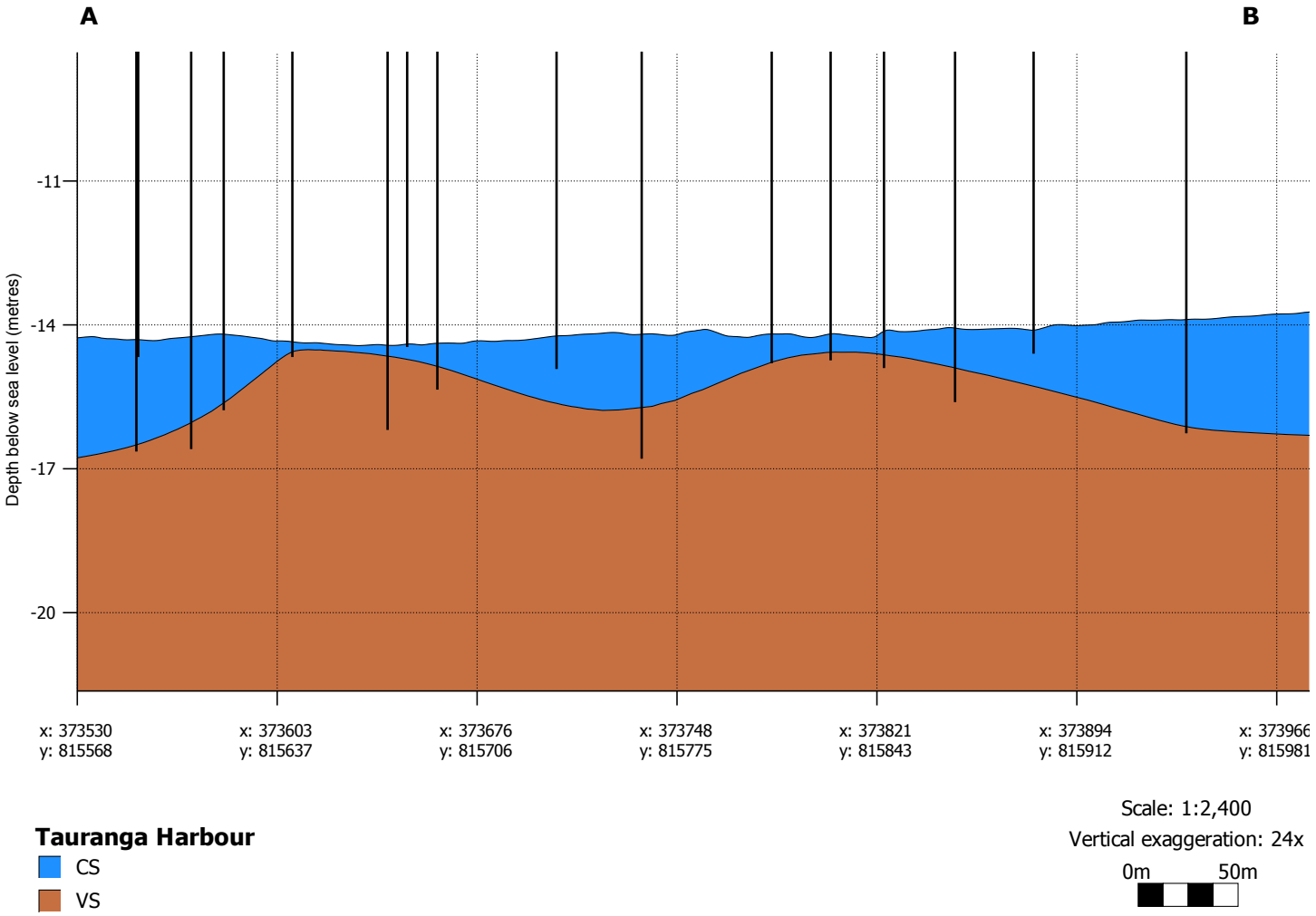

Figure 5.10: Cross section (b) of the Entrance Channel. The black lines protruding down into the sediment show the locations of boreholes within 100 m of the cross section.

de Lange et al. (2014) is correct these ridges and valleys continue further across. A lack of clear data has prevented further modelling of this area.

Chapter 6

Discussion

Introduction

This chapter will discuss the correlation of the facies identified in this study with the facies identified in other studies. It will also discuss the paleogeography of the area, and propose a new model for its development through the Pleistocene to Holocene (previously discussed in Section 2.5.4).

Facies Correlation

I propose the following facies correlations with the work done by Davis and Healy (1993) and Moon et al. (2013):

- The terrestrial **Volcanic Sand** facies discussed in section 4.7.1 to correlates with the 'pumiceous sand and mud' in Davis and Healy (1993) and the 'pumiceous sands' and the 'pumiceous sands and silts intermixed' in Moon et al. (2013). This is due to its similar texture (fine sands) and position in the stratigraphic column.
- The lacustrine **Silt** facies discussed in section 4.7.2 correlates with the 'shelly mud' in Davis and Healy (1993) and the 'silt' unit identified in Moon et al. (2013). This is due to its similar texture, and its position in the harbours stratigraphy.
- The **Coastal Sands** facies discussed in section 4.7.3 correlates with the 'shelly sand' in Davis and Healy (1993) and the 'Holocene sand and silt with shell fragments' in Moon et al. (2013). This is due to its similar texture (medium to coarse sand) and composition (containing bioclasts), as well as its stratigraphic position.

The **Pumiceous Sands** facies discussed in section 4.7.4 was not found in the studies done by Davis and Healy (1993), Healy et al. (2009) Moon et al. (2013), or Upiap (2015), however similar sediment was identified by de Lange, W. P. (1988).

The volcanic sand facies most likely represents either Pahoia tephras (Section 2.5.1.3) or Hamilton Ash (Section 2.5.1.6) based on the characteristics of the sediment and its position in the stratigraphic column. If the date of 9420 $\pm$ 100 from Davis and Healy (1993) is used, it is probably Hamilton Ash. It is also possible that the VS sediments cored from Stella Passage (where the date obtained by Davis and Healy (1993) is from) and those cored in the Entrance Channel are two different tephra successions.

A generalised stratigraphic column of Maunganui Roads is presented in Figure 6.1, showing the generalised layout of the different facies and their composition. It shows that the volcanic sand facies is overlain by the lacustrine silt (as described by Moon et al. (2013)) before being overlain by a thick succession of Holocene coastal sands and thin pumiceous sand waves.

Source

Each of the facies identified in this study represents a change in sediment source. The volcanic sands facies is probably a succession of tephras. These tephras are likely sourced from the Taupo Volcanic Zone, as if the date from Davis and Healy (1993) is correct, the Taupo Volcanic Zone is the active volcanic centre at that time (Section 2.5) (Briggs et al., 2005). Within this succession of tephras there are a series of hiatus events, leading to the development of paleosols.

The silt facies is probably sourced from the volcanic sand facies. The silt facies contains a high proportion of grains within the six to four ϕ range, similar to the volcanic sands facies. It does not contain any volcanic glass, which is abundant in the VS, due to the chemical instability of volcanic glass (Staudigel and Hart, 1983). The low energy environment means that only the finer grained VS sediments are transported. Moon et al. (2013) also thought this was a reworked tephra succession.

Healy et al. (2009) suggested that the coastal sands facies was transported from offshore into Tauranga Harbour during the Holocene Marine Transgression. I agree with this, as the CS facies contains much coarser sediment than is found in either the VS or S facies. Individual quartz grains coated in limonite are found in Cutter Channel and Maunganui Roads, suggesting sediment transport from the area of geothermal seepage in the Entrance Channel into the Harbour.

The Pumiceous Sands facies is likely a mix of sediment sourced from ignimbrite cliff erosion from within of the harbour, and Coastal Sands input from outside of the harbour. The pumice within the sediments is sourced from the ignimbrite cliff erosion. The coarser sediment (2 to -1 ϕ) has a similar grain size distribution (Figure 4.64) to the CS (Figure 4.62).

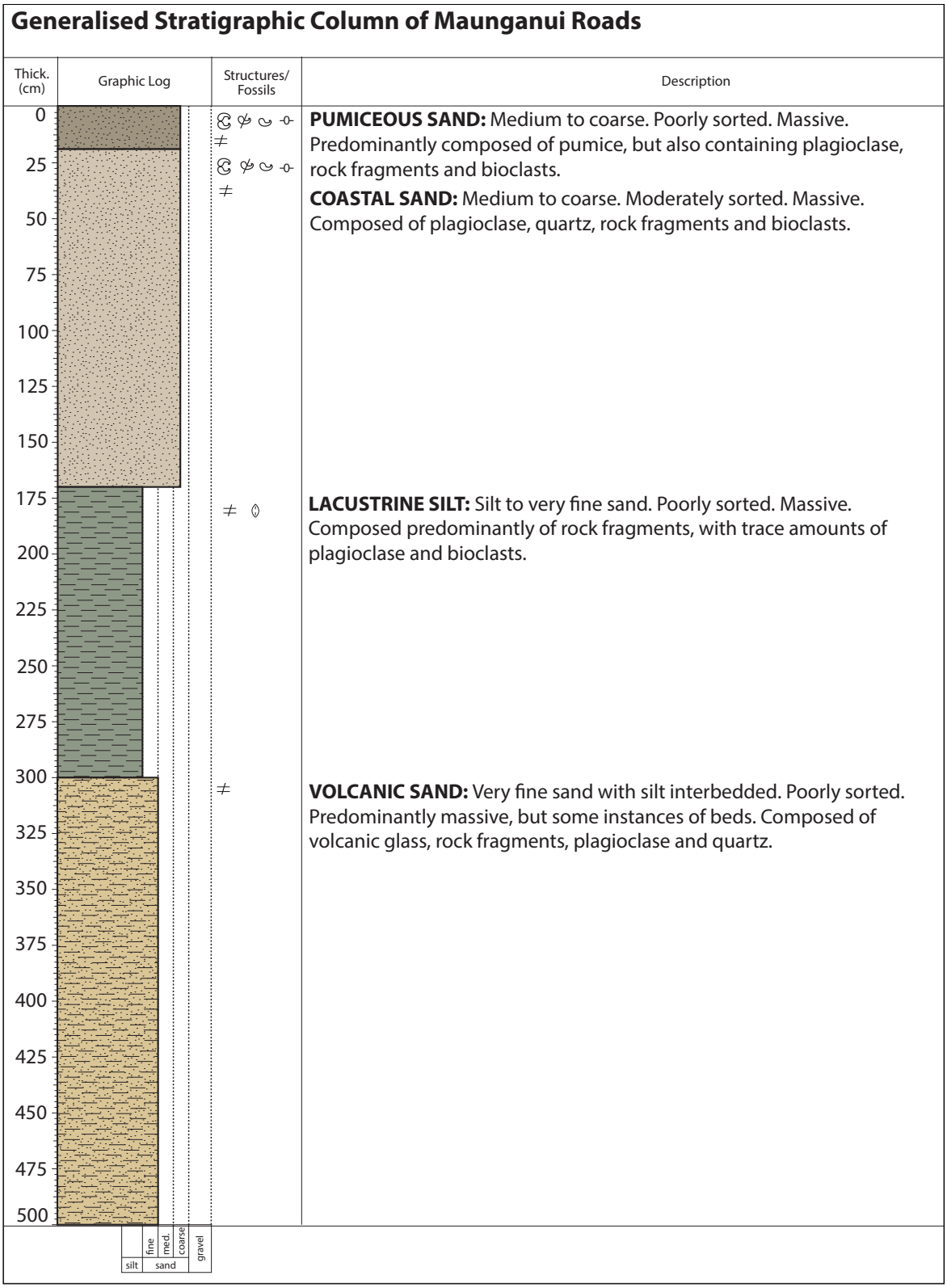

Figure 6.1: Generalised stratigraphic column of Maunganui Roads, showing the generalised layout of the facies.

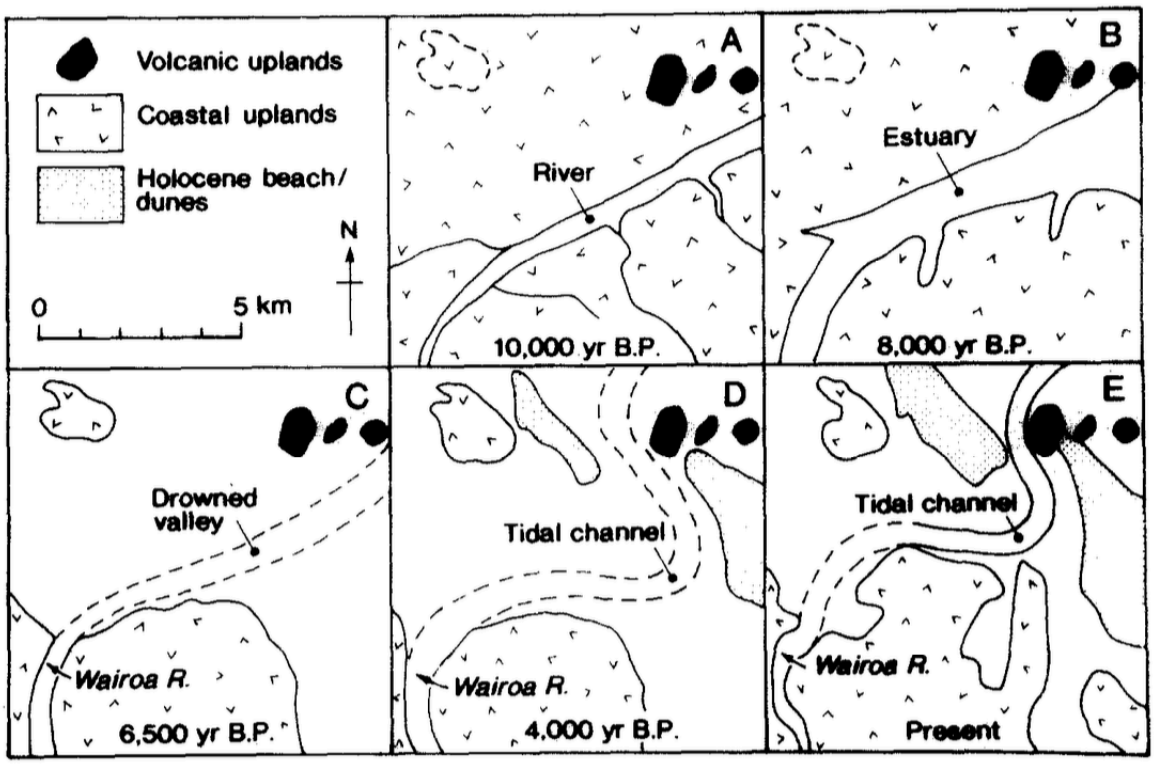

Figure 6.2: Evolution of Tauranga Harbour as proposed by Davis and Healy (1993).

Distribution of silty sediments

The distribution of silty sediments within the dredged shipping channel is discussed in Section 5. The results show that there are ridges of silty sediment present in each of the five areas of the dredged shipping channel (Figure 4.1). There is variation however in the height of these ridges, and these data sets are not conclusive. In Cutter channel for instance, de Lange et al. (2014) report that the ridge of VS sediment shown in figure 5.5 outcrops above the surface, and that a further ridge may occur in the vicinity of Pilot Bay.

Further ridges and valleys will likely also occur outside of the Entrance Channel. Two are identified in the vibracore data from within the Entrance Channel presented in Figure 5.10. It is likely that these ridges extend outside of the area vibracored. Most likely, the vibracorer has just caught the top of a much greater ridge system that represents underlying paleotopography.

Little data exists outside of the dredged shipping channel. It has been suggested that the ebb-tidal delta is draped over the top of silty terrestrial sediment (de Lange et al., 2015). de Lange et al. (2014) found that the Mount Maunganui ryholite dome does not extend beneath the dredged shipping channel.

Chronology of the development of Tauranga Harbour

As discussed in Section 2.5.4.1, a number of radiocarbon dates exist for sediments within Tauranga Harbour. Several dates exist for the coastal sand facies, ranging

from 6,790 ± 100 yr BP (Davis and Healy, 1993) to 106.6 ± 0.2 yr BP (Christophers, 2015). Davis and Healy (1993) dated their 'esturaine mud' to 8,100 ± 80 yr BP, and Christophers (2015) dated a sandy peat at the base of Coastal Sands to be 7,676 ± 30 yr BP. I interpret this to suggest that sea level rise did not inundate the current harbour area until around 7,600 yr BP. The only date that exists for the Volcanic Sand facies is 9420 ± 100 yr BP (Davis and Healy, 1993). Several authors suggest these sediments and other silty sediments underlying these are from the Pleistocene (e.g. Healy et al. (2009), Moon et al. (2013), de Lange et al. (2014), Christophers (2015)). However, there are no dates to prove this. They assert it though as it seems logical that the underlying sediments would be inundated by the Holocene marine transgression, creating the unconformity. I interpret the Pumiceous Sand to represent very recent sedimentation because of its stratigraphic position. However, no dates exist for this.

Davis and Healy (1993) developed a chronology of the different paleogeographic settings for Tauranga Harbour (Figure 6.2). Using data obtained during this research and from other more recent research, I present an updated chronology for the harbour (Figure 6.3). It begins over 10,000 years ago during the Pleistocene, with a braided river system approximately 300 m across (Figure 6.3a). Multiple shallow channels were present, with small swamps and lakes with peat formations nearby (Moon et al., 2013). Moon et al. (2013) suggest that this environment was then inundated by sea level rise, which they suggest to represent Marine Oxygen Isotope Stage 11 approximately 427,000 years ago, as this is the most similar to present-day conditions. No dates exist however to confirm this, so this has not been included in Figure 6.3.

This was followed by terrestrial deposition of Volcanic Sands which were then eroded to create the ridge and valley topography that underlies the harbour (Moon et al., 2013). This is followed by the development of a lake (the lacustrine silt) in the Stella Passage – Maunganui Roads area (Figure 6.3b). This would have been a shallow lake, 1–1.5 km across. The sediment within this lake is sourced from the Volcanic Sands. This lake would have had a fluvial input close to VC12, however flow velocity will have been slow. The lake was likely thermally stratified, creating anoxic conditions at the base of the lake. This led to the dissolution of diatoms. The lake was relatively shallow and likely had a short lifespan.

This lake probably survived up until 7,600 yr BP, when Holocene sea level rise inundates the area and the deposition of coastal sands commences, leading to the creation of the barrier island (Matakana Island) (Figure 6.3c) and the tombolo (Mount Maunganui) (Figure 6.3d). This barrier island likely contained two tidal inlets until ~5000 yr BP and then ~3,500 yr BP (Figure 2.9) (Shepherd et al., 1997, 2000; de Lange et al., 2015). As the barrier island continues to form, however, these were blocked, and this led to the development of the southern harbour inlet, in roughly

its present day position. The inlet narrows overtime, however it is held in place by the Mount Maunganui rhyolite dome (de Lange et al., 2015). During this period, an influx of sediment was brought in from offshore (the Coastal Sand facies). The influx of sediment offshore has been limited by the development of the Matakana barrier island and the Mount Maunganui tombolo, leading to sediment input from cliff erosion from around the harbour. This has accumulated as sand waves that migrate through the dredged channel (the Pumiceous Sand facies).

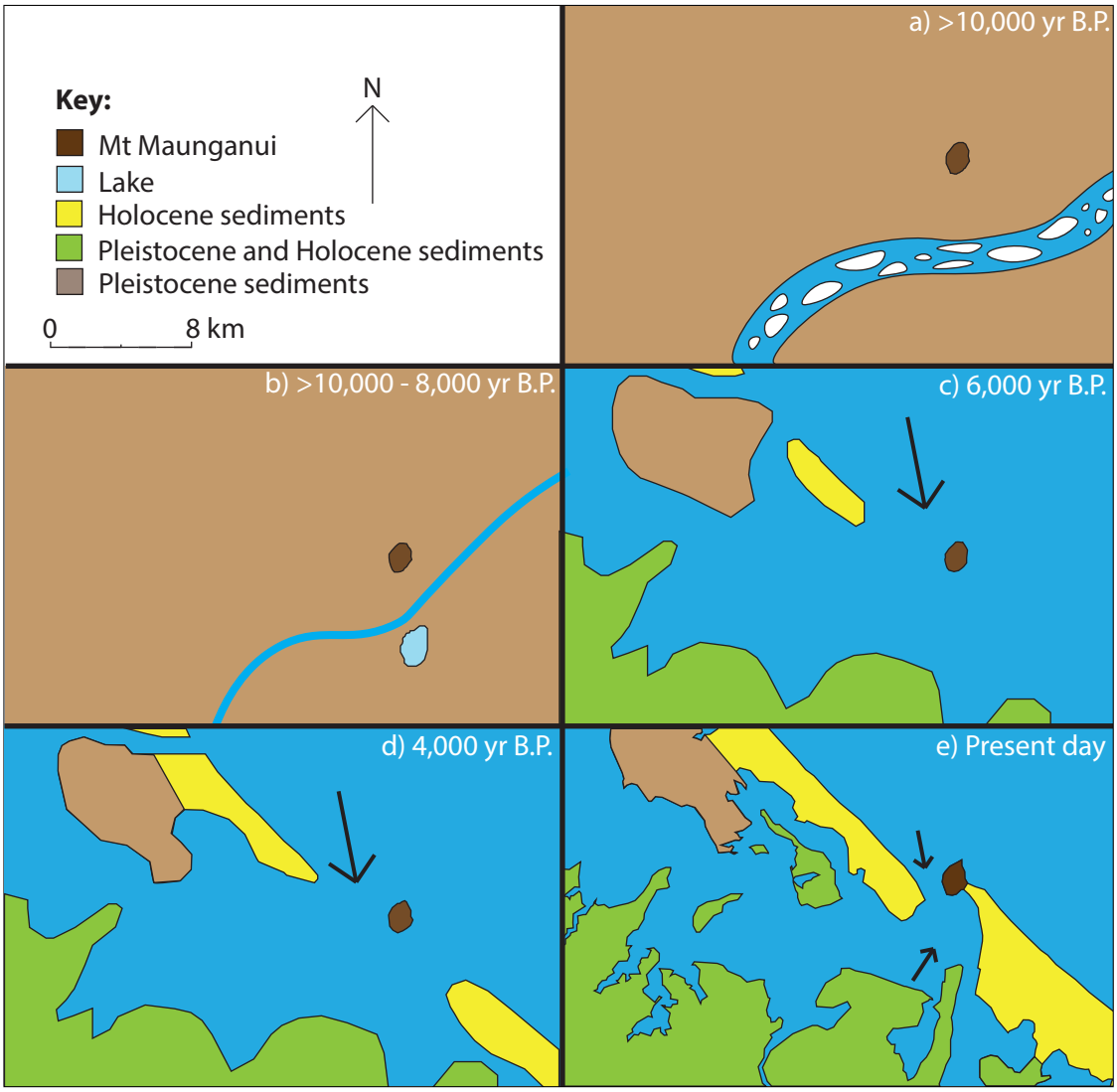

Figure 6.3: Chronology of Tauranga Harbour proposed by this study. It shows the presence of a braided river channel (a) transporting coarse sediment through the region. Then between >10,000 - 8,000 yr B.P. a lake develops in the area of what is now Stella Passage, with an alluvial system proposed to be nearby (b). Then following the Holocene marine transgression, sand spits begin to form, and the coastal sands facies is deposited. At 6,000 yr B.P. two inlets exist in Matakana island. Around 5,000 yr B.P. one of these closes up (d). Coastal sands continue to develop, leading to the creation of the Mount Maunganui tombolo.

Chapter 7

Conclusion

Summary of Research Findings

The objectives for this research are listed below:

1. Describe 86 vibracores, and use conduct grain size, optical mineralogy, magnetic susceptibility and geochemical analysis on samples. This objective was achieved in Chapter 4.

2. Conduct a facies analysis on the identified lithologies. This was achieved in Chapter 4 and summarised in Table 4.8.

3. Develop a 3-D stratigraphic model of the subsurface of Tauranga Harbour. This was achieved in Chapter 5. However, the model is limited in scope outside of the dredged shipping channel.

Lithological Facies

Four main facies were identified in this research:

- The **Volcanic Sands** (VS) facies was found in Stella Passage, Maunganui Roads South, Cutter Channel and the Entrance Channel. It is assumed that this facies underlies the entire channel. It is commonly massive, poorly sorted silt to fine sands. VS units are usually composed of volcanic glass shards, lithics, plagioclase, quartz and hornblende. Geochemically, they are high in potassium and low in sulphur and calcium. I interpret this facies to be a series of tephras, deposited in a terrestrial environment.

- The **Silt** (S) facies is found in Maunganui Roads South and Maunganui Roads. It is a massive, poorly sorted silt. It is rich in lithics, but also contains trace amounts of plagioclase and bioclasts. Geochemically, it has high aluminium and iron, but low calcium and barium. I interpret this facies to be a lacustrine

deposit, sourced from reworked VS units. It was deposited in an anoxic environment, and the lake likely had a short lifespan. The lake had a source close to VC12, where fluvial material is deposited.

- The **Coastal Sand** (CS) facies is found in Maunganui Roads South, Maunganui Roads, Cutter Channel, and the Entrance Channel. It is a massive, moderately sorted, medium to coarse sand. Compositionally, it contains plagioclase, quartz, lithics, bioclasts and hornblende. Geochemically, it has a high Si/Al ratio and a low Zr/Fe ratio. I interpret this facies to be deposited in a highly productive shallow marine coastal environment, during the Holocene marine transgression.

- The **Pumiceous Sand** (PS) facies is found at the tops of cores in Maunganui Roads South, Maunganui Roads, Cutter Channel, and the Entrance Channel. It is a massive, poorly sorted medium to coarse sand. It contains well rounded pumice clasts. Compositonally, it contains volcanic glass, lithics, plagioclase, quartz, and bioclasts. It is high in potassium, and has an elevated Zr/Fe ratio. I interpret this facies to be formed in a marine environment, sourced from ignimbrites eroding around the harbour. This facies forms sand waves in the shipping channel.

Source Changes

During the deposition of the Volcanic Sands facies, the source was from local or regional volcanics, likely the Taupo Volcanic Zone. During the deposition of the lacustrine Silt facies, the sediment is sourced from the VS facies. The Holocene marine transgression then brings an influx of coarse, CS sediment to the harbour, inundating the VS and S successions. The development of Matakana Island and the Mount Maunganui tombolo limits sediment supply from outside the harbour, leading to increased sedimentation from within the harbour. The erosion of ignimbrite cliffs from around the harbour leads to the deposition of the PS facies.

Distribution

The 3-D model of the harbours stratigraphy shows a several ridges of the VS facies oscillating close to the surface in Cutter Channel and the Entrance Channel. In Stella Passage this ridge is already at the surface, having been partially dredged through in the past. In Maunganui Roads there is a ridge of the Silt facies which in one area reaches the surface. Draped over this ridge and valley topography is the Coastal Sands facies.

Paleogeography

Over 10,000 yr BP the region was a terrestrial environment with a braided river. This is then followed by deposition of the VS facies from subsequent volcanic eruptions. Between >10,000 and 8,000 yr BP, there is development of a lacustrine environment in which the S facies is deposited. This is then followed by the Holocene marine transgression approximately 7,600 yr BP, bringing an influx of offshore sediment and the deposition of the CS facies. This influx of sediment caused the development of the Matakana barrier island and the Mount Maunganui tombolo, limiting sediment supply from offshore. This lead to a greater proportion of sediment coming from within the harbour. The erosion of ignimbrite cliff faces has contributed to this modern sedimentation, and lead to the deposition of the PS facies in sand waves through the dredge channel.

Further Research

Further research into the harbour should consider the following areas:

- **Dates.** A variety of dates exist for the upper parts of the harbour stratigraphy. However it has been asserted by prior researchers that much of the silty sediment beneath the CS and PS is of Pliestocene age. However, no dates exist to prove this. Dating these sediments would help identify the source of the VS sediments (likely Taupo volcanic zone), the lifespan of the lacustrine environment around Maunganui Roads, and whether or not the quartz sands identified by Moon et al. (2013) are indeed from Marine Oxygen Isotope Stage 11 approximately 427,000 years ago. Dating these sediments is difficult however, as radiocarbon dating is is only useful up to around 40,000 yr BP (Prescott and Robertson, 1997). As the volcanic sands sediments identified are reworked in some parts, other types of dating could be difficult (Rasmussen, 2005).

- **Distribution of sediments outside of the shipping channel.** This study (and others) have focussed almost entirely on the stratigraphy of the shipping channel. However, little is known about the distribution of the sediments outside the channel. Such research could investigate whether the ebb-tidal delta is draped over silty terrestrial sediments.

- **Distibution of the sediments beneath the VS facies.** This study has focused on the stratigraphy of the sediments in the top 3-5 metres of the subsurface. Further research could consider the stratigraphy of the sediments beneath the VS facies (Healy et al., 2009; Moon et al., 2013; Upiap, 2015), which have been studied within Stella Passage but have not been extensively studied elsewhere in the shipping channel or the harbour as a whole.

References

Abrahim, G. M., Nichol, S. L., Parker, R. J., and Gregory, M. R. (2008). Facies depositional setting, mineral maturity and sequence stratigraphy of a Holocene drowned valley, Tamaki Estuary, New Zealand. *Estuarine, Coastal and Shelf Science*, 79(1):133–142.

Al-Dabbas, M. and McManus, J. (1987). Shell fragments as indicators of bed sediment transport in the Tay Estuary. *Proceedings of the Royal Society of Edinburgh. Section B. Biological Sciences*, 92(3-4):335–344.

Albarède, F. (2003). *Geochemistry*. Cambridge University Press.

Allaby, M., editor (2013). *Facies*. Oxford University Press, 4 edition.

ARANZ Geo Ltd (2015). Leapfrog geo.

Babu, N., Suresh Babu, D. S., and Mohan Das, P. N. (2006). Impact of tsunami on texture and mineralogy of a mjaor placer deposit in southwest coast of India. *Environmental Geology*, 52(1):71–80.

Bell, R. G., Goff, J., Downes, G., Berryman, K., Walters, R. A., Chagué-Goff, C., Barnes, P., and Wright, I. (2004). Tsunami Hazard for the Bay of Plenty and Eastern Coromandel Peninsula: Stage 2. Technical report, Environment Waikato, Hamilton. Environment Waikato Technical Report 2004/32.

Blanchet, C., Thouveny, N., and Vidal, L. (2009). Formation and preservation of greigite (Fe3S4) in sediments from the Santa Barbara Basin: Implications for paleoenvironmental changes during the past 35 ka. *Paleoceanography*, 24(2).

Blanchet, C. L., Thouveny, N., Vidal, L., Leduc, G., Tachikawa, K., Bard, E., and Beaufort, L. (2007). Terrigenous input response to glacial/interglacial climatic variations over southern Baja California: a rock magnetic approach. *Quaternary Science Reviews*, 26(25–28):3118 – 3133.

Blott, S. J. and Pye, K. (2001). GRADISTAT: a grain size distribution and statistics package for the analysis of unconsolidated sediments. *Earth surface processes and Landforms*, 26(11):1237–1248.

Boggs, S. J. (2009). *Petrology of Sedimentary Rocks*. Cambridge University Press.

Boggs, S. J. (2011). *Principles of Sedimentology and Stratigraphy*. Cambridge University Press.

Brannigan, A. M. (2009). Change in geomorphology, hydrodynamics and surficial sediment of the Tauranga Entrance tidal delta system. Master's thesis, University of Waikato, New Zealand.

Briggs, R., Hall, G., Harmsworth, G., Hollis, A., Houghton, B., Hughes, G., Morgan, M., and Whitbread-Edwards, A. (1996). Geology of the Tauranga Area. Occassional Report 22, Bay of Plenty Regional Council; University of Waikato; Institute of Geological and Nuclear Sciences Limited.

Briggs, R., Houghton, B., McWilliams, M., and Wilson, C. (2005). 40Ar/39Ar ages of silicic volcanic rocks in the Tauranga-Kaimai area, New Zealand: Dating the transition between volcanism in the Coromandel Arc and the Taupo Volcanic Zone. *New Zealand Journal of Geology and Geophysics*, 48(3):459–469.

Briggs, R. M. and Fulton, B. W. J. (1990). Volcanism, structure and petrology of the Whiritoa-Whangamata coastal section, Coromandel Volcanic Zone, New Zealand: Facies model evidence for the Tunaiti caldera. *New Zealand Journal of Geology and Geophysics*, 33(4):623–633.

Brunsack, H. J. and Gieskes, J. M. (1983). Interstitial water trace-element chemistry of laminated sediments from the Gulf of California, Mexico. *Marine Chemistry*, 14:89–106.

Cardinal, D., Savoye, N., Trull, T. W., André, L., Kopczynska, E. E., and Dehairs, F. (2005). Variations of carbon remineralisation in the southern ocean illustrated by the baxs proxy. *Deep Sea Research Part I: Oceanographic Research Papers*, 52(2):355 – 370.

Christophers, A. (2015). Paleogeomorphic reconstruction of the Omokoroa Domain, Bay of Plenty, New Zealand. Master's thesis, University of Waikato.

Clement, A. J. H., Sloss, C. R., and Fuller, I. C. (2010). Late Quaternary geomorphology of the Manawatu coastal plain, North Island, New Zealand. *Quaternary International*, 221(1-2):36 – 45.

Collinson, J. D. (1969). The sedimentology of the Grindslow Shales and the Kinderscout Grit: a deltaic complex in the Namurian of northern England. *Journal of Sedimentary Research*, 39(1).

Cooper, R. A. and Agterberg, F. P. (2004). *The New Zealand geological timescale*, volume 22. Institute of Geological & Nuclear Sciences Limited.

Croudace, I. W. and Rothwell, R. G., editors (2015). *Twenty years of XRF core scanning marine sediments: what do geochemical proxies tell us?*, volume 17. Springer Science.

Dalrymple, R. W. (2010). Interpreting sedimentary successions: Facies, facies analysis and facies models. In James, N. P. and Dalrymple, R. W., editors, *Facies Models 4*, chapter 2, pages 3–19. Geological Association of Canada, Newfoundland, Canada.

Davey, F., Henrys, S., and Lodolo, E. (1995). Asymmetric rifting in a continental back-arc environment, North Island, New Zealand. *Journal of Volcanology and Geothermal Research*, 68(1):209–238.

Davis, R. A. and Healy, T. R. (1993). Holocene coastal depositional sequences on a tectonically active setting: southeastern Tauranga Harbour, New Zealand. *Sedimentary Geology*, 84(1):57–69.

de Lange, W., Moon, V., and Fox, B. (2014). Distribution of the silty sediments in the shallow subsurface of the shipping channels of Tauranga Harbour. Environmental Research Institute Report 43, University of Waikato, Environmental Research Institute, Faculty of Science and Engineering, The University of Waikato, Hamilton.

de Lange, W., Moon, V., and Johnsto, R. (2015). Evolution of the Tauranga Harbour entrance: Influences of tsunami, geology and dredging. In *Australasian Coasts and Ports Conference 2015*.

de Lange, W. P. (1988). *Wave climate and sediment transport within the Tauranga Harbour, in the vicinity of Pilot Bay*. PhD thesis, University of Waikato, Hamilton, New Zealand.

Dearing, J. (1999). Environmental magnetic susceptibility. *Using the Bartington MS2 System*.

Dearing, J. A., Elner, J. K., and Happey-Wood, C. M. (1981). Recent sediment flux and erosional processes in a Welsh upland lake-catchment based on magnetic susceptibility measurements. *Quaternary Research*, 16(3):356–372.

Dehairs, F., Baeyens, W., and Goeyens, L. (1992). Accumulation of suspended barite at mesopelagic depths and export production in the southern ocean. *Science*, 258(5086):1332–1335.

Demaison, G. and Moore, G. T. (1980). Anoxic environments and oil source bed genesis. *AApG Bulletin*, 64(8):1179–1209.

Dickson, A. J., Leng, M. J., Maslin, M. A., and Röhl, U. (2010). Oceanic, atmospheric and ice-sheet forcing of the South East Atlantic Ocean productivity and South African monsoon intensity during MIS-12 to 10. *Quaternary Science Reviews*, 29(27 - 29):3936 – 3947.

Donato, S., Reinhardt, E., Boyce, J., Rothaus, R., and Vosmer, T. (2008). Identifying tsunami deposits using bivalve shell taphonomy. *Geology*, 36(3):199–202.

Dougherty, A. J. and Dickson, M. E. (2012). Sea level and storm control on the evolution of a chenier plain, Firth of Thames, New Zealand. *Marine Geology*, 307-310:58 – 72.

Engel, M. and Brückner, H. (2011). The identification of palaeo-tsunami deposits–a major challenge in coastal sedimentary research. *Coastline Reports*, 17:65–80.

Friedman, G. M. (1967). Dynamic processes and statistical parameters compared for size frequency distribution of beach and river sands. *Journal of Sedimentary Research*, 37(2):327–354.

Friedman, G. M. (1979). Address of the retiring President of the International Association of Sedimentologists: Differences in size distributions of populations of particles among sands of various origins. *Sedimentology*, 26(1):3.

Froggatt, P. C. and Lowe, D. J. (1990). A review of late Quaternary silicic and some other tephra formations from New Zealand: their stratigraphy, nomenclature, distribution, volume, and age. *New Zealand journal of geology and geophysics*, 33(1):89–109.

Funk, J., Von Dobeneck, T., and Reitz, A. (2003). Integrated rock magnetic and geochemical quantification of redoxomorphic iron mineral diagenesis in late quaternary sediments from the equatorial atlantic. In *The South Atlantic in the Late Quaternary*, pages 237–260. Springer.

Gale, S. J. and Hoare, P. G. (1991). *Quaternary sediments: petrographic methods for the study of unlithified rocks*. New York.

Gibb, J. (1986). A New Zealand regional Holocene eustatic sea-level curve and its application to determination of vertical tectonic movements. *Royal Society of New Zealand Bulletin*, 24:377 – 385.

Graeam, L. M. (1995). Recolonistation of a relocated boulder reef in Tauranga Harbour, New Zealand. Master's thesis, University of Otago.

Hancock, N., Hume, T., and Swales, A. (2009). Tauranga Harbour Sediment Study: Harbour Bed Sediments. Unpublished Client Report HAM2008-123, NIWA.

Harmsworth, G. R. (1983). Quaternary stratigraphy of the Tauranga Basin. Master's thesis, University of Waikato.

Healy, J., Thompson, B., Schofield, J., and Survey, N. Z. G. (1964). *Geological Map of New Zealand 1: 250, 000 Sheet 5. Rotorua*. Department of Scientific and Industrial Research.

Healy, T. and Roberts, S. (1997). Analysis of bottom sediment samples from the Stella Passage. Report to port of tauranga ltd., University of Waikato.

Healy, T., Thompson, G., Grace, R., and Spiers, K. (2009). Assessment of Environmental Effects for Port of Tauranga Channel Deepening and Widening. Technical report, University of Waikato, Port of Tauranga Limited, Salsbury Avenue, Mount Maunganui, New Zealand.

Heap, A. and Nichol, S. (1997). The influence of limited accommodation space on the stratigraphy of an incised-valley succession: Weiti River estuary, New Zealand. *Marine Geology*, 144(1):229–252.

Hepp, D. A., Mörz, T., Hensen, C., Frederichs, T., Kasten, S., Riedinger, N., and Hay, W. W. (2009). A late Miocene–early Pliocene Antarctic deepwater record of repeated iron reduction events. *Marine Geology*, 266(1):198–211.

Hodell, D. A., Channell, J. E., Curtis, J. H., Romero, O. E., and Röhl, U. (2008). Onset of "Hudson Strait" Heinrich events in the eastern North Atlantic at the end of the middle Pleistocene transition (640 ka)? *Paleoceanography*, 23(4).

Hollis, A. G. (1995). The Volcanic Geology of the Central Tauranga Basin. Master's thesis, University of Waikato.

Honjo, S., Fischer, A. G., and Garrison, R. (1965). Geopetal pyrite in fine-grained limestones. *Journal of Sedimentary Research*, 35(2).

Houghton, B. and Cuthbertson, A. (1989). Sheet T14 BD—Kaimai. *Geological map of New Zealand*, 1(50).

Houghton, B. F., Wilson, C. J. N., McWilliams, M. O., Lanphere, M. A., Weaver, S. D., Briggs, R. M., and Pringle, M. S. (1995). Chronology and dynamics of a large silicic magmatic system: Central Taupo Volcanic Zone, New Zealand. *Geology*, 23(1):13–16.

Huerta-Diaz, M. A. and Morse, J. W. (1992). Pyritization of trace metals in anoxic marine sediments. *Geochimica et Cosmochimica Acta*, 56(7):2681–2702.

Kear, D. (1994). A "least complex" dynamic model for late Cenozoic volcanism in the North Island, New Zealand. *New Zealand Journal of Geology and Geophysics*, 37(2):223–236.

Konfirst, M. A., Kuhn, G., Monien, D., and Scherer, R. P. (2011). Correlation of early pliocene diatomite to low amplitude milankovitch cycles in the andrill and-1b drill core. *Marine Micropaleontology*, 80(3–4):114 – 124.

Leonard, G. S., Begg, J. G., and Wilson, C. J. N. (2010). Geology of the Rotorua Area.

Michels, K. and Healy, T. (1998). Investigation of sediments to be dredged in the lower Town Reach - Upper Stella Passage and disposed of at an inner shelf dump ground. Technical report, University of Waikato.

Mohtadi, M., Romero, O. E., Kaiser, J., and Hebbeln, D. (2007). Cooling of the southern high latitudes during the medieval period and its effect on {ENSO}. *Quaternary Science Reviews*, 26(7–8):1055 – 1066.

Moon, V., de Lange, W., Jorat, M., Christophers, A., and Moerz, T. (2013). Subsurface stratigraphy of Stella Passage, Tauranga Harbour. Environmental Research Institute Report 28, Environmental Research Institute, Environmental Research Institute, Faculty of Science and Engineering, The University of Waikato, Hamilton.

Nathan, S. (1976). Geology of the Rotorua District. In *25th International Geological Congress Excursion Guide 55A*, pages 16–19.

Nentwig, V., Bahlburg, H., and Monthy, D. (2015). Sedimentology of coastal deposits in the Seychelles Islands—evidence of the Indian Ocean Tsunami 2004. *Pure and Applied Geophysics*, 172(3-4):641–656.

Nichols, G. (2009). *Sedimentology and stratigraphy*. John Wiley & Sons.

Opus International Consultants Ltd (2011). Sulphur Point Northern Wharf Extension - Port of Tauranga. Geotechnical Factual Report G2899, Opus International Consultants Ltd.

Oswald, J. and England, B. M. (1977). The relationship between euhedral and framboidal pyrite in base-metal sulfide ores. *Mineral Mag*, 43:297–300.

Paris, R., Lavigne, F., Wassmer, P., and Sartohadi, J. (2007). Coastal sedimentation associated with the December 26, 2004 tsunami in Lhok Nga, west Banda Aceh (Sumatra, Indonesia). *Marine Geology*, 238(1–4):93–106.

Peterson, M. and Carpenter, R. (1986). Arsenic distributions in porewaters and sediments of Puget Sound, Lake Washington, the Washington coast and Saanich Inlet, BC. *Geochimica et Cosmochimica Acta*, 50(3):353–369.

Port of Tauranga Ltd (2013). Port of Tauranga gains approval for harbour dredging. Press Release.

Prescott, J. and Robertson, G. (1997). Sediment dating by luminescence: a review. *Radiation Measurements*, 27(5–6):893 – 922.

Press, F. and Siever, R. (1986). *Earth*. New York: WH Freeman and Co, 4 edition.

Rasmussen, B. (2005). Radiometric dating of sedimentary rocks: the application of diagenetic xenotime geochronology. *Earth-Science Reviews*, 68(3–4):197 – 243.

Reineck, H.-E. and Singh, I. (1980). *Depositional Sedimentary Environments: With Reference to Terrigenous Clastics*. Springer Science & Business Media.

Ryves, D., Juggins, S., Fritz, S., and Battarbee, R. (2001). Experimental diatom dissolution and the quantification of microfossil preservation in sediments. *Palaeogeography, Palaeoclimatology, Palaeoecology*, 172(1–2):99 – 113.

Seminar, S. (1981). Comparison of methods of size analysis for sands of the Amazon-Solimões Rivers, Brazil and Peru. *Sedimentology*, 28(1):123–128.

Shepherd, M., Betts, H., McFadgen, B., and Sutton, D. (2000). Geomorphological evidence for a Pleistocene barrier at Matakana Island, Bay of Plenty, New Zealand. *New Zealand journal of geology and geophysics*, 43(4):579–586.

Shepherd, M., McFadgen, B., Betts, H., and Sutton, D. (1997). Formation, landforms and paleoenvironment of Matakana Island and implications for archaeology. *Science and Research Series, Department of Conservation*, page 102.

Sluijs, A., Bijl, P. K., Schouten, S., Röhl, U., Reichart, G.-J., and Brinkhuis, H. (2011). Southern ocean warming, sea level and hydrological change during the Paleocene-Eocene thermal maximum. *Climate of the Past*, 7(1):47–61.

Sluijs, A., Röhl, U., Schouten, S., Brumsack, H.-J., Sangiorgi, F., Sinninghe Damsté, J. S., and Brinkhuis, H. (2008). Arctic late Paleocene–early Eocene paleoenvironments with special emphasis on the Paleocene-Eocene thermal maximum (Lomonosov Ridge, Integrated Ocean Drilling Program Expedition 302). *Paleoceanography*, 23(1).

Sluijs, A., Schouten, S., Donders, T. H., Schoon, P. L., Röhl, U., Reichart, G.-J., Sangiorgi, F., Kim, J.-H., Damsté, J. S. S., and Brinkhuis, H. (2009). Warm and wet conditions in the Arctic region during Eocene Thermal Maximum 2. *Nature Geoscience*, 2(11):777–780.

Spiers, K. C., Healy, T., and Winter, C. (2009). Ebb-jet dynamics and transient eddy formation at Tauranga Harbour: Implications for Entrance Channel shoaling. *Journal of Coastal Research*, 22(3):720 – 727.

Srisutam, C. and Wagner, J. (2009). Tsunami sediment characteristics at the Thai Andaman Coast. *Pure and Applied Geophysics*, 167(3):215–232.

Statistics New Zealand (2013). Tauranga city. http://www.stats.govt.nz/Census/2013-census/profile-and-summary-reports/quickstats-about-a-place.aspx?request_value=13878&tabname. Census data. Site Accessed: 24-02-2016.

Staudigel, H. and Hart, S. R. (1983). Alteration of basaltic glass: Mechanisms and significance for the oceanic crust-seawater budget. *Geochimica et Cosmochimica Acta*, 47(3):337–350.

Sullivan, L. A. and Koppu, T. J. (1998). Iron staining of quartz beach sand in south eastern australia. *Journal of Coastal Research*, 14(3):992–999.

Syvitski, J. P. (2007). *Principles, methods and application of particle size analysis*. Cambridge University Press.

Tanner, W. F. (2007). Application of suite statistics to stratigraphy and sea-level changes. In Syvitski, J. P., editor, *Principles, methods and application of particle size analysis*, pages 285–292. Cambridge University Press.

Thompson, C. (1992). Genesis of podzols on coastal dunes in southern Queensland. I. Field relationships and profile morphology. *Soil Research*, 30(5):593–613.

Thompson, C. H. and Bowman, G. (1984). *Subaerial denudation and weathering of vegetated coastal dunes in eastern Australia*. Academic Press.

Thompson, G. (2010). Evidence of Geoffrey Thompson. Evidence given in resource consent applications by Port of Tauranga Limited.

Thompson, R., Battarbee, R., O'Sulliuan, P., and Oldfield, F. (1975). Magnetic susceptibility of lake sediments. *Limnology*.

Thomson, J., Croudace, I., and Rothwell, R. (2006). A geochemical application of the ITRAX scanner to a sediment core containing eastern Mediterranean sapropel units. *Geological Society, London, Special Publications*, 267(1):65–77.

Upiap, J. (2015). Special topic research report. Univeristy of Waikato.

van Os, B. J., Middelburg, J. J., and de Lange, G. J. (1991). Possible diagenetic mobilization of barium in sapropelic sediment from the eastern mediterranean. *Marine Geology*, 100(1–4):125 – 136. Anoxic Basins and Sapropel Deposition in the Eastern Mediterranean: Past and Present.

Vucetich, C. t. and Pullar, W. (1969). Stratigraphy and chronology of late Pleistocene volcanic ash beds in central North Island, New Zealand. *New Zealand journal of geology and geophysics*, 12(4):784–837.

Wentworth, C. K. (1922). A scale of grade and class terms for clastic sediments. *The Journal of Geology*, pages 377–392.

Whitbread-Edwards, A. N. (1994). The Volcanic Geology of the Western Tauranga Basin. Master's thesis, University of Waikato.

Wilkin, R. and Barnes, H. (1997). Formation processes of framboidal pyrite. *Geochimica et Cosmochimica Acta*, 61(2):323 – 339.

Wilkin, R., Barnes, H., and Brantley, S. (1996). The size distribution of framboidal pyrite in modern sediments: An indicator of redox conditions. *Geochimica et Cosmochimica Acta*, 60(20):3897 – 3912.

Wilson, C., Rogan, A., Smith, I., Northey, D. J., Nairn, I., and Houghton, B. (1984). Caldera volcanoes of the Taupo volcanic zone, New Zealand. *Journal of Geophysical Research: Solid Earth*, 89(B10):8463–8484.

Wilson, K., Berryman, K., Cochran, U., and Little, T. (2007). A Holocene incised valley infill sequence developed on a tectonically active coast: Pakarae River, New Zealand. *Sedimentary Geology*, 197(3):333–354.

Woodward, D. J. and Ferry, L. M. (1973). *Sheet 5, Rotorua (1st Ed) Gravity Map of New Zealand, 1:250 000. Bouger Anomalies; Isostatic Anomalies; Isostatic Vertical Gradient Anomoalies*. Department of Scientific and Intustrial Research, Wellington, New Zealand.

Yamazaki, T. (2012). Paleoposition of the Intertropical Convergence Zone in the eastern Pacific inferred from glacial-interglacial changes in terrigenous and biogenic magnetic mineral fractions. *Geology*, 40(2):151–154.

Yokoyama, Y., Maeda, Y., Okuno, J., Miyairi, Y., and T., K. (in press). Holocene Antarctic melting and lithospheric uplift history of the southern Okinawa trough inferred from mid- to late-Holocene sea level in Iriomote Island, Ryukyu, Japan. *Quaternary International*, page 7. doi:10.1016/j.quaint.2015.03.030.